THREE-DIMENSIONAL FINITE-ELEMENT TIME-DOMAIN MODELING OF THE MARINE CONTROLLED-SOURCE ELECTROMAGNETIC METHOD

A DISSERTATION
SUBMITTED TO THE DEPARTMENT OF GEOPHYSICS
AND THE COMMITTEE ON GRADUATE STUDIES
OF STANFORD UNIVERSITY
IN PARTIAL FULFILLMENT OF THE REQUIREMENTS
FOR THE DEGREE OF
DOCTOR OF PHILOSOPHY

Evan Schankee Um

March 2011

Abstract

The marine controlled-source electromagnetic (CSEM) method detects and images electrical resistivity associated with hydrocarbon, gas and CO_2 reservoirs. Its survey design and data interpretation require modeling of complex and often subtle offshore geology with accuracy and efficiency. In this dissertation, I develop two efficient finite-element time-domain (FETD) algorithms for the simulation of three-dimensional (3D) electromagnetic (EM) diffusion phenomena. The two FETD algorithms are used to investigate the time-domain CSEM (TDCSEM) method in realistic shallow offshore environments and the effects of seafloor topography and seabed anisotropy on the TDCSEM method.

The first FETD algorithm directly solves electric fields by applying the Galerkin method to the electric-field diffusion equation. The time derivatives of the magnetic fields are interpolated at receiver positions via Faraday's law only when the EM fields are output. Therefore, this approach minimizes the total number of unknowns to solve. To ensure both numerical stability and an efficient time-step, the system of FETD equations is discretized using an implicit backward Euler scheme. A sparse direct solver is employed to solve the system of equations. In the implementation of the FETD algorithm, I effectively mitigate the computational cost of solving the system of equations at every time step by reusing previous factorization results. Since the high frequency contents of the transient electric fields attenuate more rapidly in time, the transient electric fields diffuse increasingly slowly over time. Therefore, the FETD algorithm adaptively doubles a time-step size, speeding up simulations. Comparisons with analytical solutions, 3D finite-difference time-domain (FDTD) solutions and field data demonstrate the accuracy and efficiency of the FETD algorithm.

Although the first FETD algorithm has the minimum number of unknowns, it still requires a large amount of memory because of its use of a direct solver. To mitigate this problem, the second FETD algorithm is derived from a vector-and-scalar potential equation that can be solved with an iterative method. The time derivative of the Lorenz gauge condition is used to split the ungauged vector-and-scalar potential

equation into a diffusion equation for the vector potential and Poisson's equation for the scalar potential. The diffusion equation for the time derivative of the magnetic vector potentials is the primary equation that is solved at every time step. Poisson's equation is considered a secondary equation and is evaluated only at the time steps where the electric fields are output. A major advantage of this formulation is that the system of equations resulting from the diffusion equation not only has the minimum number of unknowns but also can be solved stably with an iterative solver in the static limit. The accuracy and efficiency of the Lorenz-gauge FETD algorithm is verified through comparisons with analytical and 3D FDTD solutions. The detailed comparisons between the two FETD algorithms are presented.

The developed FETD algorithms are used to simulate the TDCSEM method in shallow offshore models that are derived from SEG salt model. In the offshore models, horizontal and vertical electric-dipole-source configurations are investigated and compared with each other. FETD simulation and visualization play important roles in analyzing the EM diffusion of the TDCSEM configurations. The partially-'guided' diffusion of transient electric fields through a thin reservoir is identified on the cross-section of the seabed models. The modeling studies show that the TDCSEM method effectively senses the localized reservoir close to the large-scale salt structure in the shallow offshore environment. Since the reservoir is close to the salt, the non-linear interaction of the electric fields between the reservoir and the salt is observed both on the cross-section and along the seafloor.

Regardless of whether a horizontal or vertical electric-dipole source is used in the shallow offshore models, inline vertical electric fields at intermediate-to-long offsets are approximately an order of magnitude smaller than horizontal counterparts due to the effect of the air-seawater interface. Consequently, the vertical electric-field measurements become vulnerable to the receiver tilt that results from the irregular seafloor topography. The 3D modeling studies also illustrate that the short-offset VED-E_x configuration is very sensitive to a subtle change of the seafloor topography around the VED source. Therefore, the VED-E_x configuration is vulnerable to measurements and modeling errors at short offsets. In contrast, the VED-E_z

configuration is relatively robust to these problems and is considered a practical short-offset configuration. It is demonstrated that the short-offset configuration can be used to estimate the lateral extent and depth of the reservoir.

Vertical anisotropy (i.e. transverse isotropy) in background also significantly affects the pattern in electric field diffusion by elongating and strengthening the electric field in the horizontal direction. As the degree of vertical anisotropy increases, the vertical resistivity contrast across the reservoir interface decreases. As a result, the week reservoir response is increasingly masked by the elongated and strengthened background response. Consequently, the TDCSEM method loses its sensitivity to the reservoir. The modeling studies show that correct interpretations of TDCSEM measurements require accurately modeling of irregular seafloor topography and seabed anisotropy.

Acknowledgements

First, I would like to express my sincere gratitude to my advisor, Jerry Harris for his guidance, support, and encouragements during my graduate studies. Through numerous research meetings with him, I learned not only geophysical insights and wisdom but also how to communicate scientific ideas.

My sincere gratitude goes out to my co-advisor, David Alumbaugh at Schlumberger-EMI and UC-Berkeley. He has provided crucial guidance and support at every moment during my graduate studies since 2003. Without his guidance, I could not have turned myself into an electromagnetic geophysicist.

I would like to express my sincere gratitude to my academic committee members, Margot Gerritsen and Rosemary Knight. They were willing to serve as my committee members although my research topics were rare in school of earth sciences. It was always wonderful to have their insightful suggestions and criticisms even during such short annual reviews and qualifying exam. Tapan Mukerji kindly served as a university chair in my defense.

Several other people also deserve my thanks for their help. Nestor Cuevas at EMI provided profound discussions about electromagnetic theories. Jiuping Chen at EMI taught me about how to use and modify his inversion code. Discussions with Seunghee Lee, a former EMI scientist helped me to understand electromagnetic geophysics in many different ways. My thanks also extend to other EMI people for their kindness whenever I visited EMI.

Professor Andreas Hördt at Institute for Geophysics and Extraterrestrial Physics kindly provided field data for me. Mike Commer and Gregory Newman at Lawrence Berkeley National Laboratory allowed me to use their finite-difference codes since 2003. Ryang-Hyun Cho, a computer scientist at Daum answered my numerous questions. Claude Reichard, the director at Technical Writing Program kindly helped me to improve my journal articles. Gboyega Ayeni (Stanford Exploration Project) kindly provided the SEG Salt Model.

I express my thanks to Stanford Wave Physics (SWP) people: Yemi Arogunmati, Claudia Baroni, Jolene Robin-McCaskill, Armando Sena, Bouko Vogelaar, Youli Quan, and Tieyuan Zhu. I express my special thanks to Yemi, Jolene, Armando and Bouko for proofreading my dissertation and articles. The collaboration with Professor Haohuan Fu at Tsinghua University was an excellent opportunity to learn his advanced programming practices. I also thank to Tara Ilich, Student Service Manager in Geophysics for her kind help through my PhD studies.

I wish to express my thanks for financial support during my graduate studies. The support includes a Littlefield Fellowship from the School of Earth Sciences (2006), a ConocoPhilips Fellowship (2007), the Mrs. C. J. Belani Fellowship for Computational Geosciences from the Stanford Center for Computational Earth and Environmental Science (2008), and a Chevron Stanford Graduate Fellowship (2008 to 2011).

Last but not the least, I would like to express my love and gratitude to my parents, Chung-In and Kwang-Sook. Their emphasis on education drove me to the completion of my graduate studies. I always thank my brother Eugene for his emotional support and for taking care of my parents during my long absence. I also express my deep gratitude to my parents-in-law for their support and prayer for my wife Bo Young and me. Finally, my gratitude goes to Bo Young. I have always felt happy to share my life with you **.

Contents

List of Tables

List of Figures

Chapter 1. Introduction

The main foci of this dissertation are two-fold: to develop efficient finite-element time-domain (FETD) algorithms for the simulation of electromagnetic (EM) diffusion phenomena in general anisotropic conductive earth media, and to investigate the diffusion physics of the marine controlled-source electromagnetic (CSEM) method in representative shallow offshore models through FETD numerical modeling experiments. This chapter introduces the research motivation and goals of this dissertation by introducing a traditional marine CSEM method, the expanded use of CSEM in shallow water environments, and computational EM geophysics relevant to CSEM simulations.

1.1 Brief introduction to the marine CSEM method

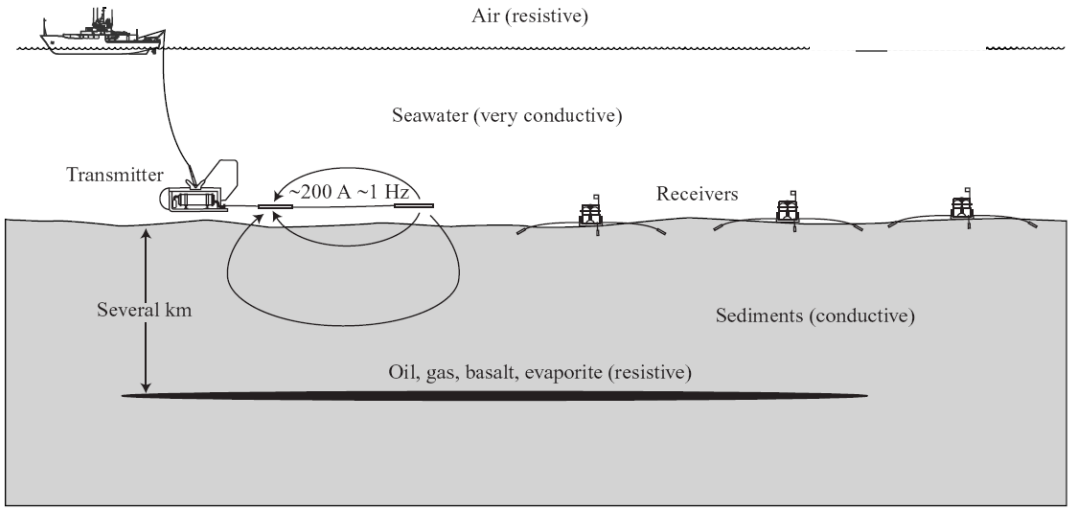

Figure 1.1. Conceptual diagram of the marine CSEM method (modified from Weiss and Constable, 2006).

The marine CSEM method (Figure 1.1) was originally developed in academia for crustal research and methane hydrates mapping in recent decades (Young and Cox, 1981; Cox et al., 1986; Cheesman et al., 1987; Yu and Edwards, 1992; Edwards,

1997). Since the CSEM method first succeeded in identifying hydrocarbon reservoirs in offshore Angola (Eidesmo et al., 2002), the method has rapidly evolved from an anomaly detection tool to a sophisticated acquisition and multi-dimensional modeling-based tool for imaging hydrocarbon reservoirs (Abubakar et al, 2008; Commer and Newman, 2008). The method typically employs a towed electric-dipole source and an array of seafloor receivers. The source is usually towed just a few tens of meters above the seafloor to ensure the maximum coupling between the generated EM fields and the seabed. The measured seafloor EM fields are analyzed to estimate the electrical resistivity structure of the seabed. The fundamental physics of the marine CSEM method and other details are presented in Chapter 2.

For exploration purposes, the marine CSEM method is typically operated in the frequency domain. The sensitivity of the frequency-domain CSEM (FDCSEM) method to a reservoir is influenced not only by its acquisition layout but also by the seawater depth (Um and Alumbaugh, 2007; Andréis and MacGregor, 2008; Chave, 2009). As the seawater depth gradually decreases, the 'airwave' is increasingly less attenuated through the seawater column. The strong 'airwave' starts to mask a weak reservoir response at seafloor receivers. Consequently, the FDCSEM method loses its sensitivity to the reservoir. Several approaches have been proposed to overcome the 'airwave' effect in shallow water, but the effectiveness of the approaches depends on characteristics of the noise and reservoir signal levels relative to the 'airwave' (Weidelt, 2007; Chen and Alumbaugh, 2009).

Compared with the FDCSEM method, the time-domain CSEM (TDCSEM) method is relatively new as a marine hydrocarbon exploration tool but has recently been recognized as an alternative to the FDCSEM method in shallow water (Weiss, 2007; Chave, 2009). When an impulsive current is injected, some EM energy diffuses upward through a shallow water column, propagate through the atmosphere and diffuse back through the water column. The shallower the water column is, the earlier the 'airwave' arrives at receiver locations. In contrast, a deep reservoir response arrives slowly through the conductive seabed. Thus, in shallow water, the 'airwave' response can be separated from the reservoir response due to different arrival times of the two

responses. Therefore, in shallow water and land environments, the TDCSEM method can be an useful alternative to the FDCSEM method.

In this dissertation, I present a three-dimensional (3D) numerical modeling analysis of the TDCSEM method in complex shallow offshore models that have been derived from a representative seismic model. This comprehensive modeling analysis provides a detailed investigation of 1) the essential diffusion phenomena of the TDCSEM method for shallow-water hydrocarbon explorations, 2) the sensitivity of various TDCSEM configurations, and 3) the effects of seafloor topography and seabed anisotropy on the TDCSEM method.

However, modeling transient EM diffusion phenomena in such complex earth models can be extremely computationally intensive and has been an important research topic in computational EM geophysics for many years (Everett and Edwards, 1992; Wang and Hohmann, 1993; Commer and Newman, 2004; Börner et al., 2008). The next subsection reviews a finite-difference time-domain (FDTD) method, which is the most popular computational EM method applicable to the modeling research above, and compares it with a finite-element time-domain (FETD) method that I will use in my research.

1.2 FDTD and FETD modeling

Introduced by Goldman and Stoyer (1983) for EM geophysics, FDTD methods have become one of the standard tools used to simulate EM methods in geophysics. Their popularity is due to the fact that FDTD methods are relatively straightforward to implement, highly efficient, and can provide accurate solutions over a wide range of EM simulations. Among the variety of FDTD algorithms, the most popular one is probably a 3D FDTD algorithm coupled with a staggered grid technique and the Du Fort-Frankel method (Wang and Hohmann, 1993). As EM geophysics research increasingly resorts to larger and larger models, this particular FDTD algorithm has been translated into a parallel computational version (Commer and Newman, 2004).

Although the 3D FDTD algorithm has enjoyed considerable popularity, it also has well known drawbacks. Its practical weakness is that large complex geological

structures (e.g. topography, salt domes and reservoirs), which do not conform to rectangular grids, need to be captured by a stair-step approximation. The stair-step approximation might seem to adequately model significant inhomogeneity using a series of very small grids in a parallel-computing environment. However, the stair-step modeling approach can introduce unnecessarily small grid spacing, resulting in an inefficiently small time step size in the Du Fort-Frankel method.

Alternatively, this dissertation presents FETD algorithms. In contrast to FDTD methods, FETD methods are based on a geometry-conforming unstructured mesh and allow precise representations of arbitrarily irregular topography and complex geological structures in a computationally elegant way. Even for an earth model that confirms to rectangular grids, FETD methods provide much more efficient spatial discretization than FDTD methods.

To illustrate this aspect, Figure 1.2 shows a simple rectangular reservoir model.

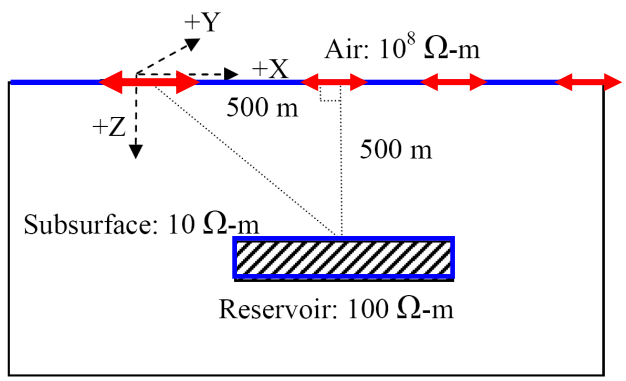

Figure 1.2. The cross-sectional view of the reservoir model with the survey configuration. The large and small red arrows are a source and receivers, respectively.

When the reservoir model is discretized, both FDTD and FETD models need to employ small cells around the source to handle high-frequency EM fields at early times (Figures 1.3a and 1.3c).

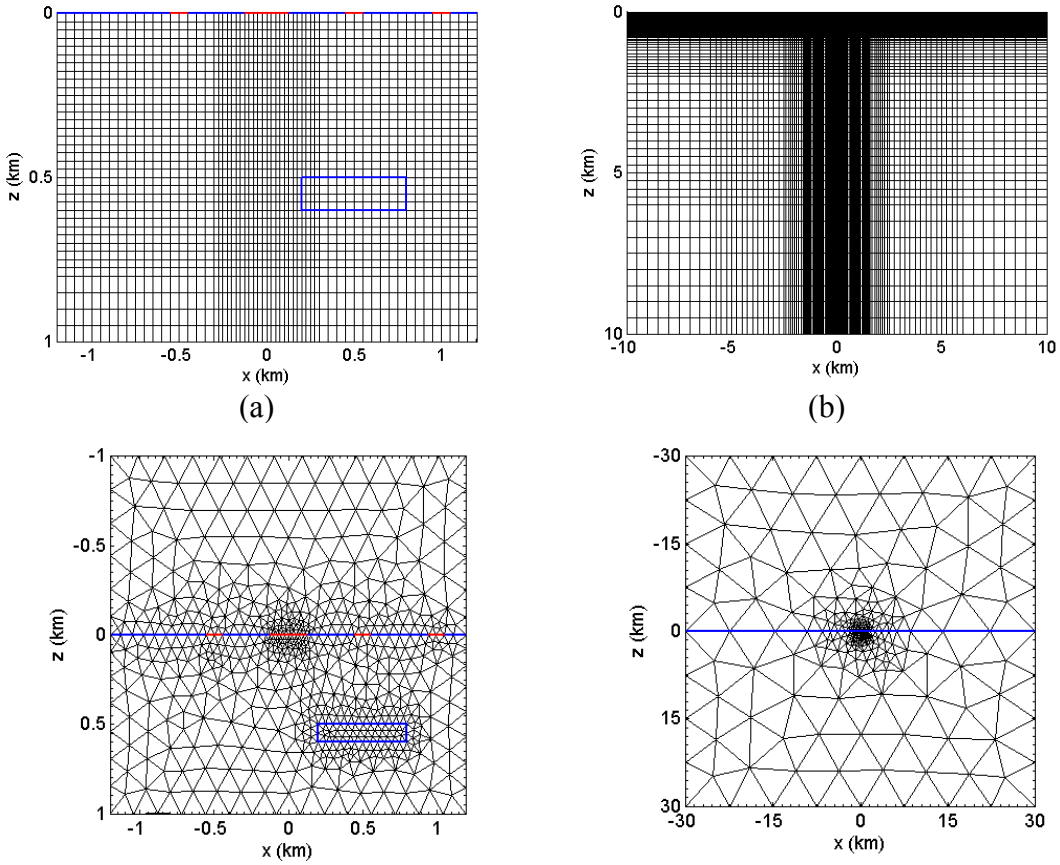

Figure 1.3. Cross-sectional views of FDTD grids and FETD meshes for the reservoir model shown in Figure 1.2. (a) The central portion of the half-space FDTD grids. (b) The entire view of the FDTD grids. (c) The central portion of the whole-space FETD meshes. (d) The entire domain of the FETD mesh. The air-earth interface at z=0 km is blue. In (a) and (c), the blue rectangular box represents the reservoir. The red line at x = 0 km is an electric-dipole source. The other small red lines at z = 0 km are receivers.

However, the fine FD cells need to extend to the computational boundaries of the model due to the structured nature of the FD grids (Figure 1.3b). In contrast, the fine FE cells quickly grow away from the source (Figure 1.3d). Consequently, in transient EM diffusion simulations, the FETD discretization produces a significantly smaller number of unknowns to solve than the FDTD discretization.

Compared with FDTD methods, the adoption of FETD methods for EM wave and diffusion problems was rather slow in both engineering and geophysics literature. One

reason for this was that node-based FETD methods do not correctly represent the discontinuity of normal field components at material interfaces. This problem was solved with the introduction of edge-based functions that correctly represent the discontinuities of EM fields at the interfaces (Nédélec, 1980 and 1986). Another reason for less popularity of FETD methods is due to the fact that FETD methods generally require solving a matrix equation at every time step regardless of implicit or explicit time discretization (Gockenbach, 2002). Therefore, for a given number of unknowns, FETD methods are computationally more expensive than explicit FDTD methods. As will be shown, this computational burden needs to be mitigated to make FETD algorithms practical.

In this dissertation, I present two efficient FETD algorithms for simulating the TDCSEM method. The core of my FETD algorithms are summarized in two aspects. First, in the formulation of the FETD algorithms, I minimize the number of unknowns by choosing an adequate form of EM governing equations and/or defining an efficient geophysical gauge condition. Second, in the implementation of the FETD algorithms, I effectively mitigate the computational cost of solving the matrix equation at every time step by utilizing an adaptive time-step-doubling method and reusing the intermediate computation results. Employing a serial version of the FETD algorithms, I can rapidly simulate and analyze the TDCSEM method for complex offshore environments where traditional FDTD algorithms need to resort to a massively-parallel computer with hundreds of nodes.

1.3 Chapter description

The following is a brief description of each chapter in this dissertation.

Chapter 2 introduces the marine CSEM method and describes its benefits over seismic methods and wire-line logging methods. I review the EM governing equations and EM detection processes of the marine CSEM method. The CSEM survey system and configurations are also described.

In Chapter 3, an FETD algorithm is derived from the electric-field full wave equation via Galerkin method. The displacement current term is removed. The

resulting system of FETD equations is discretized in time using an implicit backward Euler scheme. The spatial discretization for transient EM diffusion problems is discussed. Once the electric fields are determined by solving the system of FETD equations, the time derivatives of magnetic fields are interpolated at detector locations via Faraday's law. To simulate a step-off source waveform, I formulate a 3D finite-element direct-current (FEDC) algorithm that solves Poisson's equation for the electrostatic initial condition.

Chapter 4 presents numerical solution approaches for the FTED algorithm described in Chapter 3. The system of FETD equations is solved using a sparse direct method. When advancing the solution in time, the FETD algorithm adjusts the time step at intervals by examining whether the current step size can be doubled without affecting the accuracy of the solution. A comparison of example TDCSEM simulations with analytic and 3D FDTD solutions demonstrates the accuracy and the performance of the FETD algorithm. A trial-and-error forward-modeling approach is also demonstrated to interpret TDCSEM field data.

Chapter 5 presents a Lorenz-gauge FETD algorithm that is derived from a vector-and-scalar-potential equation. A variant of the Lorenz gauge condition decouples the single vector-and-scalar-potential equation into 1) a diffusion equation for magnetic vector potentials and 2) Poisson's equation for scalar electric potentials. The diffusion equation for the time derivative of the magnetic vector potential is the primary equation and is solved at every time step. In contrast, Poisson's equation is considered a secondary equation and is evaluated only at the time steps where the electric fields are sampled. Therefore, in contrast to traditional vector-potential approaches, this variant of the Lorenz-gauge vector-potential approach avoids having to solve a single large system of equations for both vector and scalar potentials at every time step.

Chapter 6 presents numerical solution approaches of the Lorenz-gauge FETD algorithm presented in Chapter 5. The accuracy and the performance of the Lorenz-gauged FETD algorithm are demonstrated. In contrast to the FETD algorithm presented in Chapter 3, iterative solutions of the Lorenz-gauge FETD algorithm are

stable in the static limit. Systematic comparisons between the two FETD algorithms are presented.

Chapter 7 describes the construction procedures of FE offshore models for TDCSEM simulations. The geometry of an FE offshore model is derived from a realistic seismic model that includes complex seafloor topography and salt structures. Some modifications are made to reflect more realistic TDCSEM survey scenarios. Calibration procedures of FETD meshes are discussed in detail.

In Chapter 8, the TDCSEM method is simulated in the offshore models described in Chapter 7. Horizontal and vertical electric-dipole-source configurations are compared. The 'guided' diffusion of the electric fields through a reservoir is visualized on the cross-section of the models. By inter-relating the cross-sectional distribution of the electric fields to the seafloor measurements, I present sensitivity analyses of various TDCSEM configurations in shallow water. The effects of irregular seafloor topography and seabed anisotropy are also investigated.

Chapter 2. Marine Controlled-Source Electromagnetic Method

Seismic reflection methods have been considered a primary geophysical tool to explore offshore hydrocarbon reservoirs, since they not only delineate seabed structures with a high resolution but also provide information about other characteristics of potential hydrocarbon reservoirs, such as porosity, lithology and other rock properties. However, a major drawback of the seismic methods is a lack of confidence in their ability to determine whether or not a potential reservoir is hydrocarbon-saturated (Eidesmo et al., 2002; Ellingsrud et al., 2002). It is known that approximately 90 % of seismic reservoir structures are not filled with hydrocarbon (Thirud, 2002).

EM methods have the potential to distinguish between hydrocarbon-saturated and seawater-saturated reservoirs, because the rock resistivity, which EM methods are sensitive to, strongly depends on the pore fluid properties. For example, seawater is very conductive, whereas hydrocarbon is resistive (Keller, 1987). Accordingly, wire-line logging data typically show that a hydrocarbon-saturated reservoir is one to three orders of magnitude more resistive than a seawater-saturated reservoir (Eidesmo et al., 2002; Ellingsrud et al., 2002; Wright et al., 2002; Ziolkowski et al., 2007).

Traditionally, seabed electrical resistivity has been obtained as supplementary information during wire-line logging of wells. Although this borehole-based technique provides direct information about resistivity structures, the information is limited in terms of spatially-sampled volume. Furthermore, drilling a well is increasingly expensive with great water depth. The use of the marine CSEM method has been motivated by its particular sensitivity to thin resistive structures (e.g. hydrocarbon and gas reservoirs), which enables geophysicists to directly distinguish between hydrocarbon- and seawater-saturated reservoirs without drilling a well. In this chapter, I review the fundamental physics of the marine CSEM method and its survey configurations.

2.1 Electromagnetic diffusion physics of the marine CSEM method

The fundamental physics of the marine CSEM method is sometimes described using wave-propagation as an analogy for diffusion, which can lead to incorrect physical insights, as pointed out by Edwards (2005), Um and Alumbaugh (2007), Weidelt (2007), and Chave (2009). Accordingly, I review the electromagnetic diffusion physics for the marine CSEM method.

2.2.1 Maxwell's equations

The governing physics of the marine CSEM method is represented by Maxwell's equations (Ward and Hohmann, 1987; Jackson, 1998) which include the following vector quantities: the electric field, $\mathbf{e}(\mathbf{r},t)$ (V/m), the magnetic field flux density, $\mathbf{b}(\mathbf{r},t)$ (T) and the electric flux density $\mathbf{d}(\mathbf{r},t)$ (C/m^2):

$$\nabla \cdot \mathbf{d}(\mathbf{r},t) = q\,; \tag{2.1}$$

$$\nabla \cdot \mathbf{b}(\mathbf{r},t) = 0\,; \tag{2.2}$$

$$\frac{\partial \mathbf{b}(\mathbf{r},t)}{\partial t} = -\nabla \times \mathbf{e}(\mathbf{r},t)\,; \tag{2.3}$$

$$\nabla \times \frac{1}{\mu_0}\mathbf{b}(\mathbf{r},t) = \mathbf{j}(\mathbf{r},t) + \frac{\partial \mathbf{d}(\mathbf{r},t)}{\partial t}\,, \tag{2.4}$$

where μ_0 is the magnetic permeability (H/m), $\mathbf{j}(\mathbf{r},t)$ is the current density, q is the charge density (C/ m^3), $\mathbf{r}$ is a position vector (m), and t denotes time (s).

In this dissertation, the magnetic permeability within the earth and air is assumed to be constant and is set to that of free space ($4\pi \times 10^{-7}$ H/m). This assumption is valid in non-ferromagnetic materials. Equation 2.1 is Gauss's law: the electric flux density through any closed surface is proportional to the enclosed electric charge. Equation 2.2 states that the magnetic field flux density is solenoidal. Equation 2.3 is Faraday's law: the induced electromotive force in any closed path is proportional to the rate of change in the magnetic flux density. Equation 2.4 is Ampere's law: the circulation of

the magnetic flux density around a closed path is equal to the current enclosed by the path.

Pertinent constitutive relationships are

$$\mathbf{j}(\mathbf{r},t) = \boldsymbol{\sigma}\mathbf{e}(\mathbf{r},t) + \mathbf{j}_s(\mathbf{r},t)\,; \tag{2.5}$$

$$\mathbf{d}(\mathbf{r},t) = \varepsilon_0\mathbf{e}(\mathbf{r},t)\,; \tag{2.6}$$

$$\mathbf{b}(\mathbf{r},t) = \mu_0\mathbf{h}(\mathbf{r},t)\,, \tag{2.7}$$

Where $\boldsymbol{\sigma}$ is generally the 3x3 symmetric electric-conductivity (S/m) tensor and is the inverse of the resistivity (Ωm) (Nabighian, 1988), $\mathbf{j}_s(\mathbf{r},t)$ is the current source (A), ε is the dielectric permittivity (F/m), and $\mathbf{h}(\mathbf{r},t)$ is the magnetic field (A/m).

The dielectric permittivity is generally a tensor quantity but is assumed to be a constant scalar quantity in this dissertation. As will be shown later, a term associated with the dielectric permittivity becomes negligible in the frequency range of interest. The conductivity tensor of a medium reduces to a scalar value when the medium is isotropic. If the medium is anisotropic, but two of the orthogonal coordinate directions are selected to lie in the directions of maximum conductivity and minimum conductivity, the non-diagonal elements of the tensor become zeros. If the medium is anisotropic, and the coordinate system is arbitrarily oriented, the off-diagonal terms become non-zero.

Using the constitutive relationships, one can combine Maxwell's equations and obtain the electric-field and magnetic-field full-wave equations for conductive media:

$$\frac{1}{\mu_0}\nabla\times\nabla\times\mathbf{e}(\mathbf{r},t) + \varepsilon_0\frac{\partial^2\mathbf{e}(\mathbf{r},t)}{\partial t^2} + \boldsymbol{\sigma}\frac{\partial\mathbf{e}(\mathbf{r},t)}{\partial t} + \frac{\partial\mathbf{j_s}(\mathbf{r},t)}{\partial t} = 0\,; \tag{2.8}$$

$$\frac{1}{\mu_0}\nabla\times\nabla\times\mathbf{b}(\mathbf{r},t) + \varepsilon_0\frac{\partial^2\mathbf{b}(\mathbf{r},t)}{\partial t^2} + \boldsymbol{\sigma}\frac{\partial\mathbf{b}(\mathbf{r},t)}{\partial t} - \nabla\times\mathbf{j_s}(\mathbf{r},t) = 0\,. \tag{2.9}$$

2.2.2 EM diffusion equations

An electric-dipole source transmits very low-frequency EM signals (typically less than 10 Hz) to probe deep seabed structures. At such low frequencies, the second

terms (i.e. the displacement terms) of equations 2.8 and 2.9 are much smaller than the third terms (i.e. the conduction terms); this is because the EM fields change very slowly in time, ε for most rocks is small (10^{-9} to 10^{-11} F/m), and the conductivities in typical marine sediments and rocks are large (10^{0} to 10^{-6} S/m) (Constable, 2010). For example, for the medium whose σ and ε are 10^{-5} S/m and 10^{-11} F/m, respectively, the coefficient of the displacement term is six orders of magnitude smaller than that of the conduction term. Therefore, in the range of CSEM frequencies, the second terms of equations 2.8 and 2.9 are negligible and can be dropped:

$$\frac{1}{\mu_0}\nabla\times\nabla\times\mathbf{e}(\mathbf{r},t)+\boldsymbol{\sigma}\frac{\partial\mathbf{e}(\mathbf{r},t)}{\partial t}+\frac{\partial\mathbf{j_s}(\mathbf{r},t)}{\partial t}=0\,; \tag{2.10}$$

$$\frac{1}{\mu_0}\nabla\times\nabla\times\mathbf{b}(\mathbf{r},t)+\boldsymbol{\sigma}\frac{\partial\mathbf{b}(\mathbf{r},t)}{\partial t}-\nabla\times\mathbf{j_s}(\mathbf{r},t)=0\,. \tag{2.11}$$

As a result, the marine CSEM method is considered an EM diffusion problem.

2.2.3 Electromagnetic detection processes of the marine CSEM method

The interaction between low-frequency EM fields and a thin structure (e.g. a resistive, hydrocarbon-saturated or conductive, seawater-saturated reservoir) in a background medium is primarily governed by two EM interface conditions. The results of that interaction are 1) inductive and 2) galvanic effects and 3) the 'guided' diffusion of the EM fields through the resistive reservoir (Edwards, 2005; Um and Alumbaugh, 2007; Weidelt, 2007; Cuevas et al., 2010).

When current flow is parallel to the interfaces of the resistive reservoir, the tangential electric fields across the interfaces are continuous; i.e.,

$$\mathbf{e}_1^T(\mathbf{r},t)=\mathbf{e}_2^T(\mathbf{r},t)\,, \tag{2.12}$$

where the subscript indicates the medium in which the electric field exists, and the superscript indicates that the electric field is tangential to the interface separating the two media.

If the thin structure is more conductive than the surrounding medium, this interface condition will result in strong electric currents parallel to the interface, as indicated by equation 2.5. These strong currents within the conductive structure will in turn generate magnetic fields described by equation 2.4. This inductive mechanism is the primary source of large anomalous responses for conductive structures.

However, when a structure is thin and resistive, induction alone does not produce a measurable response for the structure whose thickness is much less than its depth of burial below the measurement surface ([1]Hördt et al., 2000). It is for this reason that a thin resistive reservoir is not easily detectable using the marine magnetotelluric method (Constable and Weiss, 2006). To detect a thin resistive structure, one needs to generate currents that are normal to the boundaries. When this occurs, the governing interface condition is the continuity of normal current density; i.e.,

$$\mathbf{j}_1^{\mathrm{N}}(\mathbf{r},t) = \mathbf{j}_2^{\mathrm{N}}(\mathbf{r},t)\,, \tag{2.13}$$

where the superscript indicates that the current density is normal to the interface separating the two media. Combining equation 2.13 with equation 2.1 shows a buildup of surface charge on the interface:

$$q_s = \mathbf{j}_2^{\mathrm{N}}(\mathbf{r},t)\left(\frac{\varepsilon_0}{\sigma_1} - \frac{\varepsilon_0}{\sigma_2}\right), \tag{2.14}$$

where q_s is the anomalous surface charge, and the conductivity is assumed to have scalar values. This charge buildup in turn produces detectable perturbations in the background EM fields that are measured along the seafloor.

The third effect associated with the sensitivity of the CSEM method is the partially-'guided' diffusion of the EM fields. When a thin resistive structure is embedded within a conductive medium, the structure can channel EM energy preferentially in the radial direction (Chave, 2009). The EM energy gradually leaks out through the surface of the resistor into the conductive surrounding medium and can also abruptly leak out at the tips of the resistor. Assuming a one-dimensional thin reservoir, the 'guided' diffusion effect produces increasing sensitivity with increasing source-receiver offsets. In contrast, the background EM fields and galvanic effect are predominant in the vicinity of the source.

The last phenomenon that affects the physical detection process of the marine CSEM method is EM attenuation. The rate of attenuation of diffusing EM fields in an isotropic conductive medium is often described in terms of the plane-wave skin depth:

$$\delta = \sqrt{\frac{1}{\pi f \mu_0 \sigma}}, \tag{2.15}$$

where f is the frequency. As the source-receiver offset gradually increases, the CSEM fields are eventually attenuated below the sensor noise levels. Representative source-moment-normalized noise levels of the electric and magnetic sensors are $2\text{x}10^{-15}$ V/Am^2 and $2.52\text{x}10^{-10}$ nT/Am, respectively (Um and Alumbaugh, 2007). The skin depth can also be related to the wavelength via

$$\lambda = 2\pi\delta. \tag{2.16}$$

2.3 Diffusion of Transient Electric field in Earth

When a transient electric current is injected into the earth, the injected and induced current diffuse into the deeper part of the earth. The diffusion process is mainly controlled by the subsurface distribution of the conductivity. Accordingly, the diffusion process has been extensively studied for uniform, layered, multi-dimensional earth models with different sources and current waveforms (Nabighian, 1979; Hoversten and Morrison, 1982; Newman et al., 1986; Strack; 1992; Verma, 1999).

To illustrate basic characteristics of the diffusion process in the earth, I review the diffusion of the transient currents excited with a loop source. According to Nabighian (1979), for a uniform half space, the velocity of the peak of the current is given as

$$\text{Vertical velocity: } V_z = 1.1284\sqrt{\frac{1}{\sigma\mu_0 t}}; \tag{2.17}$$

$$\text{Horizontal velocity: } V_h = 1.0455\sqrt{\frac{1}{\sigma\mu_0 t}}; \tag{2.18}$$

$$\text{Total radial velocity: } V_\rho = 1.5384\sqrt{\frac{1}{\sigma\mu_0 t}}. \tag{2.19}$$

The velocity is inversely proportional to $\sqrt{t}$. It means that the transient currents diffuse increasingly slow in time. The velocity is also inversely proportional to $\sqrt{\sigma}$. Therefore, as shown in Figure 2.1a, the diffusion process occurs relatively slowly in a conductive environment (e.g. seabed environments), whereas it occurs relatively fast in a less conductive environment (e.g. land environments). Another characteristic of the diffusion process is that an injected current broadens with time as shown Figure 2.1b. These characteristics are used later to efficiently implement FETD algorithms.

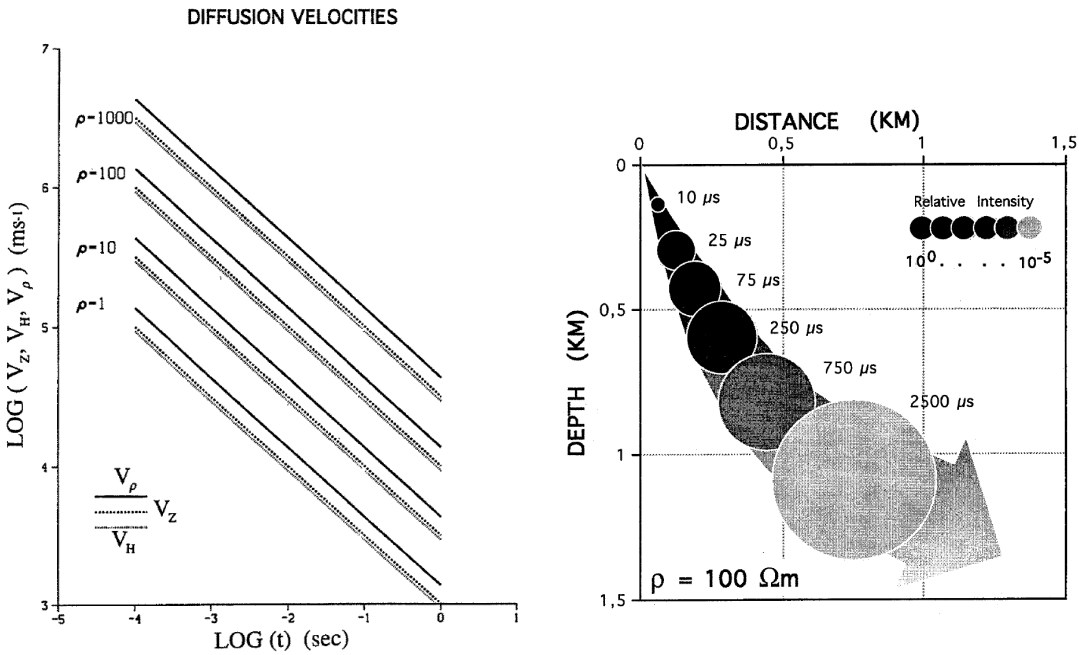

(a) (b)

Figure 2.1. Characteristics of the current diffusion (from courtesy of Verma, 1999). (a) Vertical, lateral and radial diffusion velocities as a function of time in a uniform half-space for various resistivity values. (b) Broadening of an injected current with time as it diffuses into the earth; the figure is schematic and presents the relative variations.

2.4 CSEM acquisition system and survey configuration

The marine CSEM method consists of a deep-towed electric-dipole source and an array of seafloor EM receivers (Constable, 2010). The source (Figure 2.2a) is typically 50 to 300 m long and transmits as much as a thousand amps of current into the seawater. The source is towed close to the seafloor (commonly at a height of 25 to 100 m) to maximize coupling of seafloor rocks and sediments and to minimize coupling with the air. For the FDCSEM method, the source currents are typically binary waveforms with a 0.1 to 0.25 Hz fundamental and higher harmonics. For the TDCSEM method, an impulse waveform is preferred. The impulse waveform is not directly excited but rather is obtained by taking time derivatives of the step-off responses or by utilizing pseudo-random binary-sequence techniques (Commer et al., 2006). As discussed in Chapter 1, whether the FDCSEM method or the TDCSEM method is employed depends on seawater depth.

A seafloor receiver (Figure 2.2b) consists of electric- and sometimes magnetic-field sensors and a data-logging system, and is deployed on the seafloor from a survey vessel. The receiver includes a concrete anchor to hold it securely to the seafloor, an acoustic release mechanism to release the anchor, and flotation to bring the receiver back to the sea surface. The receivers record time-series data of the electric field and the magnetic flux density and store them on a data-storage device.

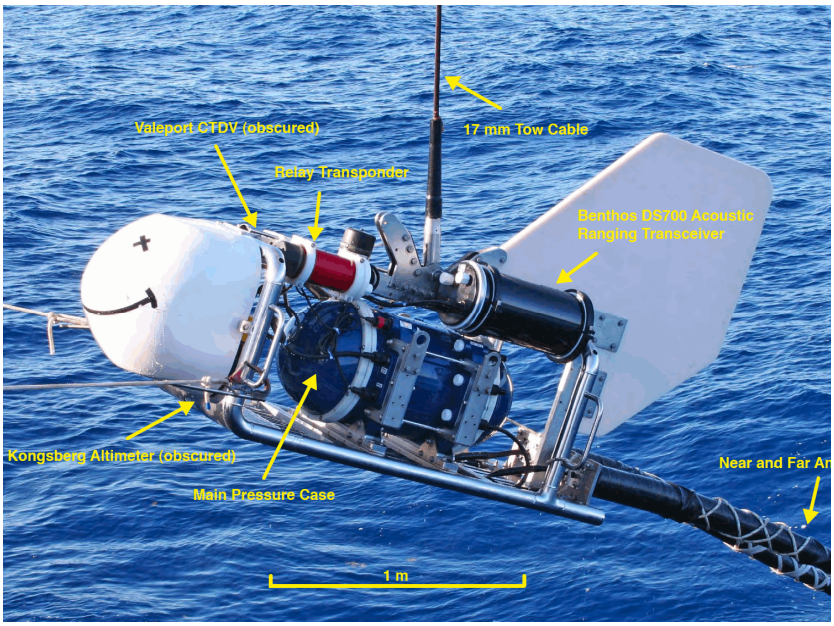

(a)

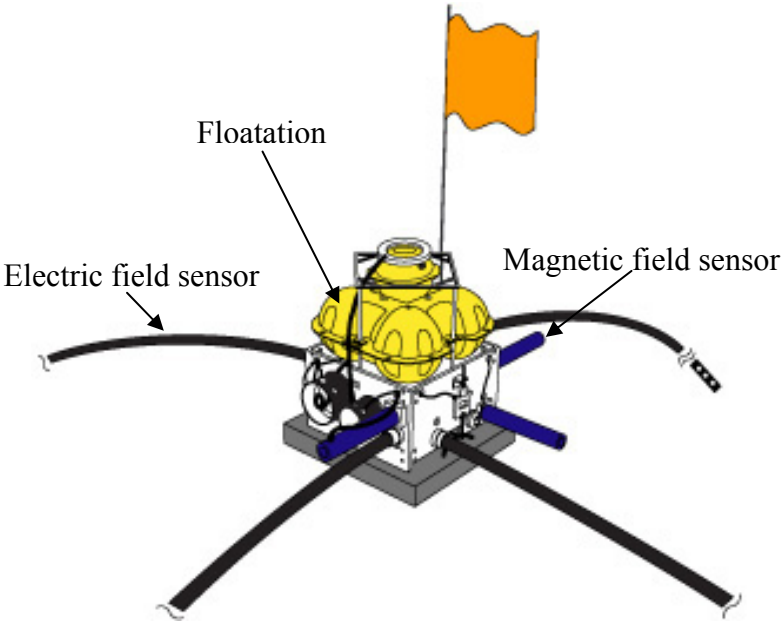

(b)

Figure 2.2. (a) The deep-towed electric-dipole source. (b) The seafloor receiver system (from courtesy of the Marine Electromagnetic Laboratory at Scripps).

The marine CSEM method has two fundamental source-receiver configurations shown in Figure 2.3: inline (radial) and broadside (azimuthal).

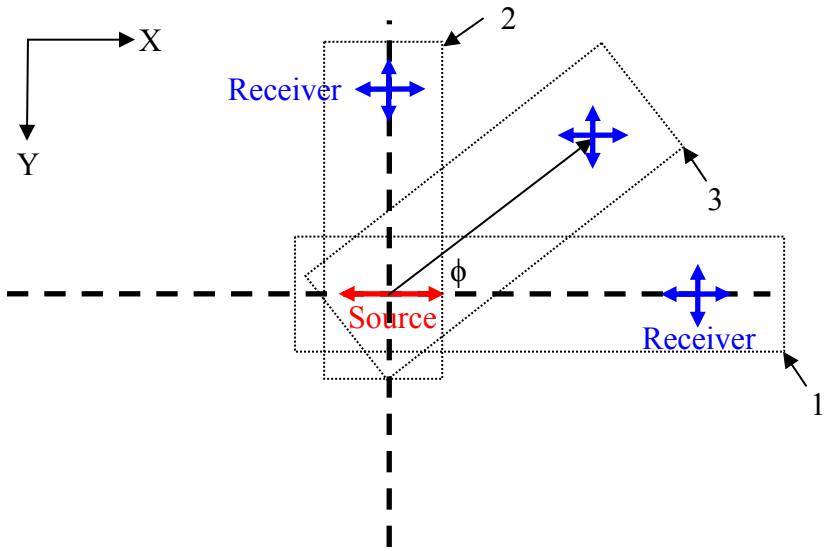

Figure 2.3. A plan view of CSEM source-receiver configurations. Three numbered rectangular boxes are used to identify different configurations. The inline and broadside configurations are numbered as 1 and 2, respectively. An intermediate configuration is numbered as 3. The angle ϕ is measured counterclockwise from the positive x-direction.

For the inline configuration (ϕ=0° and 180°, where ϕ is the angle between the orientation of a horizontal electric-dipole source and the line between the center of the source and a receiver), the y-component of the electric field goes to zero. For the broadside configuration (ϕ=90° and 270°), the x-component of the electric field goes to zero. At intermediate angles, both x- and y-components of the electric fields are measured on the seafloor. Although the inline configuration is more sensitive to a thin electrical resistor than the broadside configuration, the broadside configuration is also used to reduce the ambiguity in CSEM data interpretations (Eidesmo et al., 2002).

Chapter 3. 3D FETD Formulation of the Electric-Field Diffusion Equation

Various FETD formulations for EM wave simulations have been developed using different forms of EM governing equations: coupled Maxwell's equations, scalar and vector potentials with a gauge condition, and the electric-field wave equation (Biro and Preis, 1989; Lee et al., 1997; Jin, 2002; Taflove and Hagness, 2005). Although the equations equivalently describe EM phenomena, each has its own advantages and disadvantages in the implementation of the FETD method (Zhu and Cangellaris, 2006). In this chapter, I derive the basis of an FETD formulation from the electric-field full wave equation and move to its diffusion version. The primary advantage of this EM governing equation over others is that I can consider only the electric fields as my primary unknowns, thus minimizing the total number of unknown parameters.

I focus on an FETD formulation for an exploration-scale diffusion problem. The development of its FETD formulation is somewhat similar to that of wave problems that have been broadly investigated in engineering computational electromagnetics (Cangellaris et al., 1987; Gedney and Navsariwala, 1995; Lee et al., 1997). However, the implementation details of the FETD formulation in the exploration-scale diffusion domain are considerably different from those, especially in terms of time-stepping, boundary conditions and mesh design. The differences will be discussed in detail.

My FETD formulation is distinguished from other exploration-scale FETD solutions in some other important aspects. First, I compute FETD solutions directly in the time domain, whereas other published methods (e.g. Everett and Edwards, 1992; Börner et al., 2008) use the transform of finite-element frequency-domain solutions. With a step-off source, my direct time-domain approach requires that I calculate the initial electric fields; I do this using Poisson's equation before time-stepping, which is similar to Commer and Newman (2004).

Second, in the direct time-domain computation, the primary computational cost is the repeated time-stepping, which requires the solution of a matrix equation at every

time step. In order to mitigate the computational cost, I reuse the sparse LU factorization of the matrix equation unless a time-step size is changed. As a result, the computational cost at most time steps reduces to that of backward and forward substitution of a sparse matrix equation. Third, by using the characteristics of transient EM field diffusion in a conductive medium reviewed in chapter 2, I adaptively double the time-step size to speed up solution processes over a large range of time. As demonstrated in Chapter 4, this time-stepping approach helps avoid impractical small changes of the time-step size that would result in expensive LU factorizations.

Finally, I combine my FETD with a secondary-potential FE solution, whereas Commer and Newman (2004) incorporate their FDTD with a total-potential finite-difference solution. The adoption of the secondary-potential method considerably improves the accuracy of the initial electric fields required for step-off simulations. The accurate computation of the initial electric fields is critically important in step-off simulations, because inaccurate initial electric fields can result in errors of subsequent times, like a static shift of transient electromagnetic (TEM) sounding curves. This type of error is difficult to identify, because it does not change the overall shape of the sounding curves.

This chapter is organized as follows: First, I review the development of a system of differential equations that approximates the solution of the full electric-field wave equation and migrates to its diffusion form. Second, I discretize the system in the temporal and spatial domains and transform it into the final 3D FETD formulation. Finally, I describe two important aspects of the 3D FETD implementation: boundary conditions and initial conditions.

3.1 Development of FETD formulation

Based on Chapter 2, I first start from an FETD development of the full electric-field wave equation (Gedney and Navsariwala, 1995). In a given computational domain, $\mathbf{V}$, the electric-field wave equation is given as

$$\frac{1}{\mu_0}\nabla\times\nabla\times\mathbf{e}(\mathbf{r},t)+\varepsilon_0\frac{\partial^2\mathbf{e}(\mathbf{r},t)}{\partial t^2}+\boldsymbol{\sigma}\frac{\partial\mathbf{e}(\mathbf{r},t)}{\partial t}=-\frac{\partial\mathbf{j}_\mathbf{s}(\mathbf{r},t)}{\partial t}, \tag{3.1}$$

where $\mathbf{e}(\mathbf{r},t)$ is the electric field at time t at position $\mathbf{r}\in\mathbf{V}$, μ_0 is the magnetic permeability of free space, ε_0 is the dielectric permittivity of free space, $\boldsymbol{\sigma}$ is the electric conductivity, and $\mathbf{j}_\mathbf{s}(\mathbf{r},t)$ is the electric-current source term.

To transform equation 3.1 into an FETD approximate equation, a residual vector $\mathbf{p}$ is defined as

$$\mathbf{p}(\mathbf{r},t)\equiv\frac{1}{\mu_0}\nabla\times\nabla\times\mathbf{e}(\mathbf{r},t)+\varepsilon_0\frac{\partial^2\mathbf{e}(\mathbf{r},t)}{\partial t^2}+\boldsymbol{\sigma}\frac{\partial\mathbf{e}(\mathbf{r},t)}{\partial t}+\frac{\partial\mathbf{j}_\mathbf{s}(\mathbf{r},t)}{\partial t}. \tag{3.2}$$

The domain $\mathbf{V}$ is discretized into a number of finite elements. The residual vector for each element is forced to be zero in a weighted-integral sense. Among several different shapes of finite elements, a tetrahedral element (Figure 3.1) is chosen, because it can efficiently handle complex geometry.

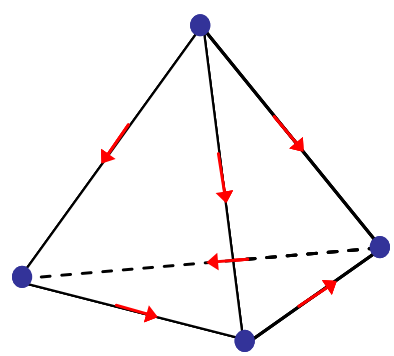

Figure 3.1. A tetrahedral element. The unknown electric fields (red arrows) are assigned on the edges. The unknown potentials (blue dots) are assigned on the nodes.

This process is expressed in the following equation:

$$\iiint_{V^e}\mathbf{n}_i^e(\mathbf{r})\cdot\mathbf{p}^e(\mathbf{r},t)dV=0, \tag{3.3}$$

where the superscript e denotes the eth tetrahedral element, $\mathbf{n}_i^e(\mathbf{r})$ is a set of weighting functions with i varying from 1 to n, and V^e is the volume of the eth tetrahedral element.

If the set of $\mathbf{n}_i^e(\mathbf{r})$ functions used in equation 3.3 is also chosen as the basis set, the electric field can be expanded as

$$\mathbf{e}^e(\mathbf{r},t) = \sum_{j=1}^{n} \mathbf{e}_j^e(\mathbf{r},t) = \sum_{j=1}^{n} u_j^e(t)\mathbf{n}_j^e(\mathbf{r}), \tag{3.4}$$

where $u_j^e(t)$ is the unknown amplitude of the electric field on edge j of the eth element, which needs to be determined via FETD computations. As shown in Figure 3.1, the unknown electric fields are assigned to the edges of a tetrahedral element. As a result, each tetrahedral element has 6 unknowns. In the application of the Galerkin method to EM modeling, edge-based functions are chosen as both weighting and basis functions. The functions guarantee the continuity of the tangential electric fields and can accommodate the discontinuity of the normal electric field across the element edges (see Appendix A for details). Substituting equation 3.4 into equation 3.3 provides the following system of second-order ordinary differential equations:

$$\mathbf{A}^e \frac{d^2\mathbf{u}^e(t)}{dt^2} + \mathbf{B}^e \frac{d\mathbf{u}^e(t)}{dt} + \mathbf{C}^e\,\mathbf{u}^e(t) + \mathbf{s}^e = 0, \tag{3.5}$$

where the (i,j) element of matrices $\mathbf{A}^e$, $\mathbf{B}^e$ and $\mathbf{C}^e$ and the ith element of vectors $\mathbf{s}^e$ and $\mathbf{u}^e$ are given by the following:

$$\text{(i,j) element of permittivity matrix } \mathbf{A}^e = \iiint_{V^e} \varepsilon^e \mathbf{n}_i^e(\mathbf{r}) \cdot \mathbf{n}_j^e(\mathbf{r}) dV\,; \tag{3.6}$$

$$\text{(i,j) element of conductivity matrix } \mathbf{B}^e = \iiint_{V^e} \boldsymbol{\sigma}^e \mathbf{n}_i^e(\mathbf{r}) \cdot \mathbf{n}_j^e(\mathbf{r}) dV\,; \tag{3.7}$$

$$\text{(i,j) element of permeability matrix } \mathbf{C}^e = \frac{1}{\mu_0} \iiint_{V^e} \nabla \times \mathbf{n}_i^e(\mathbf{r}) \cdot \nabla \times \mathbf{n}_j^e(\mathbf{r}) dV\,; \tag{3.8}$$

$$\text{i element of source vector } \mathbf{s}^e = \iiint_{V^e} \mathbf{n}_i^e(\mathbf{r}) \cdot \frac{\partial \mathbf{j}_s(\mathbf{r},t)}{\partial t} dV\,; \tag{3.9}$$

$$\text{Unknown vector } \mathbf{u}^e = [u_1^e \quad u_2^e \quad \ldots \quad u_n^e]. \tag{3.10}$$

In equation 3.5, the first term is related to the EM displacement current. Because the displacement current is much smaller than the conduction current in the EM diffusion regime (Chapter 2), this first term is negligible and can be dropped. By dropping the term, equation 3.5 no longer explains the full wave phenomenon but reduces to the

diffusion equation. Since the second term of equation 3.5 is also negligible in the air, the so-called 'airwave' effect is established without any time delay (Goldman et al., 1985). Therefore, equation 3.5 without the displacement term does not explain the travel time of the electric field through the air. However, when one considers a typical maximum CSEM source-receiver offset (e.g. 10 km) and the wavelength of the airwave (e.g. 3×10^3 - 3×10^7 km for a frequency range of 0.01 - 100 Hz), the ignored time delay is negligibly small and does not affect the accuracy of CSEM simulation results (Chave, 2009).

In this diffusion regime, equation 3.5 eventually reduces to a system of diffusion equations. The system of equations is considered local, because it results from integration over each individual tetrahedral element. To assemble local systems into a single global system, all nodes and edges in the computational domain are numbered globally. The spatial relationship between global nodes and global edges(i.e. the connectivity information) is analyzed (see Appendix B for details). After the global system is assembled, the superscript *e* is dropped as shown below:

$$\mathbf{B}\frac{d\mathbf{u}(t)}{dt}+\mathbf{C}\mathbf{u}(t)+\mathbf{s}=0. \tag{3.11}$$

As a side note, the FETD formulation approach presented here can also be applied to the finite-element frequency-domain (FEFD) formulation. The FEFD formulation is different from the FETD formulation, because the FEFD formulation does not include a time-derivative term but instead has complex numbers. Nonetheless, the two formulations are similar. The differences and similarities between the two formulations are discussed in Appendix C.

3.2 Discretization in time and space

Since equation 3.11 is a time-dependent system of ordinary differential equations, it can be discretized in time using a FD method. To choose an effective FD method, I must consider the physics of EM diffusion. Because of the low-frequency EM sources that I wish to simulate and the large contrast in electrical conductivity between the subsurface medium and air, equation 3.11 is very stiff in time (Haber et al., 2004). Therefore, if I choose an explicit time-discretization method, equation 3.11 will

require a very small time step Δt to satisfy stability conditions. For this reason, an explicit time-discretization method would not be efficient, especially when marine CSEM responses are simulated over a large range of time (e.g. 10^{-6} to 10^{2} seconds) due to the slow EM diffusion in conductive marine environments.

Thus, I choose an implicit time discretization, specifically the backward Euler (BE) method. As detailed in Appendix D, the BE method is unconditionally stable, regardless of the choice of Δt. Furthermore, when a mesh cannot support high-frequency contents of the transient fields at early times, the BE method strongly suppresses high-frequency oscillations (Hairer and Wanner, 1991). The accuracy of the BE method is set to second order for rather complex source waveforms (e.g. a half-sine waveform) and first order for a simple step-off and step-on source waveform. The latter choice is made because there is no benefit to using a higher-order scheme for a source waveform that is only once differentiable (Haber et al., 2004). Applying the BE method to equation 3.11 produces

$$\mathbf{D}\mathbf{u}^{n+2} = \mathbf{B}(4\,\mathbf{u}^{n+1} - \mathbf{u}^{n}) - 2\Delta t\mathbf{s}^{n+2} \tag{3.12a}$$

for the second-order BE method, where $\mathbf{u}(t) = \mathbf{u}(n\Delta t) = \mathbf{u}^{n}$ and $\mathbf{D} = (3\mathbf{B} + 2\Delta t\mathbf{C})$, and

$$\mathbf{D}u^{n+1} = \mathbf{B}u^{n} - \Delta t\mathbf{s}^{n+1} \tag{3.12b}$$

for the first-order BE method, where $\mathbf{D} = (\mathbf{B} + \Delta t\mathbf{C})$.

For the solutions of equations 3.12 to accurately approximate true electric fields, the spatial discretization of the computational domain is as important as the temporal discretization. As a general rule for the spatial discretization, an element size is smallest near a source but gradually grows away from the source (Wang and Hohmann, 1992). The growth rate is defined as the maximum rate at which the element size can grow from a region with small elements to a region with larger elements. The growth rate is empirically determined, but it is usually less than or equal to a factor of 2 from one edge to the next. In addition, the mesh should be fine in conductive areas and can be coarse in more resistive areas, because the wave length (chapter 2) is proportional to the resistivity of the areas (Hördt and Müller, 2000). Such a mesh design is illustrated in Figure 1.3. In short, the FE mesh reflects model inhomogeneity as well as

diffusion and attenuation characteristics of transient EM fields with time. Examples of FE mesh construction are presented in the next chapter.

3.3 Boundary conditions

To obtain a unique numerical solution for a given differential equation, geophysically meaningful conditions need to be imposed at the boundaries of the computational domain. As element sizes grow with increasing offset from the source position, I simply extend the boundaries of the computational model sufficiently away from the source. Then, homogeneous Dirichlet boundary conditions are applied to the FETD matrix-vector equation simply by setting the electric fields on the external edges to zeros and removing the edges from the matrix-vector equation. As a result, the number of unknowns in equation 3.12 reduces from the number of total edges to the number of internal edges. I believe that the homogeneous Dirichlet boundary condition is the most practical choice for EM diffusion simulations, since its implementation neither requires modifying the original form of the governing equation nor results in any extra computation at each time step. My numerical experiments suggest that the use of the element growth rate can efficiently discretize a very large computational domain required for implementing the homogeneous Dirichlet boundary condition. For example, the volume of the central portion of the reservoir model shown in Figure 1.3 is 5 km^3 and consists of 69,908 tetrahedral elements. In contrast, the volume of the entire computational domain is 216,000 km^3 and consists of 131,741 tetrahedral elements.

3.4 Initial condition and FEDC formulation

In order to advance the temporal solution of equations 3.12, I first need to set up the initial electric field. The initial values of the electric fields are different according to different source waveforms (Figure 3.2). For example, when an earth model is excited using a step-on or half-sine, the initial electric field is simply zero everywhere in the model. However, when a step-off source waveform is employed, the initial electric

field is not zero but a solution of the direct current (DC) resistivity problem. In this case, the initial electric field can be decomposed into two parts (Commer and Newman, 2004):

$$\mathbf{e}_{initial} = \mathbf{e}_{source} + \mathbf{e}_{DC}, \tag{3.13}$$

where $\mathbf{e}_{initial}$ is the initial electric-field vector, $\mathbf{e}_{source}$ is the electric field through a source, and $\mathbf{e}_{DC}$ is the static DC electric field in the model.

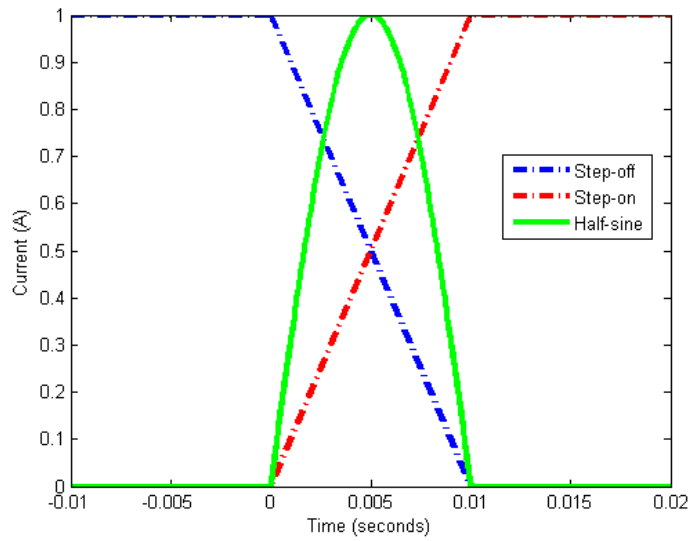

Figure 3.2. Transient source waveforms. The ramp time for the step-off and the step-on waveforms is set to 0.01 seconds. The period of the half-sine waveform is set to 0.02 seconds.

The electric field $\mathbf{e}_{source}$ is determined by applying Ohm's law to the tetrahedral elements containing the source. The electric field $\mathbf{e}_{DC}$ is determined by calculating electric potentials at the nodes of the finite elements (Figure 3.1). Therefore, each tetrahedral element has four unknown potentials. This calculation reduces to a 3D Poisson problem, as is common in 3D resistivity modeling (Dey and Morrison, 1978, Lowry et al, 1988, and Li and Spitzer, 2002). I solve the 3D Poisson's equation for general anisotropic conductivity media using a secondary-potential approach (Li and Spitzer, 2005). Compared with the total-potential approach, the secondary-potential approach considerably improves the solution accuracy in the vicinity of a source by removing the singularity associated with the end points of the dipole source. As a

result, the secondary-potential approach effectively prevents numerical static-shift errors in step-off sounding curves.

To maintain the consistency in the development procedures of the FETD formulation, a finite-element direct-current (FEDC) formulation is summarized below using a weighted-residual method instead of a variational principle. The DC resistivity problem is described with the Poisson equation:

$$\nabla \cdot (\boldsymbol{\sigma} \nabla \phi(\mathbf{r})) = -\nabla \cdot \mathbf{j_s}(\mathbf{r}), \tag{3.14}$$

where $\phi(\mathbf{r})$ is the potential at position $\mathbf{r}$. The potential is decomposed into a primary potential $\phi_p(\mathbf{r})$ and a secondary potential $\phi_s(\mathbf{r})$:

$$\phi(\mathbf{r}) = \phi_p(\mathbf{r}) + \phi_s(\mathbf{r}). \tag{3.15}$$

The primary potential is caused by a current source in a homogeneous whole-space with the primary-conductivity tensor $\boldsymbol{\sigma}_p$, and it can be calculated analytically at the FE nodes. The secondary potential satisfies the following equation:

$$\nabla \cdot (\boldsymbol{\sigma}_s \nabla \phi_s(\mathbf{r})) = -\nabla \cdot \mathbf{j_s}(\mathbf{r}), \tag{3.16}$$

where $\boldsymbol{\sigma}_s = \boldsymbol{\sigma} - \boldsymbol{\sigma}_p$.

A scalar residual for the eth tetrahedron is again defined as

$$\mathrm{p}^e(\mathbf{r}) = \nabla \cdot (\boldsymbol{\sigma}_s \nabla \phi_s(\mathbf{r})) + \nabla \cdot \mathbf{j_s}(\mathbf{r}). \tag{3.17}$$

The residual for each tetrahedral element is minimized in a weighted average sense:

$$\iiint_{V^e} \omega(\mathbf{r})\, \mathrm{p}^e(\mathbf{r}) dv = 0, \tag{3.18}$$

where $\omega(\mathbf{r})$ is a weighting function.

By substituting equation 3.17 into equation 3.18, using Green's theorem and finally enforcing Dirichlet boundary conditions, one obtains

$$\begin{aligned}\iiint_{V^e} [\frac{\partial \omega(\mathbf{r})}{\partial x} \{\sigma^e_{s11} \frac{\partial \phi^e_s}{\partial x} + \sigma^e_{s12} \frac{\partial \phi^e_s}{\partial y} + \sigma^e_{s13} \frac{\partial \phi^e_s}{\partial z}\} + \frac{\partial \omega(\mathbf{r})}{\partial y} \{\sigma^e_{s21} \frac{\partial \phi^e_s}{\partial x} + \sigma^e_{s22} \frac{\partial \phi^e_s}{\partial y} + \\ \sigma^e_{s23} \frac{\partial \phi^e_s}{\partial z}\} + \frac{\partial \omega(\mathbf{r})}{\partial z} \{\sigma^e_{s31} \frac{\partial \phi^e_s}{\partial x} + \sigma^e_{s32} \frac{\partial \phi^e_s}{\partial y} + \sigma^e_{s33} \frac{\partial \phi^e_s}{\partial z}\}] dv = \iiint_{V^e} \omega(\mathbf{r}) \nabla \cdot \mathbf{j_s}(\mathbf{r}) dv,\end{aligned} \tag{3.19}$$

where σ^e_{sij} denotes the element in row i and column j of the conductivity tensor $\overline{\overline{\boldsymbol{\sigma}}}^e_s$.

The unknown potential at a point inside the eth element is interpolated using the set of four Lagrange polynomials or node-based functions (Appendix A) $n_j^e(\mathbf{r})$ as follows:

$$\phi^e(\vec{r}) = \sum_{j=1}^{4} \phi_j^e n_j^e(\mathbf{r}), \tag{3.20}$$

where ϕ_j^e is the potential at the jth node of the eth element.

The Lagrange polynomials are also used as the weighting function $\omega(\mathbf{r})$. Substituting equation 3.20 into equation 3.19 and replacing $\omega(\mathbf{r})$ by $n_i^e(\mathbf{r})$ yield

$$\begin{pmatrix} m_{11}^e & m_{12}^e & m_{13}^e & m_{14}^e \\ m_{21}^e & m_{22}^e & m_{23}^e & m_{24}^e \\ m_{31}^e & m_{32}^e & m_{33}^e & m_{34}^e \\ m_{41}^e & m_{42}^e & m_{43}^e & m_{44}^e \end{pmatrix} \begin{pmatrix} \phi_{s1}^e \\ \phi_{s2}^e \\ \phi_{s3}^e \\ \phi_{s4}^e \end{pmatrix} = \begin{pmatrix} q_1^e \\ q_2^e \\ q_3^e \\ q_4^e \end{pmatrix}, \tag{3.21a}$$

where

$$\begin{aligned} m_{ij}^e = \iiint_{V^e} [& \frac{\partial n_i^e(\mathbf{r})}{\partial x} \{\sigma_{s11}^e \frac{\partial n_j^e(\mathbf{r})}{\partial x} + \sigma_{s12}^e \frac{\partial n_j^e(\mathbf{r})}{\partial y} + \sigma_{s13}^e \frac{\partial n_j^e(\mathbf{r})}{\partial z}\} \\ & + \frac{\partial n_i^e(\mathbf{r})}{\partial y} \{\sigma_{s21}^e \frac{\partial n_j^e(\mathbf{r})}{\partial x} + \sigma_{s22}^e \frac{\partial n_j^e(\mathbf{r})}{\partial y} + \sigma_{s23}^e \frac{\partial n_j^e(\mathbf{r})}{\partial z}\} + \\ & \frac{\partial n_i^e(\mathbf{r})}{\partial z} \{\sigma_{s31}^e \frac{\partial n_j^e(\mathbf{r})}{\partial x} + \sigma_{s32}^e \frac{\partial n_j^e(\mathbf{r})}{\partial y} + \sigma_{s33}^e \frac{\partial n_j^e(\mathbf{r})}{\partial z}\}] dv, \end{aligned} \tag{3.21b}$$

and

$$\mathrm{q}_i^e = \iiint_{V^e} n_i^e(\mathbf{r}) \nabla \cdot \mathbf{j_s}(\mathbf{r}) dv.$$

Again, equation 3.21a is considered local, because it comes from each tetrahedral element. Using the node-connectivity information (Appendix B), these local matrix equations for the individual elements are assembled into a single global matrix equation for the secondary potential.

Once the secondary potentials at all nodes are calculated, one can easily determine the electric-field vectors along the edges of each tetrahedral element. These electric fields provide the initial values for equations 3.12 when a step-off source waveform is employed. Once the electric fields are calculated, the magnetic fields can be easily

interpolated using the computed electric fields and Faraday's law (Newman and Alumbaugh, 1995).

3.5 Conclusions

I have formulated the 3D FETD algorithm for simulating transient EM diffusion in general anisotropic conductive media excited by arbitrarily configured electric dipoles. This is the first time-stepping-based FETD algorithm in the EM geophysics literature. The electric-field wave equation is transformed into a system of FETD equations using the Galerkin method, with homogeneous Dirichlet boundary conditions. The displacement term is then removed for low-frequency diffusion problems.

To ensure both numerical stability and a large time step size, the system of the FETD equations is discretized in time using an implicit backward Euler scheme. The computational domain is discretized using tetrahedral elements, by considering both model inhomogeneity and diffusion characteristics of transient EM fields with time. In order to set up initial electric fields for a step-off source waveform over an arbitrary conductivity model of the subsurface for a step-off source waveform, the secondary potential FEDC algorithm is formulated to solve Poisson's equation.

The primary advantage of the FETD algorithm is that it solves the governing equation not for both the electric and magnetic fields but for the electric fields alone. Consequently, this approach minimizes the total number of unknowns to solve. Since the unknown electric fields are assigned to internal edges in the computational domain, the total number of unknowns in the problem is equal to the number of internal edges. When it is necessary to obtain the magnetic fields, the magnetic fields at detector positions are interpolated using the computed electric fields via Faraday's law.

Chapter 4. Solutions of the Electric-Field Diffusion-Equation-based FETD Formulation

So far, I have formulated both FETD and FEDC algorithms. In this chapter, I first develop efficient implementation approaches for the FETD algorithm. In the development of FETD implementation approaches, I focus on the algorithm-based acceleration of the FETD algorithm, rather than hardware-based acceleration. Second, I validate the 3D FETD algorithm through detailed comparison with one-dimensional (1D) analytical and 3D FDTD simulation results, and I also present a performance analysis of the FETD algorithm. Third, using my 3D FETD algorithm, I present simulation results of the TDCSEM method for a simple field scenario of a water layer above a gently dipping seafloor. Finally, I interpret field TDCSEM data over simple geology using a trial-and-error FETD forward-modeling approach.

4.1 Numerical implementation approaches

The most expensive part of the FETD computation is advancing the solution to equations 3.12 in time. To mitigate this potentially high computation cost, I take advantage of the fact that for a fixed Δt, the matrix **D** does not vary in time. Therefore, matrix **D** should be computed only once within a time-stepping loop. When a direct solver is employed with a constant Δt, the matrix needs to be factorized into corresponding lower and upper triangular matrices **L** and **U** only once. Eventually, after the explicit factorization, the computational cost in every time step reduces to that of forward and backward substitutions, resulting in a much cheaper computational cost per time step. When an iterative solver is employed to solve equations 3.12, a preconditioner also needs to be computed only once if Δt is constant.

In this rendition of the algorithm, I choose a direct solver (Davis, 2006) over an iterative solver, because the use of an iterative solver for equation 3.1 can result in

poor convergence and spurious solutions in the static limit (See Appendix E and Chapter 5 for further discussion). Before a direct factorization starts, the matrix is reordered to minimize fill-ins in the resulting triangular matrices (Demmel, 1997). Minimizing fill-ins is critically important to reduce both the computation and memory costs. Once the factorization generates triangular matrices, they are repeatedly used to advance the solution of equations 3.12 via forward and backward substitutions.

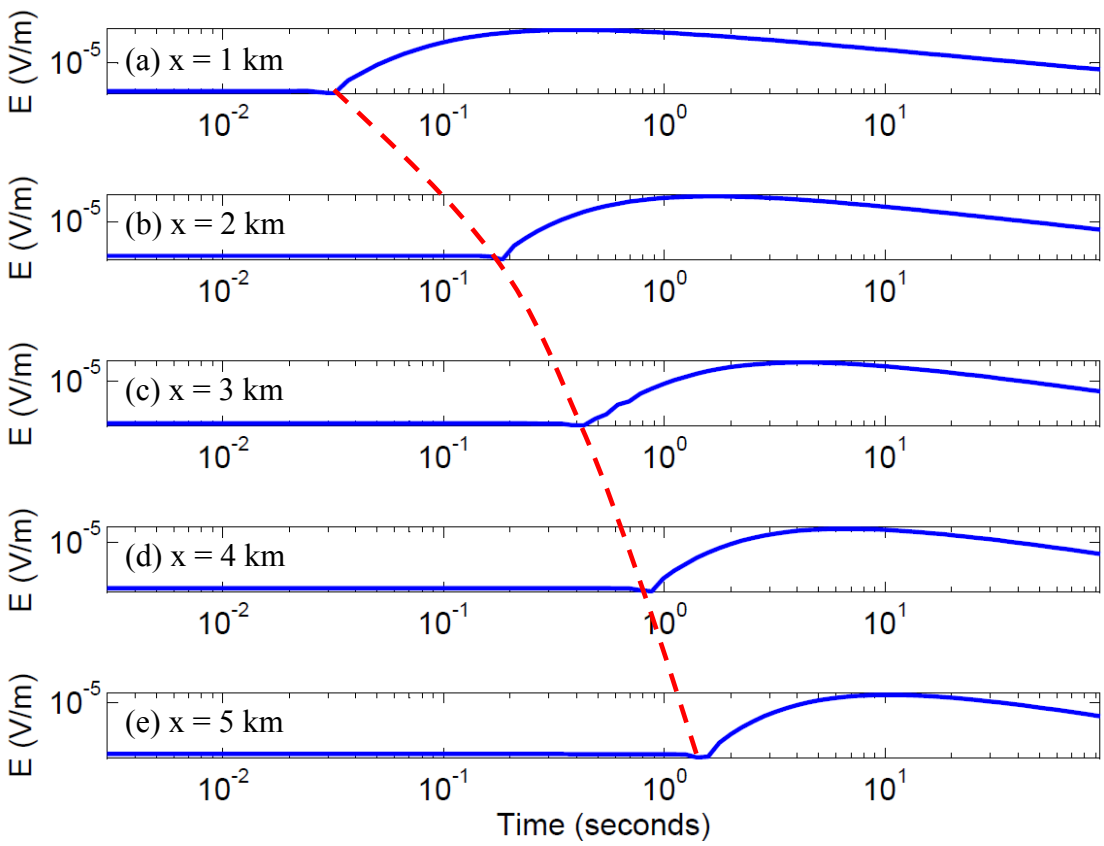

Figure 4.1. The diffusion of the electric field excited by an impulse electric dipole in 0.3 Ωm whole space. The source is 250 m long and is placed at x = 0 km. The broken red line traces the onset of the electric fields at the constant spatial interval (i.e. 1 km).

Although the constant Δt eliminates the need to refactorize the FE matrix at every time step, the constant Δt is not a practical choice for simulating diffusive EM responses, over a large range of time (e.g. 10^{-6} to 10^{2} seconds). To explain the impractical aspect of the use of the constant Δt, Figure 4.1 illustrates the diffusion

phenomenon of an injected current source in a conductive medium. As shown in Figure 4.1, the diffusion velocity of the electric field decreases with increasing time due to attenuation and dispersion in conductive media (Nabighian, 1988). This is because the high-frequency contents of the electric field attenuate more rapidly in the conductive earth media. The distribution of the electric field also increasingly broadens and looses its sharpness with time. Therefore, as the diffusion continues, one can take increasingly large time steps in order to sample the electric field and thus advance the solution quickly without affecting the accuracy. In other words, it is desirable to increase Δt as an efficient problem-solving strategy. However, optimizing and changing Δt at every time step would require significant computational overhead, resulting in a net loss of the computational benefits from a larger Δt.

Therefore, I attempt to double Δt every *m* constant time steps, where *m* is an input parameter. Through numerical modeling experiments, the default *m* for marine and land CSEM simulations is set to 100 and 200, respectively. The idea behind setting the different default values is that the attenuation occurs more rapidly in time in a conductive marine model than a less conductive land model. When the FETD algorithm tries to switch a time step size from Δt to $2\Delta t$ every *m* constant time steps, the electric field solution vectors (**e**) are computed at a given time using both Δt and $2\Delta t$. Then, a relative difference between the two electric-field solution vectors is computed 'element-by-element':

$$\Delta e_i = \mathrm{abs}\left(\frac{e_i^{2\Delta t} - e_i^{\Delta t}}{e_i^{\Delta t}}\right), \tag{4.1}$$

where the superscript designates a time-step size, the subscript i designates the element index of the electric field solution vector **e**, and function abs (x) returns the absolute value of x.

If the maximum value of Δe_i is smaller than a tolerance, $2\Delta t$ is accepted as a new time step size. If the tolerance criterion is not satisfied, the algorithm rejects $2\Delta t$ and continues using the current Δt. However, the triangular matrix for $2\Delta t$ is stored for future use after another *m* constant time steps. In short, equation 4.1 checks if the doubled time-step size is small enough for accurately advancing the current electric

fields. An adequate default tolerance was explored by comparing FETD solutions with analytical solutions that are discussed in the next section. Based on the numerical experiments, the default tolerance is set to 10^{-6}. For brevity, I call this approach the adaptive time-step-doubling method.

4.2 Validation and performance analysis

In order to demonstrate the accuracy and performance of the FETD implementation strategies described above, the serial implementation, named FETDEM3D, is written in MATLAB 7.5, from which several external routines are also called. The MATLAB portion of FETDEM3D mainly includes FE preprocessing tasks (e.g. evaluation and assembly of FETD matrices), whereas the external routines are responsible for the main FE computations (e.g. factorization of the FETD system matrices, and backward and forward substitutions); the direct matrix factorization is performed using SuiteSparse 3.2 and other auxiliary routines authored by Davis (2006); fill-reducing ordering of sparse matrices is performed using METIS 4.0 (Karypis and Kumar, 1999); 3D FE discretization is carried out using the Delaunay algorithm and others in the COMSOL Multiphysics 3.5a software package (2008, COMSOL). Figure 4.2 describes an overall structure of the FETD implementation.

The FETD computations presented here were carried out on a single-core Opteron 875 2.2 GHz using 8 GB memory running Red Hat Linux. The results are compared with the 3D FDTD solutions of Commer and Newman (2004) and the EM1D analytical solutions (K. H. Lee, personal communication, 2007). The expressions for the EM1D with different source-receiver configurations can be found in Stoyer (1976) and Ward and Hohmann (1987). Note that the analytical solution first computes the frequency-domain responses at a selected number of frequencies and then converts the responses in the time domain using inverse fast-Fourier-transform routines. Although my FETD algorithm can simultaneously handle multiple arbitrarily configured electric dipoles that are excited with various source waveforms (Figure 3.2) over general anisotropic media, only single step-off electric-dipole responses over isotropic media are considered in this section for comparison and verification purposes.

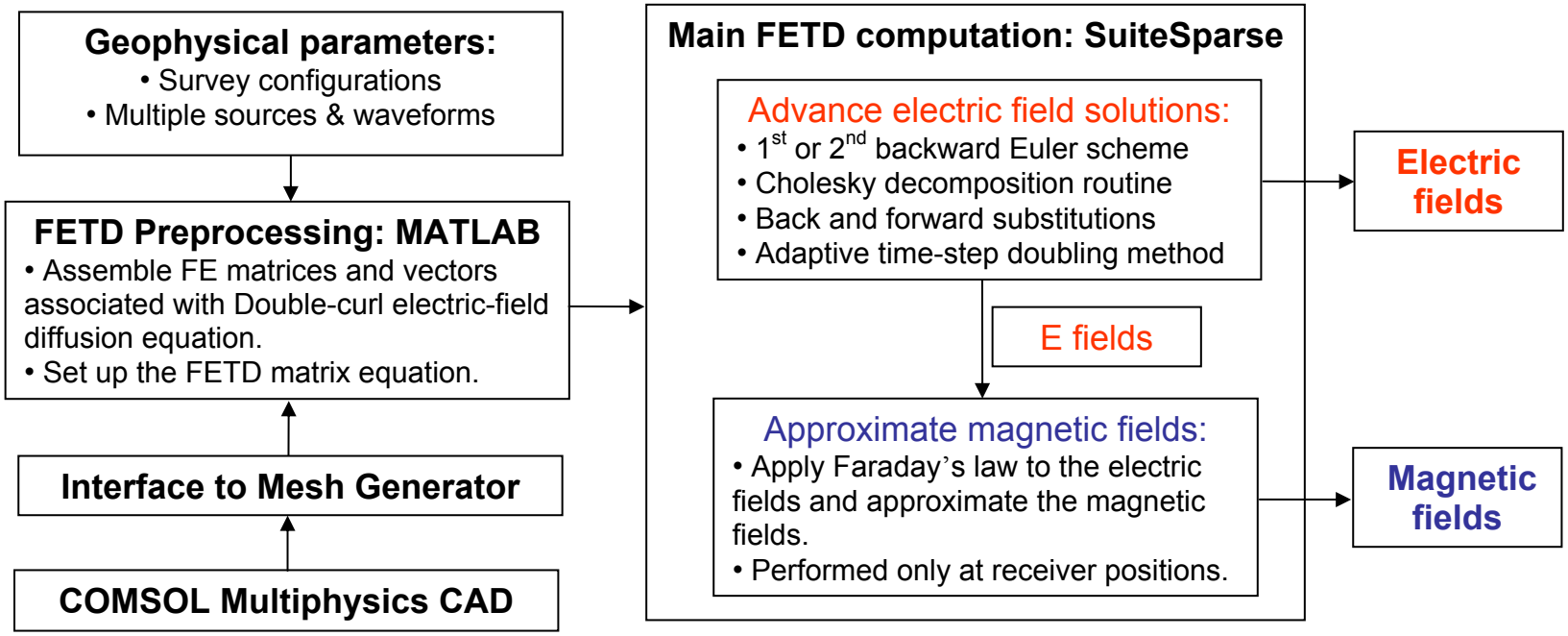

Figure 4.2. The composite diagram describing the FETD implementation.

4.2.1 Homogeneous seafloor model

The first example is a simple marine TDCSEM simulation. Figure 4.3 illustrates a homogeneous seafloor model with a seawater column 400 m deep. An electric-dipole source 250 m long is placed 50 m above the seafloor. Its ramp-off time is set to 0.01 seconds. Two arrays of eight 10 m long seafloor receivers are placed 1 km apart along the x and y axes, from x=1 km through 8 km (i.e. the inline configuration) and y=1 km through 8 km (i.e. the broadside configuration). The spectral analysis (Appendix F) is used to determine a proper initial time step size (t_o= 0.002 seconds) for the given source-receiver configuration in the given model. To ensure both numerical stability and accuracy, the resistivity of the air is empirically set to 10,000 Ω-m. The relationship between numerical stability, accuracy and the resistivity of the air is discussed in detail in Chapter 6.

Figure 4.4 shows The FETD mesh for the homogeneous model. The boundaries of the model are extended to 100 km from the model center to eliminate possible artificial boundary effects at the receiver positions. The 250-m-long source is discretized using ten 25-m-long edges. My numerical experiments indicate that a finite-length electric-dipole source can be accurately approximated using 5 to 10 edges. The receivers are discretized using a single 10-m-long edge. In order to discretize the model economically, element growth factors ranging from 1.5 to 2.0 are used in most areas. Small elements in the vicinity of the source and the receivers gradually grow. However, inside the seawater column, which has a thickness of 400 m, tetrahedral elements are prohibited from growing rapidly in the x- and y- directions to avoid skewing the elements too much. The skewness of an element is measured using the aspect ratio (see Appendix G). Based on my numerical experiments, the aspect ratio should be larger than 0.1 for accurate solutions. Consequently, the model is discretized into a rather large number (108,540) of tetrahedral elements, generating 125,883 unknowns.

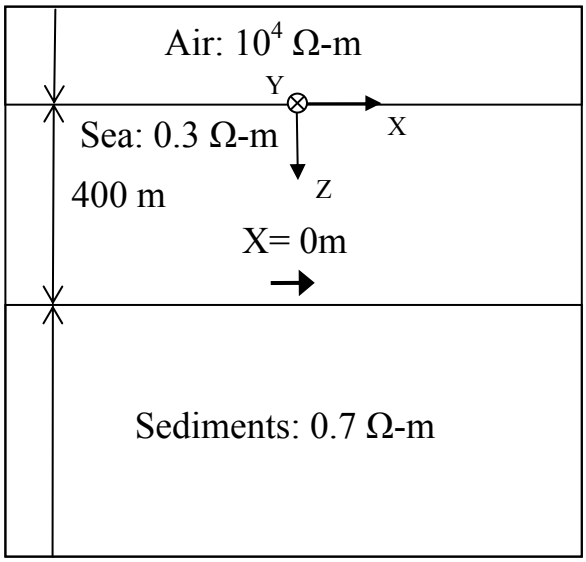

(a)

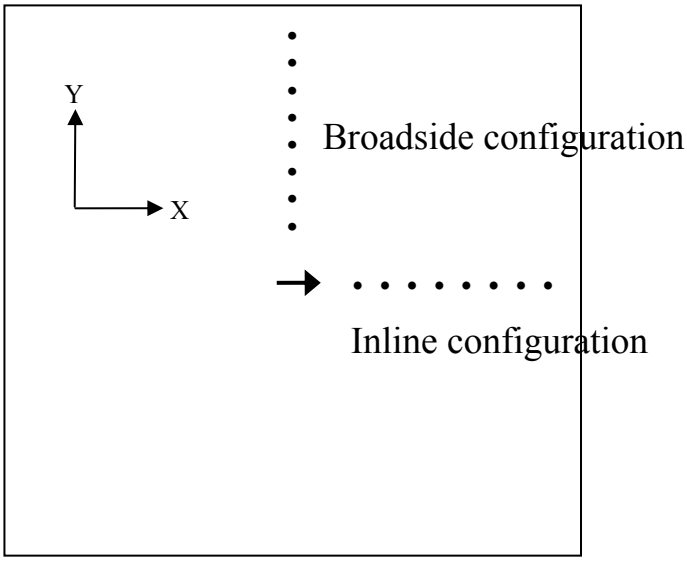

(b)

Figure 4.3. (a) The x-z section (Y=0 m) of the homogeneous seafloor model. The black horizontal arrow is an electric-dipole source. Its center is placed at (0 m, 0 m, 350 m). (b) The TDCSEM configuration on the seafloor (x-y plane). Receiver positions are denoted as •, and their spacing is 1 km.

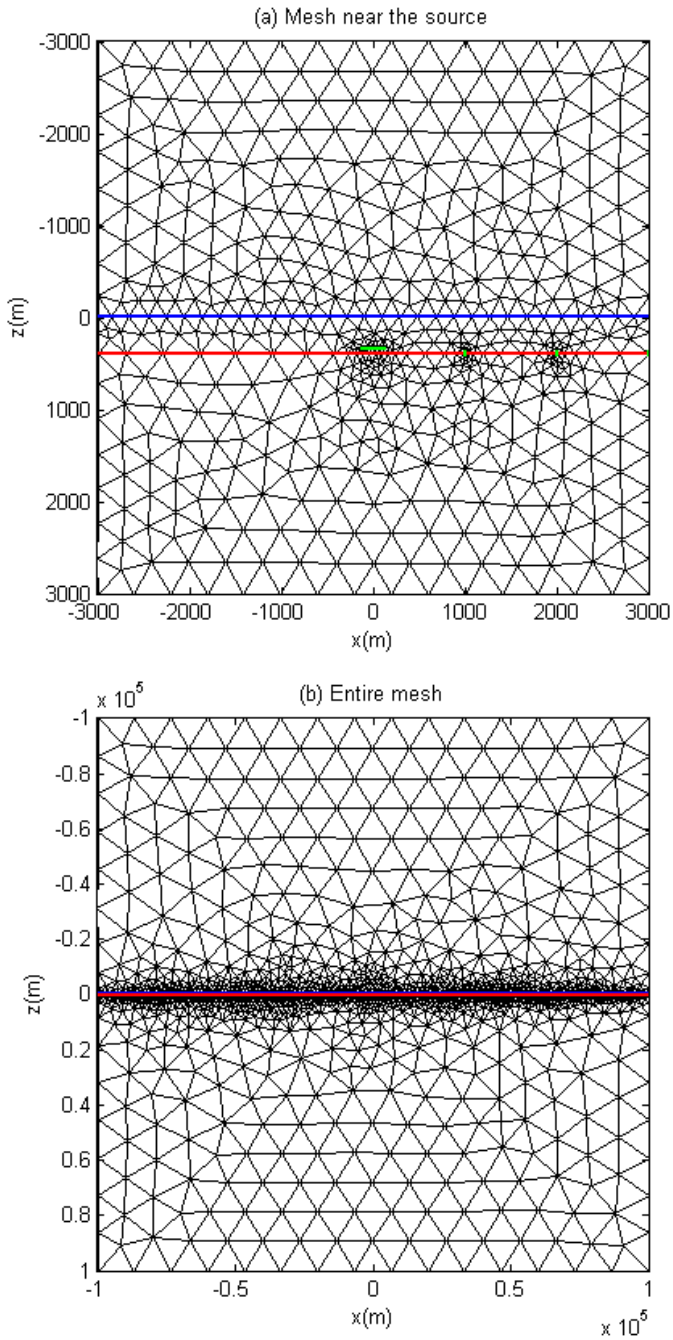

Figure 4.4. A cross-sectional view (Y = 0 m) of the 3D FETD mesh used for the homogeneous seafloor shown in Figure 4.2. In (a) and (b), the air-seawater interface is blue, and the seafloor is red. In (a), the green line segment above the center of the seafloor is a 250-m-long electric-dipole source, and the three shorter green line segments are the seafloor detectors.

Figure 4.5 shows both the inline and broadside responses over the model and their relative percentage errors with respect to the analytical solutions. Overall good agreement is observed for both solutions. The electric fields do not change in early time because it takes time for the electric fields to diffuse from the source position to the receiver positions. Therefore, the relative errors observed in early times mainly come from the DC resistivity problem (i.e. the Poisson equation). As time-stepping continues, the oscillation of percentage errors gradually increases due to the error migration from early to late time, but errors remain within 3 % and 5% in the x- and z-directions, respectively. Although whether or not the range of errors can be considered acceptable depends on modeling problems and goals, the range is sufficiently smaller than or at least comparable to that found in FDTD modeling research (e.g. Wang and Hohmman, 1993; Commer and Newman, 2004).

Note that the z-components of the electric fields (E_z) are more vulnerable to the error migration than the x-components of the electric fields (E_x). When an x-oriented electric-dipole source is simulated, such an error pattern is repeatedly observed in my modeling experiments. I believe that this is because the amplitudes of E_z are an order of magnitude smaller than those of E_x, and therefore are more easily contaminated with numerical noise. The y-components of the electric fields (E_y) clearly show typical sign reversals observed in the broadside configuration. In the vicinity of the sign reversals, the percentage errors sharply increase but quickly reduce, verifying the accuracy of the FETD algorithm.

In Figure 4.5g, the analytical algorithm first computes the analytical solutions for the z-components of magnetic fields (B_z) and then numerically approximates their time derivatives ($\partial B_z \partial t$). The approximations are somewhat noisy at very early times (e.g. 0.01 to 0.05 seconds) due to catastrophic cancelation, and thus they are not plotted in that time range. The noise resulting from the numerical approximation is still seen as a stair-step pattern at early times (e.g. 0.05 to 1 seconds) in Figure 4.5g. However, at intermediate and late times (1 to 100 seconds), the $\partial B_z \partial t$ curves of both the analytical and FETD solutions show excellent agreement with low percentage errors (e.g. < 2 %), confirming the accuracy of the FETD algorithm.

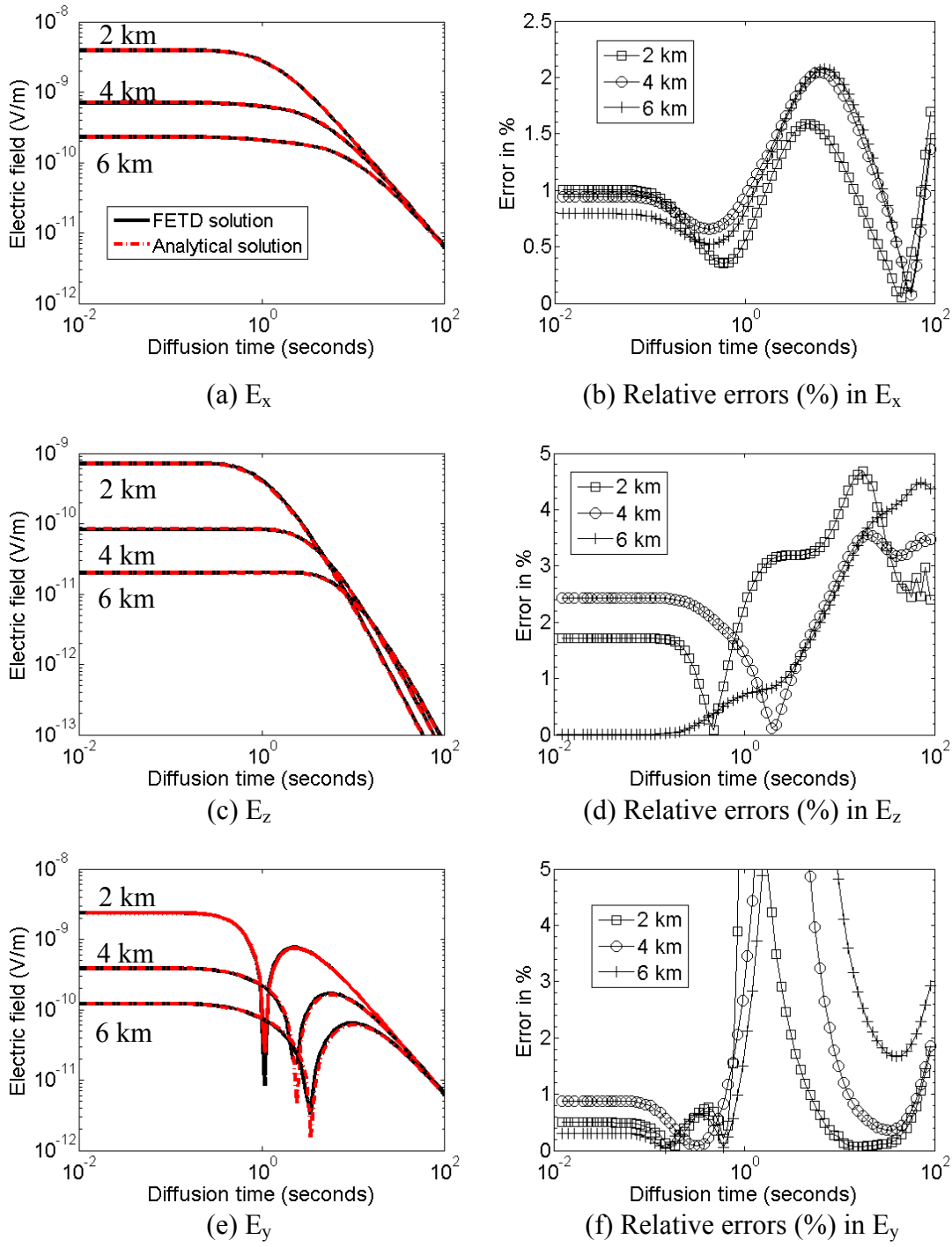

(a) E_x (b) Relative errors (%) in E_x

(c) E_z (d) Relative errors (%) in E_z

(e) E_y (f) Relative errors (%) in E_y

Figure 4.5. TDCSEM inline and broadside responses for selected receiver positions over the model shown in Figure 4.3. The left column contains the EM fields; the right column contains the percentage difference (e.g. error) between the analytical and the FETD solutions.

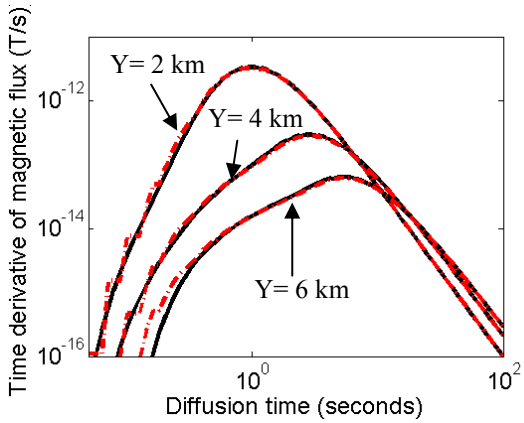

(g) $dB_z dt$

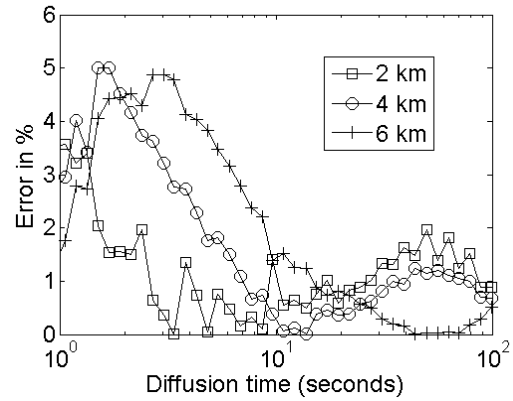

(h) Relative errors (%) in $dB_z dt$

Figure 4.5. Continued.

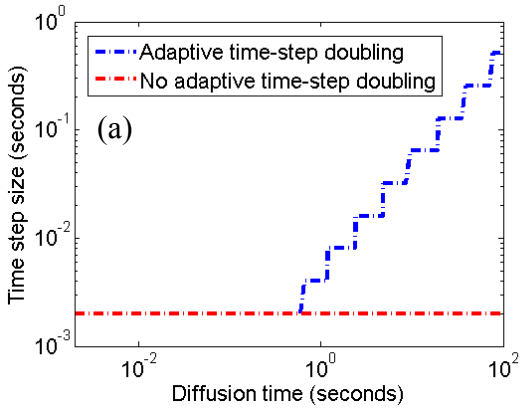

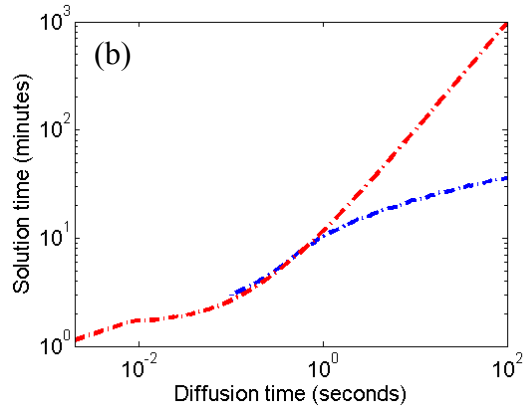

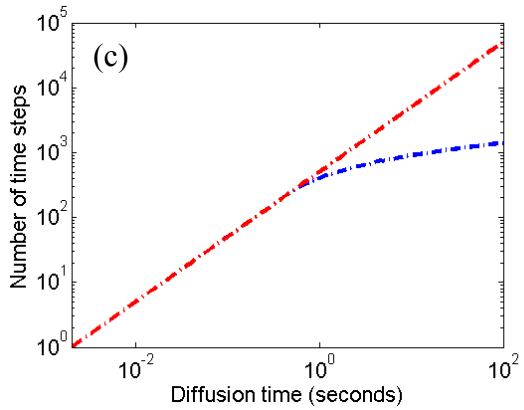

Figure 4.6. Comparison of computational efficiency in the model shown in Figure 4.3, with and without doubling the time step. (a) The evolution of the time-step size as a function of diffusion time. (b) The solution time as a function of diffusion time. (c) The number of time steps as a function of diffusion time. The diffusion time is the time scale in which the EM diffusion phenomena occur.

Figure 4.6 summarizes the performance and effectiveness of the adaptive time-step-doubling method. Without the method, the simulation took 16.2 hours with 50,000 time steps to complete the simulation. In contrast, when the doubling method was employed, the simulation was completed in just 36 minutes with 1,393 time-steps. The time-step-doubling procedures were applied eight times, which implies that the factorization of matrix D in equation 3.12 is performed only nine times to complete the simulation.

To examine the impact of the time-step doubling method on the accuracy, the FETD solutions with the constant time-step (i.e. 0.002 seconds) and their percentage errors are plotted in Figure 4.7 and are compared with the solutions with the time-step doubling method (Figure 4.5). As expected, the comparison shows that the accuracy of the FETD solutions with and without the time-step doubling method is nearly identical, illustrating that the time-step doubling method little affects the accuracy.

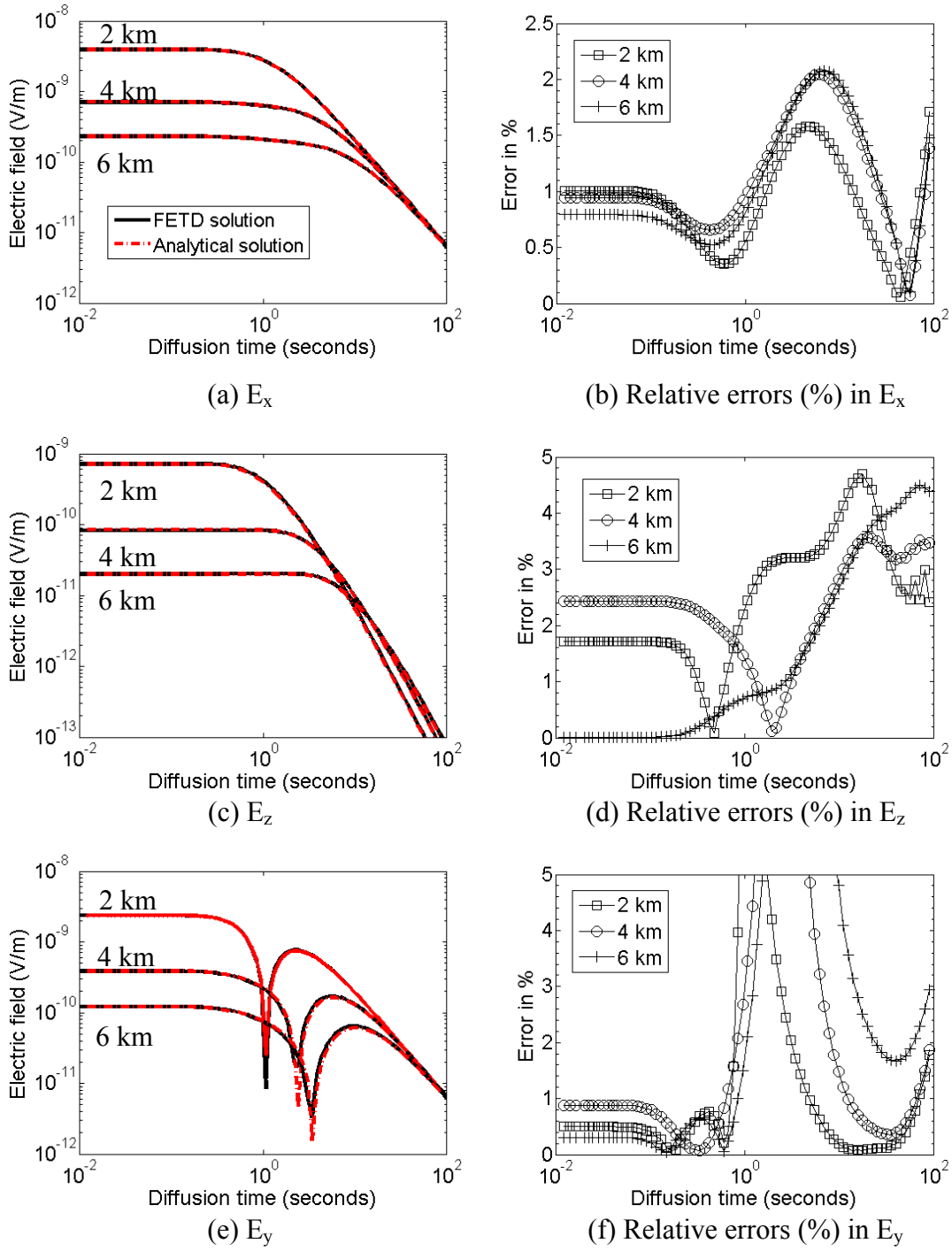

Figure 4.7. TDCSEM inline and broadside responses over the model shown in Figure 4.3. The constant time step (0.002 seconds) is used during the entire diffusion time. The left column contains the EM fields; the right column contains the percentage difference (e.g. error) between the analytical solutions and the FETD solutions.

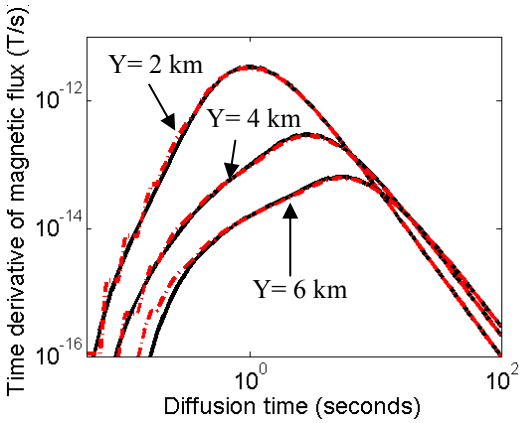

(g) $dB_z dt$

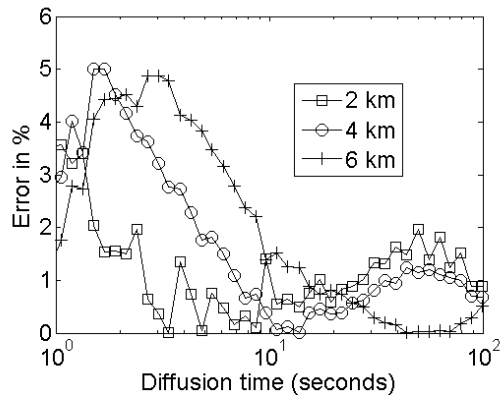

(h) Relative errors (%) in $dB_z dt$

Figure 4.7. Continued.

4.2.2 Seafloor model with resistive layer

In the next example, a 100- Ω-m resistive layer (e.g. oil or CO_2 reservoir) 100 m thick is inserted into the previous model at a depth of 1 km below the seafloor as shown in Figure 4.8. The other simulation parameters are kept the same. The model is discretized into 209,252 tetrahedral elements, generating 243,543 unknowns along the edges of the tetrahedral elements. Again, a large number of tetrahedral elements are required to discretize the thin 1D reservoir, because elements cannot grow rapidly in the thin reservoir. It took 68 minutes to simulate this seafloor model with eight time-step-doubling procedures. The inline and broadside electric-field responses over the model are shown in Figures 4.6. The FETD solutions agree well with the analytical 1D solutions.

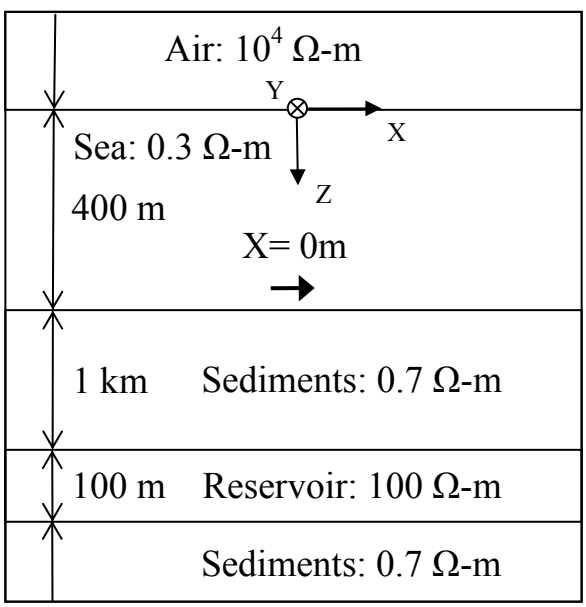

Figure 4.8. The x-z section (Y=0 m) of the 1D reservoir model. The same inline and broadside as shown in Figure 4.3b is employed here.

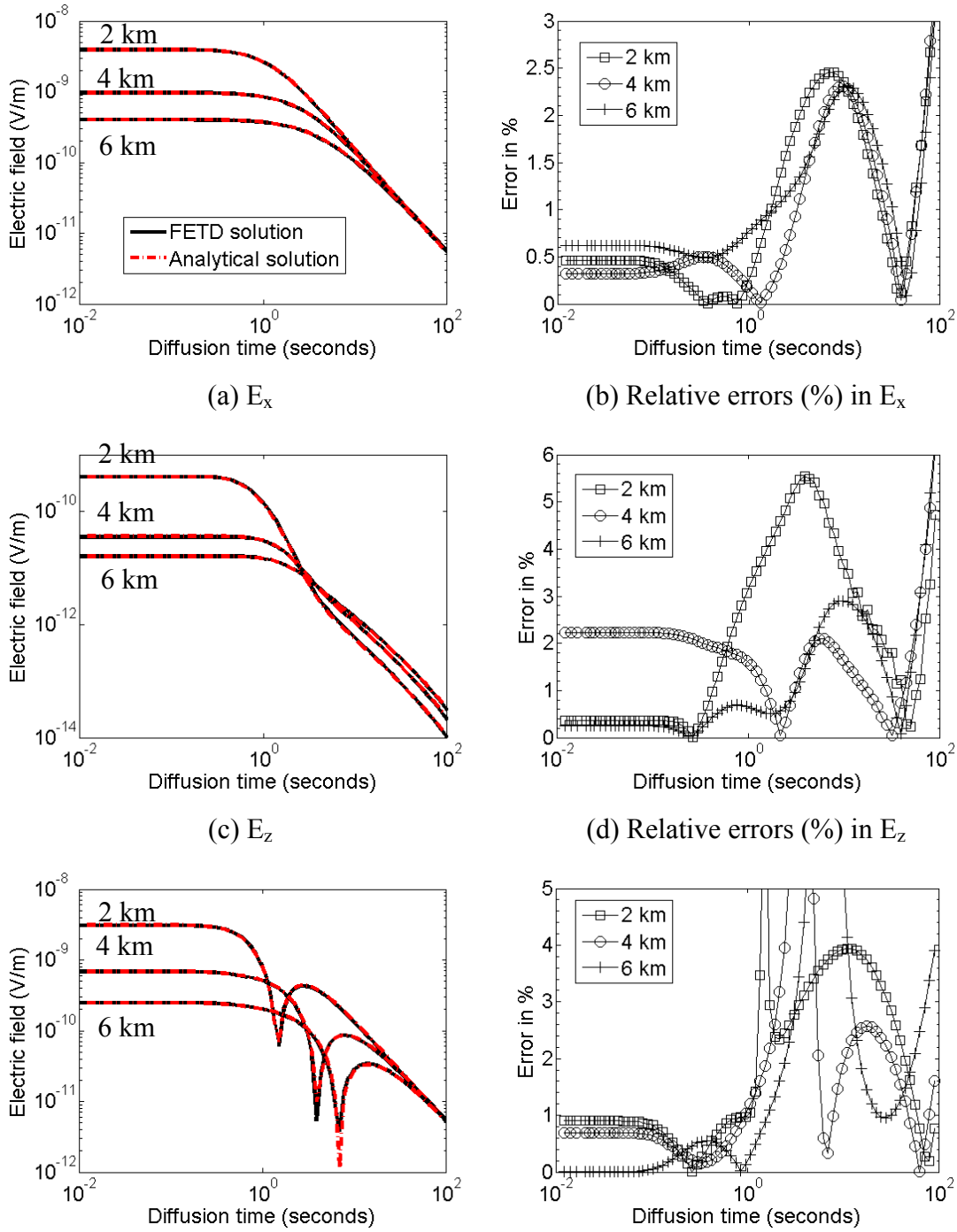

(a) E_x (b) Relative errors (%) in E_x

(c) E_z (d) Relative errors (%) in E_z

(e) E_y (f) Relative errors (%) in E_y

Figure 4.9. TDCSEM inline and broadside responses for the three receiver positions over the model shown in Figure 4.8. The left column contains the EM fields; the right column contains the percentage difference (e.g. error) between the analytical solutions and the FETD solutions.

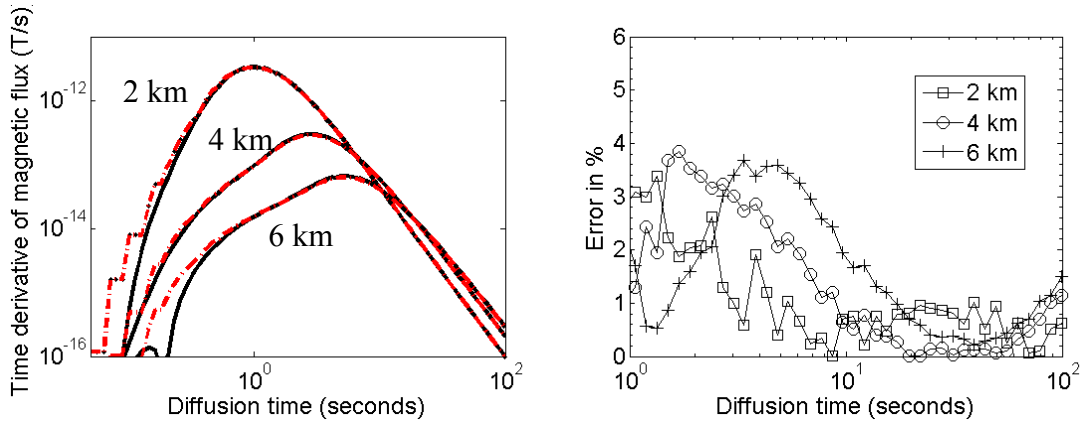

(g) $dB_z dt$ (h) Relative errors (%) in $dB_z dt$

Figure 4.9. Continued.

4.2.3 Land model with 3D gas reservoir

The next example is a 3D resistive gas reservoir shown in Figure 1.2. In this model, the resistivity of the air is set to $1x10^8$ Ω-m, which is four orders of magnitude larger than that of the air in the seafloor models. Note that the background subsurface of the gas reservoir model is about an order of magnitude more resistive than the seabed of the previous seafloor models. However, my numerical modeling experiments indicate that such a highly resistive air layer is required to ensure accurate solutions when sources and receivers are placed at the air-earth interface. As a side note, I was able to set the resistivity of the air to maximum $1x10^{12}$ Ω-m in this model when a direct solver is used. Beyond this limit, matrix **D** in equation 3.12 becomes too poorly conditioned, resulting in inaccurate and unstable solutions.

The inline TDCSEM responses over the gas reservoir are simulated using both FDTD and FETD algorithms. A 250-meter-long electric dipole, whose ramp-off time is set to $1x10^{-4}$ seconds is placed at the center of the model. The FDTD modeling results for the model are computed using the 3D FDTD solution (Commer and Newman, 2004). The FDTD model consists of 139-by-99-by-71 grid cells in the x-, y- and z-directions, with the computational domain boundaries 10 km from the source. The FDTD model has 977,031 cells and 2,931,093 unknowns. The FDTD grids used for this model are shown in Figures 1.3a and 1.3b. In contrast, the FETD model has

114,116 tetrahedral elements and 131,741 unknowns. Note that the total number of grid cells required for the FDTD model is nearly nine times larger than that for the FETD model. The comparison above illustrates the fact that an FETD mesh can economically discretize a large computational domain with a relatively small number of unknowns.

The cross-sectional view (Y=0) of the FETD mesh used for the model is shown in Figures 1.3c and 1.3d. In the FETD mesh design, I deliberately use very fine elements around the source to accurately resolve the very early time behavior of the TEM fields for verification purposes, even though the early time TEM fields don't convey useful information about the 3D reservoir. Note that such a mesh generation is practically feasible only in FE modeling, since fine meshes in the center of the model do not have to extend to the computational boundaries of the FETD model (Key and Weiss, 2006). The mesh boundary of the FETD model is 30 km from the source in order to ensure accurate solutions at very late times. It took 53 minutes to complete the FETD simulation, with a total of 1,559 time steps, when the adaptive time-step-doubling method was employed. The FETD and FDTD simulation results are plotted in Figure 4.10 and show good agreement.

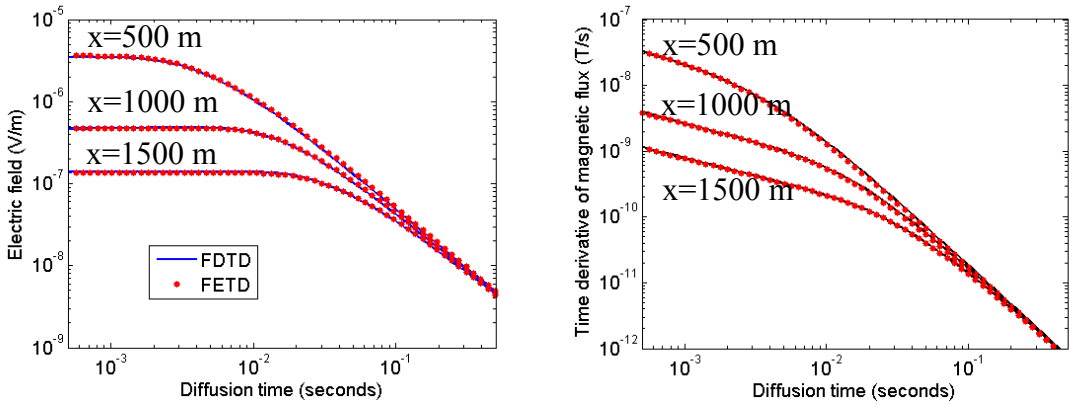

(a) Ex (b) $dB_y dt$

Figure 4.10. TDCSEM inline responses at three receiver positions over the model shown in Figure 1.2.

4.2.4 Dipping seafloor model

Marine TDCSEM responses are calculated for a two-dimensional (2D) seafloor (Figure 4.11), gently dipping at 4 degrees, with and without a 3D hydrocarbon reservoir. In order to examine the effects of ignoring the sloping seafloor on the marine TDCSEM method, a flat seafloor model with and without the same hydrocarbon reservoir is also simulated. The flat seafloor model has a uniform 400-meter-thick seawater column. The dipping and flat seafloor models are discretized into 165,528 tetrahedral elements with 191,780 unknowns and 127,046 tetrahedral elements with 146,871 unknowns, respectively. The simulations are completed in 65 minutes and 41 minutes, respectively.

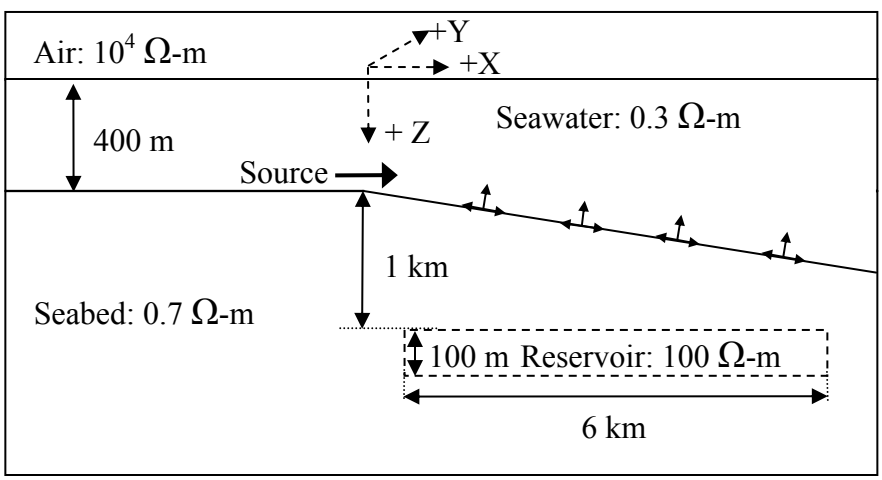

Figure 4.11. A gently dipping seafloor structure with and without a reservoir. The small, triple-arrow symbols indicate EM receivers. The dip angle of the seafloor is 4°. A 250-m-long electric-dipole source is placed 50 m above the seafloor. The reservoir position is outlined with the dashed box. The size of the reservoir is 6 x 6 x 0.1 (km) in the x-, y- and z-directions, respectively. Its axis base point is (1 km, -3 m, 1500 m).

The inline E_x and E_z responses for the flat and dipping seafloor models with and without the reservoir are compared with each other at three receiver positions in Figure 4.12. The noticeable differences observed in Figure 4.12 can be attributed to a combination of the following factors: First, receivers on the slope have thicker water column above them as the source-receiver offset increases. As a result, they record a different level of the 'airwave' effect from those on the flat seafloor. Second, receivers on the slope measure stronger reservoir effects than those on the flat seafloor, because of their shorter distance from the resistive reservoir. Third, receivers on the slope are tilted toward the slope. Thus, the x- and z-components of the receivers do not point in the same directions as the x- and z-components of receivers on the flat seafloor. Because the amplitudes of horizontal electric fields are much larger than those of vertical electric fields, the tilt of a receiver's coordinate system due to the slope has a significant impact, especially on the vertical electric-field measurements.

Next, by assuming that the tiltmeter readings of the receivers (i.e. 4 degrees) are available, receivers' coordinate systems are correctly rotated. The corrected E_x and E_z responses for the dipping seafloor models are compared with those for the flat seafloor models (Figure 4.13). The small amount of the rotation produces little difference in the E_x responses, indicating that the E_x responses are robust to the receiver tilt. In contrast, the corrected E_z responses become closer to those for the flat seafloor models than the uncorrected E_z responses, but the differences are noticeable. In short, a gently-dipping, simple, 2D seafloor structure can significantly affect the TDCSEM measurements. As demonstrated above, seafloor topography needs to be modeled with special care, and tiltmeter readings should be used to properly rotate seafloor measurements. In Chapters 7 and 8, I will revisit the seafloor topography problem by analyzing various TDCSEM source-receiver configurations in more sophisticated topography models.

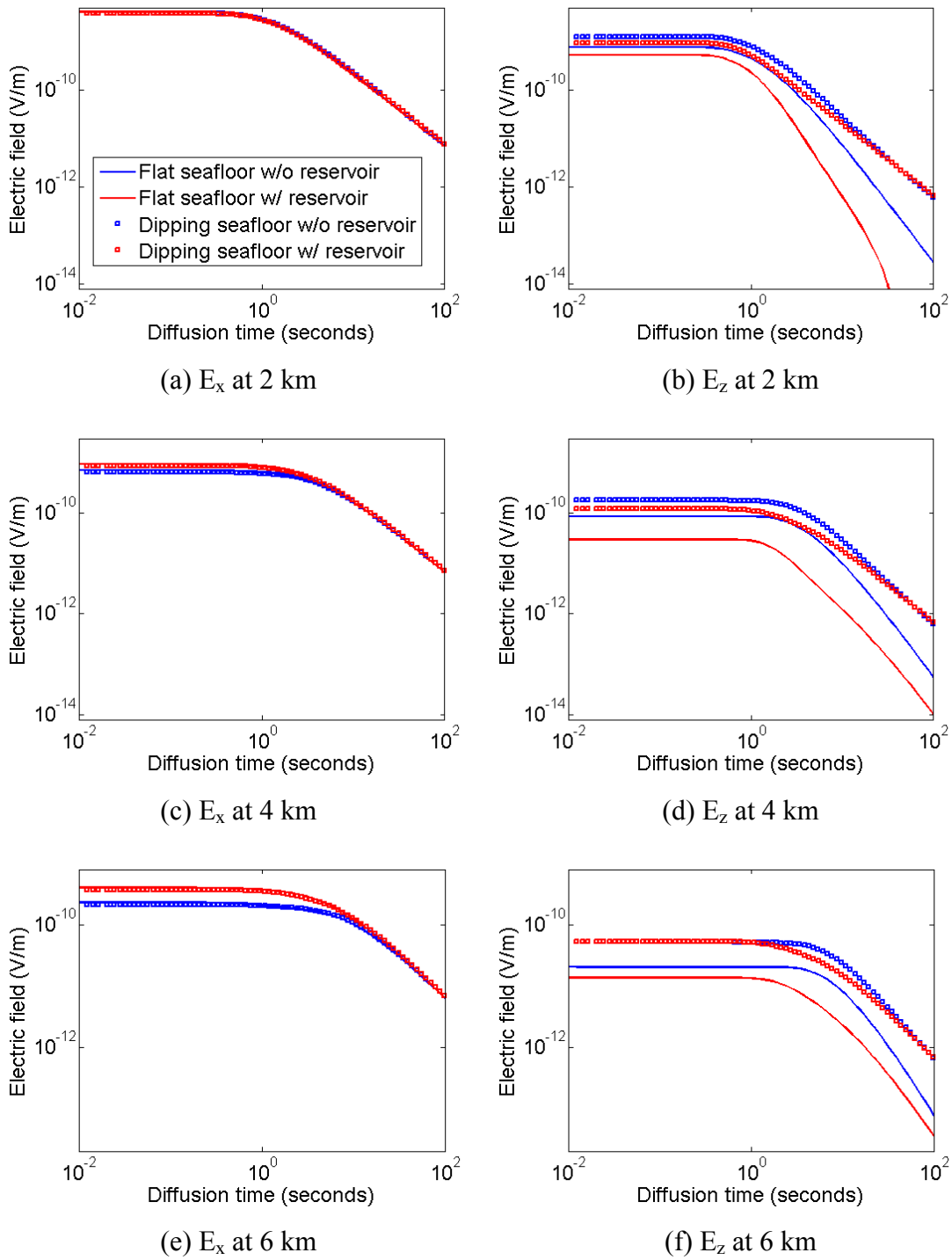

Figure 4.12. The inline TDCSEM responses over the model shown in Figure 4.11. The coordinates of the receivers are not corrected.

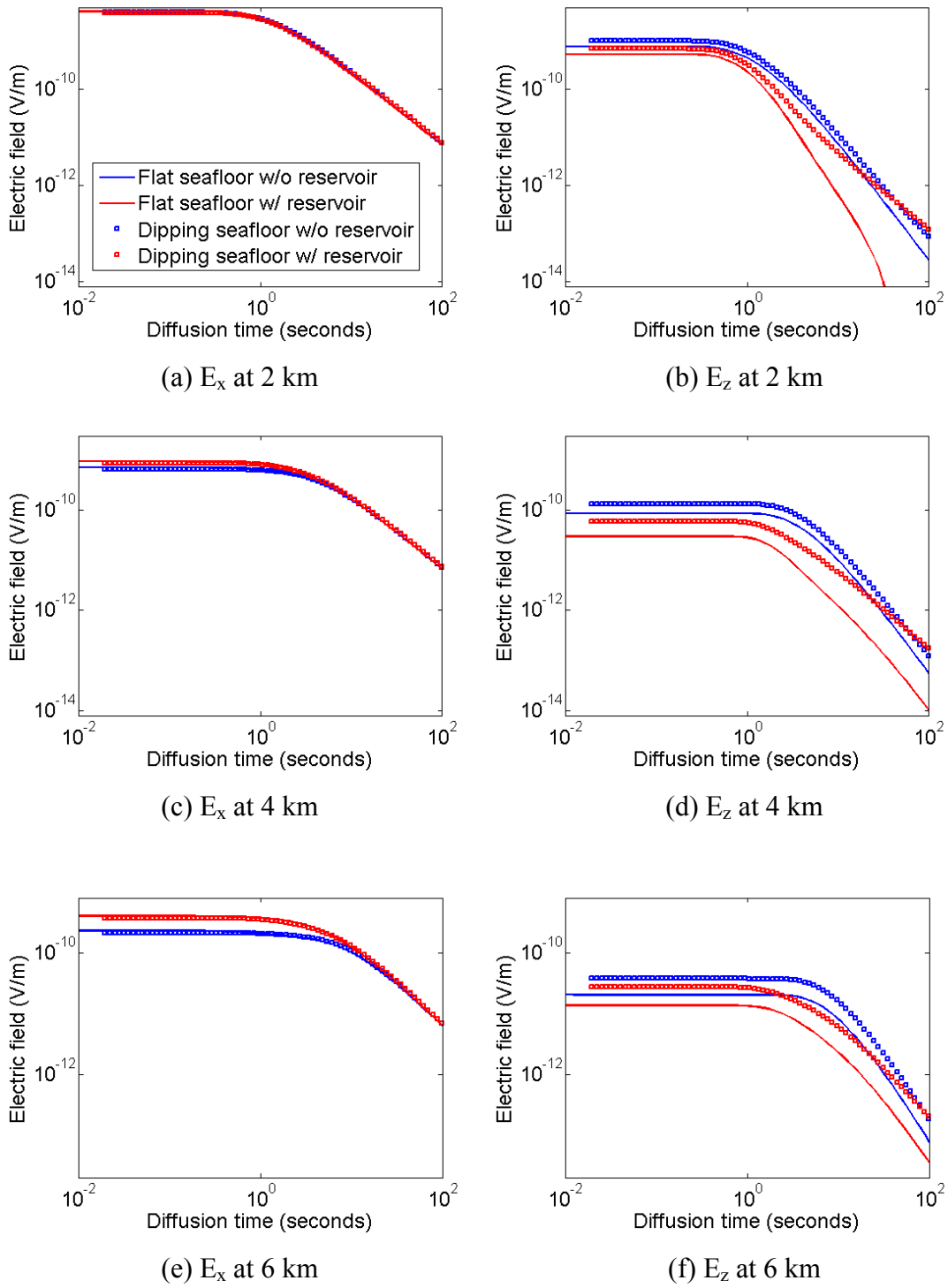

(a) E_x at 2 km (b) E_z at 2 km

(c) E_x at 4 km (d) E_z at 4 km

(e) E_x at 6 km (f) E_z at 6 km

Figure 4.13. The inline TDCSEM responses over the model shown in Figure 4.11. The coordinates of the receivers are corrected.

4.2.5 Interpretation of TDCSEM field data

In contrast to the previous modeling examples, this section presents the FETD-based interpretation of the TDCSEM field data collected in the Odenwald area, Germany (Hördt et al., 2000). Figure 4.14a shows a map of this area. Shaded areas indicate the Odenwald crystalline rock, with lighter and darker variations denoting granites and diorites, respectively. Sediments are white, and the large white area in the west is the Upper Rhine Graben. Although the overall geological structure of this area is fairly one-dimensional, the field data are corrupted with anomalies from local inhomogeneity. Therefore, 1D inversion approaches do not give reasonable results.

A 3D FDTD-based inversion algorithm (Newman and Commer, 2005) was recently developed to fully take into account the 3D nature of field data. However, the inversion algorithm is not yet routinely applicable to field situations, because it requires massively parallel computing facilities to tackle the enormous computational cost of solving 3D FDTD forward-modeling problems. In contrast, as demonstrated in this chapter, the 3D FETD algorithm is much more efficient in terms of memory usage and solution time. Therefore, in this section, I attempt to find a 3D FETD model that gives a reasonable fit to the field data using a trial-and-error forward-modeling strategy.

The TDCSEM data-acquisition layout is shown in Figure 4.14a. In the legend, LOTEM stands for long-offset transient electromagnetics (Strack, 1992). The broadside land TDCSEM configuration is often called LOTEM. Receiver spread 6 with transmitter 3 is treated in detail as investigated in Hördt et al. (2000). The electric-dipole transmitter is set to 1.24 km. The length of the electric-dipole receivers is set to 100 m. To better illustrate the spatial distribution of the configuration shown in Figure 4.14a, the coordinates of the transmitter and the receivers are replotted on the 2D plane (Figure 4.14b). The origin of the coordinates in the 2D plane is set to the center of the transmitter. Note that the receivers are not oriented along the lines that connect them to the center of the transmitter but are parallel to the transmitter's orientation.

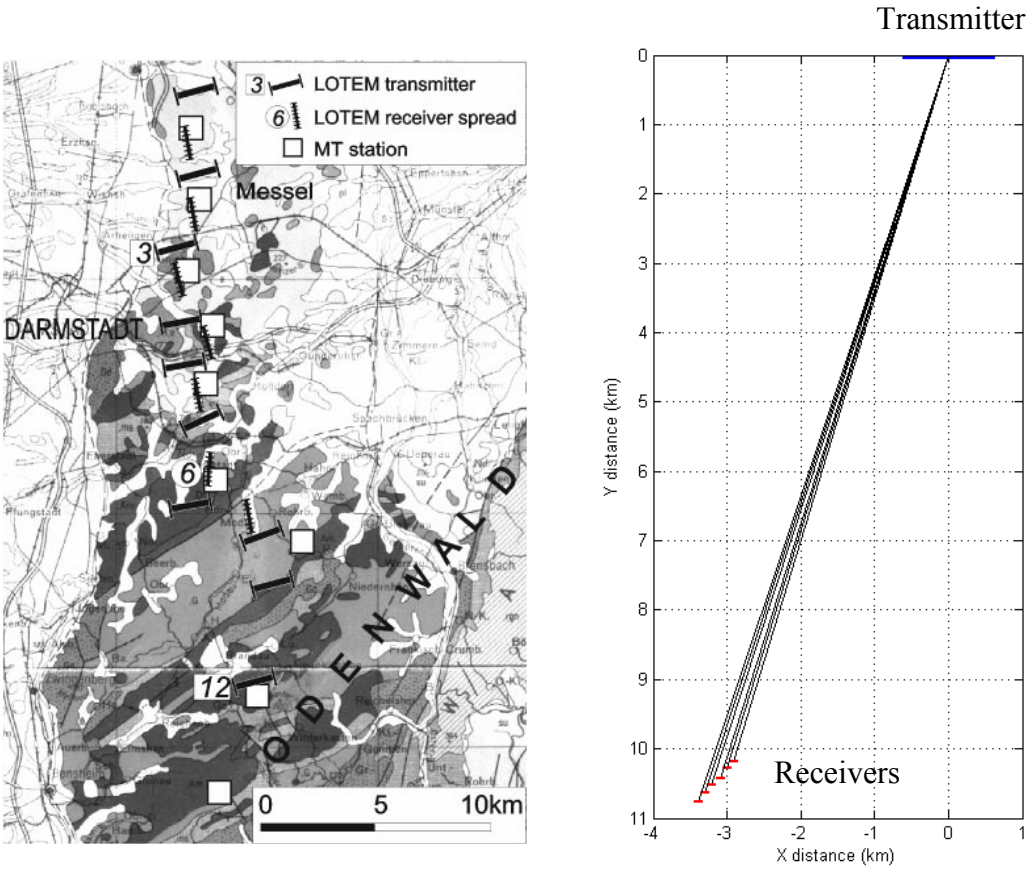

(a) (b)

Figure 4.14. (a) The overall distribution of transmitters and receivers (Hördt et al., 2000). The lengths of the transmitter and of the spreads are exaggerated for the sake of visibility. (b) Detailed relative locations of transmitter 3 (blue) and receiver spread 6 (red) on the x-y plane. The black solid lines connect the center of each receiver with the center of the transmitter. Receivers are numbered from 1 to 6 from the lower left to the upper right.

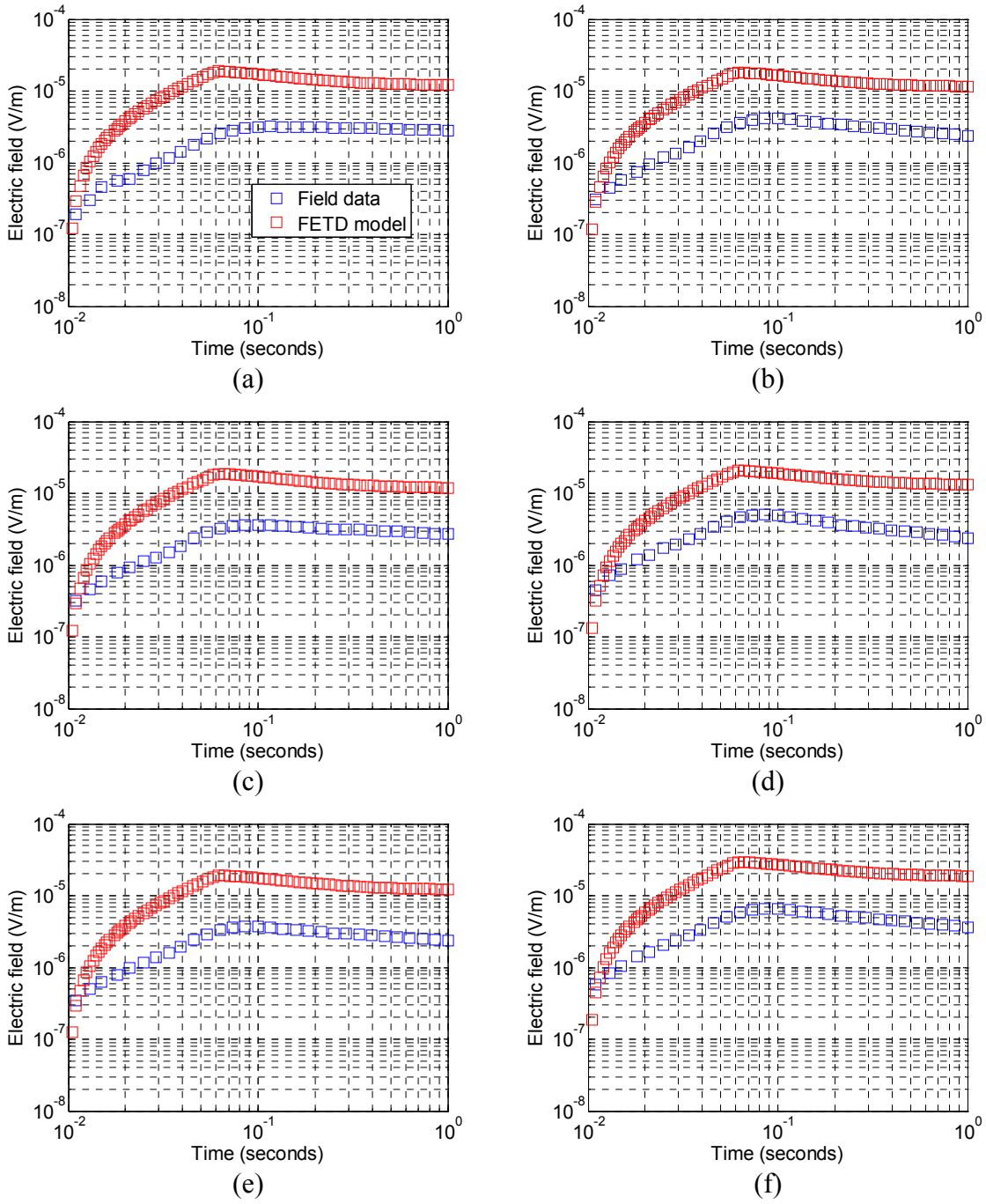

Figure 4.15. The comparison of the field data and the FETD modeling data. The FETD modeling data are computed over the model described in Figure 4.16a. (a) Receiver 1. (b) Receiver 2. (c) Receiver 3. (d) Receiver 4. (e) Receiver 5. (f) Receiver 6.

To examine the effects of the local inhomogeneity on the TDCSEM survey, the field data are first compared with the modeling data resulting from a 1D starting FETD model (Figure 4.15). The starting FETD model is illustrated in Figure 4.16a (Hördt et al., 2000). As shown in Figure 4.15, the resulting FETD modeling data and the field data are fairly similar in shape, but the field data are consistently shifted down in amplitude for all six receiver positions. Thus, an experienced interpreter would be able to deduce that there is a conductive body near the transmitter. The conductive body traps the transient currents inside it for the entire measurement time and consistently shifts down the electric-field amplitudes at the receiver positions (Um, 2005).

To determine the size and position of the conductive body, about 80 FETD models have been constructed and simulated. Average solution time per model is about 11 minutes on a 2.26 GHz Intel Nehelem single core using 8 GB memory. Figures 4.16b through 4.16i show eight selected FETD models that have a 10-Ω-m resistive rectangular conductor at various positions in the vicinity of the transmitter. The resulting FETD modeling data are compared with the field data in Figures 4.17 through 4.24.

When the upper-left corner of the 3D conductor is placed at (x=2 km, z=-0.5 km), as shown in Figure 4.16b, the fit between the field data and the modeling data significantly improves at late times (Figure 4.17). However, significant misfits are still observed at early and intermediate times. These observations indicate that the field data do contain the information about the large-scale 1D background geology, but that the 3D conductor does not adequately model the local inhomogeneity that affects the early- and intermediate-time data. As the conductor gradually moves from the lower-right corner below the transmitter to directly below the transmitter (Figures 4.16b through 4.16h), the fitness improves at intermediate times but deteriorates at late times (Figure 4.17 through Figure 4.23).

This problem is eventually fixed by reducing the thickness of the conductor by 50 % as shown in Figure 4.16i. The comparison of the field data and the final modeling data are presented in Figure 4.24. Excellent overall agreement between the two data sets is observed at intermediate and late times, but some large discrepancies persist at early

times. This is probably due to 1) inevitable limits of replacing the true local inhomogeneity with the simplified rectangular conductor, 2) the effects of the topography on the field data, and 3) background noise in the early-time field data, among other complications.

In this section, I have presented trial-and-error forward modeling to demonstrate that the FETD algorithm can be used to interpret real field data. The FETD algorithm rapidly computes TDCSEM responses to a model, but the trial-and-error forward modeling is still cumbersome and time-consuming. Therefore, this interpretation approach cannot be considered practical. This modeling work illustrates the necessity of developing fast 3D FETD-based imaging algorithms for routine TDCSEM interpretations.

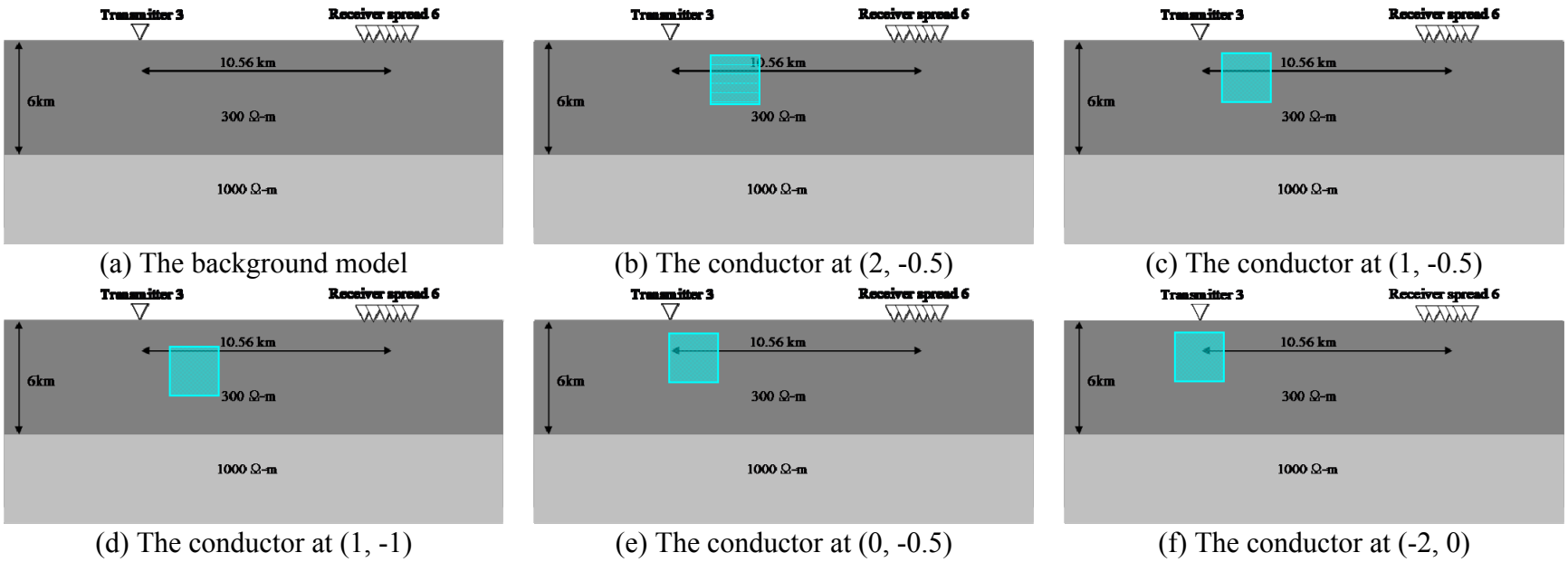

(a) The background model (b) The conductor at (2, -0.5) (c) The conductor at (1, -0.5)

(d) The conductor at (1, -1) (e) The conductor at (0, -0.5) (f) The conductor at (-2, 0)

Figure 4.16. Earth models used in the trial-and-error forward-modeling analysis. The resistivity of the rectangular conductor is set to 10 Ω-m. Its size is 4x4x4 km in (b) through (h) and 4x4x2 km in (i). The location of the conductor is defined as the coordinate (x km, z km) of its upper-left corner.

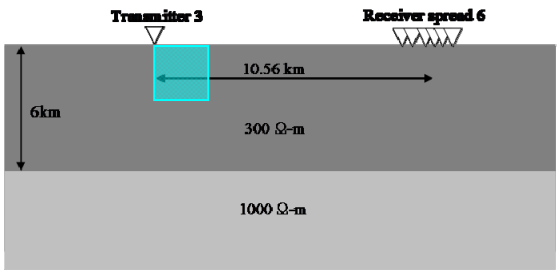

(g) The conductor at (0, 0)

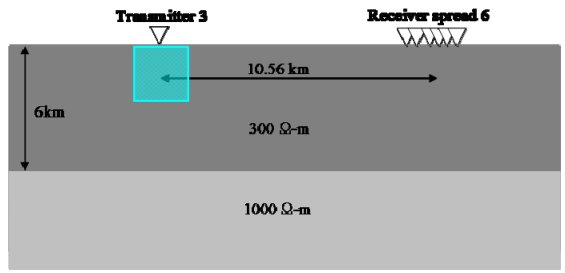

(h) The conductor at (-2, 0)

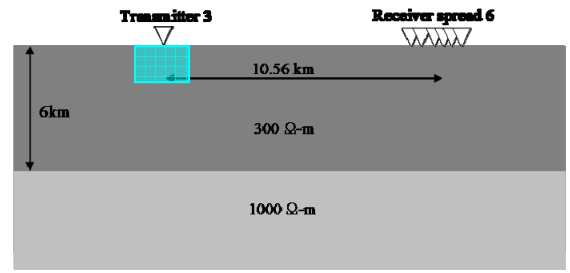

(i) The conductor at (-2,0)

Figure 4.16. Continued.

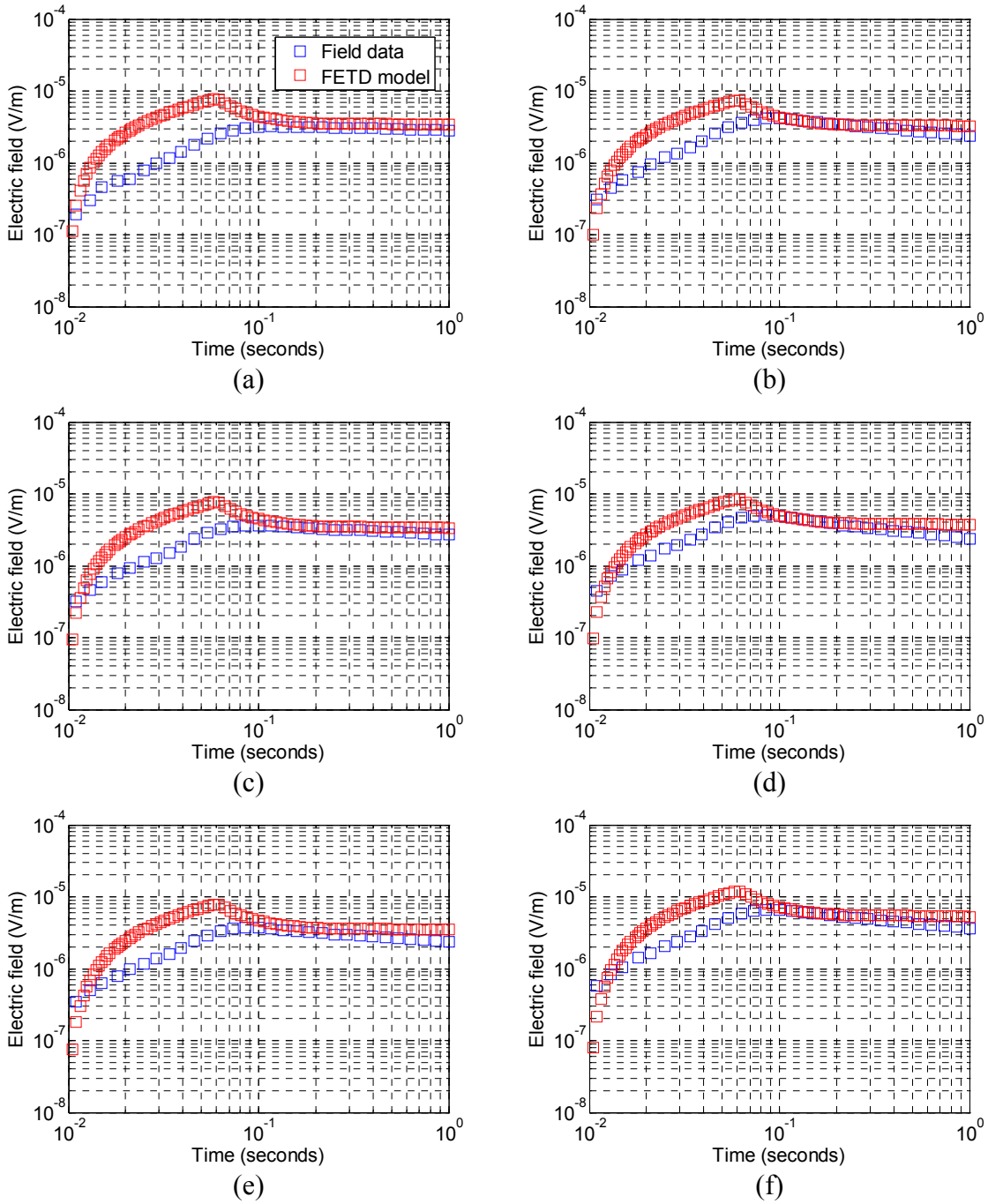

Figure 4.17. The comparison of the field data and the FETD modeling data. The FETD modeling data are computed over the model described in Figure 4.16b. (a) Receiver 1. (b) Receiver 2. (c) Receiver 3. (d) Receiver 4. (e) Receiver 5. (f) Receiver 6.

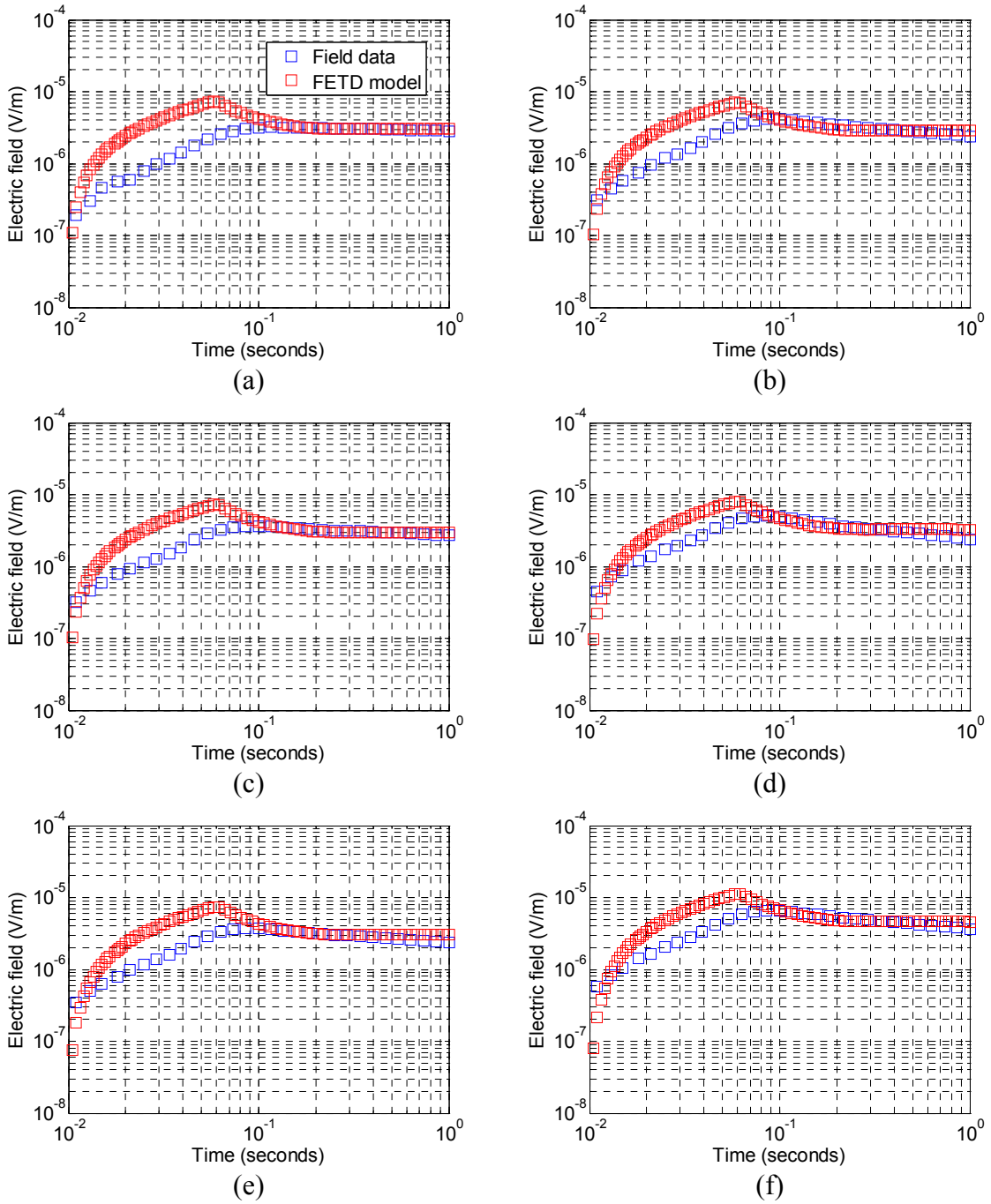

Figure 4.18. The comparison of the field data and the FETD modeling data. The FETD modeling data are computed over the model described in Figure 4.16c. (a) Receiver 1. (b) Receiver 2. (c) Receiver 3. (d) Receiver 4. (e) Receiver 5. (f) Receiver 6.

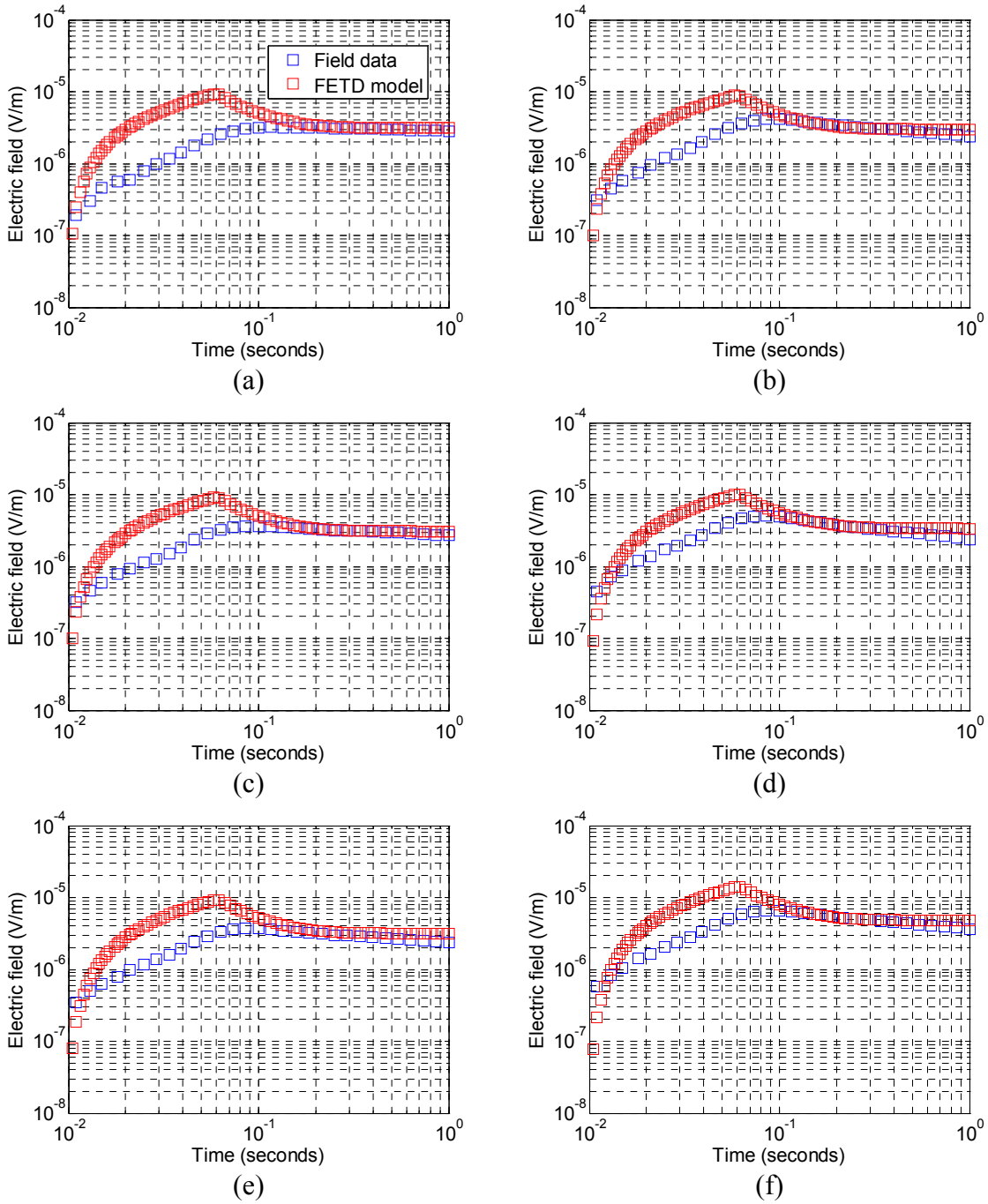

Figure 4.19. The comparison of the field data and the FETD modeling data. The FETD modeling data are computed over the model described in Figure 4.16d. (a) Receiver 1. (b) Receiver 2. (c) Receiver 3. (d) Receiver 4. (e) Receiver 5. (f) Receiver 6.

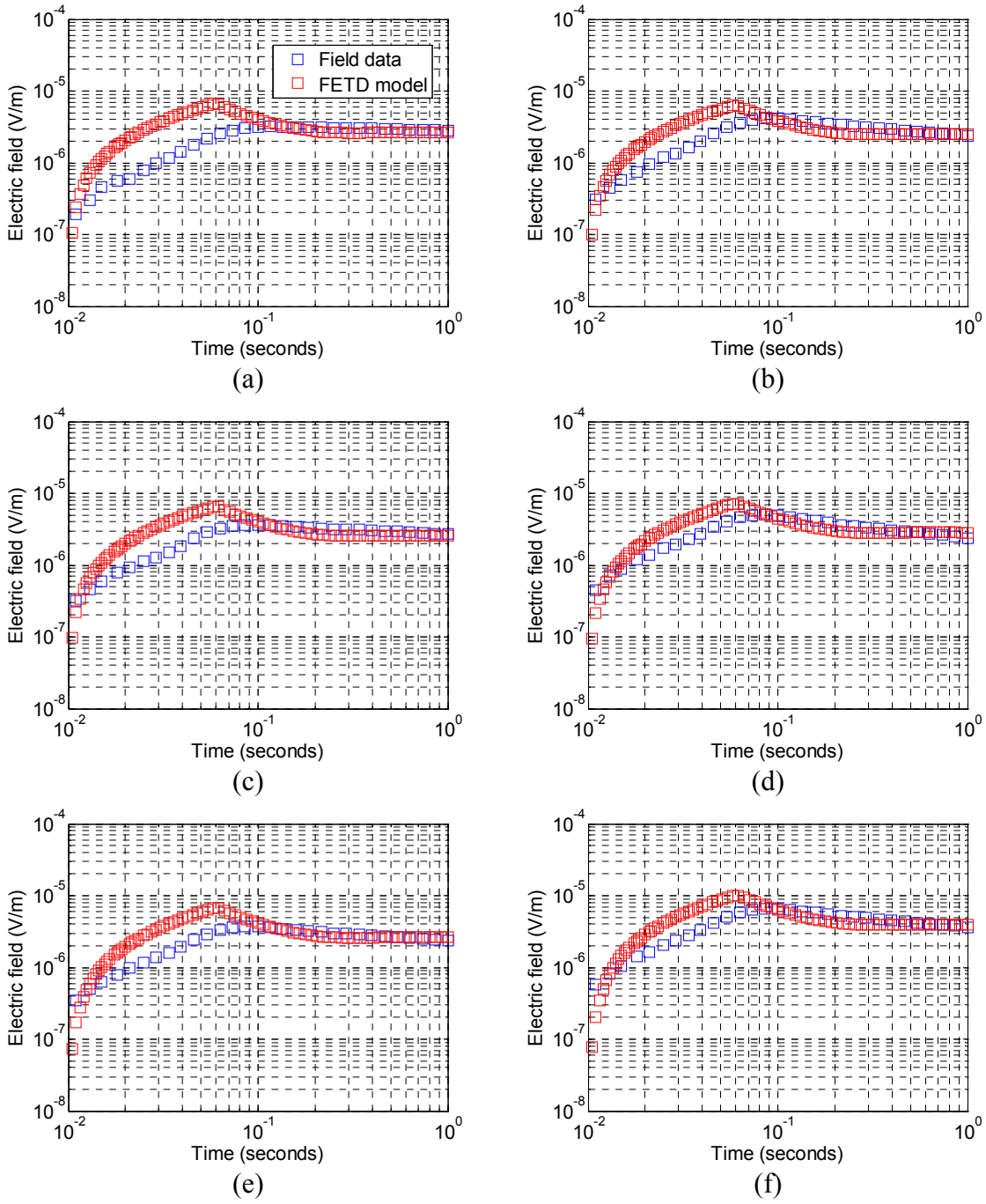

Figure 4.20. The comparison of the field data and the FETD modeling data. The FETD modeling data are computed over the model described in Figure 4.16e. (a) Receiver 1. (b) Receiver 2. (c) Receiver 3. (d) Receiver 4. (e) Receiver 5. (f) Receiver 6.

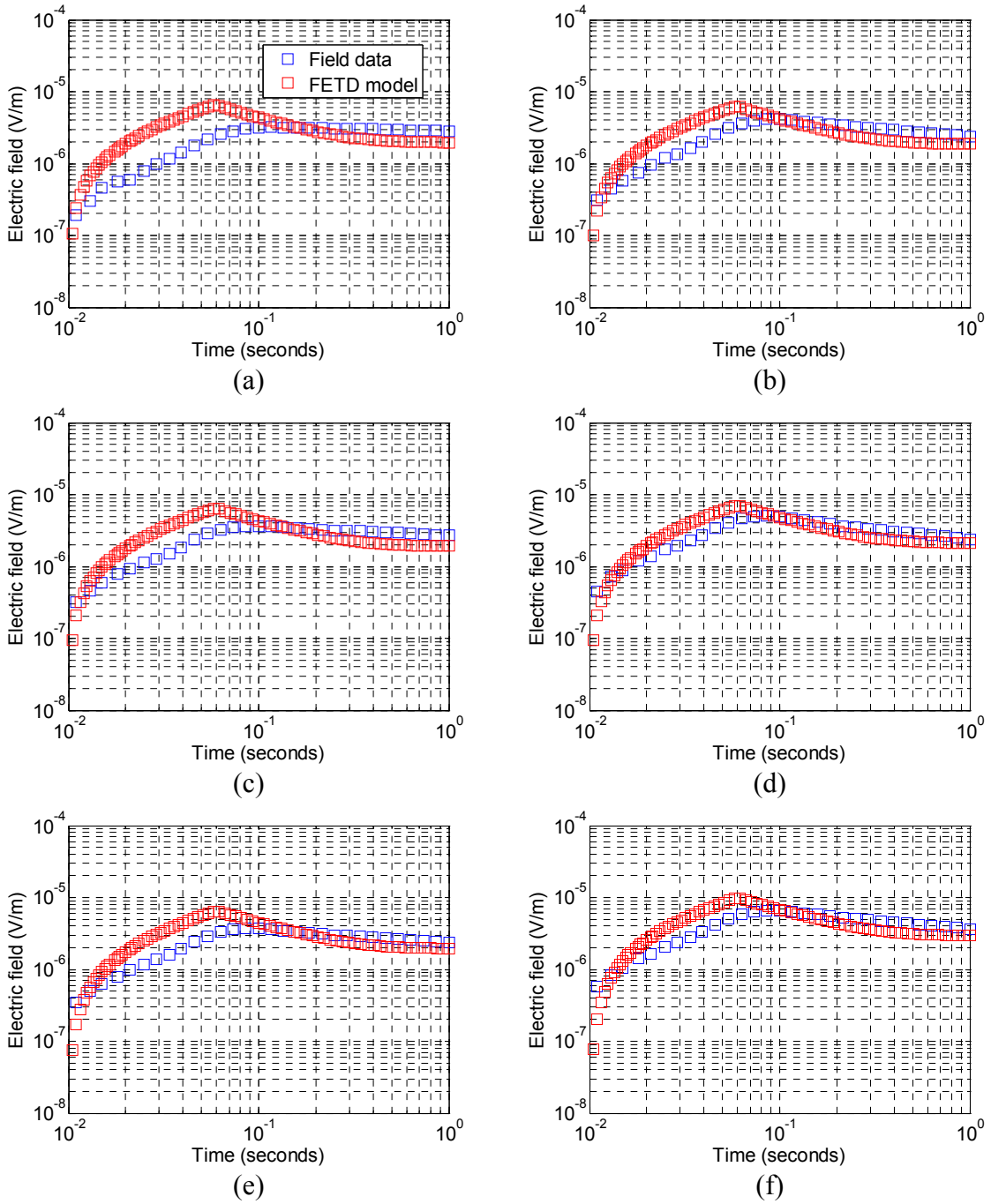

Figure 4.21. The comparison of the field data and the FETD modeling data. The FETD modeling data are computed over the model described in Figure 4.16f. (a) Receiver 1. (b) Receiver 2. (c) Receiver 3. (d) Receiver 4. (e) Receiver 5. (f) Receiver 6.

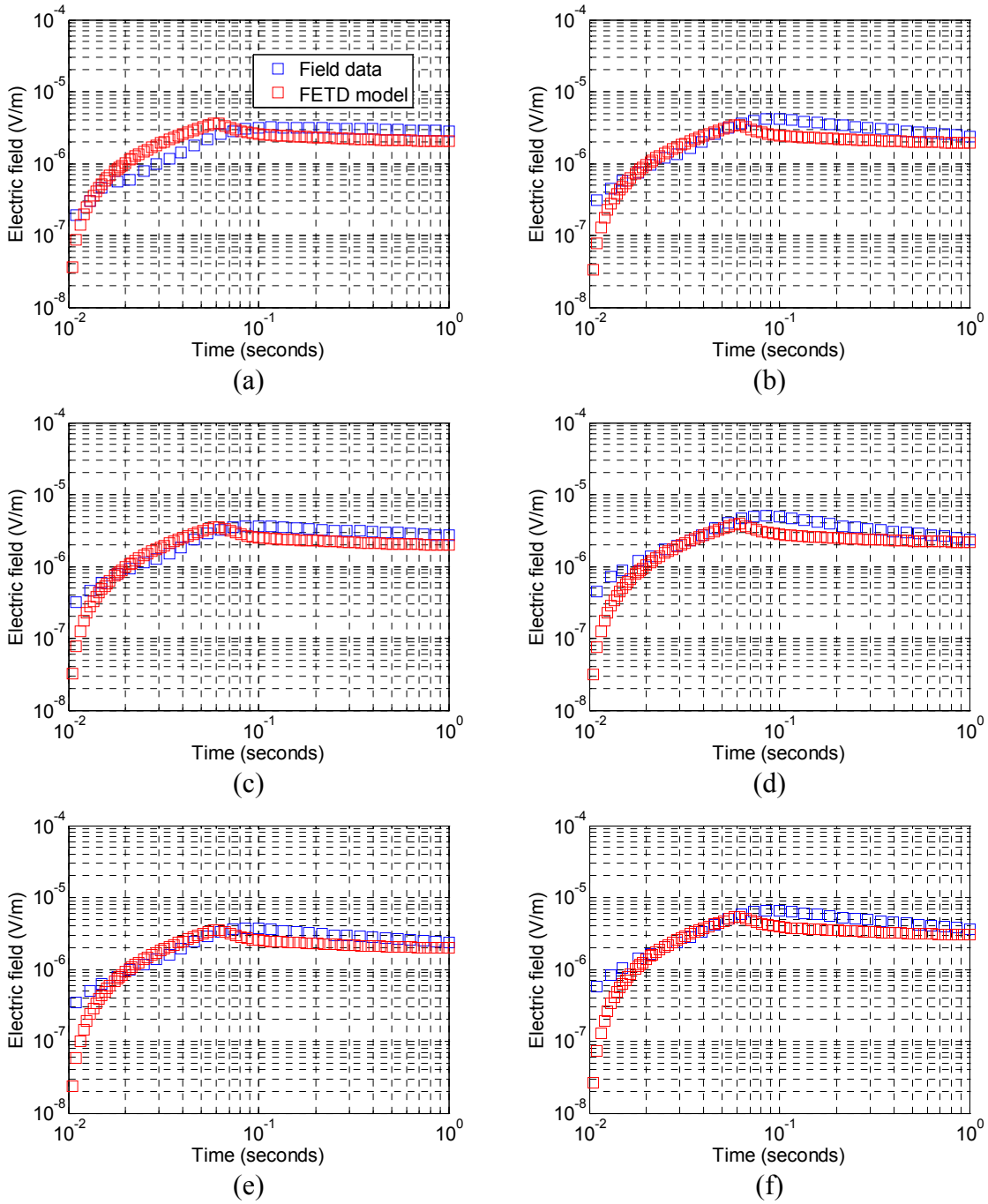

Figure 4.22. The comparison of the field data and the FETD modeling data. The FETD modeling data are computed over the model described in Figure 4.16g. (a) Receiver 1. (b) Receiver 2. (c) Receiver 3. (d) Receiver 4. (e) Receiver 5. (f) Receiver 6.

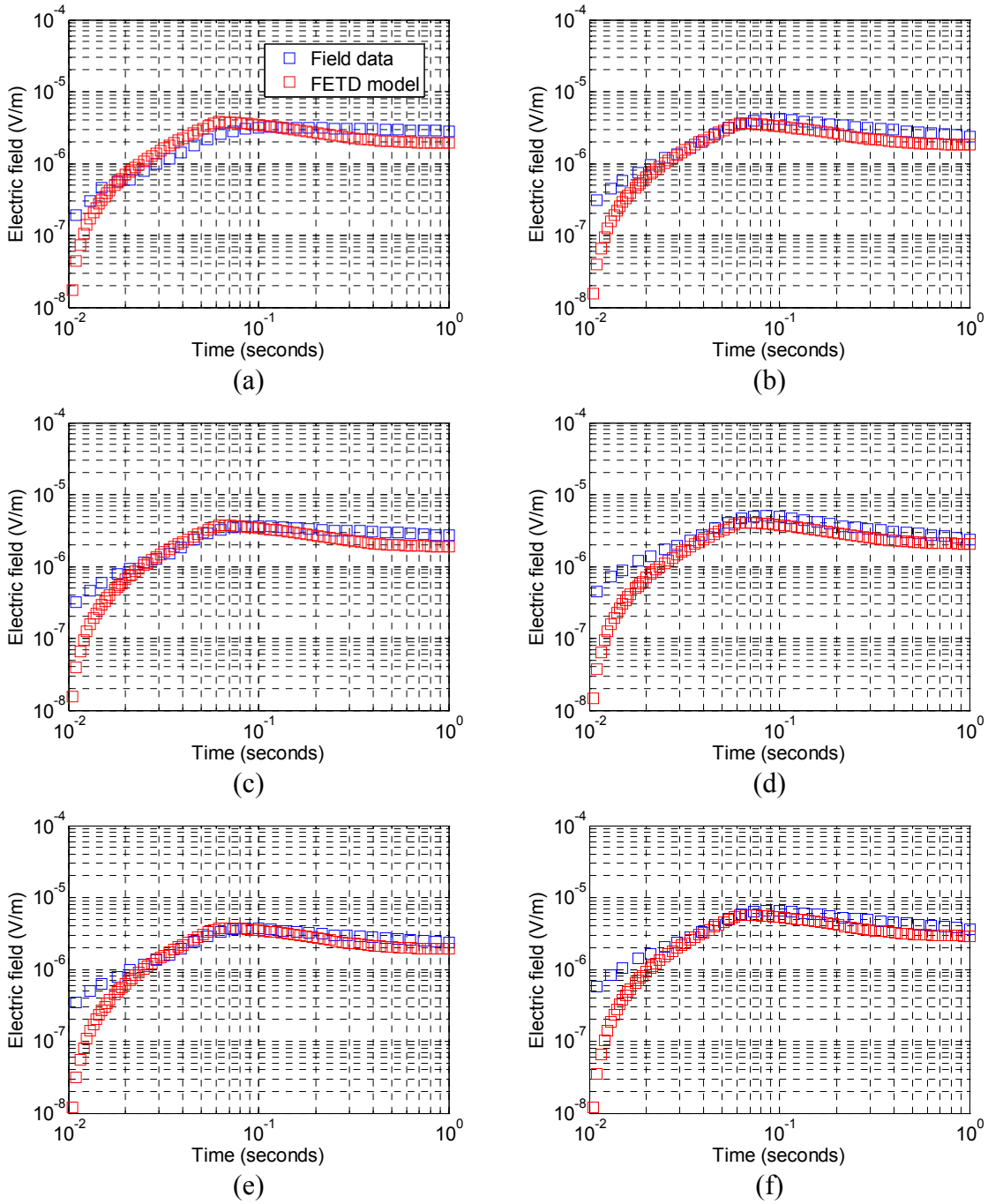

Figure 4.23. The comparison of the field data and the FETD modeling data. The FETD modeling data are computed over the model described in Figure 4.16h. (a) Receiver 1. (b) Receiver 2. (c) Receiver 3. (d) Receiver 4. (e) Receiver 5. (f) Receiver 6.

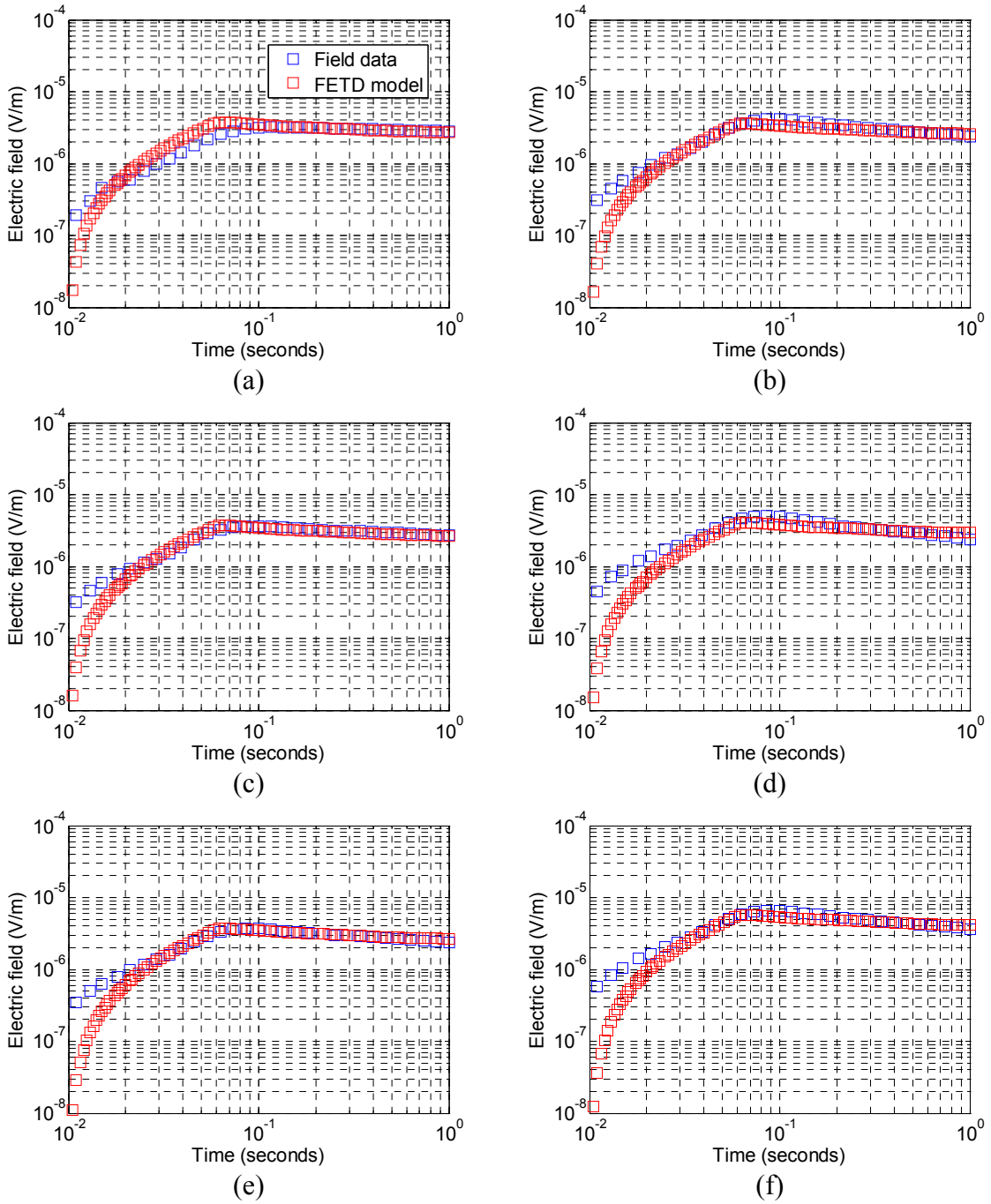

Figure 4.24. The comparison of the field data and the FETD modeling data. The FETD modeling data are computed over the model described in Figure 4.16i. (a) Receiver 1. (b) Receiver 2. (c) Receiver 3. (d) Receiver 4. (e) Receiver 5. (f) Receiver 6.

4.4 Conclusions

I have described the implementation details of the FETD algorithm. The core basis of the implementation is that the velocity of the transient electric fields excited by a dipole source increasingly decreases with increasing time. Therefore, the FETD algorithm can take increasingly larger time steps in time, speeding up FETD simulations. The inherently high computational effort associated with solving the resultant FETD matrix-vector equation at every time step is mitigated by refactorizing the FETD matrix only when the time-step size is changed. Therefore, with a constant time-step size, the computational cost at every time step reduces to that of forward and backward substitutions.

By adaptively doubling the time-step size at intervals, the FETD algorithm trades the computational cost of refactorizing the FETD matrix for a faster advance in FETD solution. The adaptive doubling of the time step plays an important role in accelerating the FETD computation, especially in a marine TDCSEM simulation, where EM diffusion processes occur slowly until very late times, because of the high electrical conductivities of the seawater and seabed. Examples of 3D FETD simulations are compared with analytical and 3D FDTD solutions to demonstrate the accuracy and the efficiency of the presented FETD algorithm.

I have simulated the effects of a gently dipping 2D seafloor on the TDCSEM responses. The simulations show that the effects depend not only on the dip of the seafloor, but also on which component of the electric field is measured on the seafloor. In short, the modeling study suggests that seafloor topography should be carefully incorporated into a model to account for the tilt of each receiver's coordinate system due to seafloor slope.

Finally, I have interpreted field TDCSEM data using a trial-and-error forward-modeling approach. Although I am able to construct a 3D FETD model that gives a reasonable fit between the field data and FETD solutions, this approach requires considerable modeling labor, suggesting that 3D FETD-based imaging algorithms should be developed for practical TDCSEM interpretations.

Chapter 5. 3D FETD Formulation of the Lorenz-Gauge Vector-Potential Equation

The FE formulation can be approached in a variety of ways. One popular approach is based on the electric-field wave equation (Gedney and Navsariwala, 1995; Lee, 1997; Jin, 2002). As presented in Chapters 3 and 4, this approach can be readily used for geophysical EM modeling by neglecting the displacement-current term and keeping the conduction-current term. In such an FE formulation, only the electric fields are solved and found. When it is necessary to obtain the magnetic fields, the magnetic fields at detector positions are interpolated using Faraday's law (Alumbaugh et al., 1996). Therefore, this approach minimizes the number of unknowns in a system of FE equations.

However, a major drawback of the approach for geophysical applications is that the double-curl electric-field diffusion equation can exhibit poor convergence and spurious solutions in the static limit when an iterative solver is used (See Appendix E). One way of preventing these problems is to explicitly implement the divergence-free condition (Smith, 1996). Another approach used to address the convergence problem is to simply replace the iterative solver with a direct solver (Dyczij-Edlinger et al., 1998). However, although recent advances in computer hardware and algorithms make it increasingly tractable to use a direct solver for large-scale problems (e.g. Börner et al., 2008; Oldenburg et al., 2008; Schwarzbach et al., 2009; Silva et al., 2009; Um et al., 2009; Börner , 2010), a direct solver generally requires larger memory.

Another approach to the FE formulation is based on vector-potential equations (Biro and Preis, 1989). In this approach, the EM equations are written in terms of vector and scalar potentials along with a gauge condition. One popular choice for a gauge condition in geophysical FE modeling is the Coulomb gauge (Badea et al., 2001; Stalnaker and Everett, 2006). Along with a vector-calculus identity, the Coulomb gauge removes the double-curl operator of the vector-potential equation and replaces it

with a Laplacian operator. Subsequently, the divergence-free condition is explicitly enforced. The resultant system of FE equations shows improved convergence and no spurious solutions in the static limit. However, a drawback of the Coulomb gauge is that the newly introduced scalar potential increases the size of the system matrix (Dyczij-Edlinger et al., 1998).

Another possible choice for a gauge condition is the Lorenz gauge (Bryant et al., 1990). The idea behind the Lorenz gauge is to split the single vector-and-scalar-potential equation into two separate equations: a diffusion equation for the vector potential and Poisson's equation for the scalar potential. Only the former is solved and advanced at every time step, whereas the latter is solved only at the time steps where the electric fields need to be sampled. Therefore, in contrast to the Coulomb gauge, the Lorenz gauge avoids having to solve a single large system of FE equations for both vector and scalar potentials at every time step.

Despite this advantage, the accuracy of the Lorenz gauge FE formulation becomes problematic when a model has inhomogeneous conductivities (Bryant et al., 1998). In addition, the Lorenz-gauge FE formulation experiences poor convergence and spurious solutions in the static limit, because the formulation retains the double-curl operator. Consequently, direct application of the published Lorenz-gauge FE formulation to geophysical EM modeling is impractical.

In this chapter, I present a new Lorenz-gauge FE formulation for modeling the TDCSEM method. My formulation retains the computational advantage of the Lorenz gauge without the problems of the classical formulation. Five important features characterize my new formulation. First, I employ the time derivative of the Lorenz gauge. Second, I replace the double-curl operator of the diffusion equation with the Laplacian operator, which prevents the problem of poor convergence and spurious solutions in the static limit. Third, I develop a FE formulation with edge-based functions to handle the discontinuity of the vector potential at material interfaces. Fourth, my FE formulation does not solve the equation for the vector potential, but instead for the time derivative of the vector potential; this approach avoids the additional computation needed for numerically determining the initial values of the

vector potential. Finally, I utilize an adaptive time-stepping method to efficiently advance FE solutions in time.

The remainder of this chapter is organized as follows. First, I describe the fundamental EM equations in the diffusion domain. Based on these equations, I develop a set of vector- and scalar-potential equations using the time derivative of the Lorenz gauge. Next, my Lorenz-gauge condition is compared with conventional Lorenz-gauge conditions, and its benefits for geophysical applications are discussed. Finally, from the vector- and scalar-potential equations, I derive the corresponding system of FE equations using the Galerkin method with edge- and node-based functions.

5.1 Theoretical development of the Lorenz-gauge vector potential equation and its characteristics

5.1.1. Lorenz-gauge vector potential equation

As discussed in Chapter 2, Maxwell's equations for diffusive fields in the time domain are given by

$$\frac{\partial \mathbf{b}(\mathbf{r},t)}{\partial t} = -\nabla \times \mathbf{e}(\mathbf{r},t)\,; \tag{5.1}$$

$$\nabla \times \frac{1}{\mu_0}\mathbf{b}(\mathbf{r},t) = \boldsymbol{\sigma}\mathbf{e}(\mathbf{r},t) + \mathbf{j}_\mathbf{s}(\mathbf{r},t)\,, \tag{5.2}$$

where $\mathbf{e}(\mathbf{r},t)$ and $\mathbf{b}(\mathbf{r},t)$ are the electric field and magnetic flux density at time t at position $\mathbf{r}$, respectively, μ_0 is the magnetic permeability of free space, $\boldsymbol{\sigma}$ is the electric conductivity, and $\mathbf{j}_\mathbf{s}(\mathbf{r},t)$ is an impressed electric current source.

In equation 5.2, the magnetic permeability within the earth and air is assumed to be constant, and is set to that of free space. The displacement current has been neglected in equation 5.2, because it is much smaller than the conduction current in the diffusion domain. I represent $\mathbf{e}(\mathbf{r},t)$ and $\mathbf{b}(\mathbf{r},t)$ by a magnetic vector potential $\mathbf{A}(\mathbf{r},t)$ and a scalar electric potential $\phi(\mathbf{r},t)$

$$\mathbf{b}(\mathbf{r},t) = \nabla \times \mathbf{A}(\mathbf{r},t)\,; \tag{5.3}$$

$$\mathbf{e}(\mathbf{r},t) = -\nabla \phi(\mathbf{r},t) - \frac{\partial \mathbf{A}(\mathbf{r},t)}{\partial t}\,. \tag{5.4}$$

As shown in Newman and Alumbaugh (1995) and Haber et al. (2000), combining equation 5.1 with equation 5.2 results in the electric-field diffusion equation

$$\frac{1}{\mu_0}\nabla \times \nabla \times \mathbf{e}(\mathbf{r},t) + \boldsymbol{\sigma}\frac{\partial \mathbf{e}(\mathbf{r},t)}{\partial t} + \frac{\partial \mathbf{j_s}(\mathbf{r},t)}{\partial t} = \mathbf{0}\,. \tag{5.5}$$

Substituting equation 5.4 into equation 5.5, I obtain the potential diffusion equation

$$\frac{1}{\mu_0}\nabla \times \nabla \times \frac{\partial \mathbf{A}(\mathbf{r},t)}{\partial t} + \boldsymbol{\sigma}\nabla\frac{\partial \phi(\mathbf{r},t)}{\partial t} + \boldsymbol{\sigma}\frac{\partial^2 \mathbf{A}(\mathbf{r},t)}{\partial t^2} - \frac{\partial \mathbf{j_s}(\mathbf{r},t)}{\partial t} = \mathbf{0}\,. \tag{5.6}$$

Instead of retaining the double-curl operator in the potential diffusion equation (Bryant et al., 1990; Bryant et al., 1998), I remove the operator from equation 5.6 using a vector-calculus identity, $\nabla \times \nabla \times \mathbf{V} = \nabla(\nabla \cdot \mathbf{V}) - \nabla^2 \mathbf{V}$. Accordingly, I obtain

$$\frac{1}{\mu_0}\nabla^2 \frac{\partial \mathbf{A}(\mathbf{r},t)}{\partial t} - \frac{1}{\mu_0}\nabla(\nabla \cdot \frac{\partial \mathbf{A}(\mathbf{r},t)}{\partial t}) - \boldsymbol{\sigma}\nabla\frac{\partial \phi(\mathbf{r},t)}{\partial t} - \boldsymbol{\sigma}\frac{\partial^2 \mathbf{A}(\mathbf{r},t)}{\partial t^2} + \frac{\partial \mathbf{j_s}(\mathbf{r},t)}{\partial t} = \mathbf{0}. \tag{5.7}$$

As equation 5.7 includes the first- and second-order time-derivatives of $\mathbf{A}(\mathbf{r},t)$, I define the first-order time-derivative of $\mathbf{A}(\mathbf{r},t)$ as

$$\mathbf{a}(\mathbf{r},t) \equiv \frac{\partial \mathbf{A}(\mathbf{r},t)}{\partial t}\,. \tag{5.8}$$

Therefore, equation 5.7 can be compactly written as

$$\frac{1}{\mu_0}\nabla^2 \mathbf{a}(\mathbf{r},t) - \frac{1}{\mu_0}\nabla(\nabla \cdot \mathbf{a}(\mathbf{r},t)) - \boldsymbol{\sigma}\nabla\frac{\partial \phi(\mathbf{r},t)}{\partial t} - \boldsymbol{\sigma}\frac{\partial \mathbf{a}(\mathbf{r},t)}{\partial t} + \frac{\partial \mathbf{j_s}(\mathbf{r},t)}{\partial t} = \mathbf{0}. \tag{5.9}$$

Equations 5.3 and 5.4 can also be rewritten using $\mathbf{a}(\mathbf{r},t)$ as shown below

$$\frac{\partial \mathbf{b}(\mathbf{r},t)}{\partial t} = \nabla \times \mathbf{a}(\mathbf{r},t)\,; \tag{5.10}$$

$$\mathbf{e}(\mathbf{r},t) = -\nabla \phi(\mathbf{r},t) - \mathbf{a}(\mathbf{r},t)\,. \tag{5.11}$$

Since a vector field is uniquely determined by both its curl and divergence, $\mathbf{a}(\mathbf{r},t)$ is not completely determined by equation 5.10. (Jackson, 1988). In other words, I am free to impose a divergence condition on $\mathbf{a}(\mathbf{r},t)$ (i.e. a gauge condition). Therefore, I choose a gauge condition as

$$\nabla \cdot \mathbf{a}(\mathbf{r},t) = -\mu_0 \boldsymbol{\sigma} \frac{\partial \phi(\mathbf{r},t)}{\partial t}. \tag{5.12}$$

As the gauge condition above looks similar to existing Lorenz-gauge conditions, it is instructive to compare equation 5.12 with the existing Lorenz-gauge conditions; Bryant et al. (1990) propose the Lorenz-gauge condition in the diffusion domain:

$$\nabla \cdot \mathbf{A}(\mathbf{r},t) = -\mu_0 \boldsymbol{\sigma} \phi(\mathbf{r},t). \tag{5.13}$$

Note that equation 5.12 is the time-derivative version of equation 5.13. The benefit of using equation 5.12 over equation 5.13 will be discussed in the next section. It is also noteworthy that the traditional Lorenz-gauge condition in the wave domain (Jackson, 1988) is given by

$$\nabla \cdot \mathbf{A}(\mathbf{r},t) = -\mu_0 \varepsilon \frac{\partial \phi(\mathbf{r},t)}{\partial t}. \tag{5.14}$$

Equation 5.14 includes the electric permittivity, ε instead of $\boldsymbol{\sigma}$. Although equations 5.12, 5.13 and 5.14 have somewhat different forms, they have the same purpose: trying to remove $\phi(\mathbf{r},t)$ from the diffusion or wave equation. Due to this similarity, I call equation 5.12 the time-derivative of the Lorenz gauge condition.

By imposing equation 5.12 on equation 5.9, I obtain

$$\frac{1}{\mu_0}\nabla^2 \mathbf{a}(\mathbf{r},t) - \boldsymbol{\sigma}\frac{\partial \mathbf{a}(\mathbf{r},t)}{\partial t} + \frac{\partial \mathbf{j_s}(\mathbf{r},t)}{\partial t} - \frac{1}{\mu_0}\boldsymbol{\sigma}^{-1}\nabla \boldsymbol{\sigma} \nabla \cdot \mathbf{a}(\mathbf{r},t) = \mathbf{0}. \tag{5.15}$$

Equation 5.15 is responsible for $\mathbf{a}(\mathbf{r},t)$ but not for $\phi(\mathbf{r},t)$. However, when $\mathbf{a}(\mathbf{r},t)$ is obtained, $\phi(\mathbf{r},t)$ is easily obtained by enforcing the conservation of electric charge:

$$\nabla \cdot \boldsymbol{\sigma}(\nabla \phi(\mathbf{r},t) + \mathbf{a}(\mathbf{r},t)) - \nabla \cdot \mathbf{j_s}(\mathbf{r},t) = \mathbf{0}. \tag{5.16}$$

The Lorenz-gauge vector-potential equation 5.15 and its auxiliary equation 5.16 provide clear computational advantages. First, equation 5.15 has only one type of unknown (i.e. $\mathbf{a}(\mathbf{r},t)$). As will be examined later, this aspect results in the minimum number of unknowns in the FE formulation of equation 5.15. Second, equation 5.15 is solved and advanced at every time step, whereas equation 5.16 is solved only at the time steps where $\mathbf{e}(\mathbf{r},t)$ needs to be sampled via equation 5.11. As a result, I avoid having to solve a single large system of FE equations for both $\mathbf{a}(\mathbf{r},t)$ and $\phi(\mathbf{r},t)$ at every time step. Note that this advantage is not obtained when $\phi(\mathbf{r},t)$ is calculated

from the time derivative of the Lorenz gauge condition, equation 5.12; in this case, because equation 5.12 includes the time derivative of $\phi(\mathbf{r},t)$, I need to solve equation 5.12 at every time step. Third, equation 5.15 can be solved iteratively in the static limit because the double-curl operator is replaced with the vector Laplacian operator (Newman and Alumbaugh, 2002).

5.1.2. Interface conditions under the Lorenz gauge condition

At this point, I examine the interface conditions of $\mathbf{a}(\mathbf{r},t)$ and $\phi(\mathbf{r},t)$ under the time derivative of the Lorenz gauge condition. It is important to examine them because their characteristics are directly related to the selection of interpolation functions in the FETD formulation as will be shown in the next section. First, I start with $\phi(\mathbf{r},t)$. From equation 5.11, it is obvious that $\phi(\mathbf{r},t)$ is continuous at the interface. Otherwise, $\nabla\phi(\mathbf{r},t)$ of equation 5.11 would become infinite at the interface and result in the infinite electric fields. Therefore, the interface condition of $\phi(\mathbf{r},t)$ is given as

$$\phi_1(\mathbf{r},t) = \phi_2(\mathbf{r},t)\,, \tag{5.17}$$

where the subscript indicates the medium in which $\phi(\mathbf{r},t)$ exists.

The interface condition of the tangential component of $\mathbf{a}(\mathbf{r},t)$ is determined by examining equation 5.10. At the interface, equation 5.10 is written as

$$\frac{\partial \mathbf{b}_1^N(\mathbf{r},t)}{\partial t} = \nabla\times\mathbf{a}_1^T(\mathbf{r},t) \text{ in medium 1;} \tag{5.18}$$

$$\frac{\partial \mathbf{b}_2^N(\mathbf{r},t)}{\partial t} = \nabla\times\mathbf{a}_2^T(\mathbf{r},t) \text{ in medium 2,} \tag{5.19}$$

where the superscripts N and T denote the normal and tangential component, respectively.

Because the normal component of $\mathbf{b}(\mathbf{r},t)$ is continuous across the interface, its time-derivative is also continuous. Therefore, the interface condition of the tangential component of $\mathbf{a}(\mathbf{r},t)$ is given as

$$\mathbf{a}_1^T(\mathbf{r},t) = \mathbf{a}_2^T(\mathbf{r},t)\,. \tag{5.20}$$

The interface condition of the normal component of $\mathbf{a}(\mathbf{r},t)$ is derived from the continuity of the normal current density across the interface, equation 2.13. By expressing equation 2.13 in term of $\mathbf{a}(\mathbf{r},t)$ and $\phi(\mathbf{r},t)$, the normal current density crossing the interface is given as

$$\mathbf{J}^N(\mathbf{r},t) = \mathbf{J}_1^N(\mathbf{r},t) = -\boldsymbol{\sigma}_1(\nabla\phi_1(\mathbf{r},t) + \mathbf{a}_1(\mathbf{r},t))\cdot\hat{\mathbf{u}}_n \text{ in medium 1;} \tag{5.21}$$

$$\mathbf{J}^N(\mathbf{r},t) = \mathbf{J}_2^N(\mathbf{r},t) = -\boldsymbol{\sigma}_2(\nabla\phi_2(\mathbf{r},t) + \mathbf{a}_2(\mathbf{r},t))\cdot\hat{\mathbf{u}}_n \text{ in medium 2,} \tag{5.22}$$

Where $\hat{\mathbf{u}}_n$ is the unit vector outward normal to the interface.

Since $\phi(\mathbf{r},t)$ is continuous across the interface, the continuity equation becomes

$$\boldsymbol{\sigma}_1(\nabla\phi(\mathbf{r},t) + \mathbf{a}_1(\mathbf{r},t))\cdot\hat{\mathbf{u}}_n = \boldsymbol{\sigma}_2(\nabla\phi(\mathbf{r},t) + \mathbf{a}_2(\mathbf{r},t))\cdot\hat{\mathbf{u}}_n\,. \tag{5.23}$$

Therefore, the interface condition of the normal component of $\mathbf{a}(\mathbf{r},t)$ is given as

$$\boldsymbol{\sigma}_1\mathbf{a}_1^N(\mathbf{r},t) + (\boldsymbol{\sigma}_1 - \boldsymbol{\sigma}_2)(\nabla\phi(\mathbf{r},t))^N = \boldsymbol{\sigma}_2\mathbf{a}_2^N(\mathbf{r},t)\,. \tag{5.24}$$

5.1.3. Physical meaning of gauge conditions

So far, I have shown the development of a new vector-scalar potential equation with the time derivative of the Lorenz gauge condition and have discussed the interface conditions of $\mathbf{a}(\mathbf{r},t)$ and $\phi(\mathbf{r},t)$. Next, I explore the physical meaning of the time derivative of the Lorenz gauge condition by comparing it with the Coulomb gauge condition (Griffiths, 1999). For the consistent comparison with the time derivative of the Lorenz gauge condition, I use the time derivative of the Coulomb gauge condition. For simplicity, I consider equation 5.9 in a unbounded medium of homogeneous isotropic conductivity (σ_0):

$$\frac{1}{\mu_0}\nabla^2\mathbf{a}(\mathbf{r},t) - \frac{1}{\mu_0}\nabla(\nabla\cdot\mathbf{a}(\mathbf{r},t)) - \sigma_0\nabla\frac{\partial\phi(\mathbf{r},t)}{\partial t} - \sigma_0\frac{\partial\mathbf{a}(\mathbf{r},t)}{\partial t} + \frac{\partial\mathbf{j}_s(\mathbf{r},t)}{\partial t} = \mathbf{0}. \tag{5.25}$$

The time derivative of the Coulomb gauge condition is given as

$$\nabla\cdot\mathbf{a}(\mathbf{r},t) = 0. \tag{5.26}$$

Putting equation 5.26 into Gauss' law, equation 5.16 yields

$$\nabla\cdot\boldsymbol{\sigma}\nabla\phi(\mathbf{r},t) = \nabla\cdot\mathbf{j}_s(\mathbf{r},t). \tag{5.27}$$

Imposing equation 5.26 on equation 5.25 yields

$$\frac{1}{\mu_0}\nabla^2\mathbf{a}(\mathbf{r},t)-\sigma_0\nabla\frac{\partial\phi(\mathbf{r},t)}{\partial t}-\sigma_0\frac{\partial\mathbf{a}(\mathbf{r},t)}{\partial t}+\frac{\partial\mathbf{j_s}(\mathbf{r},t)}{\partial t}=\mathbf{0}. \tag{5.28}$$

Note that there is a non-physical aspect about the scalar potential under Coulomb gauge; since the scalar potential is the solution of equation 5.27, the scalar potential is determined by the source instantaneously. In other words, when the source changes, the scalar potential changes without any time delay. Therefore, the scalar potential does not agree with special relativity that allows no 'message' to travel faster than the speed of light. In contrast, the vector potential changes after some amounts of time delay because it satisfies equation 5.28 (i.e. a diffusion equation). In short, in Coulomb gauge, the scalar potential is treated as a non-physical mathematical quantity.

Next, I examine a pair of the vector and scalar potential equations under the Lorenz gauge condition. By applying equation 5.12 to equations 5.25 and 5.16, respectively, I obtain

$$\frac{1}{\mu_0}\nabla^2\mathbf{a}(\mathbf{r},t)-\sigma_0\frac{\partial}{\partial t}\mathbf{a}(\mathbf{r},t)+\frac{\partial\mathbf{j_s}(\mathbf{r},t)}{\partial t}=\mathbf{0}; \tag{5.29}$$

$$\frac{1}{\mu_0}\nabla^2\phi(\mathbf{r},t)-\sigma_0\frac{\partial}{\partial t}\phi(\mathbf{r},t)-\frac{1}{\sigma_0\mu_0}\nabla\cdot\mathbf{j_s}(\mathbf{r},t)=\mathbf{0}. \tag{5.30}$$

$\mathbf{a}(\mathbf{r},t)$ and $\phi(\mathbf{r},t)$ satisfy equations 5.29 and 5.30, respectively, but the two equations have the same diffusion operator

$$\frac{1}{\mu_0}\nabla^2-\sigma_0\frac{\partial}{\partial t}. \tag{5.31}$$

Since equations 5.29 and 5.30 treat $\mathbf{a}(\mathbf{r},t)$ and $\phi(\mathbf{r},t)$ on the same diffusion basis, $\mathbf{a}(\mathbf{r},t)$ and $\phi(\mathbf{r},t)$ change together after the same amount of time delay. $\mathbf{a}(\mathbf{r},t)$ and $\phi(\mathbf{r},t)$ also satisfy the diffusion equation as the EM fields do. Therefore, from a physical point of view, the behavior of $\mathbf{a}(\mathbf{r},t)$ and $\phi(\mathbf{r},t)$ is 'natural'.

As the final note, one should not directly solve equation 5.30 for $\phi(\mathbf{r},t)$ because equation 5.30 requires the same amount of the computational cost as equation 5.29. Instead, as shown in equation 5.16, it is computationally economical to obtain $\phi(\mathbf{r},t)$ by enforcing the conservation of electric charge. Nonetheless, it is useful to place

equations 5.29 and 5.30 side-by-side for exploring the nature of $\mathbf{a}(\mathbf{r},t)$ and $\phi(\mathbf{r},t)$ under the Lorenz gauge condition.

5.2 FETD formulation of the vector-potential equation

In this section, I formulate a system of FE equations from equations 5.15 and 5.16 using the Galerkin method, along with edge- and node-based functions (Zhu and Cangellaris, 2006). Since the governing equation is solved for $\mathbf{a}(\mathbf{r},t)$ rather than $\mathbf{A}(\mathbf{r},t)$, it is unnecessary to numerically compute the initial value of $\mathbf{A}(\mathbf{r},t)$; instead, the initial value of $\mathbf{a}(\mathbf{r},t)$ is simply equal to zero. This approach also reduces the order of the time derivative in the governing equation from the second to the first, further simplifying FE formulation procedures. As a side note, because $\mathbf{a}(\mathbf{r},t)$ is computed, the time derivative of $\mathbf{b}(\mathbf{r},t)$ is computed via equation 5.10.

Tetrahedral elements are chosen to discretize the computation domain **V,** since the elements can efficiently handle complex structures. The computational domain is discretized such that a constant conductivity is assigned to a tetrahedral element. In other words, a conductivity value does not change inside an element since boundaries of conductivity distributions are discretized with edges of elements.

As shown in the previous section, the characteristics of the interface conditions of $\mathbf{a}(\mathbf{r},t)$ are that its tangential component is continuous along the interface, whereas its normal component can be discontinuous. Therefore, I can expand $\mathbf{a}(\mathbf{r},t)$ with the same edge-based functions used for the electric fields as shown below

$$\mathbf{a}^e(\mathbf{r},t) = \sum_{j=1}^{n} \mathbf{a}_j^e(\mathbf{r},t) = \sum_{j=1}^{n} a_j^e(t)\mathbf{n}_j^e(\mathbf{r}), \tag{5.32}$$

where the superscript e denotes the eth tetrahedral element, $a_j^e(t)$ is the unknown amplitude of $\mathbf{a}(\mathbf{r},t)$ on the jth edge of the eth element, and $\mathbf{n}_j^e(\mathbf{r})$ with j varying from 1 to 6 is a set of edge-based functions (Appendix A).

Before the FETD formulation is derived from equation 5.15 by applying the Galerkin method to each tetrahedral element, first recall that the computational

domain is discretized piecewise-continuously by assigning a constant conductivity value to each tetrahedral element. Therefore, the gradient of the conductivity in equation 5.15 is equal to zero inside each element. Consequently, in the finite-element space, equation 5.15 reduces to

$$\frac{1}{\mu_0}\nabla^2\mathbf{a}(\mathbf{r},t)-\boldsymbol{\sigma}\frac{\partial\mathbf{a}(\mathbf{r},t)}{\partial t}+\frac{\partial\mathbf{j}_\mathbf{s}(\mathbf{r},t)}{\partial t}=\mathbf{0}\,. \tag{5.33}$$

To derive the FE equations, first note that the left-hand side of equation 5.33 can be considered a vector residual for $\mathbf{a}(\mathbf{r},t)$. Therefore, I force the vector residual to be zero in a weighted-residual sense:

$$\iiint_{V^e}\mathbf{n}_i^e(\mathbf{r})\cdot(\frac{1}{\mu_0}\nabla^2\mathbf{a}^e(\mathbf{r},t)-\boldsymbol{\sigma}^e\frac{\partial\mathbf{a}^e(\mathbf{r},t)}{\partial t}+\frac{\partial\mathbf{j}_s^e(\mathbf{r},t)}{\partial t})dV=0, \tag{5.34}$$

where V^e is the volume of the eth tetrahedral element.

Substituting equation 5.32 into equation 5.34, using vector-calculus identities, and imposing the homogeneous Dirichlet boundary condition, I obtain a system of FE equations for the eth tetrahedral element:

$$\mathbf{A}^e\frac{d\mathbf{a}^e}{dt}+\mathbf{B}^e\mathbf{a}^e-\mathbf{s}^e=0\text{, where} \tag{5.35}$$

$$\text{(i,j) element of conductivity matrix } \mathbf{A}^\mathbf{e}=\iiint_{V^e}\boldsymbol{\sigma}^e\mathbf{n}_i^e(\mathbf{r})\cdot\mathbf{n}_j^e(\mathbf{r})dV\,; \tag{5.36}$$

$$\text{(i,j) element of permeability matrix } \mathbf{B}^\mathbf{e}=\iiint_{V^e}\frac{1}{\mu_0}(\nabla\mathbf{n}_i^e(\mathbf{r})\cdot\nabla\mathbf{n}_j^e(\mathbf{r}))dV\,; \tag{5.37}$$

$$\text{i element of source vector } \mathbf{s}^e=\iiint_{V^e}\mathbf{n}_i^e(\mathbf{r})\cdot\frac{\partial\mathbf{j}_s^e(\mathbf{r},t)}{\partial t}dV\,; \tag{5.38}$$

$$\text{Unknown vector } \mathbf{a}^e=[a_1^e\quad a_2^e\quad\ldots\quad a_6^e]\,. \tag{5.39}$$

When systems of FE equations derived from individual elements are assembled into a single large system of FE equations, the superscript *e* is dropped. The resultant global version of equation 5.35 is discretized in time using a backward Euler (BE) scheme. As mentioned in Chapter 3, the BE method is unconditionally stable, regardless of the choice of Δt. Furthermore, when the mesh fails to support high-

frequency content of transient fields in early time, the BE method strongly suppresses high-frequency oscillations (Hairer and Wanner, 1991; Haber et al., 2004).

Applying the second-order BE method to the global version of equation 5.35, I have

$$(3\mathbf{A} + 2\Delta t\mathbf{B})\mathbf{a}^{n+2} = \mathbf{A}(4\,\mathbf{a}^{n+1} - \mathbf{a}^{n}) + 2\Delta t\mathbf{s}^{n+2}, \tag{5.40}$$

where Δt is a time step size and $\mathbf{a}(t) = \mathbf{a}(n\Delta t) = \mathbf{a}^{n}$. Note that the matrix on the left-hand side of equation 5.40 is a function of Δt. Also note that the total number of unknowns for equation 5.40 is equal to the number of the internal edges in **V,** because 1) the elements of $\mathbf{a}^{n}$ are mapped onto the edges of tetrahedral elements and 2) the homogeneous Dirichlet boundary condition is imposed on the external edges on **V**. Therefore, the number of unknowns for equation 5.40 is the same as that of the system of FE equations resulting from the double-curl electric-field diffusion equation (Chapter 3).

5.3 FE formulation of the scalar potential equation

A system of FE equations for the scalar potential, equation 5.16, is derived in a similar manner. The scalar electric potential inside the eth tetrahedral element is expanded as

$$\phi^{e}(\mathbf{r},t) = \sum_{k=1}^{4} \phi_{k}^{e}(t) n_{k}^{e}(\mathbf{r}), \tag{5.41}$$

where ϕ_{k}^{e} is the potential at the kth node of the eth element, and $n_{k}^{e}(\mathbf{r})$ with k varying from 1 to 4 is a set of Lagrange polynomials or node-based functions (detailed in Appendix A). To derive FE equations for equation 5.16, the left-hand side of equation 5.16 is enforced to be zero in a weighted-residual sense:

$$\iiint_{V^{e}} n_{k}^{e}(\mathbf{r})(\nabla\cdot(\boldsymbol{\sigma}^{e}(\nabla\phi^{e}(\mathbf{r},t))) + \nabla\cdot(\boldsymbol{\sigma}^{e}\mathbf{a}^{e}(\mathbf{r},t)) - \nabla\cdot\mathbf{j}_{\mathbf{s}}(\mathbf{r},t))dv = 0. \tag{5.42}$$

Substituting equations 5.32 and 5.41 into equation 5.42, using Green's theorem, and imposing the homogeneous Dirichlet boundary condition, I arrive at a system of FE equations for the eth element:

$$\mathbf{C}^{e}\boldsymbol{\varphi}^{e} = -\mathbf{D}^{e}\mathbf{a}^{e} + \mathbf{q}^{e}, \text{ where} \tag{5.43}$$

$$\text{(i,j) element of } \mathbf{C}^e = \iiint_{V^e} \nabla n_i^e(\mathbf{r}) \cdot (\nabla \cdot \boldsymbol{\sigma}^e \nabla n_j^e(\mathbf{r})) dV \; ; \tag{5.44}$$

$$\text{(i,j) element of } \mathbf{D}^e = \sum_{j=1}^{n=6} \iiint_{V^e} (\boldsymbol{\sigma}^e \nabla n_i^e(\mathbf{r}) \cdot \mathbf{n}_j^e(\mathbf{r})) dV \; ; \tag{5.45}$$

$$\text{i element of } \mathbf{q}^e = \iiint_{V^e} n_i^e(\mathbf{r}) \nabla \cdot \mathbf{j}_\mathbf{s}(\mathbf{r}, t) dV \; ; \tag{5.46}$$

$$\boldsymbol{\varphi}^e = [\phi_1^e \quad \phi_2^e \quad \phi_3^e \quad \phi_4^e] \, . \tag{5.47}$$

Note that the matrix on the left-hand side of equation 5.43 is time-invariant. Therefore, the solution of equation 5.43 depends only on vector on the right-hand side. Using the node-connectivity information, local FE matrix equations from individual elements are assembled into a single, global FE matrix equation. In the global equation, the total number of unknowns is equal to the number of internal nodes in **V** due to the homogeneous Dirichlet boundary condition.

As the final note, if a receiver is placed inside an element, the scalar potential at the receiver position is interpolated using the scalar potential values at four nodes via equation 5.41. Then, its gradient is computed inside the element. In contrast, if a receiver is on the edge of the element, the scalar potential is determined using the scalar potential values at the two nodes that define the edge. Therefore, the gradient of the scalar potential is parallel to the edge. In other words, the second term of the left-hand side of equation 5.24, $(\nabla \phi^e(\mathbf{r}, t))^N$ does not exist along the edge. The same analysis is applied when a receiver position is on the face of an element. The term $(\nabla \phi^e(\mathbf{r}, t))^N$ does not exist on the face. However, as the general description of the interface conditions, equation 5.24 explicitly includes the term.

5.4 Conclusions

I have formulated a new, efficient 3D FETD algorithm for simulating low-frequency EM diffusion phenomena. Using the Lorenz-gauge condition, I split the single vector-and-scalar-potential equation into 1) a diffusion equation for magnetic vector potentials and 2) Poisson's equation for scalar electric potentials. The diffusion

equation for time derivatives of the magnetic vector potentials is the primary equation that is solved at every time step. Poisson's equation for scalar electric potentials is considered a secondary equation and is evaluated only at the time steps where the electric fields are sampled.

In contrast to the FETD algorithm that is developed along with the electric-field diffusion equation in Chapter 3, a major advantage of the new FETD algorithm is that the system of FETD equations resulting from the Lorenz-gauge diffusion equation not only has the minimum number of unknowns but also can be solved using an iterative solver in the static limit. It is also shown that solving the diffusion equation not for the magnetic vector potentials but for their time derivatives simplifies the problem. Furthermore, by doing this, the FETD equations have zero initial values for a step-off source waveform. Consequently, in the FETD algorithm, it is unnecessary to solve an additional equation for initial values before time-stepping.

The Lorenz-gauge diffusion equation is converted into an FETD formulation using the Galerkin method and edge-based functions. It is shown that the total number of unknowns in the FETD formulation is equal to the number of internal edges in the computational domain. Consequently, the primary Lorenz-gauge FETD algorithm has the same number of unknowns as the FETD algorithm developed in Chapter 3. The development of the FE formulation for the secondary Poisson's equation resembles that of the FEDC formulation shown in Chapter 3, but requires the combined use of edge- and node-based functions. In Chapter 6, it will be shown that the computation cost of the secondary FE formulation is insignificant.

Chapter 6. Solutions of the Lorenz-Gauge FETD Formulation

In Chapter 5, I gave the development of the systems of FETD equations in the Lorenz gauge condition. In this section, I describe efficient solution procedures for these systems. First, note that equation 5.40 can produce unique solutions in the static limit using either a direct or an iterative solver. However, I consider only the application of an iterative solver to equation 5.40, since a primary advantage of the Lorenz-gauge FE formulation over a Coulomb-gauge FE formulation is that an iterative solver can be used without augmented unknowns (i.e. $\phi(\mathbf{r},t)$). The approaches for solving equation 5.40 described below are conceptually similar to those in Chapter 4, except that some modifications are made to accommodate the use of an iterative solver.

6.1 Numerical implementation

In FETD solution procedures, the most computationally expensive part is to solve equation 5.40 at every time step. In order to alleviate the computational burden, I exploit the fact that the matrix on the left-hand side of equation 5.40 is time-invariant with a constant Δt. Therefore, for a given Δt, a preconditioner for equation 5.40 is computed only once and is repeatedly used inside a time-stepping loop. Once time-stepping starts, the previous solution is used as an initial guess for the solution at the next time step. As discussed in Chapter 4, I can take increasingly large Δt and thus, can advance the solution quickly without affecting the accuracy. Therefore, I can change Δt as a strategy for a more efficient solution.

I choose not to determine an optimal Δt at every time step but instead attempt to double Δt every m time steps, where m is an input parameter. This adaptive time-step-doubling method effectively prevents unnecessarily small changes of Δt that entail recalculating a preconditioner for equation 5.40. At every m^{th} time step, $\mathbf{a}^n$ of

equation 5.40 is computed twice, using both Δt and $2\Delta t$. Then, the difference between the two solutions is compared. If the difference is smaller than a prescribed tolerance, and if the number of iterations required for convergence with $2\Delta t$ is smaller than twice that required for convergence with Δt, then $2\Delta t$ is accepted as a new Δt.

The tolerance for the CG solver is empirically determined. Based on numerical experiments, Its default value is set to 10^{-6}. If either condition is not satisfied, I reject the new time step $2\Delta t$ and continue using Δt. However, the preconditioner for $2\Delta t$ is stored for future use as long as memory is available.

In contrast to equation 5.40, equation 5.43 is solved only at time steps where the electric field needs to be sampled. Therefore, the total computational cost of equation 5.43 depends on the sampling rate of the electric field. However, during a simulation, the total number of times the electric fields are sampled is significantly smaller than the total number of time steps required to advance the solution of equation 5.40. Also note that the matrix on the left-hand side of equation 5.43 is time-invariant. Therefore, after a preconditioner for equation 5.43 is computed, it is repeatedly used. Matrix **D** of equation 5.43 is also time-invariant and thus is evaluated only once. When I solve equation 5.43 and obtain $\phi(\mathbf{r},t)$ at all internal nodes, the electric fields are evaluated only at detector positions using equation 5.4. Finally, $\phi(\mathbf{r},t)$ is kept in the memory and is used as an initial guess for the solution of equation 5.43 at the next electric-field sampling point.

6.2 Validation and performance analysis

To verify the accuracy of my FETD formulation and demonstrate its performance, I compare my Lorenz-gauge FE solutions with analytical solutions and 3D FDTD solutions (Commer and Newman, 2004). I implement my FETD formulation using MATLAB and simulate CSEM responses over homogeneous and 3D seafloor models. The CSEM simulations presented in this section are carried out on a 2.26 GHz Intel Nehelem single-core with 48 GB memory.

Iterative solvers and preconditioners employed here are also intrinsic functions in MATLAB. To choose a proper iterative solver and preconditioner, the properties of the system matrix of equation 5.40 for the vector potential are considered. First, note that the system matrix is sparse and symmetric. Second, its diagonal elements are always positive. Therefore, to check whether or not the system matrix is symmetric positive-definite (SPD), an incomplete Cholesky factorization is tried. If the factorization succeeds, equation 5.40 is solved by the conjugate gradient (CG) method along with the existing incomplete Cholesky factorization. If the factorization fails, an LU factorization is performed. Equation 5.40 is solved by the minimum residual (MINRES) method along with the existing LU factorization. The decision steps described above are also applied to equation 5.43 for the scalar potential.

Although there is no mathematical proof that the system matrices of equations 5.40 and 5.43 are always SPD, a Cholesky factorization has always succeeded during extensive modeling experiments. Consequently, all modeling examples discussed below are computed using the CG solver. As a side note, the successive over relaxation method was also tested but was not employed here due to its impractically-slow convergence.

6.2.1 Homogeneous seafloor model

I simulate CSEM responses to a homogeneous seafloor model that consists of an infinitely thick air layer, a 400-m-thick seawater layer, and an infinitely thick seabed (Figure 4.3). Note that the resistivity of the air is set to 10,000 Ω-m. In my experience, this FE formulation works well when the air is about four orders of magnitude more resistive than the seawater. A 250-m-long x-oriented electric-dipole source is placed 50 m above the seafloor. The dipole source generates a step-off waveform whose ramp-off time is set to 0.01 seconds. Eight detectors are placed on the seafloor at 1 km spacing along the positive x-axis, and another eight detectors are placed along the positive y-axis. The detectors sample transient EM fields 20 times per decade in log scale.

Figure 4.4 shows the cross-sectional view of the FE mesh used for the model at y=0. The boundaries of the model are extended 100 km from its center in order to eliminate artificial boundary effects at the detector positions. To discretize the model economically, I grow the tetrahedral elements at factors ranging from 1.5 to 2.0 towards the computational boundaries. The model is discretized into 108,540 tetrahedral elements, resulting in 125,883 unknowns for equation 5.40 and 17,994 unknowns for equation 5.43. The mesh is fine near the source to support fast-diffusing high-frequency content early in time but gradually grows away from the source. In addition, because I want to simulate the electric fields measured by 10-m-long dipoles, the mesh is also fine near the detectors. Note also that inside the seawater column, tetrahedral elements are restricted from growing rapidly in the x- and y- directions to prevent their aspect ratios (Appendix G) from being too small. Consequently, a rather large number of tetrahedral elements is required to discretize the seawater column.

At this point, it is informative to compare the problem size of our Lorenz-gauge formulation with that of a conventional approach that solves both vector and scalar potentials simultaneously. For the given model above, the total number of unknowns for the conventional approach is the sum of the numbers of two types of unknowns: (125,883+17,994). Therefore, the size of its system matrix is (125,883+17,994)-by-(125,883+17,994). In contrast, the Lorenz-gauge FETD formulation solves the system of equations only for the time-derivatives of the vector potentials at each time step and thus, reduces the total number of unknowns by about 13% ($\sim\frac{125,883}{125,883+17,994}\times 100\%$). accordingly, the size of its corresponding system matrix is reduced by about 23% ($\sim(\frac{125,883}{125,883+17,994})^2\times 100\%$).

Equations 5.40 and 5.43 are solved using the incomplete Cholesky preconditioned CG solver. The drop tolerances of the preconditioner for equations 5.40 and 5.43 are set to 10^{-6}. It takes about 18 minutes to compute CSEM responses to the model for 854 time steps. My numerical experiments suggest that the drop tolerance of the incomplete Cholesky preconditioner should be smaller than the conductivity of the most resistive medium (i.e. the air) in a model. Otherwise, the number of iterations

required at each time step quickly increases; the CG solver may not even converge. I will further examine this issue in the next section. The FE and analytical solutions for the homogeneous seafloor model show good agreement at selected detector positions (Figure 6.1).

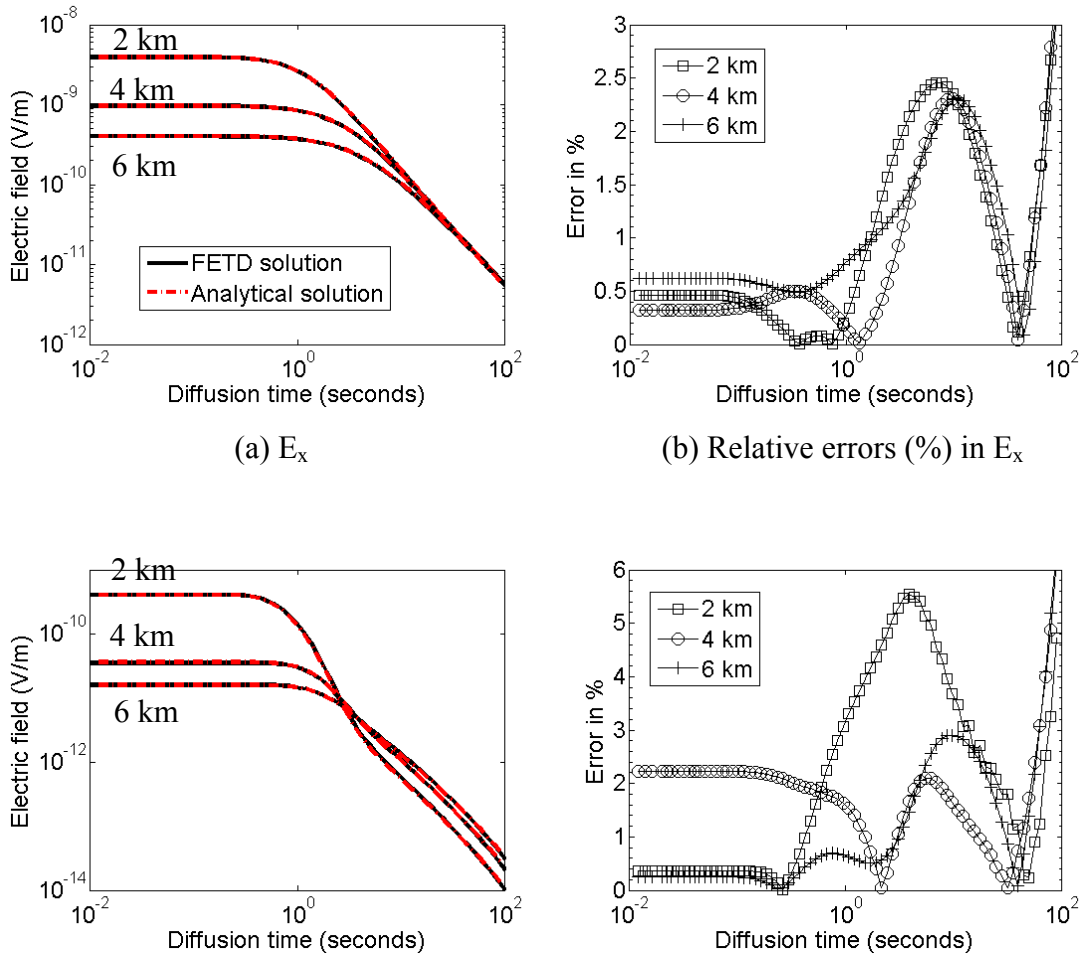

(a) E_x (b) Relative errors (%) in E_x

(c) E_z (d) Relative errors (%) in E_z

Figure 6.1. The inline and broadside CSEM responses for selected detector positions over the model shown in Figure 4.3. The left column shows the EM fields; the right column shows the percentage difference (i.e. error) between the analytical and the FETD solutions.

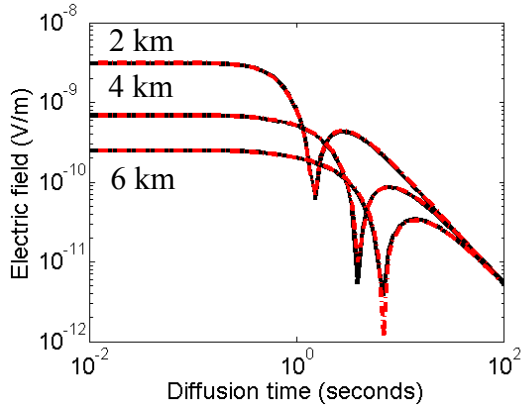

(e) E_y

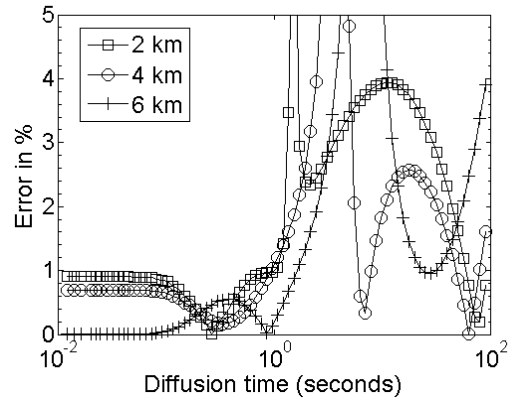

(f) Relative errors (%) in E_y

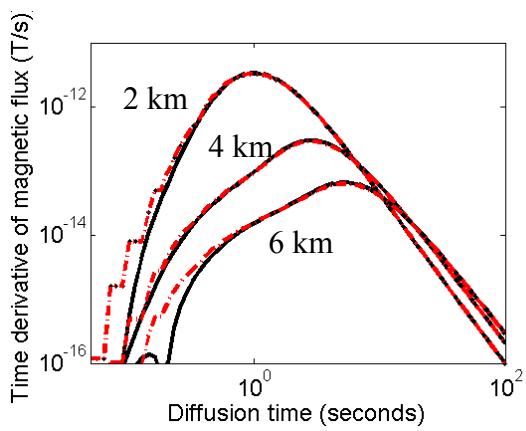

(g) $dB_z dt$

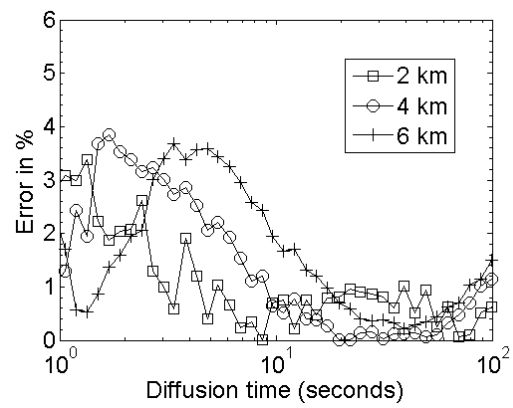

(h) Relative errors (%) in $dB_z dt$

Figure 6.1. Continued.

As time-stepping continues, the oscillation of errors gradually increases— due to error migration from early to late time—but remains within ≤ 5%. Note that the z-components of the electric fields (E_z) are somewhat more vulnerable to the error migration than the x-components of the electric fields (E_x). I observe such an error pattern repeatedly in my modeling experiments when I simulate an x-oriented electric-dipole source. I believe that this is because the amplitudes of E_z are an order of magnitude smaller than those of E_x and are therefore more easily contaminated with numerical noise. The y-components of the electric fields (E_y) show typical sign reversals observed in the broadside configuration. In the vicinity of the sign reversals

(e.g. 0.5-10 seconds), the percentage errors sharply increase, but they quickly reduce to a reasonable level away from the reversals, verifying the accuracy of the FE algorithm.

Note that the 'analytical' vertical magnetic-flux-density curves (B_z) shown in Figure 6.1g are first computed, and then their time derivatives ($\partial B_z \partial t$) are 'numerically' approximated. The approximations are noisy at very early time ranges (e.g. 0.01 to 0.05 seconds), because the numerical differentiation of nearly constant B_z in the time range causes catastrophic cancelation. Thus, $\partial B_z \partial t$ is not plotted in the early time range. The numerical noise resulting from the numerical differentiation is still seen as a stair-step pattern at early times (e.g. 0.05 to 1 seconds). However, at intermediate and late times (1 to 100 seconds), the $\partial B_z \partial t$ curve of the FE solution agrees well with the analytical solution and has low percentage error, ensuring the accuracy of the FE implementation.

To further understand the performance of the FETD formulation, three run-time characteristics of the algorithm are plotted in Figure 6.2. At each sampling point, the solution of equation 5.40 converges after a small number of iterations (Figure 6.2a). Note that the required number of iterations increases in late time. The increase is explained by the fact that Δt is successively doubled during the simulation (Figure 6.2b). Because the initial guess used for the CG solver is the solution at the previous time step, a large Δt in late time somewhat lowers the quality of the initial guess and thereby increases the required number of iterations. The successive increase of Δt also tends to slightly increase a condition number of the preconditioned system matrix, resulting in the increase of the required number of iterations for convergence. A further analysis on the impact of the time-step doubling method on the conditioning of the system matrix is discussed later.

Figure 6.2c shows the accumulated solution runtime with and without the time-step-doubling method. The time-step-doubling method results in a stair-step increase in the accumulated solution runtime. The increase is a direct result of the computational cost for constructing a new preconditioner for a newly doubled Δt. However, the benefit

of the time-step-doubling method outweighs the computational costs related to changing Δt.

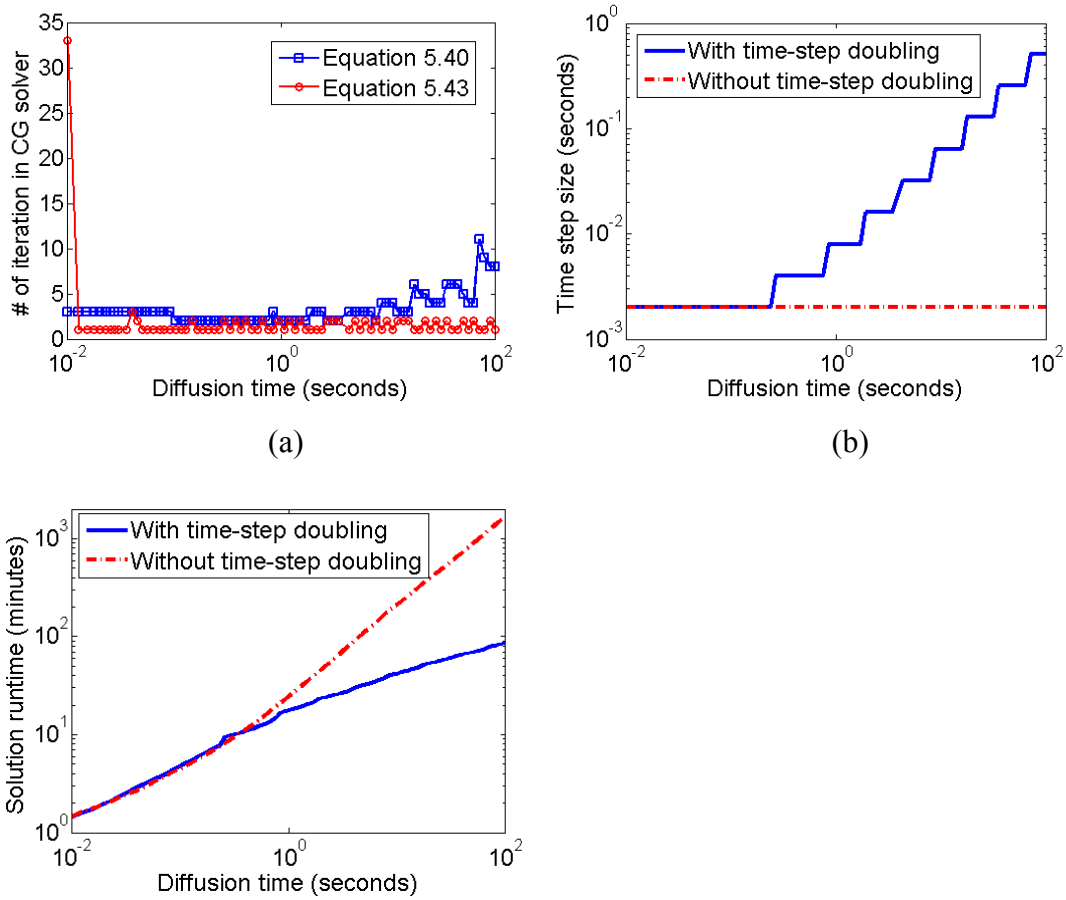

Figure 6.2. The run-time characteristics of the FETD solutions for the model shown in Figure 4.3. (a) The required number of iterations in the CG solver versus the diffusion time. (b) The time-step size versus the diffusion time. (c) The solution runtime versus the diffusion time. In (a), the number of iterations are plotted only when the EM fields are sampled. The x-coordinates of blue squares and red circles correspond to EM sampling points.

In contrast, the convergence of equation 5.39 is clearly different from that of equation 5.40 (Figure 6.2a). When the electric field is first sampled at 0.01 seconds by solving equation 5.43, an initial guess used for the CG solver is set to a zero vector. With the initial guess, the solution of equation 5.43 converges in 32 iterations. The solution is used as an updated initial guess when equation 5.43 is solved at the 2nd sampling point (0.0125 seconds). When the initial guess for the CG solver is determined in such a way, the required number of iterations quickly decreases. Finally, after the 10th sampling point (0.0350 seconds), the required number of iterations reduces to less than three, suggesting that the solution of equation 5.43 becomes nearly steady-state within the prescribed tolerance limit. As a result, the computational cost of equation 5.43 becomes negligible during the remaining diffusion simulation.

6.2.2 Seafloor model with 3D hydrocarbon reservoir

Next, I simulate TDCSEM responses over a 3D hydrocarbon reservoir (**Figure** 6.3). Six detectors are placed on the seafloor with 1 km spacing along the x-axis. The other simulation parameters are kept the same as in the previous model. The inline CSEM response over the reservoir is simulated using both the Lorenz-gauge FETD approach and an FDTD approach (Commer and Newman, 2004) for verification purposes. The FDTD model has of 89, 79, and 82 grid divisions in the x-, y- and z-directions, respectively, with the computational domain boundaries 50 km from the center of the model, resulting in 3,459,252 unknowns. In contrast, with the boundaries of the FE model expanded to 100 km from its center, I discretize the model into 81,984 tetrahedral elements, resulting in 94,848 unknowns for the equation 5.40 and 13,479 unknowns for equation 5.43. The comparison of the unknowns between the FDTD and FE models illustrates the advantage of unstructured FE meshes over structured FD grids, even though the FE solution requires solving a matrix equation.

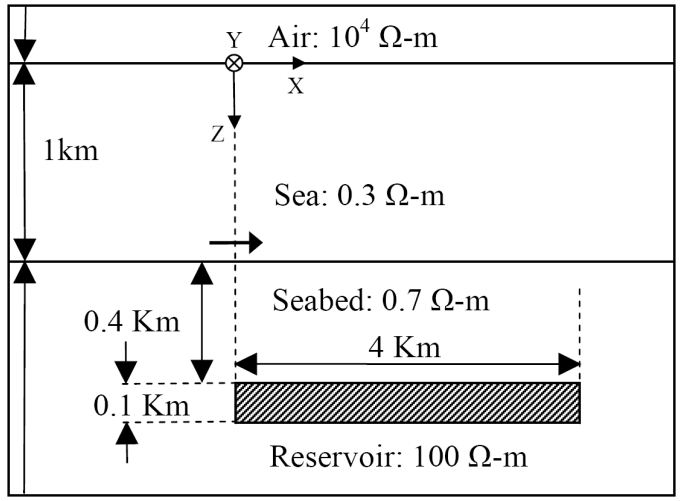

Figure 6.3. The cross-sectional view of the 3D hydrocarbon reservoir model. The size of the reservoir in kilometers is 4 x 4 x 0.1 in the x-, y-, and z-directions, respectively.

The incomplete Cholesky preconditioned CG solver, with the same drop tolerances used in the previous model, is used to solve equations 5.40 and 5.43 for the reservoir model. It takes 10 minutes to simulate the model with 1,457 time steps. The simulation results from both the FETD and FDTD methods are plotted in Figure 6.4 and show overall good agreement. Note that the percentage errors between the two solutions are not provided in this example, since the two solutions do not output the EM fields at same sampling points on the time axis. Though some deviations are observed in late time in Figure 6.4b, I believe that the deviations are the result of the boundary effects and can be removed by further expanding the boundary of the FD grid. The time derivatives of the magnetic flux density are not plotted in very early time in Figure 6.4c because of the numerical noise discussed in the previous example.

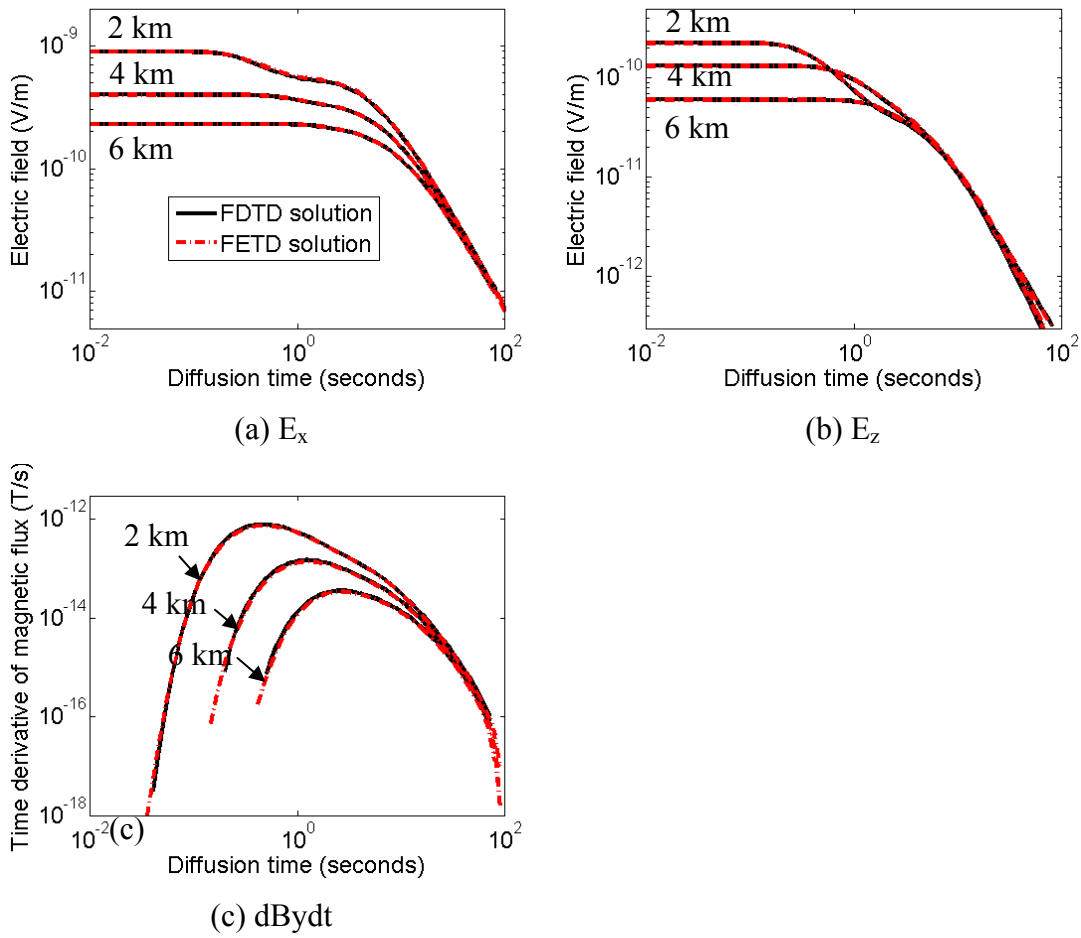

Figure 6.4. The inline CSEM responses at x coordinates of 4 km, 5 km and 6 km over the model shown in Figure 6.3. For all points, y=0 km and z=1 km. (a) E_x. (b) E_z. (c) dBydt.

6.3 Comparison of the two FETD formulations

In this section, I investigate the numerical characteristics of the Lorenz-gauge FETD formulation by comparing it with the FETD formulation (Chapter 3) based on the electric-field diffusion equation. As mentioned in Chapters 3 and 5, this FETD formulation must be implemented with a direct method for stably solving a system of FETD equations for the electric fields in the static limit. For brevity, I call the FETD formulation in Chapter 3 a direct FETD formulation. For fair comparison of the solution time, the external C routines in the direct FETD code are replaced with their

MATLAB counterparts, because the computational core of the Lorenz-gauge FETD algorithm is completely implemented using MATLAB.

Using the two FETD formulations, I simulate CSEM responses to a layered model that consists of a lower half-space (earth) and an upper half-space (air). The resistivity of the earth is fixed at 10 Ω-m, but that of the air varies from 10^3 to 10^{12} Ω-m. A reason I examine a wide range of resistivities for air is that the large contrasts in resistivity between the earth and the air can cause particular difficulties in FETD simulations, as discussed below. A 250-m-long x-oriented electric dipole is placed at the center of the model. The model is discretized into 146,199 tetrahedral elements, resulting in 169,141 unknowns for both FETD formulations. Simulation characteristics of the direct and Lorenz-gauge FETD formulations are summarized in Tables 6.1 and 6.2, respectively. CSEM responses are also plotted at selected detector positions in Figure 6.5.

First, I discuss Table 6.1 for the direct FETD formulation. The one-norm condition numbers of the system matrices increase with the resistivity value of the air. The smallest two resistivities of the air (i.e. 10^3 and 10^4 Ω-m) result in the smallest condition numbers but do not ensure a large enough contrast in the resistivity between the earth and the air. As a result, the FE solutions do not agree with the analytical solutions (Figures 6.5a and 6.5b). For the next seven resistivities of the air (i.e. 10^5 through 10^{11} Ω-m), my numerical modeling experiments agree well with the analytical solutions. With the largest resistivity of the air (i.e. 10^{12} Ω-m), the FE solutions diverge at around 0.2 seconds (Figure 6.5j), because round-off and other errors start to be amplified without control because of the extreme ill-conditioning.

Air (Ω-m)	Condition number of system matrix	Memory (MB) for triangular matrix	Total number of factorization	Total number of time-steps	Solution runtime (min)	Accuracy	Number of trials
10^3	3.22×10^{11}	1,300.749	9	1,599	30	×	1
10^4	3.22×10^{12}	1,300.749	9	1,599	30	×	1
10^5	3.34×10^{13}	1,300.749	9	1,599	30	○	1
10^6	3.36×10^{14}	1,300.749	9	1,599	30	○	1
10^7	3.25×10^{15}	1,300.749	8	1,696	33	○	1
10^8	3.22×10^{16}	1,300.749	5	4,038	56	○	1
10^9	3.22×10^{17}	1,300.749	2	25,873	303	○	1
10^{10}	3.22×10^{18}	1,300.749	0	100,000	1,185	○	1
10^{11}	3.25×10^{19}	1,300.749	0	100,000	1,237	○	1
10^{12}	3.22×10^{20}	1,300.749	•	100,000	•	×	1

Table 6.1. A summary of the direct FETD simulations with various air resistivities. When a direct FETD simulation fails, the unavailable information is denoted as •. In the seventh column, ○ and × denote accurate and inaccurate solutions, respectively.

Air (Ω-m)	Condition number of system matrix	Memory (MB) for preconditioner	Drop tolerance	Total number of preconditioner	Total number of time-steps	Solution runtime (min)	Accuracy	Number of trials
10^{3}	3.20×10^{11}	410.255	10^{-8}	10	1,198	19	×	2
10^{4}	3.22×10^{12}	454.812	10^{-8}	10	1,198	21	×	2
10^{5}	2.83×10^{13}	616.619	10^{-9}	10	1,198	22	○	2
10^{6}	3.22×10^{14}	725.853	10^{-10}	10	1,198	23	○	2
10^{7}	3.52×10^{15}	734.947	10^{-10}	10	1,198	23	○	2
10^{8}	3.22×10^{16}	866.352	10^{-12}	•	•	•	×	4
10^{9}	3.22×10^{17}	861.248	10^{-12}	•	•	•	×	4
10^{10}	3.23×10^{18}	919.516	10^{-13}	•	•	•	×	4
10^{11}	3.31×10^{19}	973.708	10^{-14}	•	•	•	×	4
10^{12}	1.01×10^{22}	1,023.284	10^{-15}	•	•	•	×	4

Table 6.2. A summary of the Lorenz-gauge FETD simulations with various air resistivities. Symbols are the same as in Table 6.1.

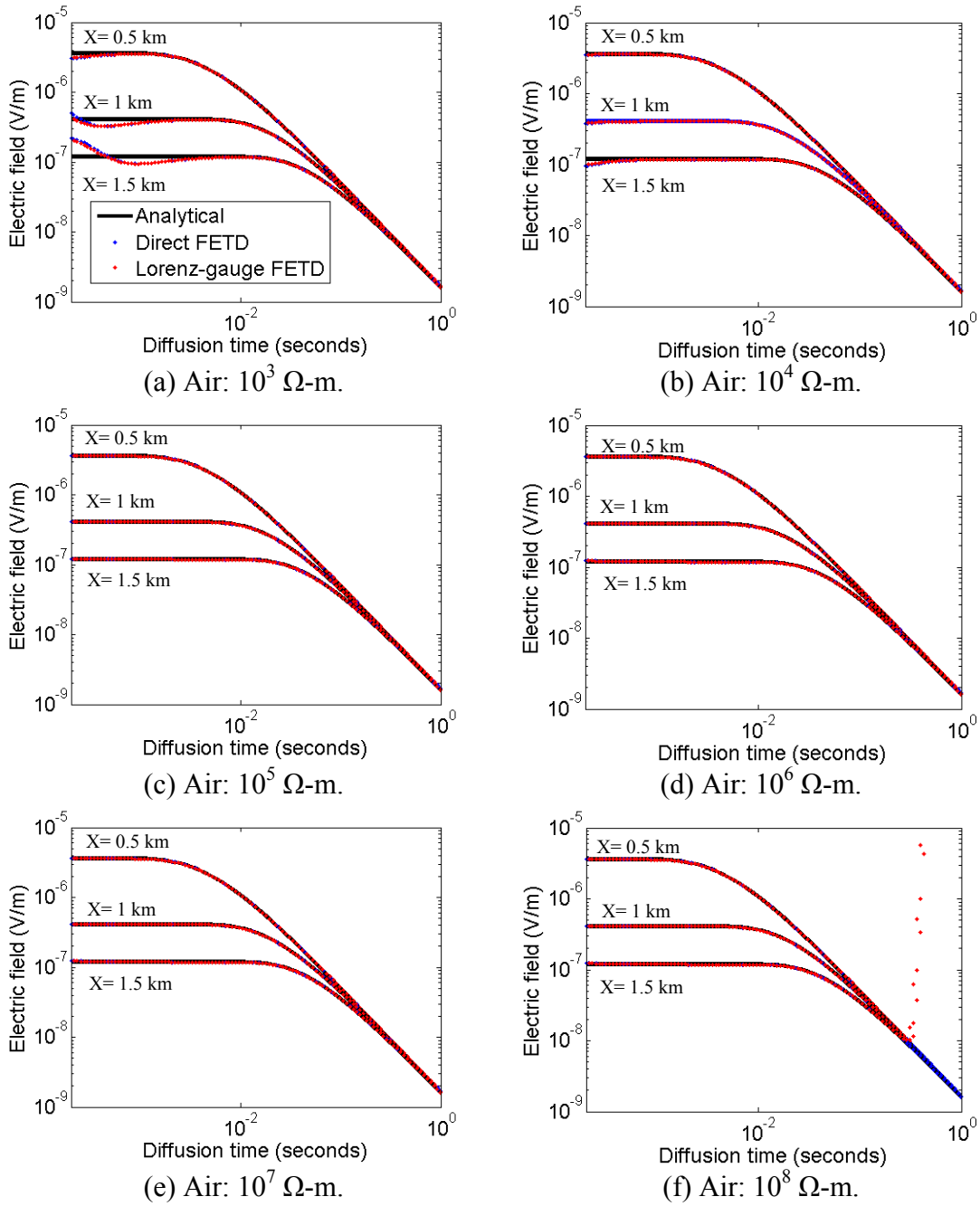

Figure 6.5. The inline E_x responses to a layered-earth model. The resistivity of the air varies. Three offsets are considered: 0.5 km, 1 km and 1.5 km. The Lorenz-gauge FE solutions are not plotted in (g) through (j) because they did not converge.

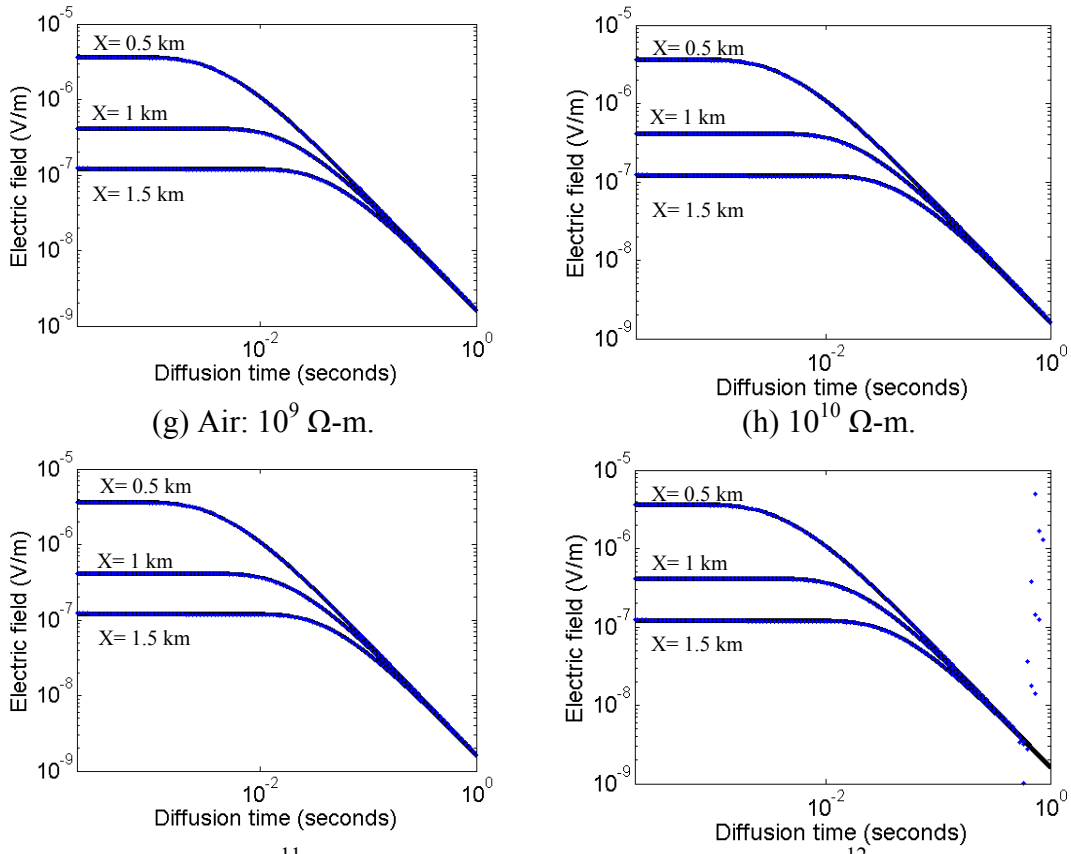

Figure 6.5. Continued.

The total number of time-steps required for the simulations increase quickly as the resistivity of the air increases beyond 10^7 Ω-m. The same is true for the corresponding solution runtimes. Indeed, this observation illustrates that the time-step-doubling method does not work effectively when system matrices are too ill-conditioned. As discussed in the second section of this chapter (Numerical implementation), the method accepts $2\Delta t$ as a new time-step for increased speed when the difference in solutions obtained using Δt and $2\Delta t$ is smaller than a tolerance related to the EM attenuation. However, when the air is too resistive, differences between the two solutions are primarily controlled not by the EM attenuation but by the error amplification due to ill-conditioning. Consequently, with the resistivity of the air higher than 10^9 Ω-m, the time-step-doubling method does not work at all, even though

the high-frequency components of the transient EM fields are more rapidly attenuated in time.

Next, I examine the Lorenz-gauge FETD formulation by comparing Table 6.1 with Table 6.2. The system matrices of the direct and Lorenz-gauge FE formulations have similar condition numbers in a wide range of air resistivities. In my numerical experiments, the Lorenz-gauge FETD formulation allows one more time-step-doubling process during the simulations, resulting in shorter solution runtimes. General benefits of the iterative solver over the direct solver also contribute to the shorter runtimes. The memory required for storing incomplete Cholesky preconditioners varies according to both preset drop tolerances and system matrices. For the resistivities of the air that produce accurate solutions, the memory for the preconditioner (Table 6.2) is about 45 to 55 % of that for the lower triangular matrices obtained from the Cholesky factorization (Table 6.1).

Despite the advantages discussed above, however, the Lorenz-gauge FETD formulation also has a disadvantage. For example, when a drop tolerance was set to 10^{-6} for a model with an air resistivity of 10^5 Ω-m, the preconditioned CG solver failed to converge after a prescribed maximum number of iterations (i.e. 30). After two trial attempts, I succeeded in finding a proper drop tolerance (10^{-9}) that not only makes the CG solver converge reasonably quickly, but also uses a reasonable amount of memory (Table 6.2). However, when the resistivity of the air is set higher than 10^7 Ω-m, I was unable to find such a drop tolerance after four trials and discontinued my tests.

The need to use trial and error to find a proper drop tolerance is an obvious drawback of the Lorenz-gauge FETD formulation. However, through extensive CSEM modeling experiments, I have found that a good estimate is to set the initial drop tolerance about a few orders of magnitude smaller than the conductivity of the air; one can try a smaller drop tolerance for a shorter solution runtime, but this requires more memory. I discuss more on this in the next section. For accurate solutions, the conductivity of the air also needs to be a few orders of magnitude smaller than that of the seawater or the earth. With such choices, I have succeeded in obtaining accurate Lorenz-gauge FETD solutions with just one or two trials. Throughout the modeling

experiments, the Lorenz-gauge FETD formulation shows solution runtimes comparable to those of the direct FE formulation and uses only 30 to 50 % of the memory required for the direct FETD formulation.

6.4 Impact of time-step doubling on conditioning of matrix

As shown in the previous modeling examples, the time-step doubling method is an essential part of the FETD algorithm for its performance. In this section, I analyze the impact of the time-step doubling method on the conditioning of the system matrix by changing both Δt and the accuracy of the preconditioner (i.e. drop tolerance). The eigenvalue distribution before and after preconditioning is also examined. This analysis provides a quantitative understanding of the rule of thumb about choosing a drop tolerance of the preconditioner and demonstrates the robustness of the time-step doubling method.

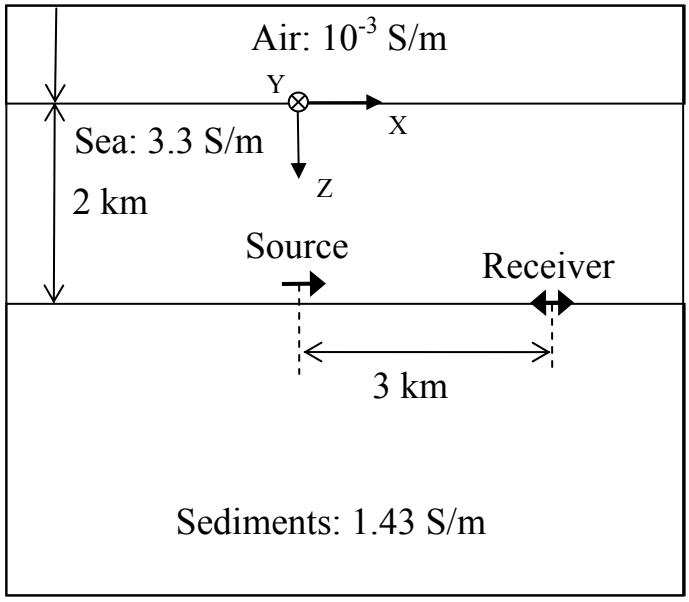

Figure 6.6. The cross-sectional view of the test model. The single source and receiver are placed at (0 km, 0 km, 1.95 km) and (3 km, 0 km, 2 km), respectively.

Since the previous models are too large to quickly compute the distribution of eigenvalues, a small test model is constructed as shown in Figure 6.6. To reduce the problem size, the test model is somewhat different from the previous models. First, the test model has only one receiver position at (3 km, 0 km , 2 km). Because small elements are required around receivers, the single source-receiver configuration reduces the problem size. Although the test model has the simplified CSEM configuration, it has representative conductivity values for the seawater column (3.33 S/m) and the seabed (1.43 S/m). To ensure numerical stabilities, the conductivity of the air is set to 10^{-3} S/m. The thickness of the seawater column is set to 2 km. In contrast to the 400 m thick seawater column of the precious models, tetrahedral elements in the 2 km thick seawater can grow more rapidly in the x- and y- directions, reducing the problem size. Accordingly, the model consists of 12,767 elements and 14,505 unknowns for equation 5.40.

The CSEM model is computed with different drop tolerances ranging from 10^{-2} to 10^{-5}. The performance is analyzed as shown in Figure 6.7. Note that as discussed in the previous section, a rule of thumb for choosing a proper drop tolerance is to set the drop tolerance a few orders of magnitude smaller than the smallest conductivity (i.e. the conductivity of the air). However, to better understand the impacts of a less accurate preconditioner on the time-step doubling method, the analysis includes the drop tolerance even larger than the smallest conductivity value (i.e. 10^{-3}).

When the least accurate preconditioner with the drop tolerance of 10^{-2} is used, the number of iterations for convergence suddenly increases at late time (Figure 6.7a). Furthermore, after around 5 seconds, the time-step size is no longer doubled (Figure 6.7b). This is because the number of iterations for convergence with $2\Delta t$ becomes larger than twice that required for convergence with Δt. As a result, the number of time-steps required for completing the simulation quickly increases (Figure 6.7c). So does the solution run time (Figure 6.7d).

However, as the drop tolerance reduces from 10^{-2} to 10^{-4}, the increase of the time-step makes little impact on the number of iterations for convergence. The time-step

doubling method also works efficiently, reducing the solution run time. When the drop tolerance reduces from 10^{-4} to 10^{-5}, the FETD performance does not improve much.

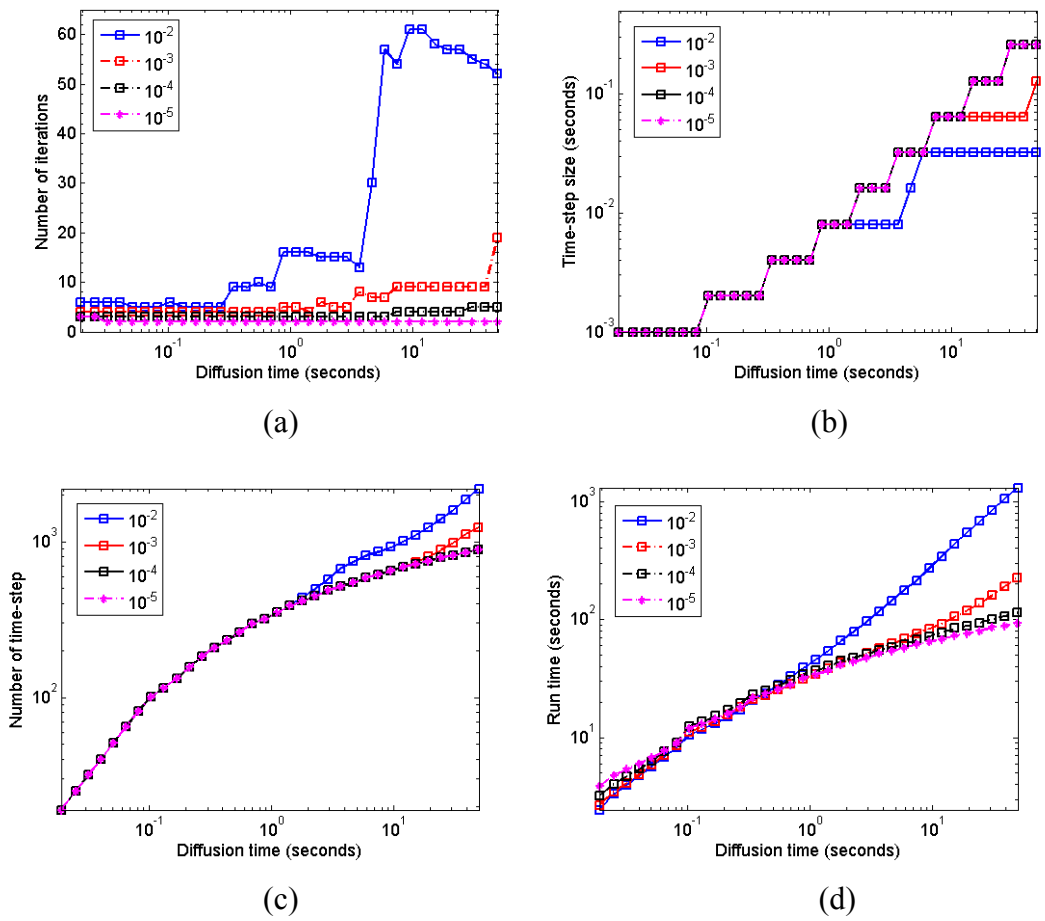

Figure 6.7. The performance analysis of the FETD algorithm for the model shown in Figure 6.6. The legend indicates the drop tolerances used in the analysis. (a) The diffusion time vs. the number of iterations required for convergence. (b) The diffusion time vs. the time-step size during the simulation. (c) The diffusion time vs. the accumulated number of time-step. (d) The diffusion time vs. the run time.

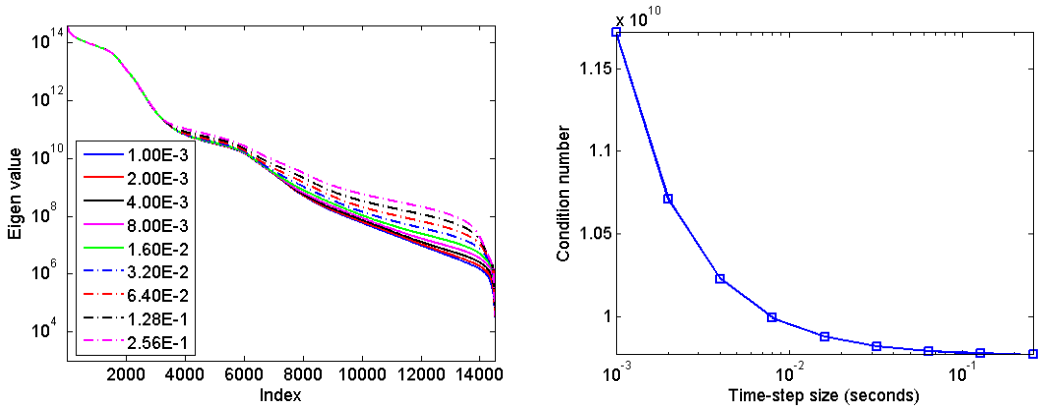

(a) (b)

Figure 6.8. (a) The eigenvalue distribution of the system matrix with time-steps ranging from 0.001 to 0.256 seconds. (b) The condition number as a function of Δt.

In order to examine the impact of the time-step size on the system matrix before preconditioning, the eigenvalue distribution of the system matrix is plotted as a function of the time-step size (Figure 6.8a). As the time-step size is successively doubled, small and intermediate eigenvalues gradually increase. In contrast, large eigenvalues do not change. As a result, The condition number slightly decreases with increasing the time-step size (Figure 6.8b).

Next, I examine the impact of the time-step size on the system matrix after preconditioning. First, I start with a preconditioner with the largest drop tolerance, 10^{-2}. After the preconditioner is applied to the system matrix with different time-step sizes, the eigenvalue distribution of the preconditioned system matrix is plotted as shown in Figure 6.9. Figure 6.10 shows the corresponding condition numbers as a function of time-step size (the blue line). When the smallest time-step size (i.e. 10^{-3}) is used in the system matrix, the eigenvalues of the preconditioned system matrix are clustered well near (1,0) as shown in Figure 6.9a. Therefore, a small condition number is read from Figure 6.10. The number of iterations for convergence is also small (Figure 6.7a). However, as the time-step size is successively doubled, the eigenvalues become less clustered (Figures 6.9d, 6.9e and 6.9f). The corresponding condition numbers also quickly increase with the time-step size (Figure 6.10). As a result, the convergence

rate quickly deteriorates (Figure 6.7a). In short, the preconditioner with the drop tolerance of 10^{-2} does not make the time-step doubling method work effectively.

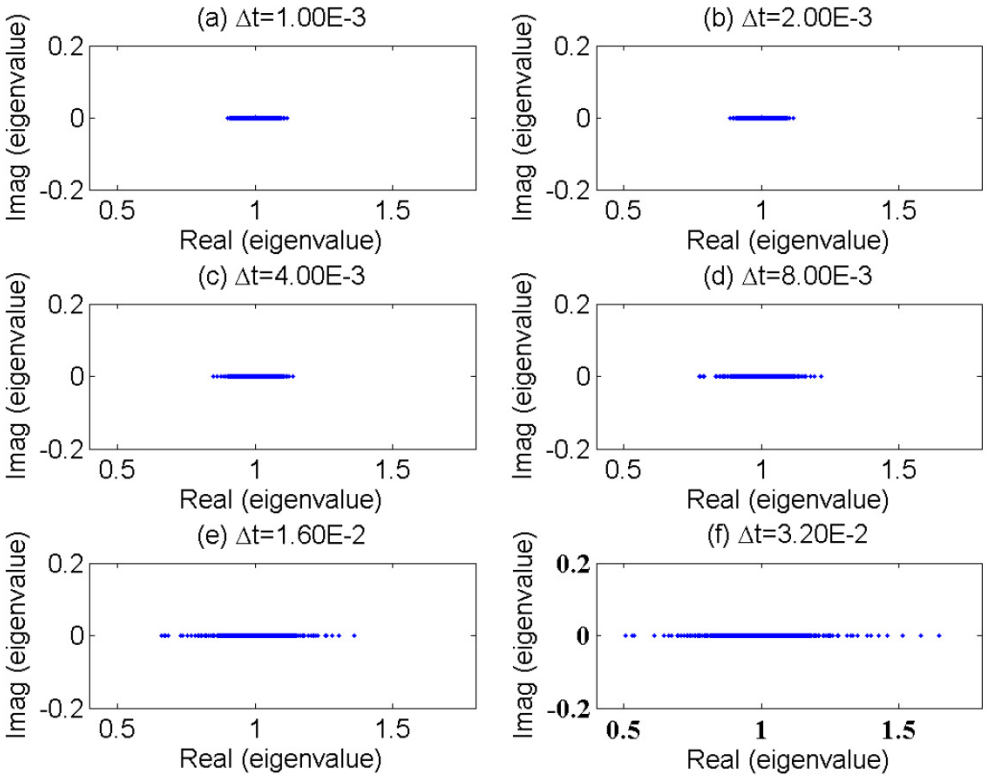

Figure 6.9. The eigenvalue distribution of the system matrix after the preconditioner with the drop tolerance of 10^{-2} is applied. Δt denotes the time-step size used in the analysis.

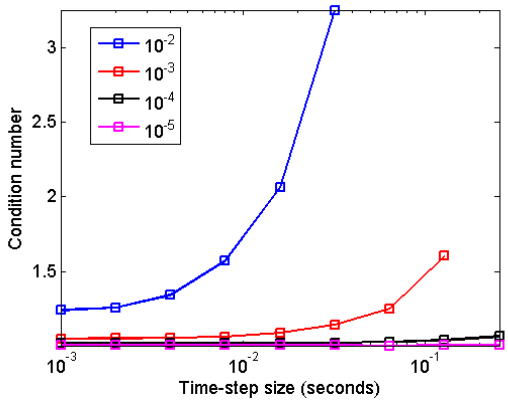

Figure 6.10. The condition numbers as a function of the time-step size after preconditioning. The legend indicates the drop tolerances used in the analysis.

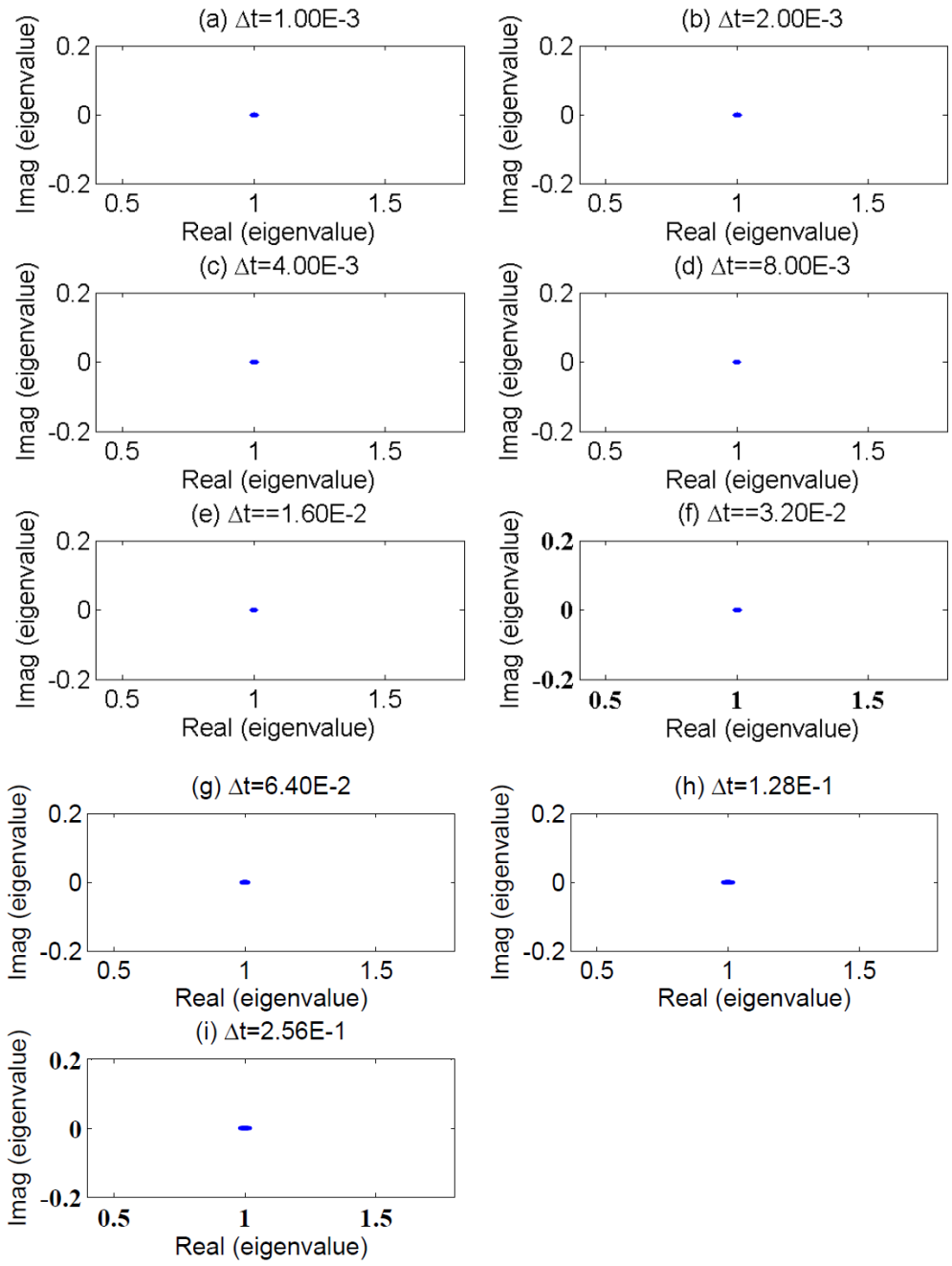

Figure 6.11. The eigenvalue distribution of the system matrix after the preconditioner with the drop tolerance of 10^{-4} is applied. Δt denotes the time-step size used in the analysis.

The same analysis procedures are repeated with the drop tolerance of 10^{-4} that is an order of magnitude smaller than the smallest conductivity and also meets the rule of thumb for a choosing the drop tolerance. The eigenvalue distribution of the preconditioned system matrix is plotted as shown in Figure 6.11. Compared with the previous example (Figure 6.9), the eigenvalue distribution is more compactly clustered at around (1,0). The increase of the time-step size insignificantly changes the distribution of the eigenvalues. Therefore, the condition numbers of the preconditioned matrices remain close to 1 (the black line in Figure 6.10). Accordingly, regardless of a time-step size, the solutions converge consistently just after a few iterations(Figure 6.7a).

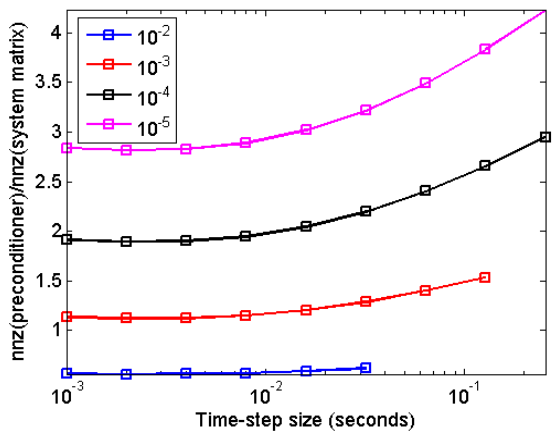

Figure 6.12. The number of non-zeros (nnz) of the preconditioner as a function of the time-step size and the drop tolerance. The legend indicates the drop tolerances used in the analysis. The size of the system matrix of equation 5.40 for the test model is 14,505×14,505 and its number of non-zeros is 232,593.

Finally, I investigate the number of non-zeros of the preconditioner as a function of the time step size and the drop tolerance (Figure 6.12). The number of non-zeros increases with the time-step size. Therefore, at a given drop tolerance, the preconditioner that is computed with the largest time-step size eventually determines the memory requirement. As shown in Figure 6.12, the memory requirement of a preconditioner that meets the rule of thumb for choosing a drop tolerance is about 3~4 times that of the system matrix. As a side note, the memory requirement for the complete Cholesky factorization is 9 times that of the system matrix.

So far, I have analyzed the performance of the time-step doubling method by relating a drop tolerance of the preconditioner to the eigenvalue distribution after preconditioning. In short, successive doubling of time-steps tends to increase the condition number of a preconditioned system matrix and thus, decrease the convergence rate. However, when a sufficiently accurate preconditioner is used, the condition number of the preconditioned matrix remains close to (1,0) through successive time-step doubling processes, ensuring fast convergence. The eigenvalue analysis provides sound explanations about not only convergence and time-stepping characteristics but also the rule of thumb for choosing a drop tolerance for a sufficiently accurate preconditioner.

6.5 Conclusions

I have implemented the Lorenz-gauge FETD algorithm using the adaptive time-step-doubling method, along with a strategy of reusing intermediate computation results inside a time-stepping loop. The approach to time-stepping is conceptually the same as the one employed in Chapter 4 for the direct FETD algorithm, except that its implementation with an iterative solver requires checking not only whether the difference in two solutions computed using Δt and $2\Delta t$ is smaller than a tolerance, but also whether the number of iterations with $2\Delta t$ is smaller than two times that with Δt. The time-stepping approach described here is extremely useful to accelerate FETD solutions in conductive earth models where FETD solutions need to be computed until very late times. Modeling examples demonstrate the accuracy of the efficiency of the Lorenz-gauge FETD algorithm.

I compare the Lorenz-gauge FETD algorithm with the direct FETD algorithm described in Chapters 3 and 4. A primary advantage of the former over the latter is that the Lorenz-gauge FETD algorithm uses an iterative solver, which uses less than half of the memory required by the direct FETD algorithm. However, an obvious drawback of the Lorenz-gauge FETD algorithm is the need to finding proper modeling parameters by trial and error. In order to minimize such efforts, I suggest the following

guidelines on the parameters. For accurate solutions, the conductivity of the air needs to be a few orders of magnitude smaller than that of the medium interfacing with the air. However, as demonstrated, air conductivity that is too low results in non-convergence of solutions. The rule of thumb for choosing a small enough drop tolerance is to set a drop tolerance to a few orders of magnitude smaller than the smallest conductivity value in a model (e.g. the conductivity of the air).

The impact of the time-step size on the Lorenz-gauge FETD algorithm is examined using the eigenvalue analysis. The impact of the time-step size on the FETD algorithm depends on the accuracy of a preconditioner. When the preconditioner is insufficiently accurate due to a large drop tolerance, the eigenvalues of the preconditioned matrix are increasingly less clustered with increasing the time-step size. Consequently, the number of iterations for convergence can abruptly increase at late times. In contrast, when the preconditioner is accurate enough, the eigenvalues remain clustered well, ensuring the efficient time-step doubling processes.

Chapter 7. 3D FETD Model Construction for TDCSEM Simulations from a Realistic Seismic Model

In Chapters 3 through 6, I formulated the two FETD algorithms and demonstrated their accuracy and performance in layered and simple 2D/3D earth models. Although the presented idealized models elucidate the numerical characteristics of the FETD algorithms and its benefits over FDTD methods, a primary purpose of developing and employing the FETD algorithms is to simulate complex geological structures where FD discretization is not considered efficient.

In the remaining two chapters of this dissertation, I simulate and analyze the TDCSEM method over realistic earth models. As a first step in this chapter, I describe the construction of realistic FE offshore models that include complex seafloor topography, reservoir and salt structures. The offshore models have relatively shallow seawater where the TDCSEM method is considered useful (Chapters 1 and 2).

7.1 FETD model construction

To construct realistic FE offshore models, I utilize the uniformly-gridded SEG salt model (Aminzadeh et al., 1997). The SEG model is 13.5 km by 13.5 km by 4.2 km in the x-, y- and z-directions, respectively, and its grid size is 20 m in all three directions. Hence, the model consists of 95,681,250 cells (675×675×210). The SEG model primarily consists of three structures: the complex seabed, the irregular seafloor topography and the salt. Among the three structures, the irregular seafloor and the salt are imported to the FE modeling space. The complex seabed stratagraphy is not inserted to the FE modeling space due to the limitation of the computing capacities of the serial computers used for this study (See the next section). Instead, I assume that the seabed is homogeneous unless salt or reservoir structures are inserted.

To convert the gridded salt and seafloor topography structures into corresponding FE structures, the surface coordinates of the structures are sampled at 200 m interval. Then, the 3D surfaces of each structure are reconstructed in the 3D FE modeling space using a Delaunay algorithm (Barber et al., 1996). During the reconstruction processes, if the sampling interval is too large (e.g. 1 km), the reconstructed structure is distorted from the original structure. However, when the sampling interval is too small (20 m), the reconstruction processes become computationally intensive and become intractable for a mesh generator (i.e. COMSOL) on a modern personal computer (e.g. 2.8 GHz Intel Duo processor with 8 GB memory). As a trade-off sampling interval, I sample the structures every 200 m in the x- and y-direction. The resulting reconstructed 3D surfaces of the seafloor and the salt are shown in Figure 7.1.

Starting with this reconstructed model, I introduce two changes that allow the model to accommodate more realistic TDCSEM survey environments. First, I increase the seawater depth by 200 m. Note that the seawater depth of the original SEG model ranges from 0 to 440 m. By increasing the seawater depth by 200 m, a 200-m-long vertical electric-dipole source can be placed anywhere above the seafloor. When the change is made, the seawater depth varies from 220 to 380 m along the survey line (Figure 7.2a). At this depth, the TDCSEM method is still a reasonable choice (Weiss, 2007).

Second, I introduce to the offshore model a cylindrical hydrocarbon reservoir whose radius and thickness are 2500 m and 100 m, respectively. The center of the reservoir is placed at (x=4500 m, y= 0 m, z=950 m). The reservoir does not intersect the salt but is slightly above it. The reservoir is also tilted by 5 degrees toward the negative x-direction. In my modeling, the resistivities of the seawater, the seabed, the reservoir and the salt are set to 0.3, 0.7, 100, and 100 Ω-m, respectively. The resistivity values are considered typical in logging data and have been widely used in CSEM and magnetotelluric modeling (Hoversten et al., 1998; Hoversten et al., 2006; Key et al., 2006; Li and Key, 2007). Figure 7.2b shows the cross-sectional view of my final offshore model.

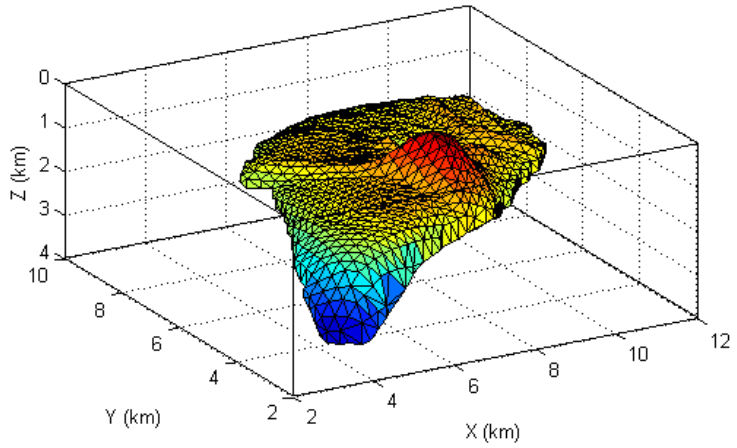

(a)

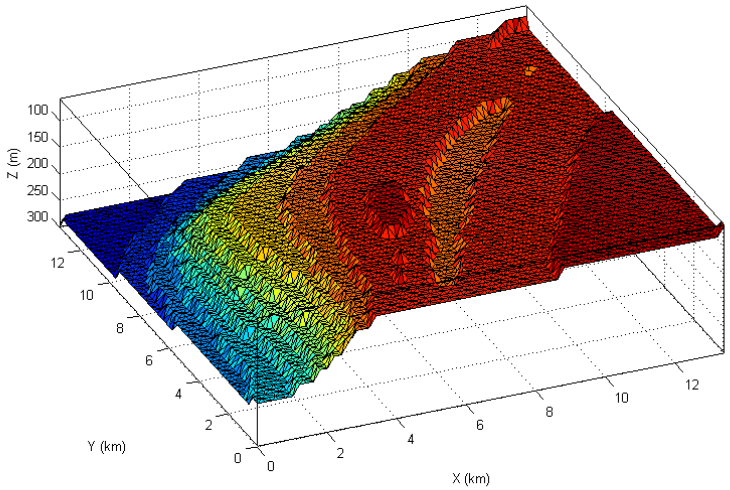

(b)

Figure 7.1. The reconstructed 3D surfaces of (a) the salt and (b) the seafloor. The vertical axis is exaggerated.

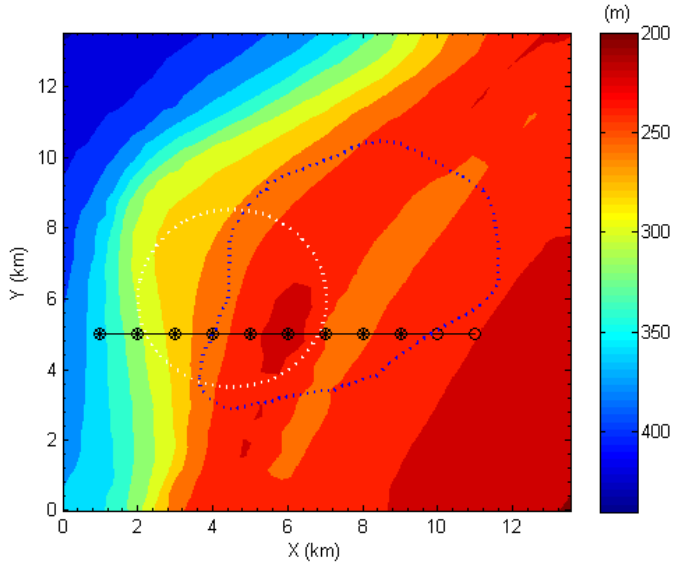

(a)

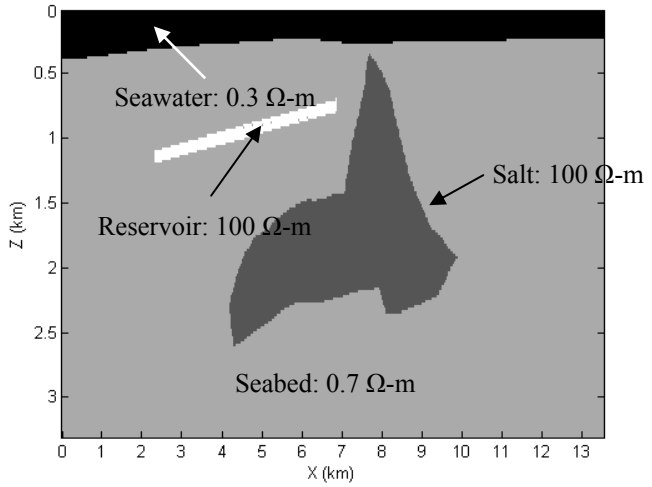

(b)

Figure 7.2. The 3D offshore model that is modified after the SEG salt model. (a) The topography map with the survey line. (b) Cross-sectional view at Y=5 km. In (a), the white broken line indicates the boundary of the hydrocarbon reservoir, and the blue broken line the boundary of the reconstructed SEG salt body. The asterisks and circles represent the source and receiver positions, respectively.

So far, the external boundaries of my FE offshore model are the same as those of the original SEG model. As discussed in Chapters 3 and 5, my FETD algorithms utilize the homogeneous Dirichlet boundary conditions. Therefore, to eliminate unwanted boundary effects at receiver locations, the external boundaries of the model should be sufficiently far from the source location (Um et al., 2010). To ensure this is the case, I first extend the seafloor topography along the boundaries of the model (Figure 7.1b) to additional 15 km in the x- and y-directions, respectively. Then, I insert the offshore model into a much larger background offshore model that measures 500 km in each direction. The layered background offshore model consists of the air, the seawater and the seabed. Their thicknesses are 250 km, 500 m and 249.5 km, respectively.

As shown in Figure 7.2a, the survey line consists of 9 source locations and 11 receiver locations. As demonstrated in Chapters 4 and 6, the FE discretization strongly depends on not only geological structures but also the source and receiver location. Around the receiver location, mesh elements should be small enough to represent a finite length of a receiver. For example, a 20-m-long electric-field dipole receiver can not be accurately approximated with 200-m-long tetrahedral elements. Around the source location, mesh elements should also be small not only to accurately discretize a finite length of the source but also to support fast-diffusing high-frequency electric fields at early times. Therefore, the source location generally requires a larger volume of small elements than the receiver location. In short, a model with more receivers and sources requires more elements.

When the survey line includes multiple sources and receivers, it is important to determine how many sources and receivers should be included in a single mesh. If a single mesh includes all sources and receivers along the survey line, I need to build only one mesh and can repeatedly reuse it for different source-receiver configurations. However, such a mesh design critically increases the number of elements. Thus, the solution cost per source becomes prohibitive. The mesh generator also has difficulties to produce such a large mesh. In contrast, when a mesh has a single source and a single receiver, the mesh has the smallest total number of elements and can be computed quickly. However, in this case, I need to manually construct 99 meshes (9

sources × 11 receivers) and simulate them separately. Again, the overall modeling cost becomes prohibitive.

In this study, I construct nine different FETD meshes for the offshore model (Figure 7.2). Each mesh includes one source location and eleven receiver locations. In fact, the opposite mesh design was also attempted; each mesh has multiple source locations rather than multiple receiver locations. However, such a mesh design turned out to be impractical because increasing the number of source locations increases the number of elements too quickly. For one source and eleven receivers, on average, the mesh consists of 412,786 tetrahedral elements, resulting in 480,868 unknowns. The average solution time for the mesh is about four hours on a 2.26 GHz Intel Nehelem single core using 10 GB memory. On the other hand, about 20,000 receivers are densely deployed in a grid pattern on the cross-section of the model (Figure 7.2b) for generating snapshots of transient electric fields. In such a case, on average, the FETD mesh consists of 1,143,938 tetrahedral elements, resulting in 1,335,541 unknowns. The average solution time for the mesh is about 15 hours on the same Nehelem core using 48 GB memory. During the simulations above, the step-off source waveform has been employed. Then, impulse responses to the models are approximated by taking time-derivatives of step-off responses (Edwards, 1997; Weiss, 2007). This indirect computation helps me reduce modeling costs since the use of an impulse waveform requires finer mesh around the source and a smaller initial time-step size than a step-off waveform.

7.2 FETD mesh calibration

To ensure the adequacy of the FETD mesh, the solutions should be compared to solutions obtained using other methods. First, to compare the FETD solutions with analytical solutions (K. H. Lee, personal communication, 2007), the resistivities of the seabed, the reservoir and the salt in the FETD meshes are set to that of the seawater. Then, I compute the FETD and analytical solutions for the half-space seawater model and compare them each other. I continue to refine the FETD meshes until the two

solutions agree to within 3 %. Next, the resistivity of the lower half-space in the FETD mesh is set to a new value (e.g. the resistivity of the seabed). The comparison procedures above are repeated. Note that this approach does not guarantee that the constructed FETD meshes produce accurate solutions, because large resistivity contrasts between the seabed, the reservoir and the salt are not considered. However, this approach allows us to quickly check, with relatively low computational cost, whether the FETD mesh is approximately correct.

Second, the resistivities of the seabed, the reservoir and the salt are reset to the original values listed in Section 7.1. Then, I compute 3D FETD solutions using two different FETD algorithms; one is based on the electric-field diffusion equation in Chapter 3, and the other on the vector-potential equation in Chapter 5. Note that the two FETD solutions have different systems of FETD equations derived from different EM governing equations but simulate the same EM diffusion physics. Therefore, when the two FETD algorithms share the same mesh, the comparison between the two FETD solutions can be used to measure the mesh quality. By checking the mesh quality through these two verification procedures, I ensure that FETD solutions are accurate enough for the numerical modeling experiments in the next chapter.

7.3 Conclusions

A set of FETD models is derived from the SEG salt model and is modified to better represent realistic TDCSEM survey scenarios. The FETD models include complex seafloor topography, the reservoir and the salt structure. The seawater depth of the original seismic model is increased by 200 m to accommodate a vertical electric-dipole source along the survey line. The FETD models are discretized according to TDCSEM survey layouts as well as EM diffusion physics. The quality of the resulting FETD meshes is verified by comparing their FETD solutions with analytical solutions and another FETD solutions. As demonstrated here, the FETD algorithms enable us to simulate TDCSEM responses over complex geological structures within 'reasonable' solution runtimes and with 'reasonable' computer resources. In the next chapter, the

offshore models serve as a virtual laboratory where the diffusion physics of various TDCSEM configurations and their characteristics are investigated.

Chapter 8. 3D FETD Modeling of the TDCSEM Method in Realistic Shallow Offshore Environments

In this chapter, I present a numerical modeling study on the electric fields produced by the TDCSEM method in the shallow offshore environments created in Chapter 7. Modeling of the TDCSEM method has been studied in past decades; typically, transient electric fields that are excited with a dipole source are examined along an array of seafloor receivers and on cross-sectional seabed using analytic, FD and FE seabed-modeling techniques (Edwards and Chave, 1986; Everett and Edwards, 1992; Um and Alumbaugh, 2005; Scholl and Edwards, 2007; Chave 2009).

However, most such studies have been carried out with simplified seabed models due to limited modeling capabilities. Although the simplified seabed models can be useful under some circumstances, they can not adequately explain representative TDCSEM exploration scenarios associated with highly complex and subtle offshore geology. The existing TDCSEM modeling studies also focus mainly on deepwater applications to crustal research, rather than shallow-water applications to hydrocarbon explorations. Moreover, the effects of seafloor topography and seabed anisotropy on the CSEM method for hydrocarbon exploration have been investigated for the frequency domain (Tompkins, 2005; Hoversten et al., 2006; Lu and Xia, 2007; Kong et al., 2008), but there has been no study of these type of features on the TDCSEM method for explorations.

To simulate TDCSEM responses over the complex geological structures within 'reasonable' solution runtimes (e.g. < 15 hours) and 'reasonable' computer resources (e.g. 2.26 GHz Intel Nehelem single core using 48 GB memory), I use the 3D FETD algorithms developed in Chapters 3 through 6. Using the FETD algorithms and the electrical offshore models constructed in Chapter 7, I carry out the following numerical experiments: First, I simulate, visualize, and analyze the electric fields excited by a horizontal electric-dipole (HED) source and their interactions with

seafloor topography, the large-scale salt structure, and the localized reservoir. Next, I investigate the sensitivity of the TDCSEM method to the reservoir close to the salt. Then, I repeat these modeling experiments with a vertical electric-dipole (VED) source. The characteristics of the VED source are compared with those of the HED source. Finally, I investigate the effects of an anisotropic seabed on the TDCSEM method.

8.1 Horizontal electric-dipole source configuration

To investigate the sensitivity of an impulse HED source to the localized reservoir close to the large-scale salt structure, I consider four different seabed scenarios: 1) a homogeneous seabed, 2) a seabed that includes only the reservoir, 3) a seabed that includes only the salt, and 4) a seabed that includes both the reservoir and the salt. For convenience sake, these four model scenarios are called 'the homogeneous seabed model', 'the reservoir-only model', 'the salt-only model' and 'the reservoir-and-salt model', respectively. For a given source location, these four different seabed scenarios can be simulated using a single FE mesh. For example, I simulate the homogeneous seabed model by setting the resistivities of the reservoir and the salt to that of the seabed. This removes any possibility of differences in responses caused by different meshes being employed.

Before I compare the seafloor electric-field measurements from the four models at selected receiver locations along the survey line, I first examine cross-sectional animations of the electric fields for each model (*figure8p1.mov; figure8p2.mov; figure8p3.mov; figure8p4.mov;* Figures 8.1, 8.2, 8.3 and 8.4). In this study, I consider multiple source positions. However, I primarily discuss the sources at x= 3 km because their electric fields interact well with both the reservoir and the salt and produce strong anomalous electric fields.

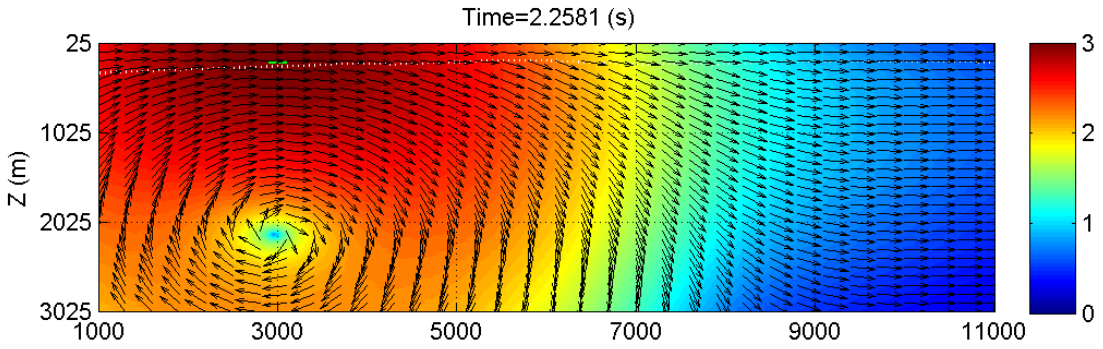

Figure 8.1. A snapshot of the animation showing the electric-field in the homogeneous seabed model. The snapshot is taken at 2.25 seconds after the HED source is excited. The animation file, *figure8p1.mov,* can be found on a companion CD. In the animation, the black arrows indicate the directions of the electric fields. The green line segment indicates the HED source position. The white broken line represents the seafloor.

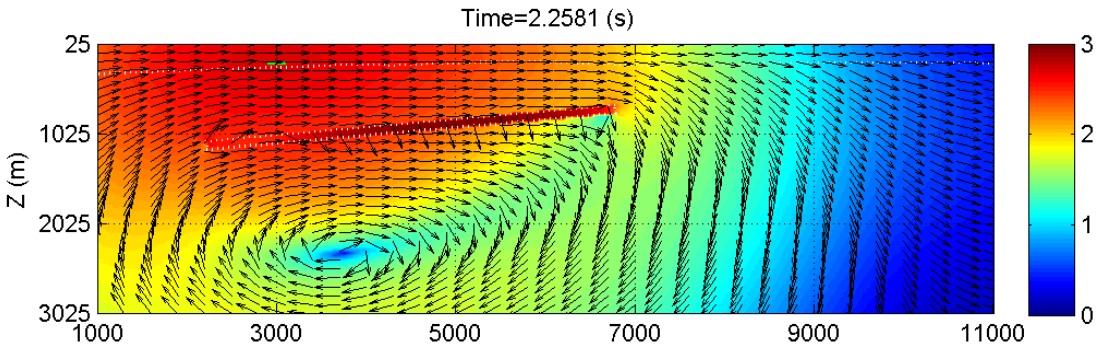

Figure 8.2. A snapshot of the animation showing the electric-field in the reservoir-only model. The snapshot is taken at 2.25 seconds after the HED source is excited. The animation file, *figure8p2.mov,* can be found on a companion CD.

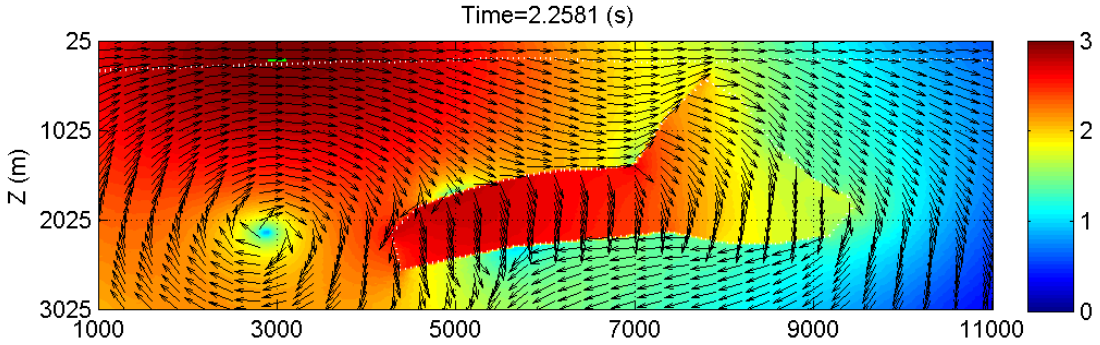

Figure 8.3. A snapshot of the animation showing the electric-field in the salt-only model. The snapshot is taken at 2.25 seconds after the HED source is excited. The animation file, *figure8p3.mov,* can be found on a companion CD.

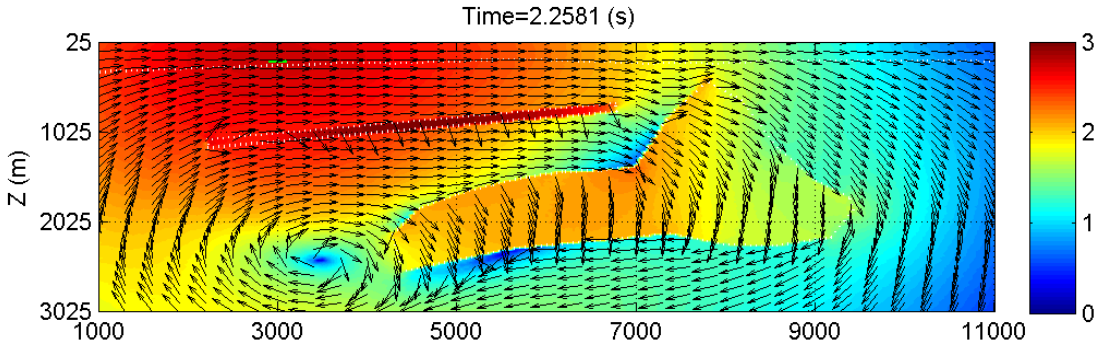

Figure 8.4. A snapshot of the animation showing the electric-field in the reservoir-and-salt model. The snapshot is taken at 2.25 seconds after the HED source is excited. The animation file, *figure8p4.mov,* can be found on a companion CD.

8.1.1 Analysis of the electric fields on cross-sections

First, I examine the animation for the homogeneous seabed model (*figure8p1.mov;* Figure 8.1). The animation consists of 34 snapshots of the electric fields on the cross-section. The snapshots are taken not at constant time intervals but at logarithmic time intervals. This is because the diffusion velocity of the electric field decreases with increasing time as its high-frequency content attenuates more rapidly over time. The background color represents the amplitude of the electric field that is normalized by its maximum on the cross-section. At a given snapshot, the range of the color varies from

0 to 3 on a log scale (base 10). The maximum amplitude of the electric field on the cross-section is set to 3; the zero amplitude is set to zero. On the cross-section, black arrows represent the direction of the electric fields.

After the excitation of the HED source, both horizontal and vertical electric fields are generated and gradually diffuse outward from the source position. In the seawater column, the electric fields are predominantly horizontal because of 1) the air-seawater interface and 2) the direction of the HED source. The high concentration of the horizontal electric fields remains close to the source location over time, indicating that at short offsets, receivers mainly record the direct diffusion through the seawater and the shallow seabed. Accordingly, at short offsets, HED-E_x responses are insensitive to the reservoir and the salt, as will be shown later.

Next, I insert the reservoir into the homogeneous seabed and examine its effects (*figure8p2.mov;* Figure 8.2). As the electric fields are normally incident upon the seabed-reservoir interface, the strong electric fields develop inside the reservoir due to the continuity of the normal current density. The electric fields inside the reservoir remain normal to the interface over time, resulting in the galvanic effects. The electric fields also diffuse significantly faster through the resistive reservoir than the conductive background seabed, and the degree of attenuation through the reservoir is insignificant compared with that through the seabed. Overall, the diffusion of the electric fields is 'guided' through the reservoir (Chave, 2009).

Next, I replace the reservoir with the salt (*figure8p3.mov;* Figure 8.3). The electric field pattern in the salt-only model is somewhat different from that in the reservoir-only model. When the electric fields are incident upon and then diffuse into the elongated part of the salt, the electric fields are not normal to the seabed-salt interface but change their direction over time inside the salt. The thick salt does not effectively ‘guide’ the electric fields inside it; as the thickness of the salt increases along the positive x-direction, the electric fields increasingly experience geometric spreading. Therefore, although the salt and the reservoir have the same resistivity (i.e. 100 Ωm), the amplitudes of the electric fields are smaller inside the salt than inside the reservoir. In short, the thick salt does not support the 'guided' diffusion.

However, even without the 'guided' diffusion, the large-scale salt still produces sufficient perturbations in the electric fields. As shown in *figure8p3.mov*, the electric fields diffuse significantly faster in the resistive salt than in the conductive seabed. Due to the large contrast of the resistivity between the seabed and the salt, the electric fields diffuse somewhat parallel to the boundaries of the salt in the seabed. For example, anomalous vertical electric fields are observed on the seafloor above the top of the salt. Overall, both along the seafloor and in the cross-section, the electric field distribution in the salt-only model is sufficiently different from the previous two examples.

Finally, I consider the reservoir-and-salt model (*figure8p4.mov;* Figure 8.4). It is of particular interest to examine the sensitivity of the TDCSEM method to the localized reservoir close to the large-scale salt. Although the volume of the reservoir is much smaller than that of the salt, the reservoir strongly perturbs the electric fields at early times due to the 'guided' diffusion. The direction of the electric fields inside the reservoir changes at late times, whereas the direction is constant in the reservoir-only model (*figure8p2.mov;* Figure 8.2). This is the result of the interaction of the electric fields between the reservoir and the salt. This interaction between the two structures makes patterns in the transient electric fields complex when viewed in a cross-section. The impact of the interaction on the seafloor measurements will be examined in the next section. Overall, the electric field distribution in the four seabed models is noticeably different, indicating that the TDCSEM method can sense them differently.

8.1.2 Analysis of the electric fields at seafloor receivers

So far, I have analyzed the electric-field diffusion in a cross-section of the 3D model. Now, I examine the electric-field measurements at four seafloor receivers whose x-coordinates are 4, 6, 8, and 10 km, respectively. The HED position is the same as in Figure 8.1. In my models, the receivers are tilted according to the seafloor topography as illustrated in chapter 4. Therefore, each receiver has its own local coordinate system. However, since the vector orthogonality of the receivers is preserved, the electric-field measurements are rotated back to the original coordinate system (i.e. the global

coordinate system) for analysis. Along the survey line, the tilt angles of the receivers do not exceed 3 degrees.

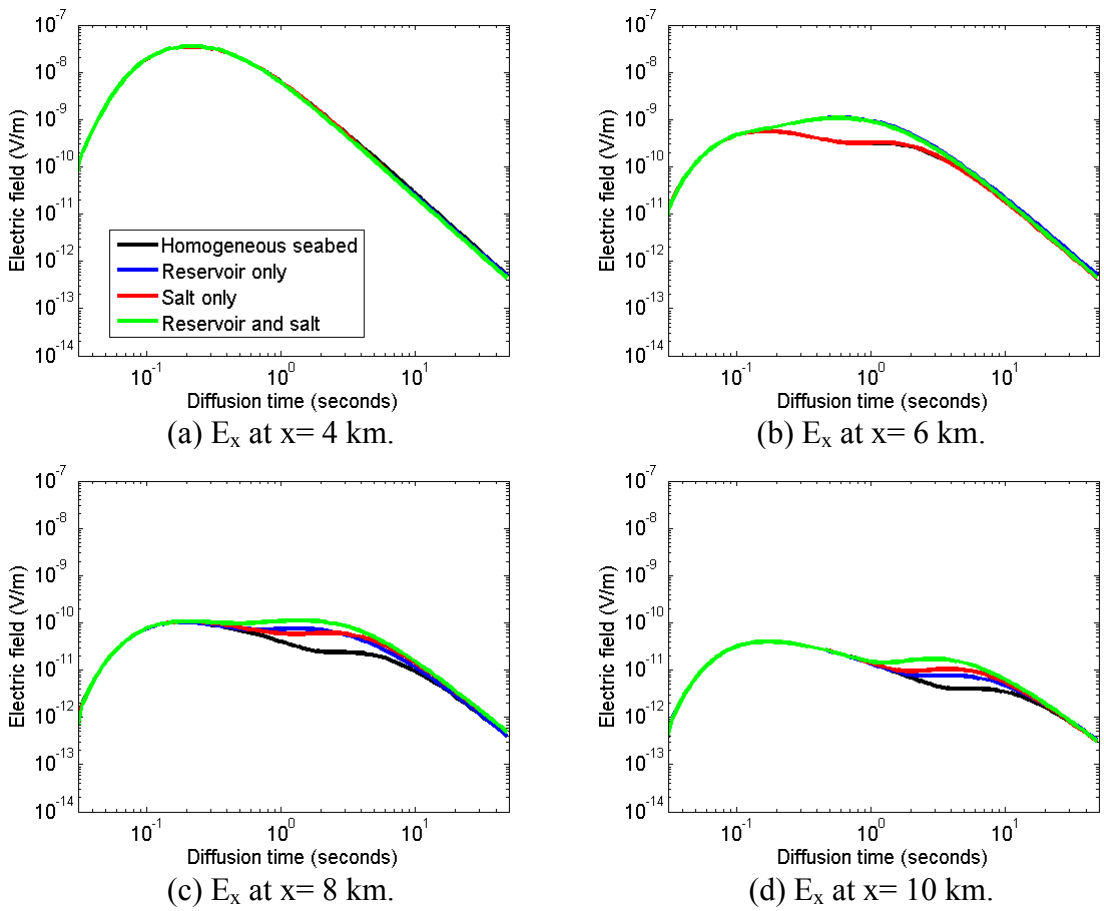

(a) E_x at x= 4 km. (b) E_x at x= 6 km.

(c) E_x at x= 8 km. (d) E_x at x= 10 km.

Figure 8.5. The seafloor E_x measurements over the four seabed models. The HED source is placed 50 m above the seafloor at x= 3 km.

The horizontal electric field (E_x) measurements are plotted in Figure 8.5. Except at the shortest offset (i.e. x = 4 km), the homogeneous seabed clearly shows a characteristic two-peak curve (Cheesman et al., 1987; Weiss, 2007). The air layer is responsible for the first peak. Both the seawater and the seabed are responsible for the second peak. There is no clear separation between the seawater effect and the seabed effect because the seabed is just about two times more resistive than the seawater. The reservoir effect and the salt effect are sequentially superimposed on the two-peak curve. As expected from the analysis of the animations in the previous sub-section, the HED-E_x configuration is insensitive to the reservoir and the salt at short offsets (e.g. Figure 8.5a). As the offset gradually increases, the sensitivity of the configuration to the structures increases, but the amplitudes of the electric fields gradually decrease.

Although the large-scale salt structure is expected to generate a larger perturbation than the reservoir, the reverse case is observed in Figure 8.5b; since the perturbation due to the salt is not clearly detected under the given HED-E_x offset, the second peak of the salt-only model is very close to that of the homogeneous seabed model. In contrast, the offset is sensitive to the presence of the reservoir. Consequently, the two reservoir-bearing models (i.e. the reservoir-only model and the reservoir-and-salt model) produce the large second peaks, and their responses resemble each other.

The vertical electric field (E_z) measurements are also sensitive to both reservoir and salt (Figure 8.6) and clearly differentiate the four different seabed models. In the E_z measurements, the homogenous seabed model can produce a larger response than the other three models. This phenomenon is not observed in the E_x measurements but is obvious when I compare the electric-field patterns of the four models (*figure8p1.mov; figure8p2.mov; figure8p3.mov; figure8p4.mov;* Figures 8.1, 8.2, 8.3 and 8.4).

Note that the amplitudes of the E_z measurements are roughly an order of magnitude smaller than those for E_x, because 1) the HED source is maximally coupled with E_x, and 2) the seafloor electric fields are predominantly horizontal because of the air-seawater interface in the shallow water. Therefore, when the receivers are tilted due to the irregular seafloor topography, E_z can be significantly contaminated with E_x. Such examples are shown in Figure 8.7. These examples suggest that the interpretation of

the E_z measurements would be erroneous without receiver-tilt corrections. Hence, the orientations of seafloor receivers must be recorded in practice to utilize E_z measurements. In contrast, the E_x measurements are less sensitive to the receiver tilt because of their relatively large amplitudes.

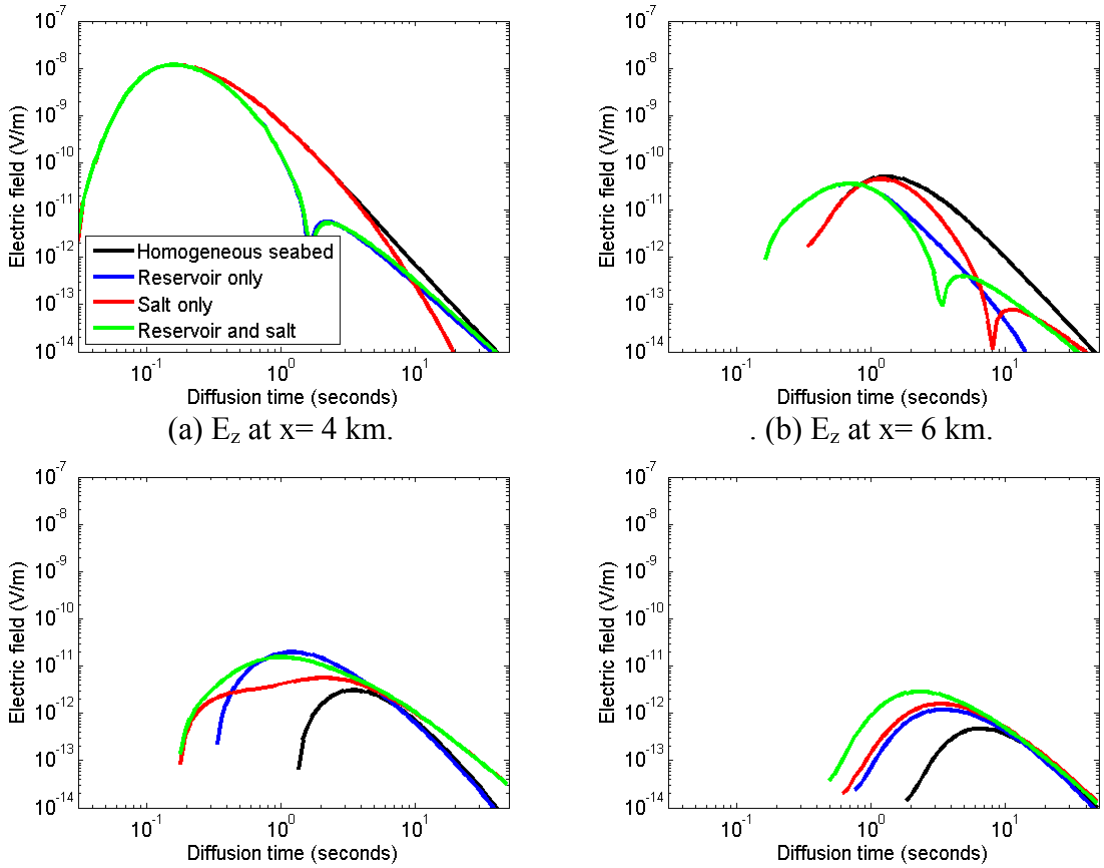

(a) E_z at x= 4 km. . (b) E_z at x= 6 km.

(c) E_z at x= 8 km. (d) E_z at x= 10 km

Figure 8.6. The seafloor E_z measurements over the four seabed models. The HED source is placed 50 m above the seafloor at x= 3 km. In (b) and (c), E_z measurements are not plotted at early time due to numerical noise.

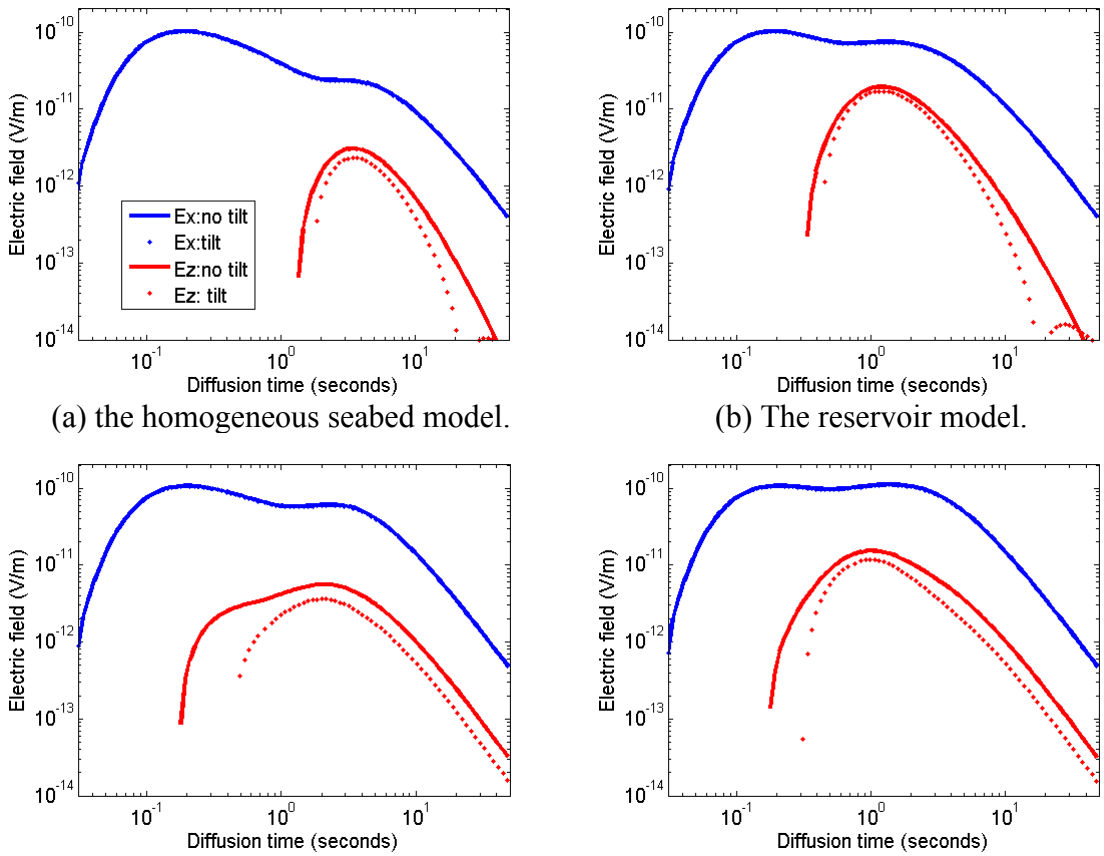

(a) the homogeneous seabed model. (b) The reservoir model.

(c) The salt model. (d) The reservoir-and-salt model.

Figure 8.7. The seafloor electric-field measurements at x= 8 km, with and without receiver-tilt corrections. The HED source is placed at x= 3 km.

To further examine the impact of the irregular seafloor topography on the TDCSEM method, the irregular seafloor is replaced with the uniform flat seafloor. In this case, I consider two different seawater depths: 220 m and 380 m. The seawater depths correspond to the shallowest and deepest seawater depth, respectively, along the survey line. For convenience sake, the two models are called flat seafloor models. The TDCSEM response to the flat seafloor models are computed using analytical solutions (K. H. Lee, personal communication, 2007) and are compared with the homogeneous seafloor model (i.e. the irregular seafloor model that has the homogeneous seabed).

In this modeling study, the flat and irregular seafloor models share the same source-receiver positions. It means that in the 220 m-deep flat-seafloor model, the source and most receivers are placed below the seabed-seawater interface, In contrast, in the 380

m-deep flat-seafloor model, the source and most receivers are placed above the interface. Although such source and receiver locations are not realistic in practice, by using the same source and receiver locations in the three models, I can consistently compare the seafloor topography effect between the three models without the effect of the different source and receiver locations.

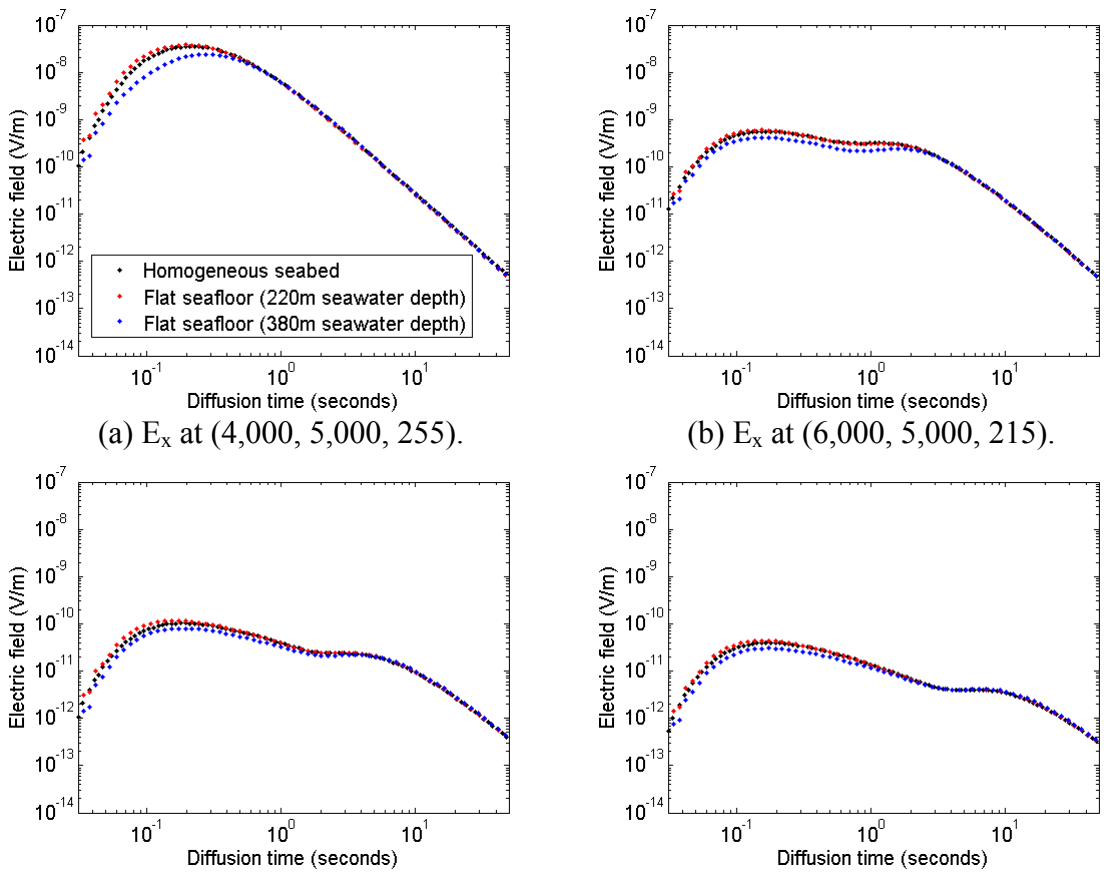

(a) E_x at (4,000, 5,000, 255). (b) E_x at (6,000, 5,000, 215).

(c) E_x at (8,000, 5,000, 248). (d) E_x at (10,000, 5,000, 235).

Figure 8.8. The seafloor E_x measurements over the flat seafloor models and the homogeneous seabed model (i.e. the irregular seafloor model that has the homogeneous seabed). The center of the 200 m long HED source is placed at (x,y,z)=(3,000 m, 5,000 m, 230 m).

Figures 8.8 shows E_x for the three models. At the given source-receiver positions, the E_x responses to the homogeneous seabed model are bounded by those to the two flat seafloor models at four receiver positions. Note that the 220 m-deep flat-seafloor model has larger 'airwave' responses than the other two models because the model has the least conductive resistivity structure above the receivers and thus the 'airwave' response is least attenuated.

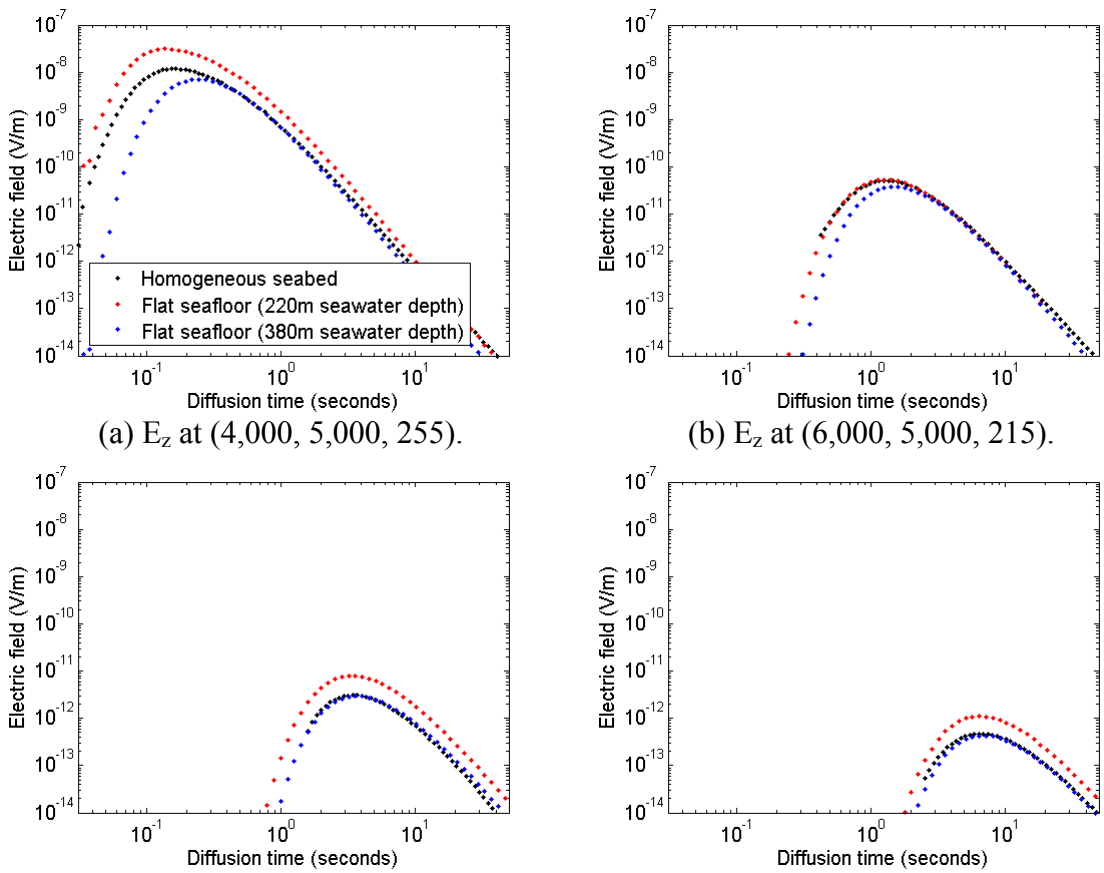

(a) E_z at (4,000, 5,000, 255). (b) E_z at (6,000, 5,000, 215).

(c) E_z at (8,000, 5,000, 248). (d) E_z at (10,000, 5,000, 235).

Figure 8.9. The seafloor E_z measurements over the flat seafloor models and the homogeneous seabed model (i.e. the irregular seafloor model that has the homogeneous seabed). The center of the 200 m long HED source is placed at (x,y,z)=(3,000 m, 5,000 m, 230 m).

Figure 8.9 shows E_z for the three models. The E_z responses to the irregular seafloor model are also bounded by those of the flat seafloor models. Although the differences between the three models illustrate the impact of the irregular seafloor topography on the TDCSEM method, the degree of the differences are relatively small compared with that of the receiver tilt. This small impact can be understood when the resistivity of the seabed is just about two times larger than that of the seawater. However, as will be shown in the next section, the irregular seafloor topography can also result in strong distortion at late time even at short offsets.

As shown here, the irregular seafloor topography can affect the 'airwave' responses by changing the thickness of the seawater column above a receiver. To further illustrate the effect, the seawater depth of the homogeneous seabed model (i.e. the irregular seafloor topography model) is increased by 500 m and 1,000 m, respectively. In other words, the seabed is moved downward by 500 m and 1,000 m, respectively. The E_x responses to the models are plotted in Figure 8.10. As the seawater depth increases, the 'airwave' response (i.e. the first peak) decreases due to increasing attenuation. As the peak also arrives at receivers increasingly later, the 'airwave' response is no longer clearly separable from the seabed response (i.e. the second peak). In such deep environments, the TDCSEM method is no longer a preferred tool (Weiss, 2007).

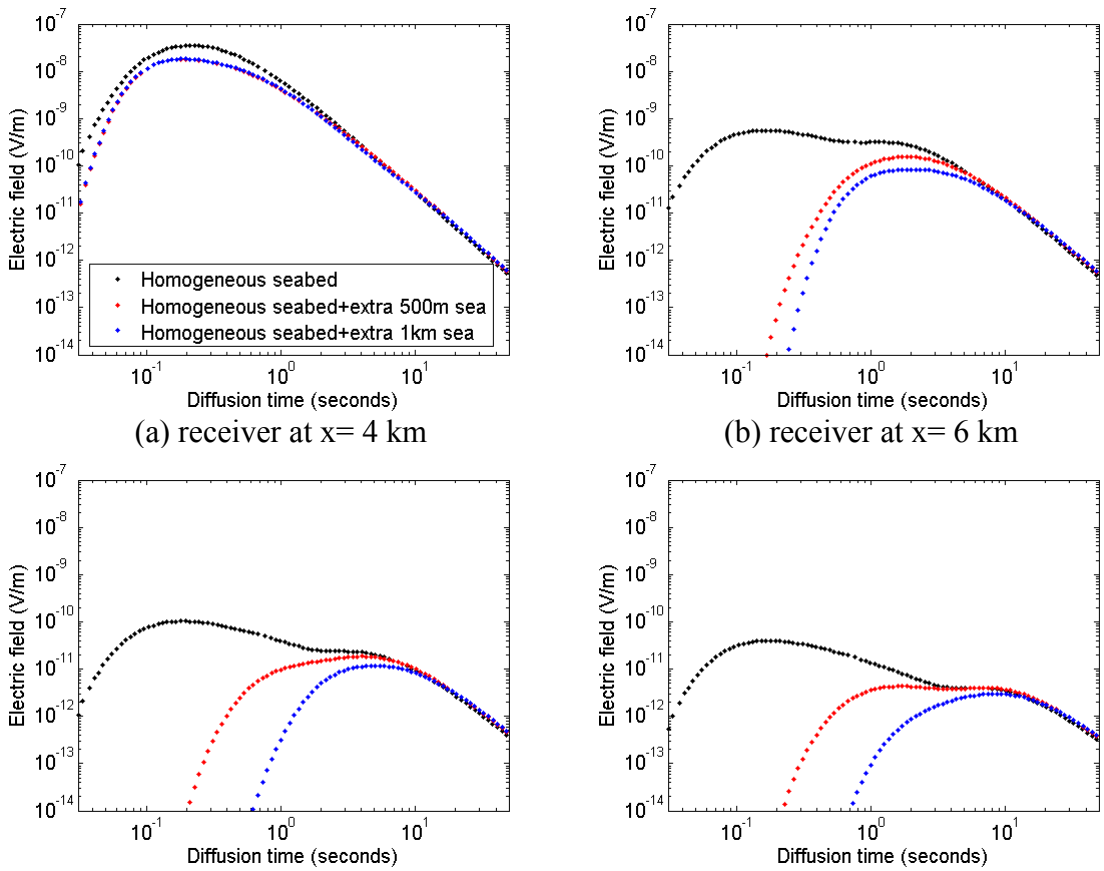

(a) receiver at x= 4 km (b) receiver at x= 6 km

(c) receiver at x= 8 km (d) receiver at x= 10 km

Figure 8.10. The seafloor E_x measurements over the homogeneous seafloor model with extra 500 m and 1,000 m thick seawater layers. The HED source is placed 50 m above the seafloor. The receivers are on the seafloor along the survey line.

Next, I examine the effect of the interaction of the electric fields between the reservoir and the salt on seafloor electric-field measurements. To do this, I first compute the linear sum of 1) the total electric fields from the homogeneous seabed model and 2) the scattered electric fields from the reservoir and the salt as shown below.

$$\mathbf{e}_{\mathrm{r}}^{\mathrm{s}} = \mathbf{e}_{\mathrm{r}}^{\mathrm{t}} - \mathbf{e}_{\mathrm{hs}}^{\mathrm{t}}; \tag{8.1}$$

$$\mathbf{e}_{\mathrm{s}}^{\mathrm{s}} = \mathbf{e}_{s}^{\mathrm{t}} - \mathbf{e}_{\mathrm{hs}}^{\mathrm{t}}; \tag{8.2}$$

$$\therefore\ \mathbf{e}_{\mathrm{rs}}^{\mathrm{ls}} = \mathbf{e}_{\mathrm{hs}}^{\mathrm{t}} + \mathbf{e}_{\mathrm{r}}^{\mathrm{s}} + \mathbf{e}_{\mathrm{s}}^{\mathrm{s}} \tag{8.3}$$

where

$\mathbf{e}^{t}_{hs}$: total electric field response from the homogeneous seabed model;

$\mathbf{e}^{t}_{r}$: total electric field response from the reservoir-only model;

$\mathbf{e}^{t}_{s}$: total electric field response from the salt-only model;

$\mathbf{e}^{s}_{r}$: scattered electric field response from the reservoir;

$\mathbf{e}^{s}_{s}$: scattered electric field response from the salt;

$\mathbf{e}^{ls}_{rs}$: linear sum of $\mathbf{e}^{t}_{hs}$, $\mathbf{e}^{s}_{r}$, and $\mathbf{e}^{s}_{s}$.

Then, I compare the linear sum with the electric field response to the reservoir-and-salt model. The difference between the twos indicates the non-linear interaction between the reservoir and the salt.

For systematic comparison, the linear sums are plotted together with the HED-E_x responses to the other four models (the left column of Figure 8.11). At x = 4 km (1 km offset, Figure 8.11a), the five curves agree well with each other. The recorded HED- E_x responses are merely the direct diffusion of the electric fields from the source through the seawater and shallow seabed. However, as the source-receiver offset increases, the unaccounted effect of the interaction is not ignorable, such that the linear sum is no longer a good approximation of the responses to the reservoir-and-salt model. For example, at x = 10 km (7 km offset, Figure 8.11g), the difference between the linear sum and the reservoir-and-salt model is larger than that between the reservoir-only and salt-only models.

The same analysis approach above is applied to the HED-E_z responses (the right column of Figure 8.11). The HED-E_z responses show much larger differences between the reservoir-and-salt model and the linear sum than the HED-E_x responses (the left column of Figure 8.11). However, the effect of the interaction on the HED-E_z responses as a function of the offset is not intuitive compared with the HED-E_x responses because 1) sign reversals exist and 2) the HED-E_z responses can often decrease when the reservoir and/or the salt is inserted into the seabed. Overall, Figure 8.11 illustrates the non-linear interaction of the electric fields between the salt and its adjacent reservoir.

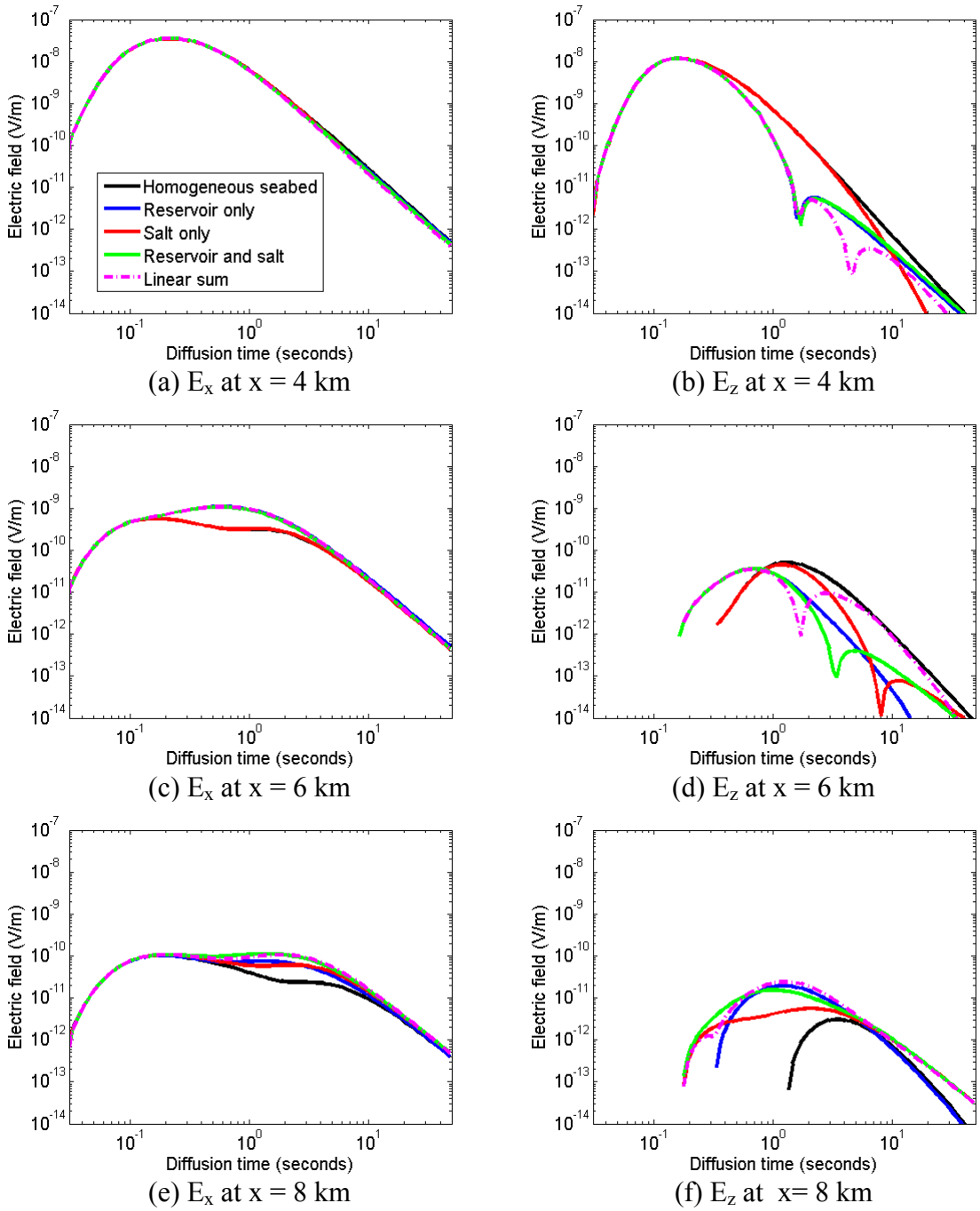

(a) E_x at x = 4 km (b) E_z at x = 4 km

(c) E_x at x = 6 km (d) E_z at x = 6 km

(e) E_x at x = 8 km (f) E_z at x= 8 km

Figure 8.11. The comparison of the TDCSEM responses to the reservoir-and-salt model and the linear sum of the total electric fields from the homogeneous seabed model and the scattered electric fields from the reservoir and the salt. The left column has the HED- E_x responses. The right column has the HED-E_z responses.

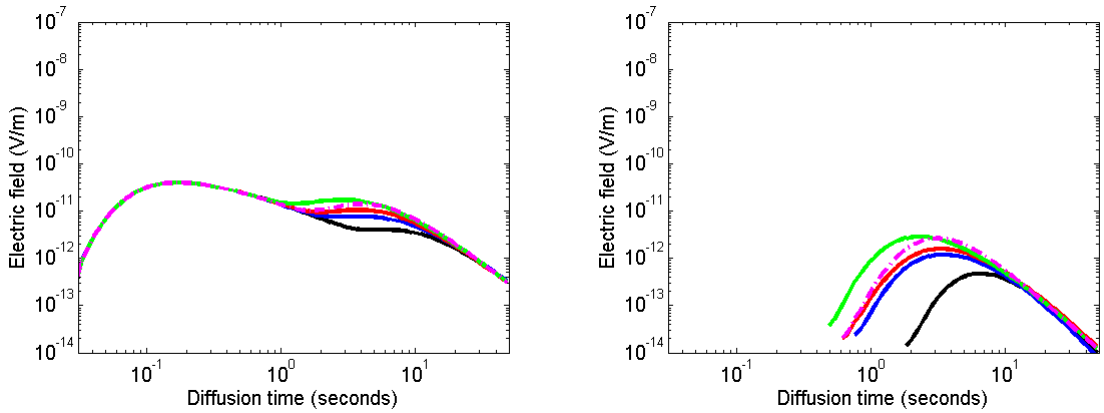

(g) E_x at x = 10 km (h) E_z at x= 10 km

Figure 8.11. Continued

8.2 Vertical electric-dipole source configuration

In this section, I examine a VED source configuration by comparing its responses with those of the HED source. The VED source is 200 m long, and its lower end-point is at the seafloor at x= 3 km. I follow the same analytical steps taken in Section 8.1. I first observe the animations of the electric fields for the four models and investigate the cross-sectional diffusion patterns in the electric fields excited by the VED source. Then, I relate the animations to the corresponding seafloor measurements.

8.2.1 Analysis of the electric fields on cross-sections

I start with the homogeneous seabed model (*figure8p12.mov;* Figure 8.12). First note that although the VED source is employed, the electric fields quickly become horizontal in the thin seawater column except in the vicinity of the VED source due to the interface condition associated wit the air-seawater interface (i.e. the continuity of the normal current density). In contrast to the electric fields excited by the HED source (*figure8p1.mov;* Figure 8.1), the maximum of the electric fields excited by the VED source does not remain close to the source location but diffuses downward in the seabed. This diffusion pattern suggests that the short-offset configuration would be useful for detecting galvanic responses to the reservoir, because the reservoir

responses would not be masked by the strong direct diffusion of the electric fields through the seawater in the vicinity of the VED source. This prediction will be confirmed in the next subsection, where seafloor electric-field measurements are examined. As the curl of the electric fields diffuses obliquely downward over time, the vertical component of the seafloor electric fields shows a sign reversal. The arrival time of the sign reversal depends on the source-receiver offset. Overall, compared with the HED source (*figure8p1.mov;* Figure 8.1), the maximum of the VED source migrates downward quickly.

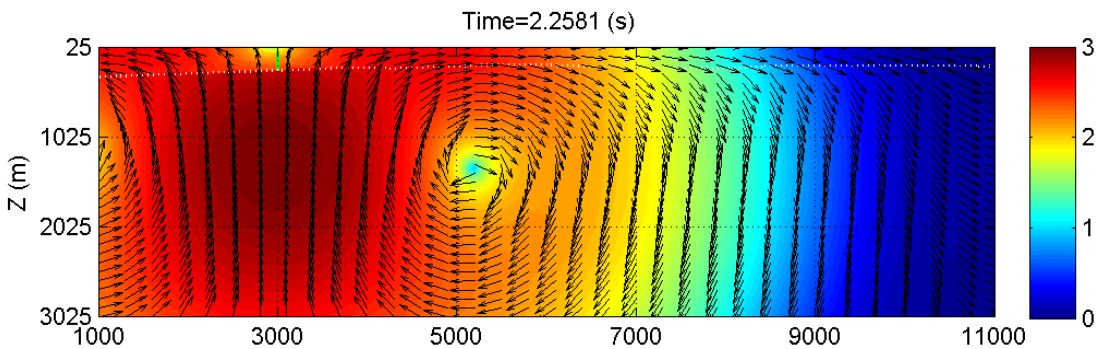

Figure 8.12. A snapshot of the animation showing the electric-field in the homogeneous seabed model. The snapshot is taken at 2.25 seconds after the VED source is excited. The animation file, *figure8p12.mov,* can be found on a companion CD.

Next, the reservoir is inserted into the homogeneous seabed model (*figure8p13.mov;* Figure 8.13). The electric fields that diffuse obliquely downward toward the left are not incident upon the reservoir. In contrast, those that diffuse obliquely downward toward the right are 'guided' through the reservoir at early time. The electric fields that diffuse directly below the source are also 'guided' through the reservoir. Note that the two 'guided' modes have different directions. Due to the strong 'guided' diffusion of the electric fields through the horizontal reservoir, the maximum of the electric fields no longer diffuses directly downward below the source. Since the high concentration of the electric fields does not remain in the vicinity of the source position, a short-offset VED-E_x and VED-E_z configurations would record measureable anomalous

responses when the configurations are directly above the reservoir and/or the salt. The usefulness of the short offset configurations will be discussed in detail later.

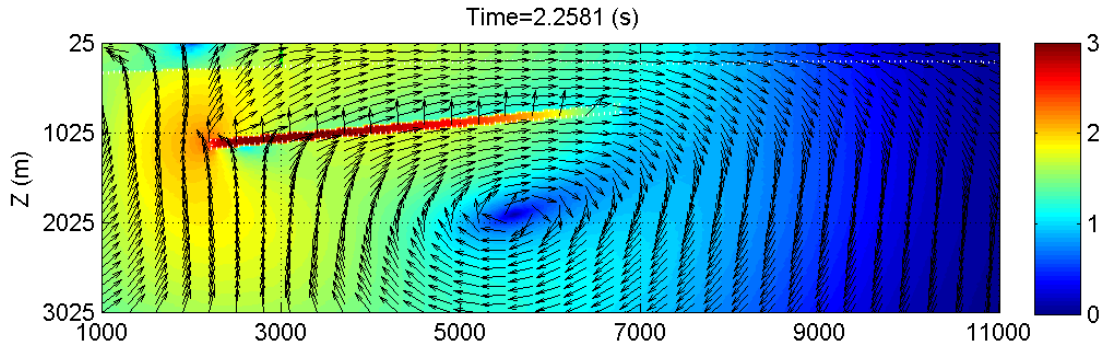

Figure 8.13. A snapshot of the animation showing the electric-field in the reservoir-only model. The snapshot is taken at 2.25 seconds after the VED source is excited. The animation file, *figure8p13.mov,* can be found on a companion CD.

Next, the reservoir is replaced with the salt (*figure8p14.mov;* Figure 8.14). The electric fields that diffuse obliquely downward toward the right are incident upon the seabed-salt interface and quickly diffuse through the salt. Some of the electric fields that diffuse directly downward the source also diffuse into the elongated part of the salt. Unlike the electric fields inside the thin reservoir, the electric fields are not effectively guided inside the thick salt. Consequently, as the electric fields diffuse inside the salt in the positive x-direction, geometric spreading decreases their amplitudes. Around the boundaries of the salt, the seabed electric fields develop parallel to the boundaries of the salt especially at late times. In short, although the salt does not support the 'guided' diffusion, the salt results in large enough perturbations in the transient electric fields for the detection.

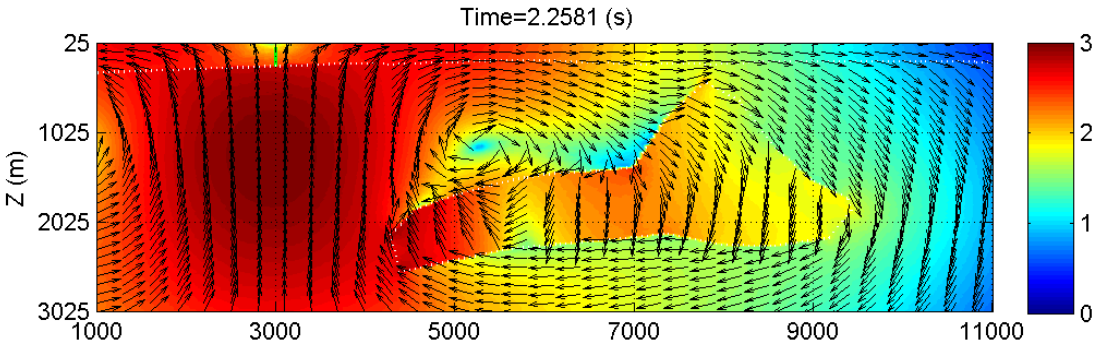

Figure 8.14. A snapshot of the animation showing the electric-field in the salt-only model. The snapshot is taken at 2.25 seconds after the VED source is excited. The animation file, *figure8p14mov,* can be found on a companion CD.

Finally, I consider the seabed model that includes both the reservoir and the salt (*figure8p15.mov;* Figure 8.15). The electric-field diffusion pattern at early times is somewhat similar to that of the reservoir-only model (*figure8p13.mov;* Figure 8.13). However, as the electric fields from the reservoir and the seabed start to interact with the salt, the electric fields on the cross-section no longer resemble *figure8p13.mov*. This animation also illustrates well the difference in the pattern of the electric fields between the 'guided' diffusion inside the thin reservoir and the 'unguided' diffusion inside the thick salt. Overall, the electric-field diffusion patterns excited by the VED source in the four seabed models are sufficiently different from each other. Seafloor electric-field measurements can distinguish among the four models as will be shown in the next subsection.

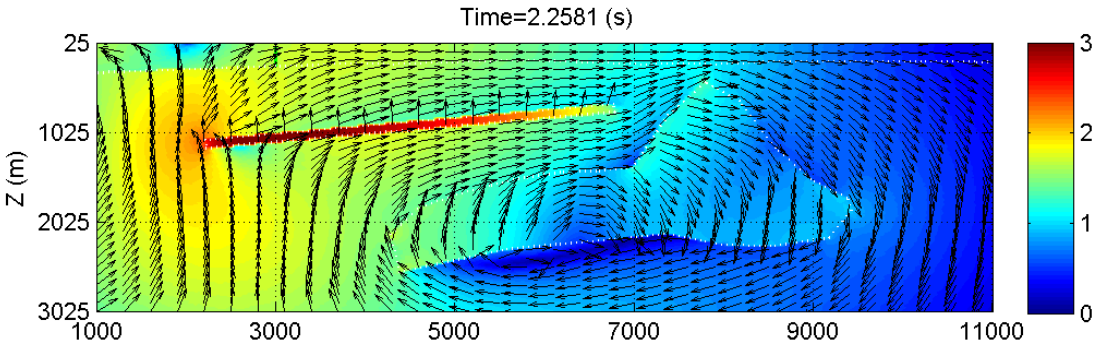

Figure 8.15. A snapshot of the animation showing the electric-field in the reservoir-and-salt model. The snapshot is taken at 2.25 seconds after the VED source is excited. The animation file, *figure8p15mov,* can be found on a companion CD.

8.2.2 Analysis of the electric fields at seafloor receivers

The seafloor E_x responses of the four models are shown in Figure 8.16. As expected, the E_x field differentiates the four models as the source-receiver offset increases. In fact, based on the principle of reciprocity, its sensitivity is also inferred from the HED-E_z configuration (Figure 8.6). However, the VED-E_x configuration seems more practical than the HED-E_z configuration since VED-E_x configuration requires accurate vertical positioning of only a single source. In contrast, the HED-E_z configuration requires accurate vertical positioning of entire array of electric-dipole receivers, as discussed in Section 8.1.2. The VED-E_x responses (Figure 8.16) are also more robust to the receiver tilt than the VED-E_z responses (Figure 8.17), because the latter are roughly an order of magnitude smaller than the former at intermediate and large offsets. The VED-E_x responses and the VED-E_z responses with and without receiver-tilt corrections are plotted in Figure 8.18, illustrating the robustness of the VED-E_x configuration to receiver tilt at larger offsets.

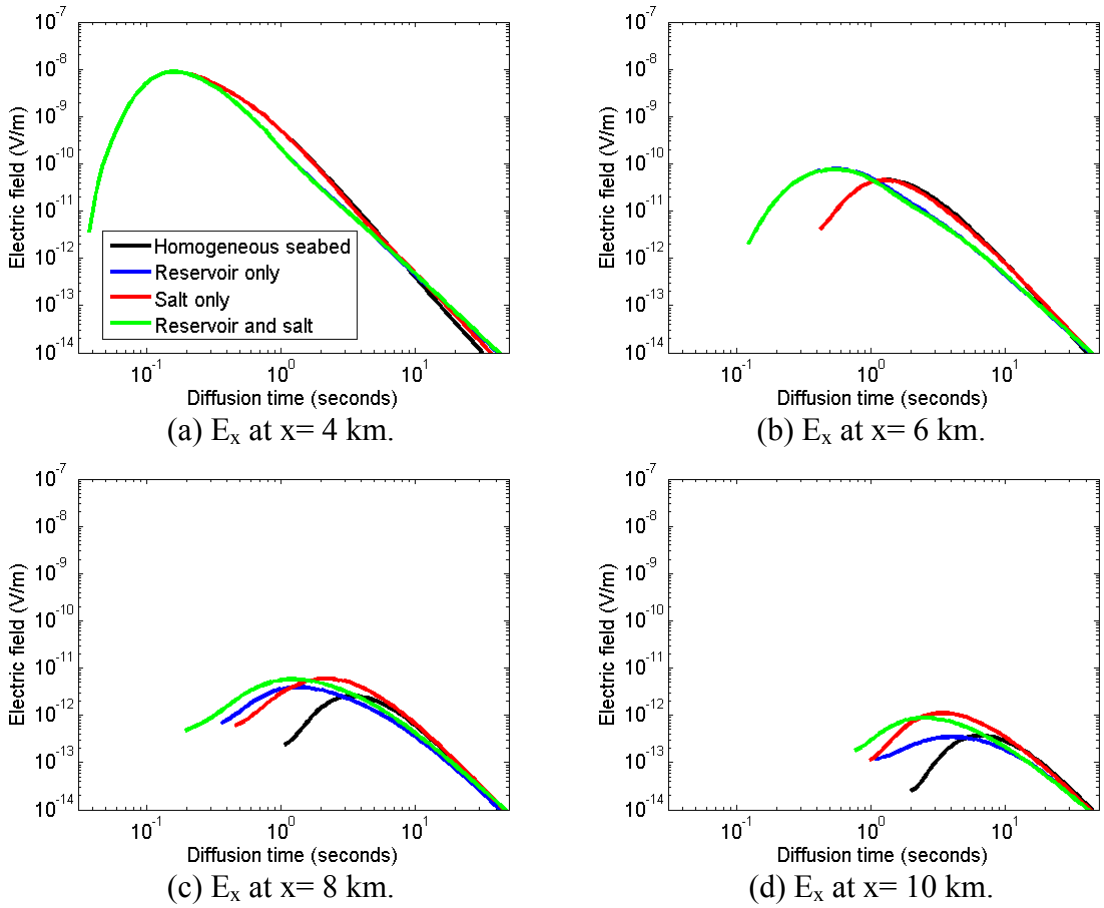

(a) E_x at x= 4 km. (b) E_x at x= 6 km.

(c) E_x at x= 8 km. (d) E_x at x= 10 km.

Figure 8.16. The seafloor E_x measurements over the four seabed models. The VED source is placed at x= 3 km.

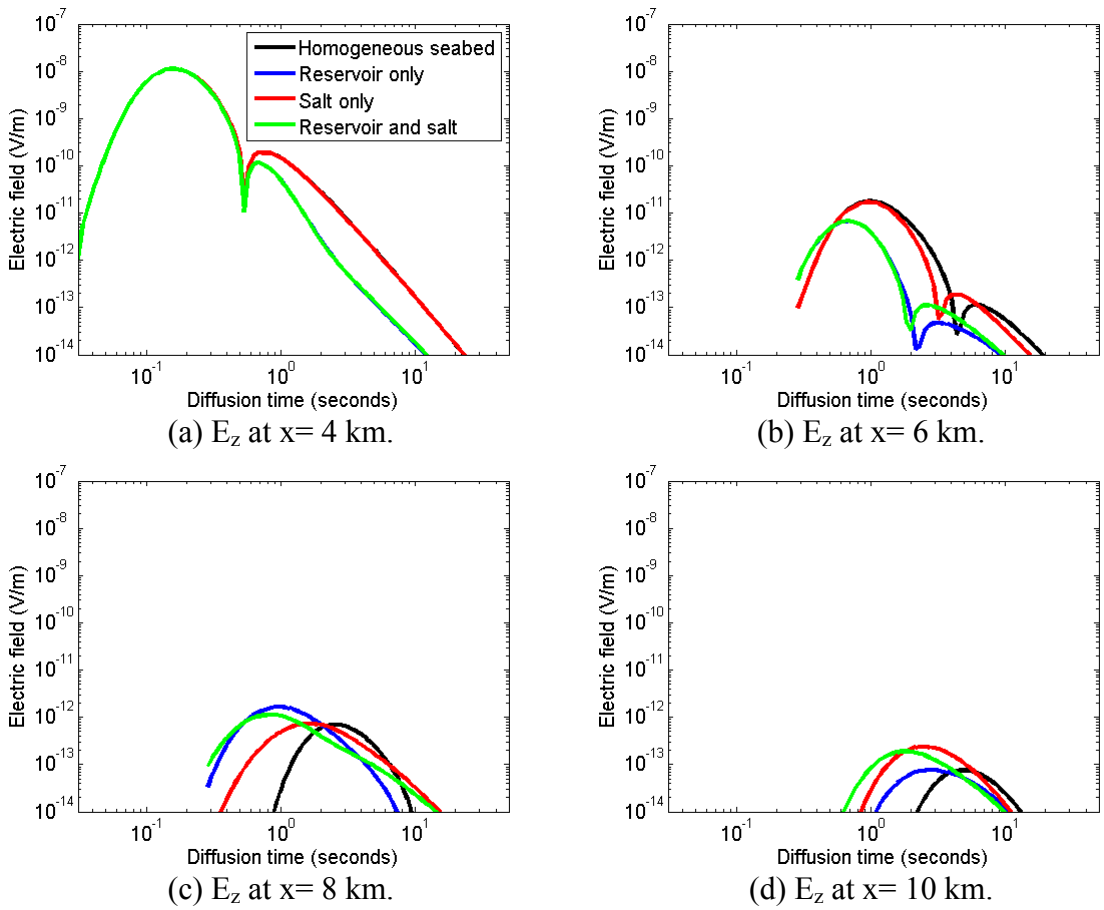

(a) E_z at x= 4 km. (b) E_z at x= 6 km.

(c) E_z at x= 8 km. (d) E_z at x= 10 km.

Figure 8.17. The seafloor E_z measurements over the four seabed models. The VED source is placed at x= 3km. The E_z measurements are not plotted at the early time (i.e. 10^{-2} to 10^{-1} seconds) in (b), (c) and (d) due to numerical noise.

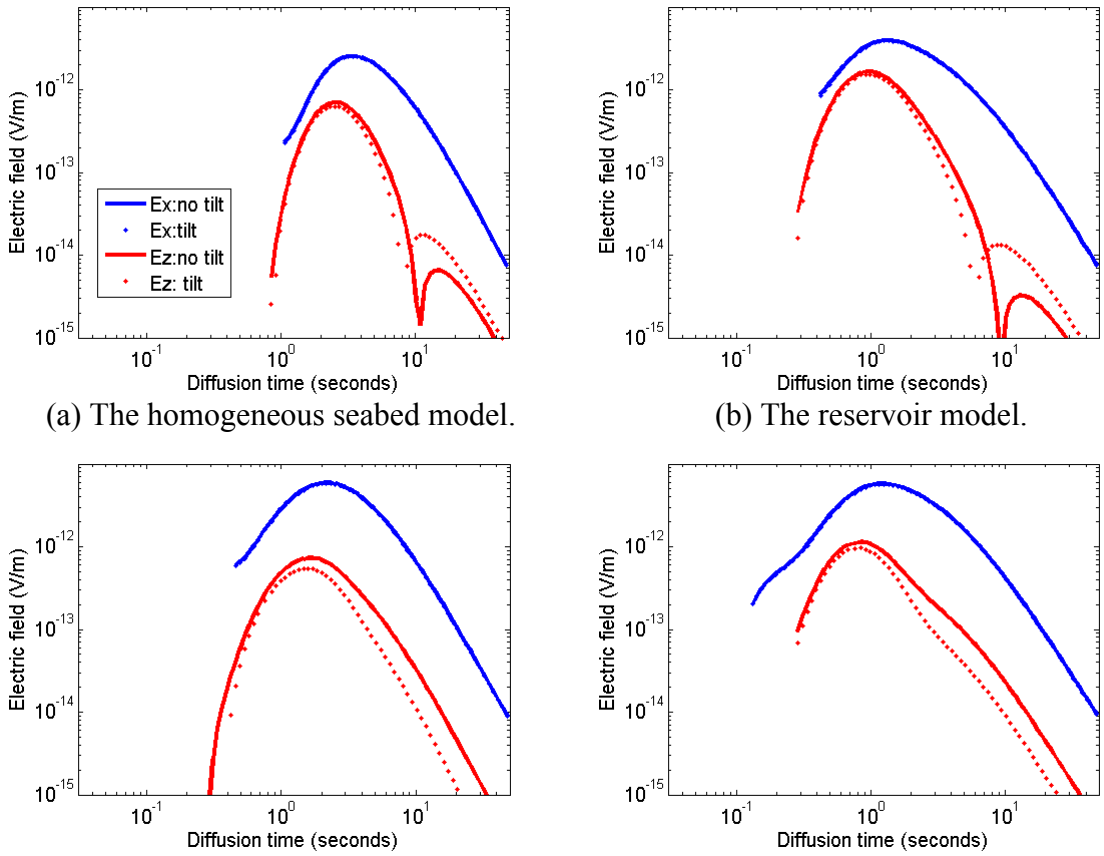

(a) The homogeneous seabed model. (b) The reservoir model.

(c) The salt model. (d) The reservoir-and-salt model.

Figure 8.18. The seafloor electric-field measurements at x= 8 km with and without receiver-tilt corrections. The VED source is placed at x= 3 km.

At intermediate-to-large offsets, both HED-E_x (Figure 8.5) and VED-E_x (Figure 8.16) configurations effectively record the reservoir effect (i.e. the 'guided' diffusion from the reservoir). However, except at 1 km offset, the HED-E_x configuration produces larger responses than those of the VED-E_x configuration. Therefore, I conclude that in the given offshore environment, the HED-E_x configuration with intermediate-to-long offsets is a practical choice to measure the 'guided' diffusion.

As shown in Figures 8.16 and 8.17, the VED-E_x and VED-E_z configurations can sense the reservoir not only at intermediate-to-large offsets, but also at short offsets (e.g. 1 km offset). The sensitivity is mainly related to the galvanic effects when the vertical currents are normally incident upon the reservoir (Cuevas et al., 2010). In this study, I examine the usefulness of the short-offset VED configurations for mapping the boundaries of the 3D reservoir. To do this, I compute the 1-km-offset VED-E_x (Figure 8.19) and VED-E_z (Figure 8.20) responses along the survey line (Figure 7.2a) over the four seabed models.

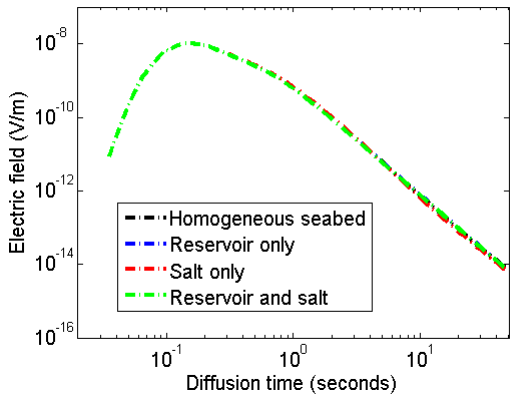

(a) (VED position in the x axis, E_x receiver position in the x axis) = (1 km, 2 km).

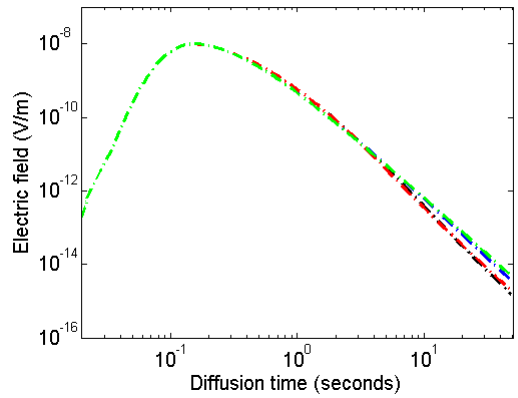

(b) (2 km, 3 km).

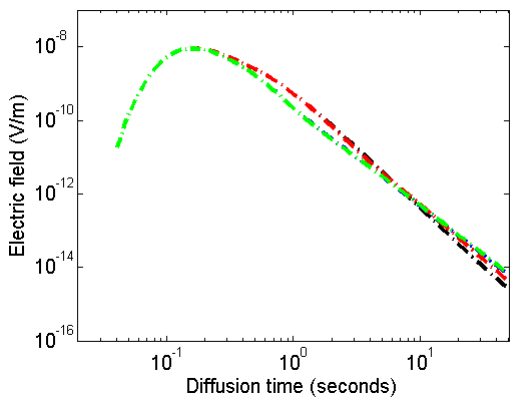

(c) (3 km, 4 km).

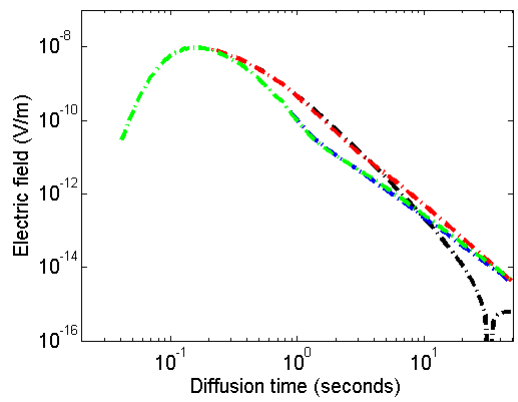

(d) (4 km, 5 km).

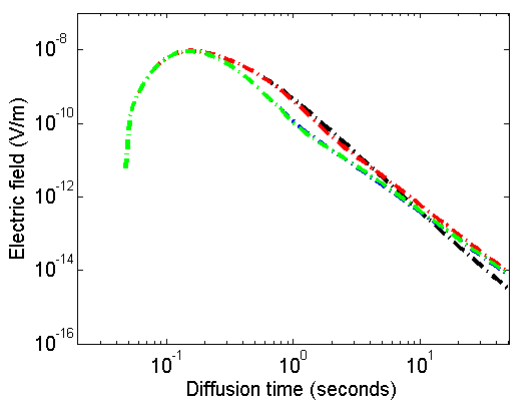

(e) (5 km, 6 km).

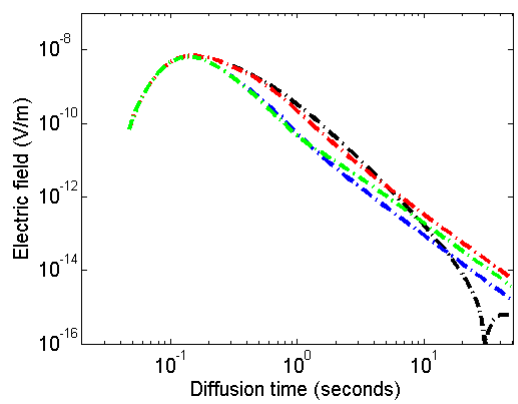

(f) (6 km, 7 km).

Figure 8.19. The short-offset VED- E_x responses at multiple positions over the four seabed models. The offset is set to 1 km.

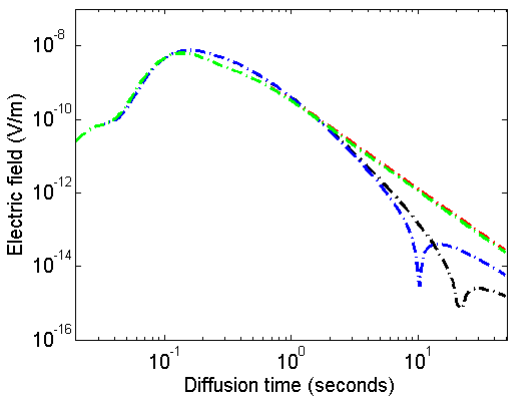

(g) (7 km, 8 km).

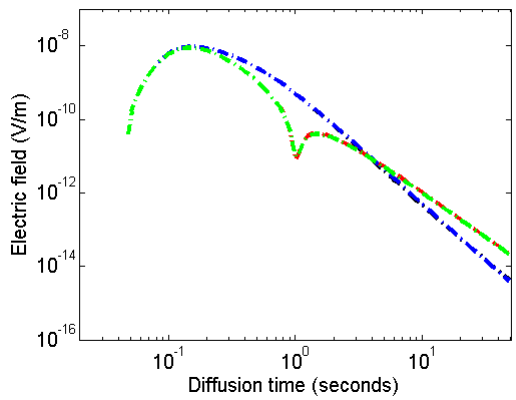

(h) (8 km, 9 km).

Figure 8.19. Continued.

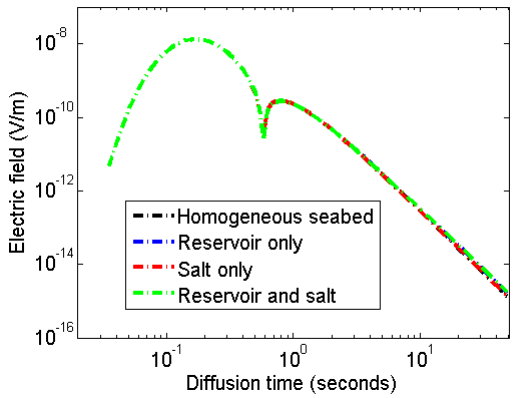

(a) (VED position in the x axis, E_z receiver position in the x axis) = (1 km, 2 km).

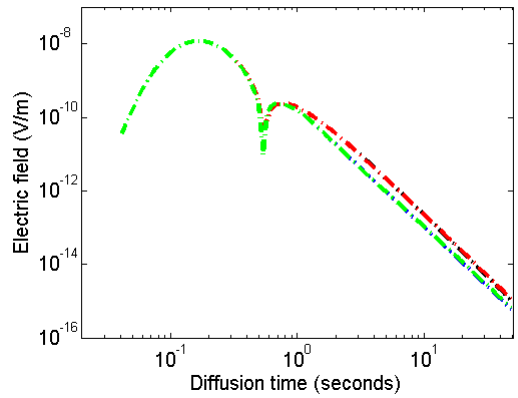

(b) (2 km, 3 km).

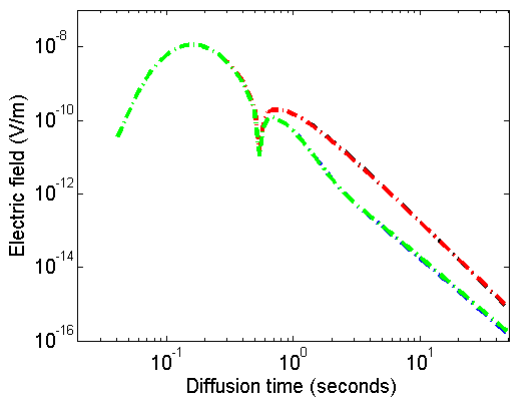

(c) (3 km, 4 km).

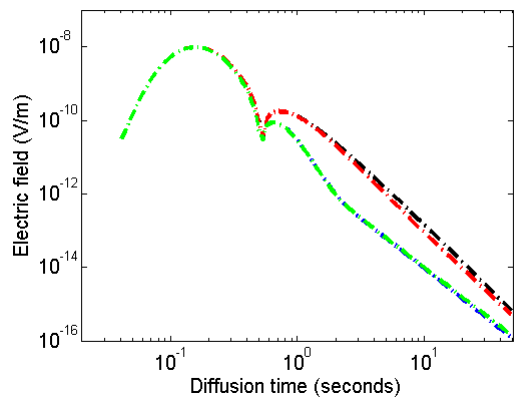

(d) (4 km, 5 km).

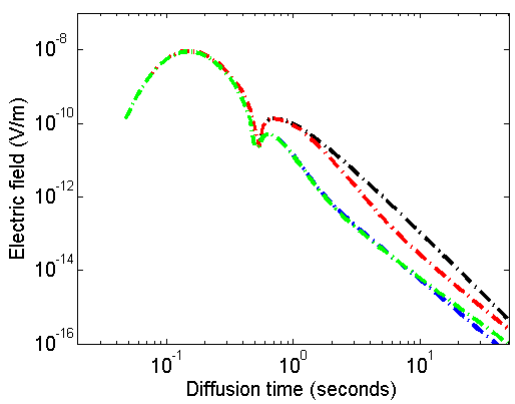

(e) (5 km, 6 km).

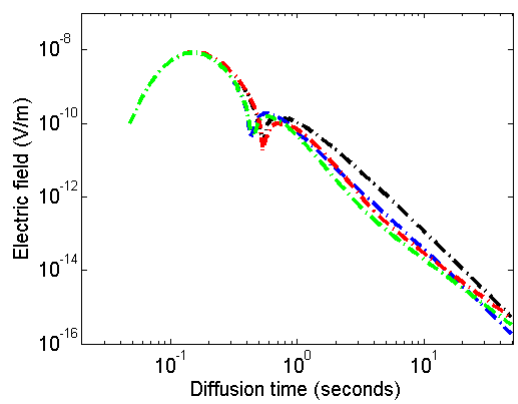

(f) (6 km, 7 km).

Figure 8.20. The short-offset VED- E_z responses at multiple positions over the four seabed models. The offset is set to 1 km.

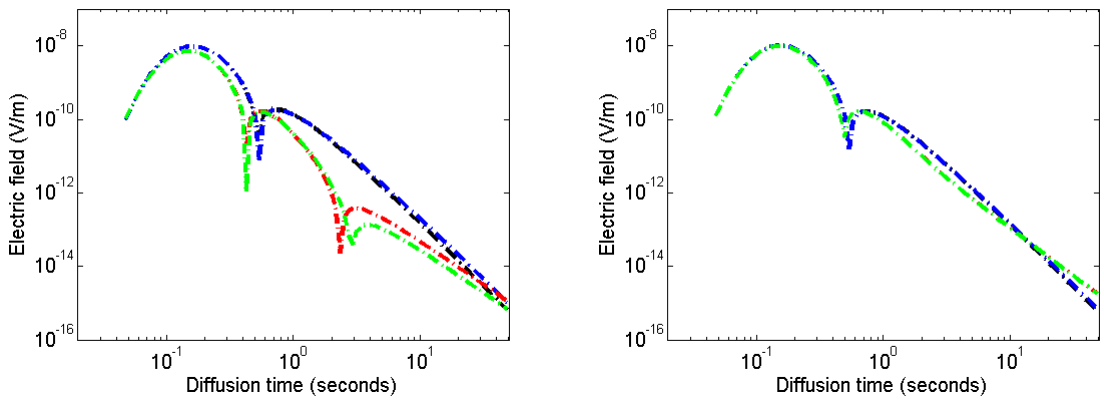

(g) (7 km, 8 km). (h) (8 km, 9 km).

Figure 8.20. Continued.

First, I compare the VED-E_x responses of the homogeneous seabed model and the reservoir model. When there is no reservoir directly below the source, the two models produce approximately the same responses (Figures 8.19a 8.19b and 8.19h). However, as the source is directly above the reservoir, the reservoir responses start to deviate from the homogeneous seabed (Figures 8.19c through 8.19g); the shallower the reservoir is, the earlier the deviation starts. Therefore, the VED-E_x responses can provide insights into the lateral extent and depth of the reservoir.

Second, I extend the comparison to the other two seabed models. The VED-E_x responses also sense the lateral extent and depth of the salt unless the salt is directly below the reservoir. In such a case, the reservoir effectively blocks the flow of the vertical electric fields toward the salt, and the anomalous galvanic effects resulting from the salt become negligible. Therefore, the VED-E_x responses become blind to the salt directly below the reservoir, showing the limitation.

Next, I examine the VED-E_z responses (Figure 8.20). The VED-E_z responses also sense the presence of the reservoir and the salt. Compared with the VED-E_x responses (Figure 8.19), the VED-E_z responses show a little bit enhanced sensitivity to the reservoir and the salt. For example, when the VED source and the receiver are placed at x = 3 and 4 km, respectively, the VED-E_z responses (Figure 8.20c) sense the reservoir more clearly than the VED-E_x responses. The VED-E_z responses show a consistent sign reversal at around 0.6 seconds. As mentioned in the previous sub-

section (8.2.1), this sign reversal is the direct result of the curl of the electric field that diffuses obliquely downward on the cross-section (Figures 8.12 through 8.15).

In contrast to the expected sign reversals shown in the VED-E_z responses (Figure 8.20), unusual sign reversals are observed in the VED-E_x responses (Figure 8.19) at late times. For example, the homogeneous seabed model shows a sign reversal at late times at receiver positions at x= 5, 7 and 8 km (Figures 8.19d, 8.19f and 8.19g). Because the homogeneous flat seafloor model produces no sign reversal, it can be inferred that the sign reversal may come from the 3D seafloor topography.

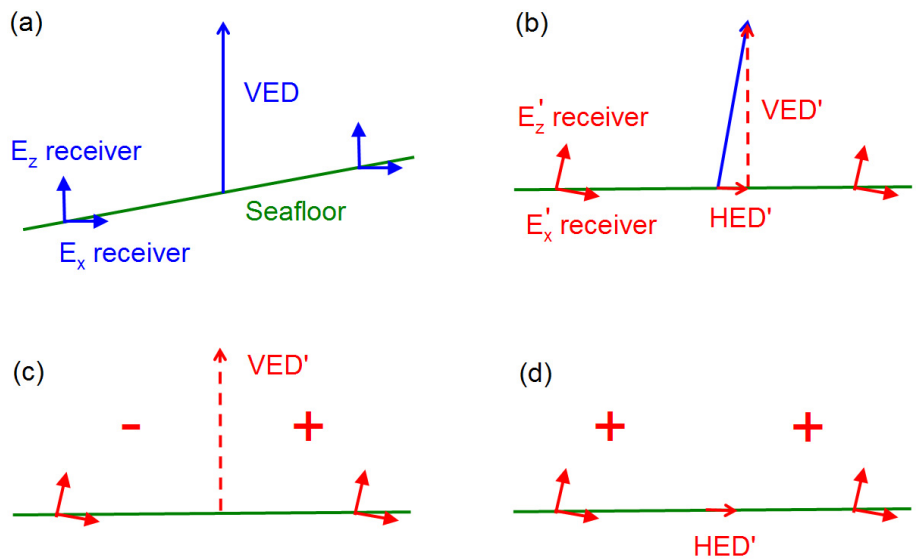

Figure 8.21. The geometric analysis of the VED-E_x configuration on the 2D sloping seafloor. (a) The VED source on the 2D sloping seafloor. The arrow of the VED source indicates the source polarization. (b) The clock-wise rotation of Figure 8.21a by the angle of the slope. The VED source is decomposed into the VED' and HED' sources. (c) The VED' source on the flat seafloor. - and + indicates the E_x direction in the left and right side of the VED' source (d) The HED' source on the flat seafloor.

The detail of the sign reversal is the effect of the sloping seafloor on the VED source that is no longer normal to the seafloor. To illustrate the effect, I consider a VED source on a simple 2D sloping seafloor model (Figure 8.21a). As the VED source is oblique to the seafloor, Figure 8.21a can be rotated clockwise by the angle of the slope. The seafloor becomes flat. The VED source is decomposed into the VED' and HED' sources (Figure 8.21b). Accordingly, the constructive and destructive interaction of the VED' and HED' fields explains the sign reversal.

For example, sometime after the VED' source is turned off, the direction of the electric field at the $E_x^{'}$ receivers in the left and right side of the VED' source are negative and positive, respectively (Figure 8.21c). In contrast, when the HED' source is turned off, the direction of the electric field at the two $E_x^{'}$ receivers is positive (Figure 8.21d). Therefore, the sign reversal of the $E_x^{'}$ receiver can be observed in the left side of the VED source (i.e. toward the sloping direction). On the other hand, both VED' and HED' fields are constructively superposed in the $E_z^{'}$ direction. Therefore, the $E_z^{'}$ receivers do not record a sign reversal related to the slope.

The sign reversal of the $E_x^{'}$ receiver (or E_x receiver in the original coordinate) usually occurs at late time as shown in Figure 8.19. To explain this, I review the electric field diffusion pattern discussed in the previous section. The electric field maximum of the VED' source diffuses outward from the source position over time. In contrast, the electric field maximum of the HED' source remains close to the source position over time. Therefore, although a gently-sloping seafloor (e.g. 2 degrees) produces a large VED' source and a small HED' source, the $E_x^{'}$ field of the HED' source can exceed that of VED' source at a short offset at late time. The sign reversal occurs.

Figure 8.22 shows 1 km-offset VED-E_x and VED-E_z responses to the homogeneous seafloor model at multiple VED positions along the survey line (Figure 7.2a). The responses are plotted at two receivers. One receiver is 1 km apart from a given VED source in the left direction (- x direction). The other one is also 1 km apart from the VED source in the right direction (+ x direction). Table 8.1 shows the average slope

angle at each VED position and its direction. By comparing Figure 8.22 with Table 8.1, it is clear that the VED-E_x responses consistently show a sign reversal in the sloping direction.

As the final note, the modeling analysis above illustrates that the VED-E_x responses is very sensitive to a subtle change of the seafloor topography. For example, the sloping seafloor of 0.5 degrees can result in a sign reversal in late-time VED-E_x responses (Figures 8.19d and 8.22c). Therefore, unless the seafloor topography is measured and modeled very accurately, the VED-E_x responses would be prone to measurement and modeling errors at short offsets. In contrast, as shown in Figure 8.22, the VED-E_z responses are robust to a subtle change of the seafloor topography and can be considered practical.

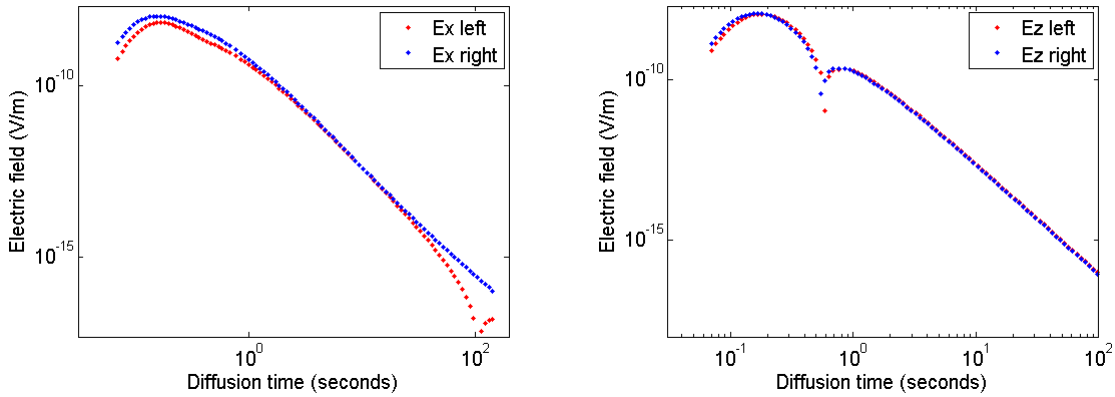

(a) VED at x = 2 km and receiver at x = 1 (left) and 3 km (right)

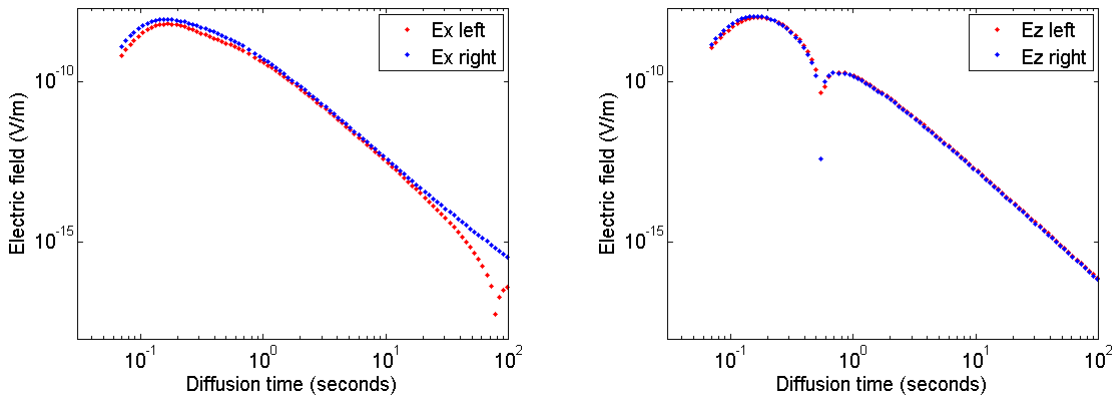

(b) VED at x = 3 km and receiver at x = 2 (left) and 4 km (right)

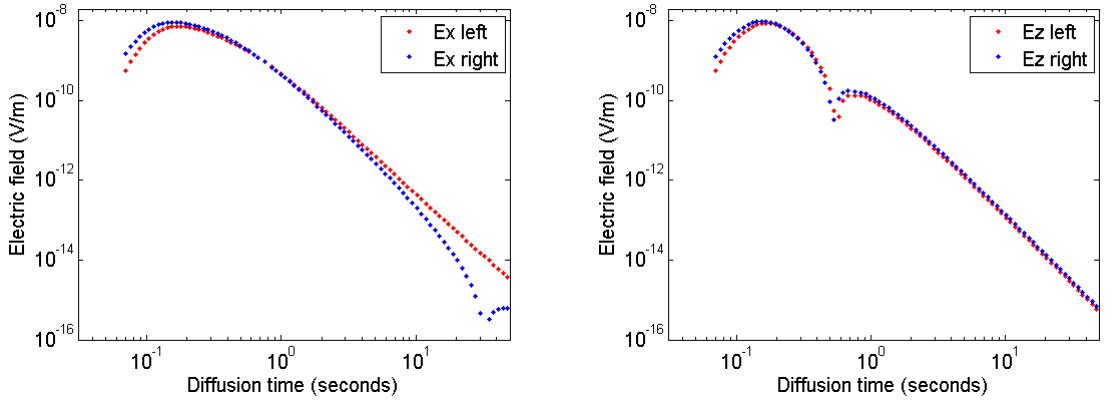

(c) VED at x = 4 km and receiver at x = 3 (left) and 5 km (right)

Figure 8.22. The VED-E_x (the left column) and the VED-E_z (the right column) responses to the homogeneous seafloor model. The E_x and E_z components are plotted at two receivers that are 1 km apart from each VED source in the left and right direction along the survey line.

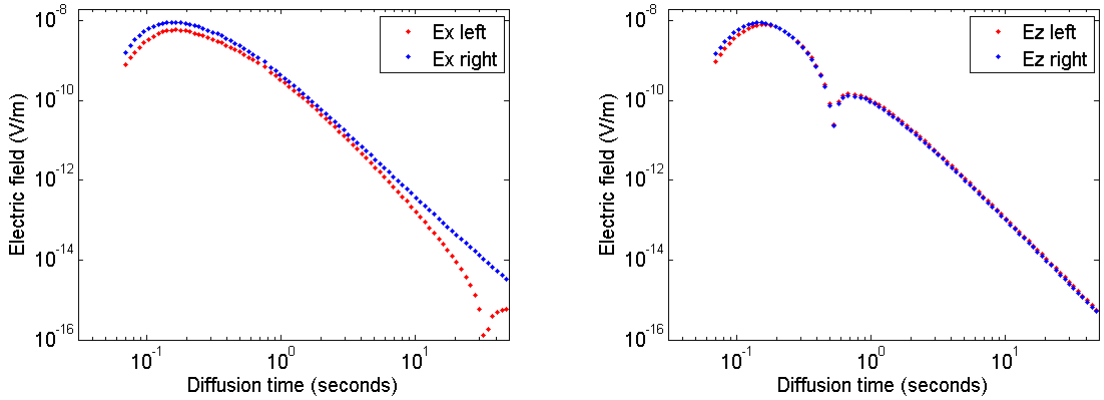

(d) VED at x = 5 km and receiver at x = 4 (left) and 6 km (right)

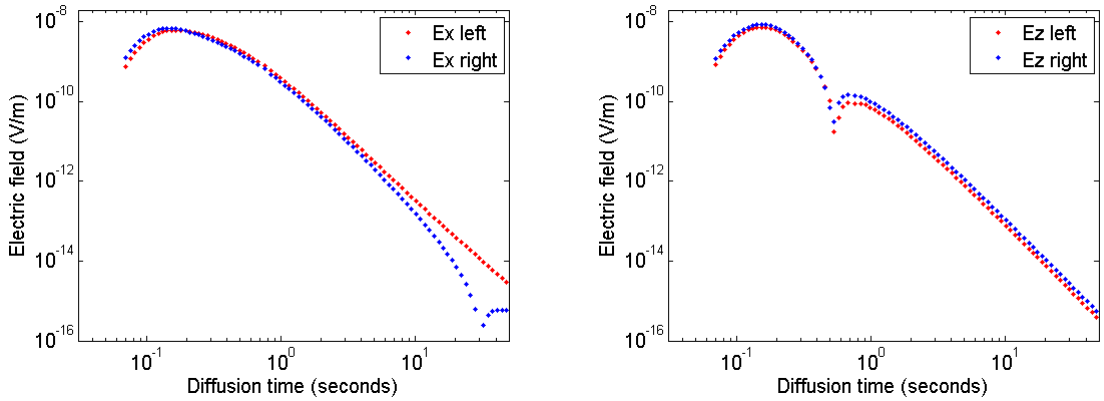

(e) VED at x = 6 km and receiver at x = 5 (left) and 7 km (right)

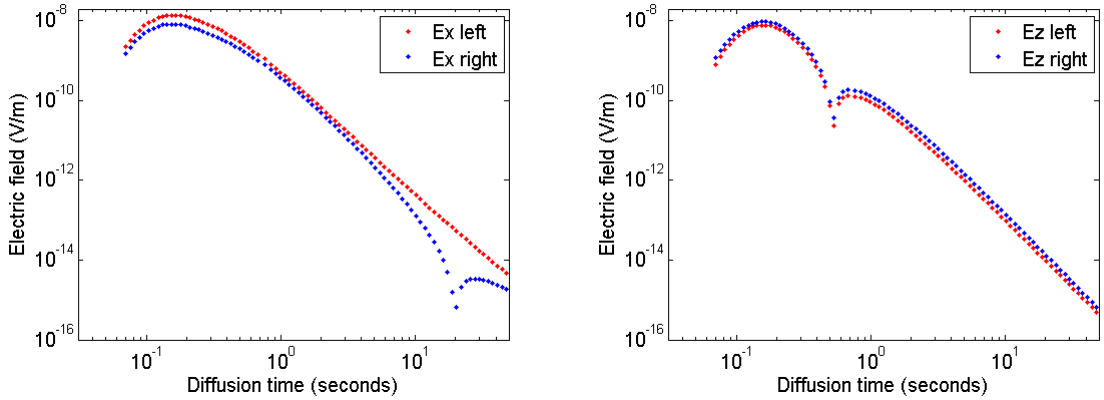

(f) VED at x = 7 km and receiver at x = 6 (left) and 8 km (right)

Figure 8.22. Continued.

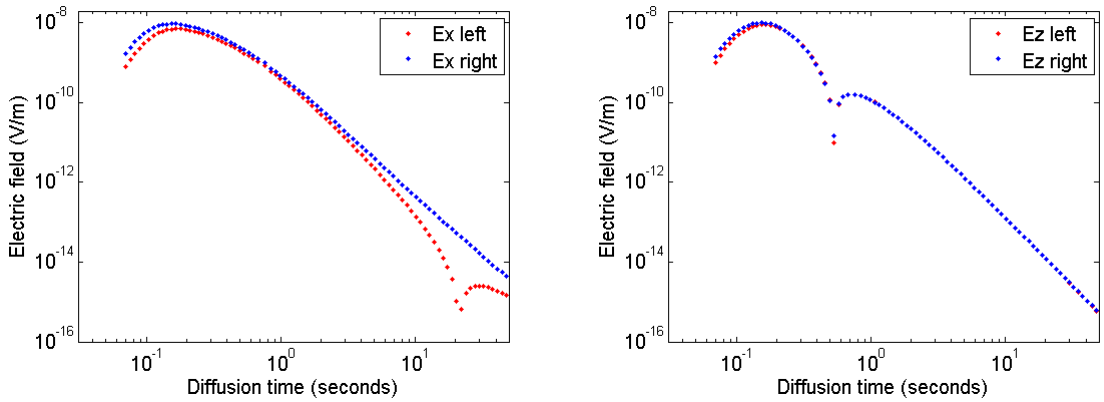

(g) VED at x = 8 km and receiver at x = 7 (left) and 9 km (right)

Figure 8.22. Continued.

VED at x =	2 km	3 km	4 km	5 km	6 km	7 km	8 km
Slope angle (direction)	2° (left)	2° (left)	0.5° (right)	2° (left)	2° (right)	2° (right)	2° (left)

Table 8.1. The average slope angle and the direction at each VED source position along the survey line (Figure 7.2a). The left and right directions indicate the negative and positive x-direction along the survey line.

8.3 Effects of a vertically anisotropic seabed

So far, I have analyzed the TDCSEM responses of isotropic seabed models. In this section, I consider modeling scenarios where a background seabed has vertical anisotropy (i.e. transverse isotropy). This type of anisotropy is commonly encountered in offshore environments, since layered seabed sequences can produce electrical anisotropy on a macroscopic scale (Keller, 1987). In this section, I employ electric-field animations for an anisotropic seabed with and without the reservoir, compare them with their isotropic counterparts, and explain the effects of the vertical anisotropy on the TDCSEM method.

First, I start with the HED source. I compare the animations of the homogeneous isotropic seabed model (*figure8p1.mov*; Figure 8.1) with its anisotropic counterparts (*figure8p23.mov*; Figure 8.23). The horizontal (ρ_h) and vertical (ρ_v) resistivities of the anisotropic seabed are set to 0. 7 Ω-m and 3.5 Ω-m, respectively (Tompkins, 2005), which result in the coefficient of anisotropy, $\lambda = \sqrt{\rho_v / \rho_h} = 2.23$. Because this anisotropic seabed is more conductive in the horizontal direction than in the vertical direction, the electric fields (*figure8p23.mov*; Figure 8.23) develop and diffuse more horizontally than its isotropic counterpart (*figure8p1.mov*; Figure 8.1). Thus, the anisotropic seabed produces a larger background response along the seafloor than the isotropic seabed. Moreover, the vertical electric fields of the anisotropic seabed develop less effectively than those of the isotropic seabed.

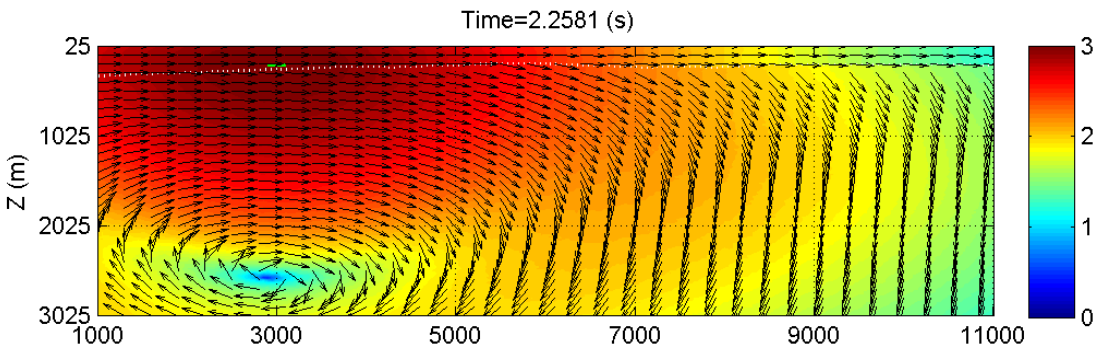

Figure 8.23. A snapshot of the animation showing the electric-field in the homogeneous anisotropic-seabed model (λ = 2.23). The snapshot is taken at 2.25 seconds after the HED source is excited. The animation file, *figure8p23.mov*, can be found on a companion CD.

Second, we insert the reservoir into the anisotropic seabed and compare the resulting electric-field systems (*figure8p24.mov*; Figure 8.24) with their isotropic counterparts (*figure8p2.mov*; Figure 8.2). The 'guided' diffusion through the reservoir is observed slightly earlier in the anisotropic model (*figure8p24.mov*; Figure 8.24) than in the isotropic model (*figure8p2.mov*; Figure 8.2), because in the anisotropic model, the electric fields diffuse faster in the positive x-direction where the reservoir is shallow. The magnitude of the 'guided' diffusion in the anisotropic model is smaller than that in

the isotropic model, because 1) the anisotropic model has a smaller vertical resistivity contrast across the reservoir than the isotropic model, and 2) the vertical electric fields of the anisotropic model are relatively weaker than those of the isotropic model. Therefore, the TDCSEM method can lose its sensitivity to the reservoir in the anisotropic background seabed, because the strong background response masks the weak 'guided'-diffusion effect.

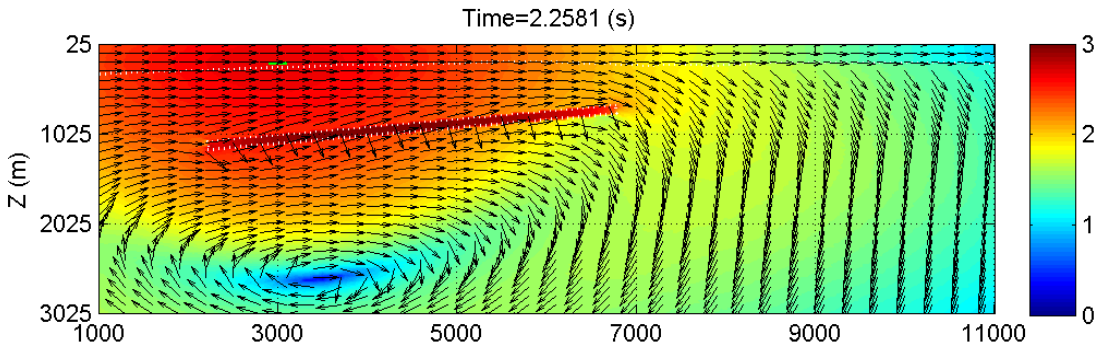

Figure 8.24. A snapshot of the animation showing the electric-field in the reservoir-only anisotropic-seabed model (λ = 2.23). The snapshot is taken at 2.25 seconds after the HED source is excited. The animation file, *figure8p24.mov*, can be found on a companion CD.

The observations discussed above help us to interpret characteristics of seafloor measurements. First, we compare seafloor HED- E_x responses from homogeneous, isotropic (λ=1) and homogeneous, anisotropic (λ=2.23) seabed models (Figure 8.25). An additional model with a coefficient of anisotropy (λ = 1.58 with ρ_h = 0. 7 Ω-m and ρ_v = 1.75 Ω-m) is used to generate intermediate responses between the two seabed models previously discussed. As expected, the second peaks (i.e. the seabed responses) of the HED- E_x responses gradually increase with the coefficient of anisotropy. Therefore, the HED- E_x responses closely resemble the HED- E_x responses to the isotropic seabed models that have the reservoir and/or the salt (Figure 8.5). This comparison demonstrates that special care should be taken not to misinterpret a homogenous anisotropic model as an isotropic seabed model with a resistor. To avoid this misinterpretation, it is helpful to notice that the short-offset HED- E_x

measurements are sensitive to the different coefficients of vertical anisotropy (Figure 8.25a) but relatively insensitive to the reservoir (Figure 8.5a). As a side note, broadside data can also be useful to identify and analyze anisotropy problems (Eidesmo et al., 2002).

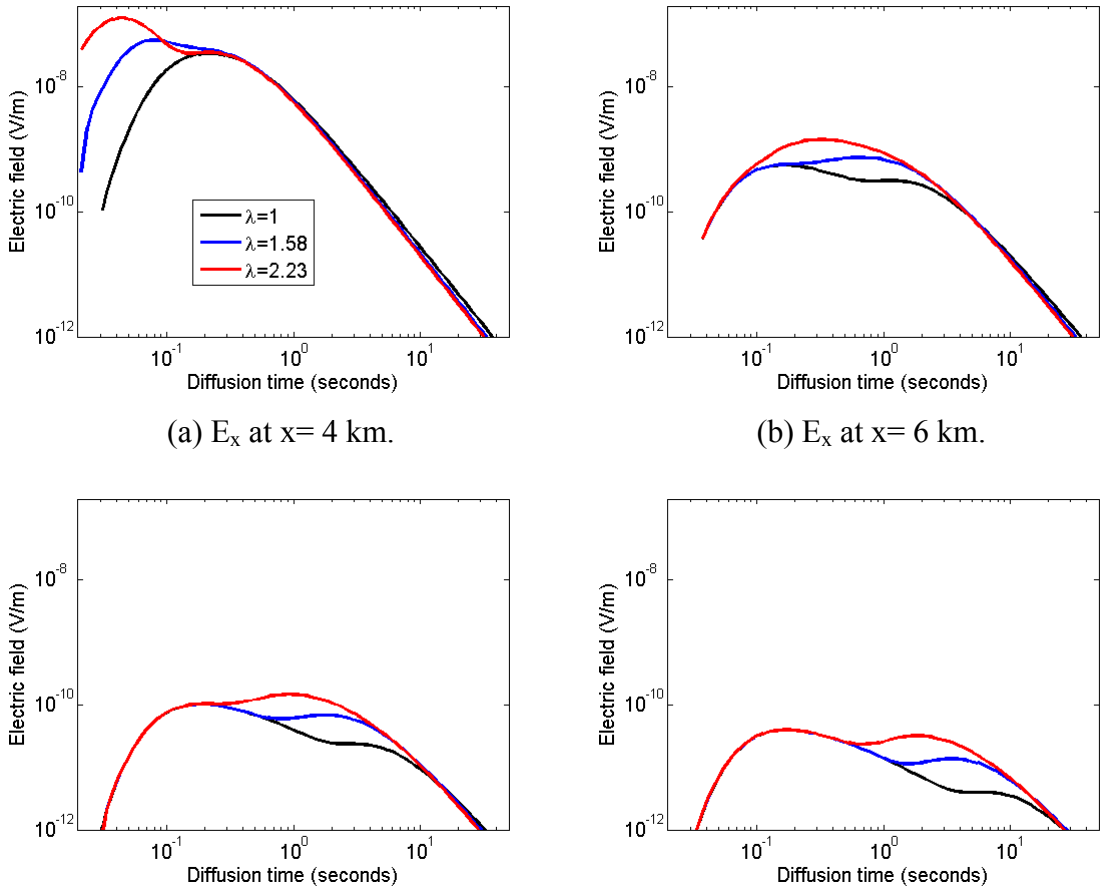

(a) E_x at x= 4 km. (b) E_x at x= 6 km.

(c) E_x at x= 8 km. (d) E_x at x= 10 km.

Figure 8.25. The seafloor E_x measurements over the three homogeneous seabed models. The HED is placed 50 m above the seafloor at x= 3 km.

Second, I compare the seafloor HED-E_x responses of the four anisotropic seabed models. The responses for λ = 1.58 and 2.23 are plotted in Figures 8.26 and 8.27, respectively. As expected from the electric-field animations, the sensitivity of the HED-E_x configuration to the reservoir and the salt gradually decreases as the

coefficient of anisotropy increases. I also confirm that the HED-E_x configuration senses the reservoir earlier in the anisotropic seabed (e.g. Figure 8.27d) than in the isotropic seabed (e.g. Figure 8.5d).

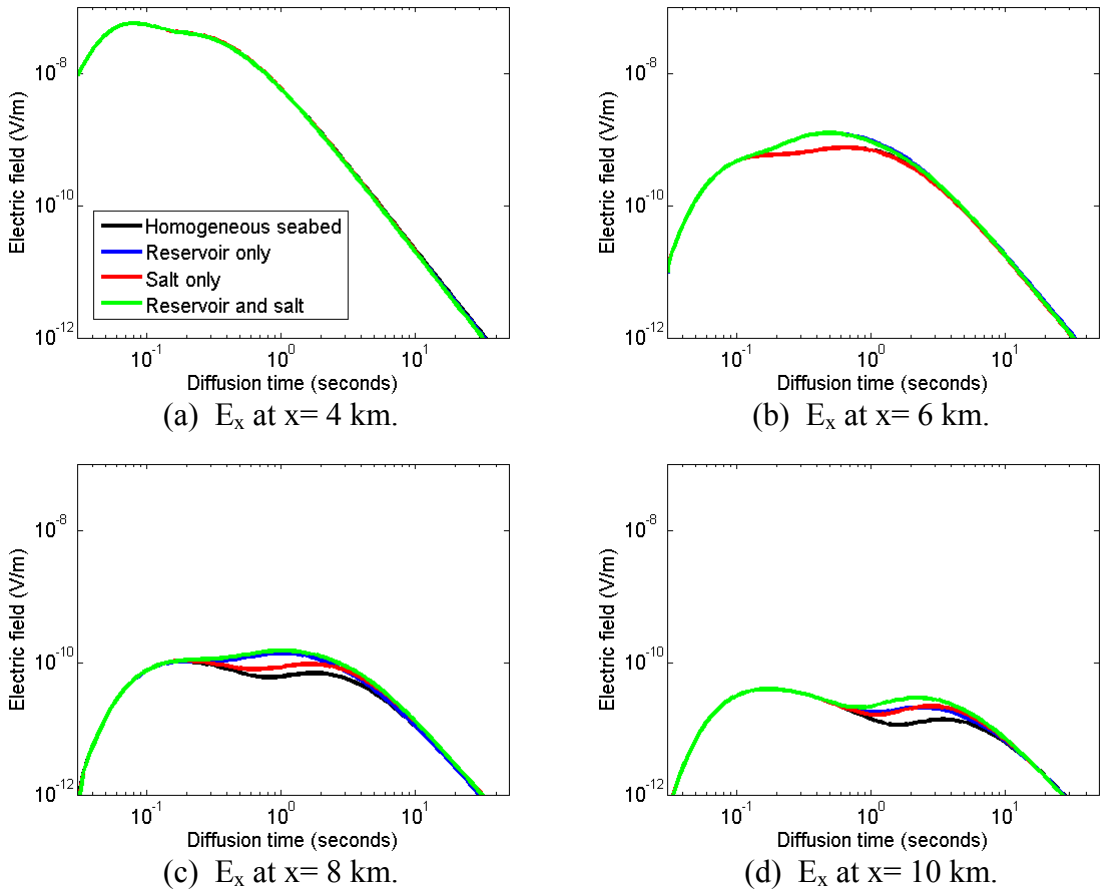

Figure 8.26. The seafloor E_x measurements over the three anisotropic seabed models. The anisotropy coefficient λ for the background seabed is set to 1.58. The HED is placed 50 m above the seafloor at x= 3 km.

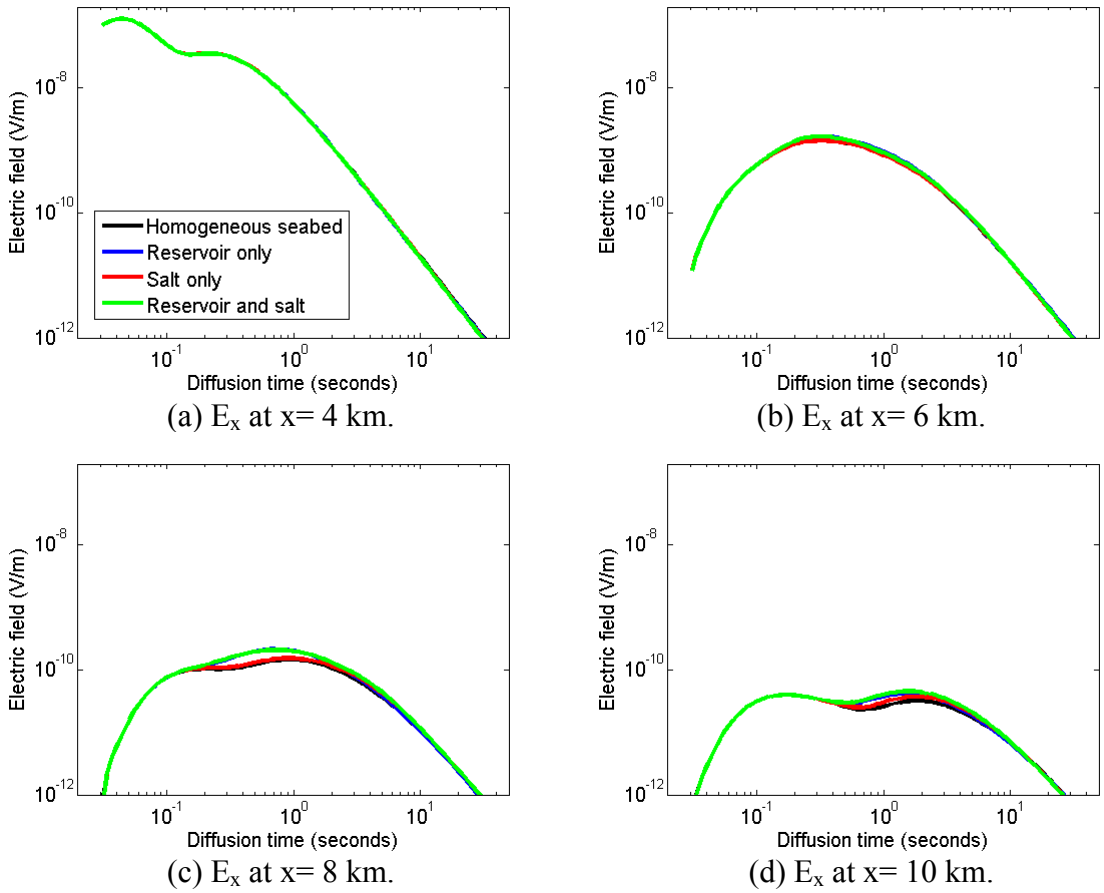

(a) E_x at x= 4 km. (b) E_x at x= 6 km.

(c) E_x at x= 8 km. (d) E_x at x= 10 km.

Figure 8.27. The seafloor E_x measurements over the three anisotropic seabed models. The anisotropy coefficient λ for the background seabed is set to 2.23. The HED is placed 50 m above the seafloor at x= 3 km.

Next, I compare the animation of the electric fields between the isotropic homogeneous seabed model and the anisotropic (λ=2.23) homogeneous seabed model (*figure8p28.mov;* Figure 8.28) when the VED source is employed. The effects of the anisotropy on the electric fields excited by the VED source are basically the same as those observed with the HED source in *figure8p23.mov* and Figure 8.23. The electric fields develop and diffuse more horizontally than its isotropic counterpart. The vertical electric fields develop less efficiently. The vertical resistivity contrast across the seabed-reservoir interface decreases. As a result, when the reservoir is inserted into the anisotropic seabed (*figure8p29.mov;* Figure 8.29), the observed 'guided' diffusion

through the reservoir decreases compared with its isotropic counterpart (*figure8p13.mov;* Figure 8.13).

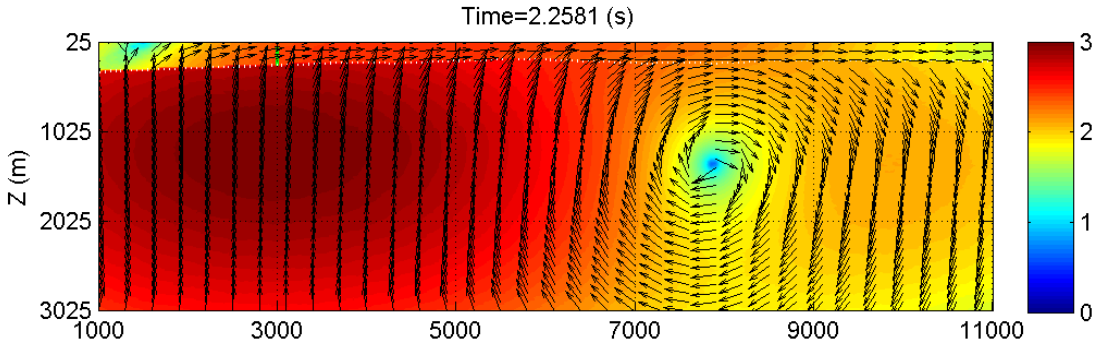

Figure 8.28. A snapshot of the animation showing the electric-field in the homogeneous anisotropic-seabed model (λ = 2.23). The snapshot is taken at 2.25 seconds after the VED source is excited. The animation file, *figure8p28.mov*, can be found on a companion CD.

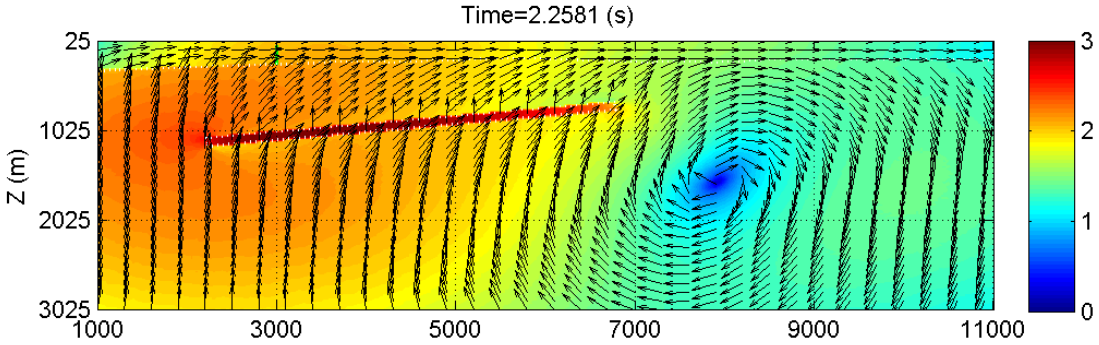

Figure 8.29. A snapshot of the animation showing the electric-field in the reservoir-only anisotropic-seabed model (λ = 2.23). The snapshot is taken at 2.25 seconds after the VED source is excited. The animation file, *figure8p29.mov*, can be found on a companion CD.

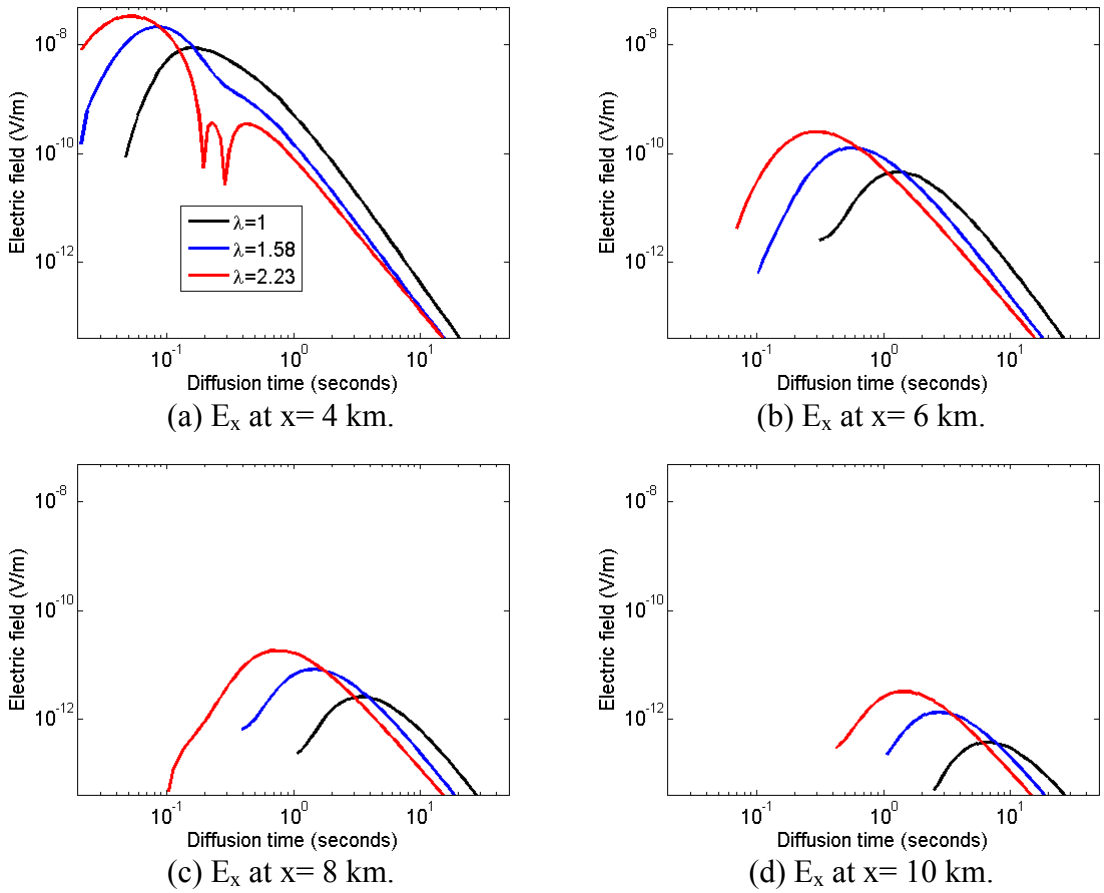

(a) E_x at x= 4 km. (b) E_x at x= 6 km.

(c) E_x at x= 8 km. (d) E_x at x= 10 km.

Figure 8.30. The seafloor E_x measurements over the three homogeneous seabed models. The VED is placed 50 m above the seafloor at x= 3 km.

Figure 8.30 shows seafloor VED-E_x responses to the homogeneous seafloor models whose λ varies from 1 to 2.23. As expected, the VED-E_x responses to the anisotropic seabed somewhat resemble those to the isotropic seabed that includes the reservoir and/or the salt (Figure 8.16). As expected from the animations, the sensitivity of the VED-E_x configuration to the reservoir and the salt gradually decreases as the coefficient of anisotropy increases (Figures 8.31 and 8.32).

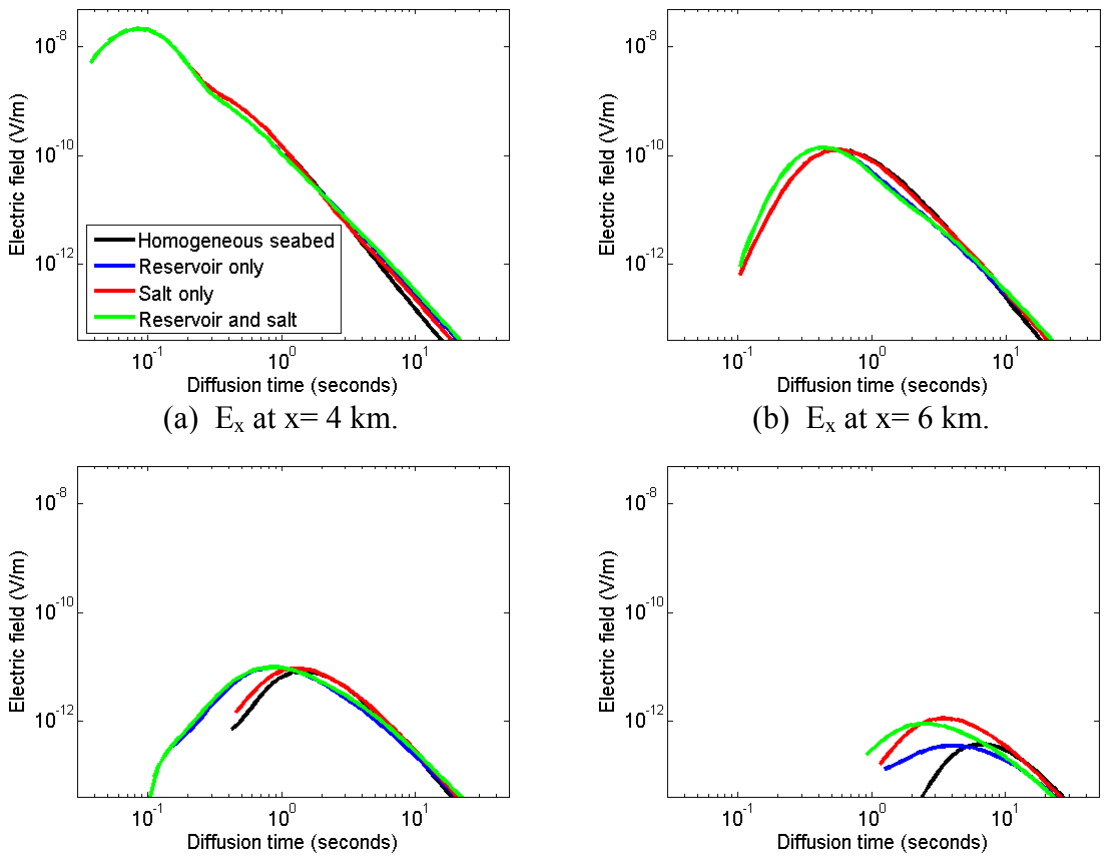

(a) E_x at x= 4 km. (b) E_x at x= 6 km.

(c) E_x at x= 8 km. (d) E_x at x= 10 km.

Figure 8.31. The seafloor E_x measurements over the three anisotropic seabed models with structures. The anisotropy coefficient λ for the background seabed is set to 1.58. The VED is placed 50 m above the seafloor at x= 3 km.

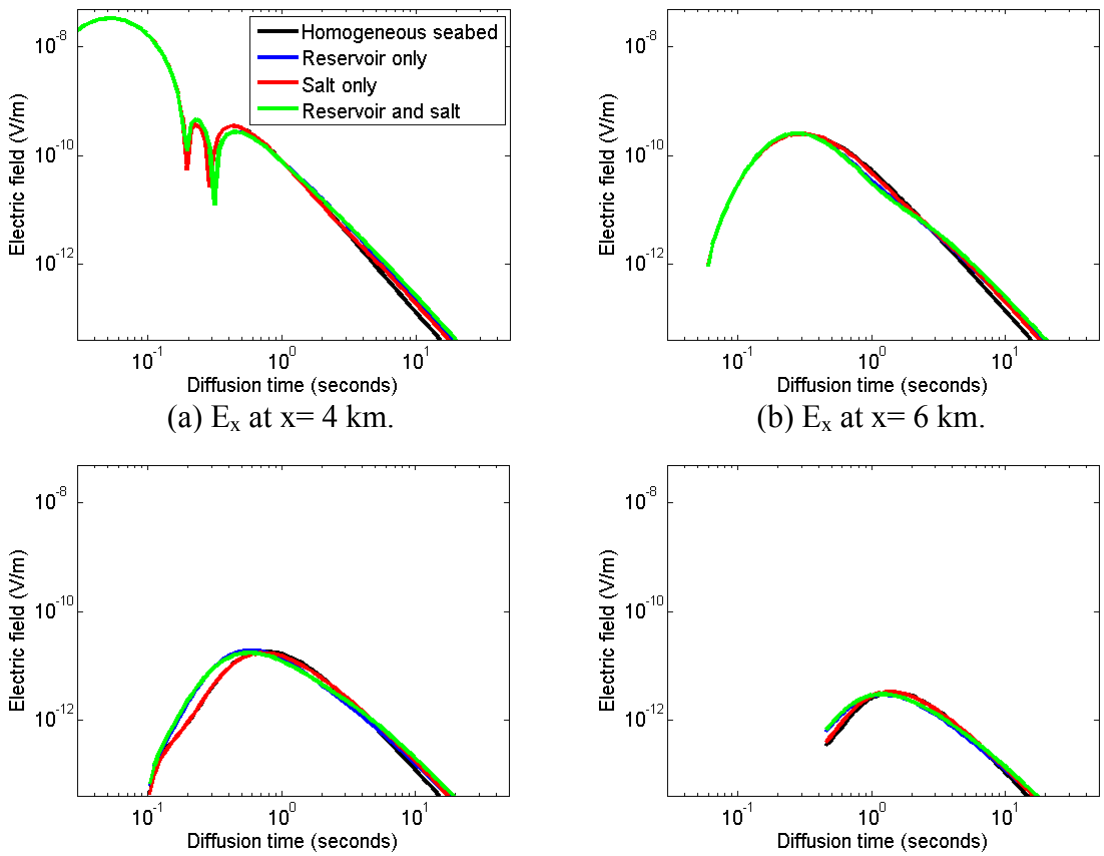

(a) E_x at x= 4 km. (b) E_x at x= 6 km.

(c) E_x at x= 8 km. (d) E_x at x= 10 km.

Figure 8.32. The seafloor E_x measurements over the three anisotropic seabed models with structures. The anisotropy coefficient λ for the background seabed is set to 2.23. The VED is placed 50 m above the seafloor at x= 3 km.

In short, the primary effects of the vertical anisotropic seabed on the transient electric fields excited by an electric dipole source can be summarized as 1) the increase of the background electric fields along the horizontal direction, 2) the decrease of the vertical electric fields that diffuses downward and 3) the decease of the contrast in the vertical resistivity between the seabed and the reservoir. Consequently, the vertical anisotropy can adversely affect the sensitivity of the TDCSEM method.

8.4 Conclusions

I have investigated the transient electric fields excited by an electric dipole source in a realistic shallow offshore environment. FETD simulation and visualization play important roles in analyzing the electric field diffusion related to the sensitivity of the TDCSEM method. The guided diffusion of the electric fields through the thin reservoir is clearly identified on the cross-section of the seabed models.

The modeling studies show that the TDCSEM method effectively senses the localized reservoir close to the large-scale salt structure in the shallow offshore environment. As the reservoir is close to the salt, the non-linear interaction of the electric fields between the reservoir and the salt is observed on the cross-section. To analyze the degree of the interaction along the survey line, I compute the linear sum of 1) the total electric fields from the homogeneous seabed model and 2) the scattered electric fields from the reservoir and the salt. The non-linear interaction between the reservoir and the salt is identified by comparing the linear sum with the electric field response to the reservoir-and-salt model.

Regardless of whether an HED or VED source is used in the given models, the seafloor vertical electric fields at intermediate/long offsets are an order of magnitude smaller than the horizontal ones, because of the effect of the air-seawater interface in the shallow water column. Consequently, the vertical electric-field measurements become sensitive to receiver tilt caused by the irregular seafloor topography. The irregular topography can influence 'airwave' responses by changing the thickness of the seawater column above a seafloor receiver. The 3D modeling studies also illustrate

that the short-offset VED-E_x configuration is very sensitive to a subtle change of the seafloor topography around the VED source. Therefore, the VED-E_x configuration is vulnerable to measurements and modeling errors at short offsets. In contrast, the VED-E_z configuration is relatively robust to these problems and is considered a practical short-offset configuration. It is demonstrated that the short-offset configuration can be used to estimate the lateral extent and depth of the reservoir.

The vertical anisotropy significantly affects the pattern in transient electric field diffusion by elongating and strengthening the electric fields in the horizontal direction. The vertical anisotropy increases the background response in the horizontal direction, decreases the development of the vertical electric fields inside the seabed and reduces the contrast in vertical resistivity between the reservoir and the seabed. The modeling studies show that to avoid erroneous interpretations, the seabed anisotropy need to be accurately measured and incorporated into TDCSEM models.

Chapter 9. References

9.1. Appendix A: edge- and node-based functions

The FETD algorithms in this dissertation utilize an edge-based function (Nédélec, 1980 and 1986; Jin 2002; Bondeson et al., 2002; Taflove and Hagness 2005) to interpolate the electric fields and the time derivative of the vector potential. The edge-based function is also called an edge element. The edge-based function for the ith edge of the eth tetrahedral element is defined as

$$\mathbf{n}_i^e(\mathbf{r}) \equiv l_i^e(\lambda_j(\mathbf{r})\nabla\lambda_k(\mathbf{r}) - \lambda_k(\mathbf{r})\nabla\lambda_j(\mathbf{r})), \tag{9.1}$$

where l_i^e is the length of the ith edge that connects nodes j and k, $\mathbf{r}$ denotes a point in the eth tetrahedral element, and a scalar function $\lambda_j(\mathbf{r})$ is given as

$$\lambda_j(\mathbf{r}) = \frac{\text{Volume of the tetrahedron formed with } \mathbf{r} \text{ and the vertices of the e}^{th} \text{ tetrahedron except vertex } j}{\text{Volume of the e}^{th} \text{ tetrahedron}}. \tag{9.2}$$

The volume of a tetrahedron can be easily computed. For example, the volume of the eth tetrahedral element, V_e is expressed as

$$V_e = \frac{1}{6}\begin{vmatrix} 1 & 1 & 1 & 1 \\ x_1^e & x_2^e & x_3^e & x_4^e \\ y_1^e & y_2^e & y_3^e & y_4^e \\ z_1^e & z_2^e & z_3^e & z_4^e \end{vmatrix}, \tag{9.3}$$

where (x_i^e, y_i^e, z_i^e) with i=1 through 4 are the vertices of the tetrahedron.

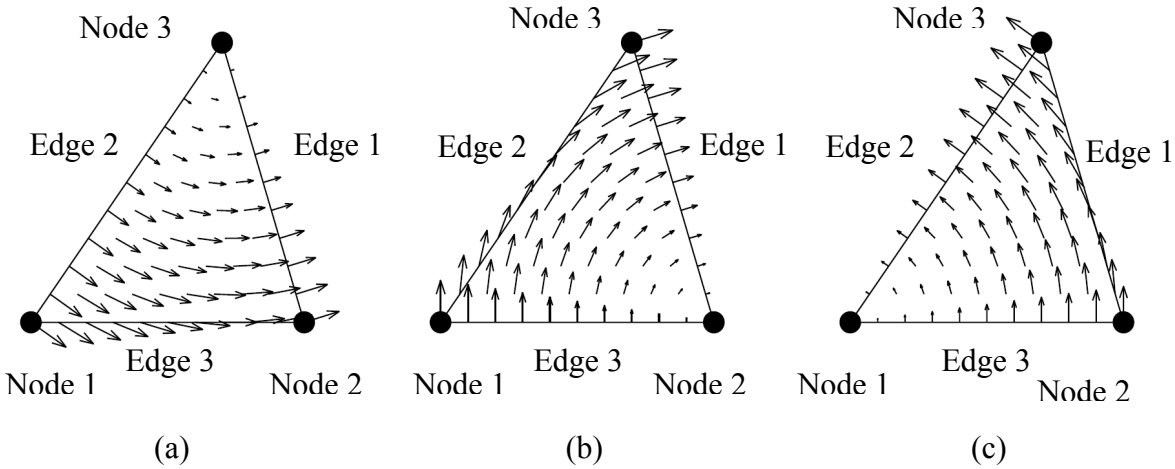

Figure 9.1. Three edge-based interpolation functions on a face of a tetrahedral element. (a) $\mathbf{n}_1^e(\mathbf{r})$. (b) $\mathbf{n}_2^e(\mathbf{r})$. (c) $\mathbf{n}_3^e(\mathbf{r})$. The arrows indicate the interpolation vector functions (Bondeson et al., 2010).

To illustrate the properties of the edge-based functions, the functions are plotted on a face of a tetrahedral element as shown in Figure 9.1. Along each edge, the tangential components of the arrows are determined by two nodes that define the edge and thus are constant. Therefore, the tangential fields are continuous along the edge. In contrast, the normal components of the arrows vary along each edge. The total amplitudes of the normal components are also influenced by the other two edge-based functions and thus can be discontinuous across the edge. Therefore, across the interface, the edge-based function guarantees the continuity of tangential fields and can also 'accommodate' the discontinuity of normal fields.

When boundary values are given to a volume of interest, the FETD algorithm uniquely determines the electric field at each edge by solving a system of FETD equations. The unique electric-field solution is supposed to satisfy the interface conditions: the continuity of the tangential electric field and the continuity of the normal current. However, if an interpolation function chosen for the FETD algorithm can not 'allow' the discontinuity of the normal electric field, the FETD algorithm fails to find the unique solution that satisfies the continuity of the normal current. In other words, the unique solutions that FETD algorithm looks for can not be expressed in

terms of the chosen interpolation function. Therefore, an interpolation function can not be chosen arbitrarily but should be chosen under the consideration of the interface conditions. From this point of view, the edge-based function is necessary for the interface conditions for the electric field and the vector potential under the Lorenz gauge condition (Chapter 5).

The FETD algorithms also utilize Lagrange polynomials or node-based functions (Volakis et al., 1998; Jin, 2002) to represent a scalar potential inside a tetrahedral element. Inside the element, the unknown potential is approximated as

$$\phi^e(\mathbf{r}(x,y,z)) = a^e + b^e x + c^e y + d^e z, \tag{9.4}$$

where a^e, b^e, c^e and d^e are coefficients.

The coefficients above are determined by enforcing equation 9.4 at four nodes of the element assuming the given value at the vertices. Thus, denoting the value of ϕ at the jth node as ϕ_j^e, I have

$$\begin{aligned}
\phi_1^e &= a^e + b^e x_1^e + c^e y_1^e + d^e z_1^e; \\
\phi_2^e &= a^e + b^e x_2^e + c^e y_2^e + d^e z_2^e; \\
\phi_3^e &= a^e + b^e x_3^e + c^e y_3^e + d^e z_3^e; \\
\phi_4^e &= a^e + b^e x_4^e + c^e y_4^e + d^e z_4^e.
\end{aligned} \tag{9.5}$$

From equation A.5, I can obtain

$$a^e = \frac{1}{6\mathrm{V_e}} \begin{vmatrix} \phi_1^e & \phi_2^e & \phi_3^e & \phi_4^e \\ x_1^e & x_2^e & x_3^e & x_4^e \\ y_1^e & y_2^e & y_3^e & y_4^e \\ z_1^e & z_2^e & z_3^e & z_4^e \end{vmatrix} = \frac{1}{6\mathrm{V_e}} (a_1^e \phi_1^e + a_2^e \phi_2^e + a_3^e \phi_3^e + a_4^e \phi_4^e); \tag{9.6}$$

$$b^e = \frac{1}{6\mathrm{V_e}} \begin{vmatrix} 1 & 1 & 1 & 1 \\ \phi_1^e & \phi_2^e & \phi_3^e & \phi_4^e \\ y_1^e & y_2^e & y_3^e & y_4^e \\ z_1^e & z_2^e & z_3^e & z_4^e \end{vmatrix} = \frac{1}{6\mathrm{V_e}} (b_1^e \phi_1^e + b_2^e \phi_2^e + b_3^e \phi_3^e + b_4^e \phi_4^e) \; ; \tag{9.7}$$

$$c^e = \frac{1}{6\mathrm{V_e}} \begin{vmatrix} 1 & 1 & 1 & 1 \\ x_1^e & x_2^e & x_3^e & x_4^e \\ \phi_1^e & \phi_2^e & \phi_3^e & \phi_4^e \\ z_1^e & z_2^e & z_3^e & z_4^e \end{vmatrix} = \frac{1}{6\mathrm{V_e}} (c_1^e \phi_1^e + c_2^e \phi_2^e + c_3^e \phi_3^e + c_4^e \phi_4^e) \; ; \tag{9.8}$$

$$d^e = \frac{1}{6\mathrm{V_e}} \begin{vmatrix} 1 & 1 & 1 & 1 \\ x_1^e & x_2^e & x_3^e & x_4^e \\ y_1^e & y_2^e & y_3^e & y_4^e \\ \phi_1^e & \phi_2^e & \phi_3^e & \phi_4^e \end{vmatrix} = \frac{1}{6\mathrm{V_e}} (d_1^e \phi_1^e + d_2^e \phi_2^e + d_3^e \phi_3^e + d_4^e \phi_4^e) \, . \tag{9.9}$$

The coefficients a_j^e, b_j^e, c_j^e and d_j^e can be determined from expansion of the determinants.

Substituting the expressions for a^e, b^e, c^e and d^e into equation A.4, I obtain

$$\phi^e(\mathbf{r}) = \sum_{j=1}^{4} \phi_j^e n_j^e(\mathbf{r}), \tag{3.20}$$

where the 'scalar' interpolation function $n_j^e(\mathbf{r})$ is given as

$$n_j^e(\mathbf{r}) = \frac{1}{6\mathrm{V_e}} (a_j^e + b_j^e x + c_j^e y + d_j^e z) \, . \tag{9.10}$$

It is known that $n_j^e(\mathbf{r})$ is one at the jth node but zero at the other three nodes; $n_j^e(\mathbf{r})$ also vanishes when $\mathbf{r}$ is on the face of the tetrahedral element opposite the jth node. As a result, inter-element continuity of the scalar potential is guaranteed. Therefore, the node-based function can be used to interpolate the scalar potential.

9.2. Appendix B: assembly of the global matrix equation

This appendix describes the process of assembling local FE matrix equations into a single global FE matrix equation. For simplicity, I consider the discretization of a simple 2D domain using three triangular elements, as shown in Figure 9.2.

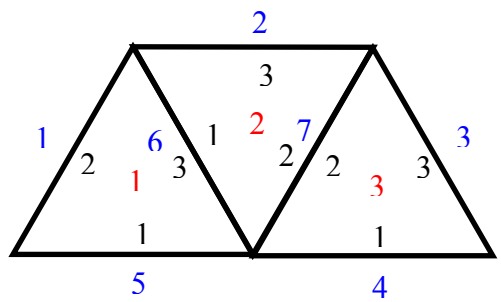

Figure 9.2. Discretization of a 2D domain using three triangular elements. The red numbers are element numbers, the blue numbers are global edge numbers, and the black numbers are local edge numbers.

The triangular elements are uniquely numbered from 1 to 3 (red). Each element has three edges. Therefore, a local FE matrix from each element is three-by-three. The total number of edges in the 2D domain is seven, and therefore the size of the global FE matrix is seven-by-seven. The edges are uniquely numbered from 1 to 7 (blue). They are referred to as global edge numbers. Inside each element, its edges are locally numbered from 1 to 3 (black). They are referred to as local edge numbers.

The assembly process begins with the formation of the connectivity table as shown in Table 9.1. For example, element 1 consists of global edge 5, 1 and 6. Global edge 5, 1 and 6 correspond to local edge 1, 2 and 3, respectively.

Element number	Local edge number 1	Local edge number 2	Local edge number 3
1	5	1	6
2	6	7	2
3	4	7	3

Table 9.1. Connectivity information based on Figure 9.2. The connectivity information is used to map local descriptions to a global description.

For element 1, I set up a local three-by-three FE matrix equation:

$$\mathbf{B}^1\mathbf{e}^1 = \mathbf{S}^1 \text{ or } \begin{pmatrix} b_{11}^1 & b_{12}^1 & b_{13}^1 \\ b_{21}^1 & b_{22}^1 & b_{23}^1 \\ b_{31}^1 & b_{32}^1 & b_{33}^1 \end{pmatrix} \begin{pmatrix} e_1^1 \\ e_2^1 \\ e_3^1 \end{pmatrix} = \begin{pmatrix} s_1^1 \\ s_2^1 \\ s_3^1 \end{pmatrix}, \tag{9.11}$$

where $\mathbf{B}^1$ is the local FE system matrix for element 1, $\mathbf{e}_i^1$ is the unknown electric field at the ith local edge of element 1, and $\mathbf{S}^1$ is a source term.

For elements 2 and 3, we also set up local FE matrix equations:

$$\mathbf{B}^2\mathbf{e}^2 = \mathbf{S}^2 \text{ or } \begin{pmatrix} b_{11}^2 & b_{12}^2 & b_{13}^2 \\ b_{21}^2 & b_{22}^2 & b_{23}^2 \\ b_{31}^2 & b_{32}^2 & b_{33}^2 \end{pmatrix} \begin{pmatrix} e_1^2 \\ e_2^2 \\ e_3^2 \end{pmatrix} = \begin{pmatrix} s_1^2 \\ s_2^2 \\ s_3^2 \end{pmatrix}; \tag{9.12}$$

$$\mathbf{B}^3\mathbf{e}^3 = \mathbf{S}^3 \text{ or } \begin{pmatrix} b_{11}^3 & b_{12}^3 & b_{13}^3 \\ b_{21}^3 & b_{22}^3 & b_{23}^3 \\ b_{31}^3 & b_{32}^3 & b_{33}^3 \end{pmatrix} \begin{pmatrix} e_1^3 \\ e_2^3 \\ e_3^3 \end{pmatrix} = \begin{pmatrix} s_1^3 \\ s_2^3 \\ s_3^3 \end{pmatrix}. \tag{9.13}$$

Once the connectivity information (Table 9.1) is formed and each local matrix equation is set up, the global FE matrix equation is created with its entries initialized to zeros:

$$\left(\begin{array}{ccccccc|c} 0 & 0 & 0 & 0 & 0 & 0 & 0 & 0 \\ 0 & 0 & 0 & 0 & 0 & 0 & 0 & 0 \\ 0 & 0 & 0 & 0 & 0 & 0 & 0 & 0 \\ 0 & 0 & 0 & 0 & 0 & 0 & 0 & 0 \\ 0 & 0 & 0 & 0 & 0 & 0 & 0 & 0 \\ 0 & 0 & 0 & 0 & 0 & 0 & 0 & 0 \\ 0 & 0 & 0 & 0 & 0 & 0 & 0 & 0 \end{array}\right). \tag{9.14}$$

First, I update equation 9.14 with equation 9.11 by assigning the entries of equation 9.11 into the entries of equation 9.14 according to Table 9.1, generating

$$\left(\begin{array}{ccccccc|c} b_{22}^1 & 0 & 0 & 0 & b_{21}^1 & b_{23}^1 & 0 & s_2^1 \\ 0 & 0 & 0 & 0 & 0 & 0 & 0 & 0 \\ 0 & 0 & 0 & 0 & 0 & 0 & 0 & 0 \\ 0 & 0 & 0 & 0 & 0 & 0 & 0 & 0 \\ b_{12}^1 & 0 & 0 & 0 & b_{11}^1 & b_{13}^1 & 0 & s_1^1 \\ b_{32}^1 & 0 & 0 & 0 & b_{31}^1 & b_{33}^1 & 0 & s_3^1 \\ 0 & 0 & 0 & 0 & 0 & 0 & 0 & 0 \end{array}\right). \tag{9.15}$$

Second, I continue to update equation 9.15 with equation 9.12, generating

$$\left(\begin{array}{ccccccc|c} b_{22}^1 & 0 & 0 & 0 & b_{21}^1 & b_{23}^1 & 0 & s_2^1 \\ 0 & b_{33}^2 & 0 & 0 & 0 & b_{31}^2 & b_{32}^2 & s_3^2 \\ 0 & 0 & 0 & 0 & 0 & 0 & 0 & 0 \\ 0 & 0 & 0 & 0 & 0 & 0 & 0 & 0 \\ b_{12}^1 & 0 & 0 & 0 & b_{11}^1 & b_{13}^1 & 0 & s_1^1 \\ b_{32}^1 & b_{13}^2 & 0 & 0 & b_{31}^1 & b_{33}^1 + b_{11}^2 & b_{12}^2 & s_3^1 + s_1^2 \\ 0 & b_{23}^2 & 0 & 0 & 0 & b_{21}^2 & b_{22}^2 & s_2^2 \end{array}\right). \tag{9.16}$$

Finally, I update equation 9.16 with equation 9.13, generating

$$\left(\begin{array}{ccccccc|c} b_{22}^1 & 0 & 0 & 0 & b_{21}^1 & b_{23}^1 & 0 & s_2^1 \\ 0 & b_{33}^2 & 0 & 0 & 0 & b_{31}^2 & b_{32}^2 & s_3^2 \\ 0 & 0 & b_{33}^3 & b_{31}^3 & 0 & 0 & b_{32}^3 & s_3^3 \\ 0 & 0 & b_{23}^3 & b_{11}^3 & 0 & 0 & b_{12}^3 & s_1^3 \\ b_{12}^1 & 0 & 0 & 0 & b_{11}^1 & b_{13}^1 & 0 & s_1^1 \\ b_{32}^1 & b_{13}^2 & 0 & 0 & b_{31}^1 & b_{33}^1 + b_{11}^2 & b_{12}^2 & s_3^1 + s_1^2 \\ 0 & b_{23}^2 & b_{23}^3 & b_{21}^3 & 0 & b_{21}^2 & b_{22}^2 + b_{22}^3 & s_2^2 + s_2^3 \end{array}\right). \tag{9.17}$$

So far, I have demonstrated the assembly of the global FE matrix equation from individual FE matrix equations using edge elements. One can easily apply the processes above to an FE problem with node elements, by replacing edge numbers with node numbers.

9.3. Appendix C: 3D FEFD formulation of the electric-field diffusion equation

In this appendix, I derive the finite-element frequency-domain (FEFD) formulation from the electric-field diffusion equation. Note that this class of FEFD algorithms recently appeared in the EM geophysics literature (Schwarzbach et al., 2009; Silva et al., 2009) and is not new. However, the purpose of this section is to demonstrate similarities and differences between FETD and FEFD formulations.

Using a phasor notation (Jackson, 1998), one can easily derive from equation 2.8 the frequency-domain electric-field full-wave equation

$$\nabla \times [\frac{1}{\mu_0} \nabla \times \mathbf{E(r)}] - \omega^2 \varepsilon \, \mathbf{E(r)} + \hat{i}\, \omega \boldsymbol{\sigma} \, \mathbf{E(r)} = -\hat{i}\, \omega \, \mathbf{J_s(r)}, \tag{9.18}$$

where $\mathbf{E(r)}$ is the electric field at angular frequency ω at position $\mathbf{r} \in \mathbf{V}$, μ_0 is the magnetic permeability of free space, ε is the dielectric permittivity, $\boldsymbol{\sigma}$ is conductivity and $J_s(\mathbf{r})$ is an electric-current source term.

As discussed in Chapter 2, the second term of the left-hand side of equation 9.18 is related to the displacement term and is negligible in the diffusion domain. Therefore, the residual vector $\mathbf{p}$ for equation 9.18 is defined without the term as

$$\mathbf{p}(\mathbf{r}) \equiv \nabla \times [\frac{1}{\mu_0} \nabla \times \mathbf{E}(\mathbf{r})] + \hat{i}\,\omega \boldsymbol{\sigma}\,\mathbf{E}(\mathbf{r}) + \hat{i}\,\omega\,\mathbf{J}_{\mathbf{s}}(\mathbf{r}). \tag{9.19}$$

The residual vector must be forced to be zero in a weighted-average sense in each tetrahedral element. This idea is expressed as the following equation:

$$\iiint_{V^e} \mathbf{n}_i^e(\mathbf{r}) \cdot \mathbf{p}^e(\mathbf{r}) dV = 0, \tag{9.20}$$

where the superscript e denotes the eth tetrahedral element, $\mathbf{n}_i^e(\mathbf{r})$ with i varying from 1 to n is a set of edge-based functions (detailed in Appendix A), and V^e is the volume of the eth tetrahedral element.

Using some vector calculus identities with Dirichlet boundary conditions, equation 9.20 reduces to

$$\begin{aligned} &\iiint_{V^e} (\nabla \times \mathbf{n}_i^e(\mathbf{r})) \cdot (\nabla \times \mathbf{E}^e(\mathbf{r})) dV + \mu\omega\hat{i} \iiint_{V^e} \mathbf{n}_i^e(\mathbf{r}) \cdot \boldsymbol{\sigma}\,\mathbf{E}^e(\mathbf{r}) dV \\ &+ \mu_0 \omega\hat{i} \iiint_{V^e} \mathbf{n}_i^e(\mathbf{r}) \cdot \mathbf{J}_{\mathbf{s}}(\mathbf{r}) dV = 0. \end{aligned} \tag{9.21}$$

If the set of $\mathbf{n}_i^e(\mathbf{r})$ functions used in equation 9.20 is also chosen as the set of basis functions for the electric fields, the electric field is expanded as

$$\mathbf{E}^e(\mathbf{r}) = \sum_{j=1}^{n} \mathbf{E}_j^e(\mathbf{r}) = \sum_{j=1}^{n} u_j^e \mathbf{n}_j^e(\mathbf{r}), \tag{9.22}$$

where u_j^e is the unknown amplitude of the electric field on edge j of the eth element.

Substituting equation 9.22 into equation 9.21 yields

$$\begin{aligned} &\sum_{j=1}^{n} u_j^e \iiint_{V^e} (\nabla \times \mathbf{n}_i^e(\mathbf{r})) \cdot (\nabla \times \mathbf{n}_j^e(\mathbf{r})) dV + \sum_{j=1}^{n} u_j^e \mu\omega\hat{i} \iiint_{V^e} \mathbf{n}_i^e(\mathbf{r}) \cdot \boldsymbol{\sigma}^e \mathbf{n}_j^e(\mathbf{r}) dV \\ &+ \mu_0 \omega\hat{i} \iiint_{V^e} \mathbf{n}_i^e(\mathbf{r}) \cdot \mathbf{J}_{\mathbf{s}}(\mathbf{r}) dV = 0. \end{aligned} \tag{9.23}$$

The matrix-vector-equation form of equation 9.23 is

$$(\mathbf{A}^e + \mu_0 \omega\hat{i}\mathbf{B}^e)\mathbf{u}^e = -\mu\omega\hat{i}\mathbf{s}^e \tag{9.24}$$

where

$$\text{the (i,j)}^{\text{th}} \text{ element of } \mathbf{A}^e = \iiint_{V^e} \nabla \times \mathbf{n}_i^e(\mathbf{r}) \cdot \nabla \times \mathbf{n}_j^e(\mathbf{r}) dV \,, \tag{9.25}$$

$$\text{the (i,j)}^{\text{th}} \text{ element of } \mathbf{B}^e = \iiint_{V^e} \mathbf{n}_i^e(\mathbf{r}) \cdot \boldsymbol{\sigma}^e \mathbf{n}_j^e(\mathbf{r}) dV \,, \tag{9.26}$$

$$\text{the i}^{\text{th}} \text{ element of } \mathbf{s}^e = \iiint_{V^e} \mathbf{n}_i^e(\mathbf{r}) \cdot \mathbf{J}_{\text{s}}(\mathbf{r}) dV \,, \tag{9.27}$$

$$\mathbf{u}^e = [u_1^e \quad u_2^e \quad \ldots \quad u_n^e] \,, \tag{9.28}$$

and n is the number of the basis function for the eth tetrahedron.

Equation 9.24 is considered local, because it results from integration over each individual tetrahedral element. Based on connectivity information about tetrahedral elements in $\mathbf{V}$, the local systems of diffusion equations assembled for the individual elements are assembled into a single global system of equations. Then, the superscript $\boldsymbol{e}$ can be dropped. As discussed in Chapter 4, the global version of equation 9.24 should also be solved using a direct solver to avoid spurious solutions and non-convergence in the static limit. The solution of the global version of equation 9.24 produces the total electric fields at the receiver positions. The associated magnetic fields are interpolated from the existing electric fields using the numerical implementation of Faraday's law.

There are clear similarities between the FEFD formulation above and the FETD formulation in Chapter 3. First, note that equations 9.25 and 9.26 are the same as equations 3.8 and 3.7, respectively. Second, equation 9.27 is different from equation 3.9, but the difference is only the application of the time derivative to the source term. The observations suggest that I can easily develop an FEFD implementation by modifying the existing FETD implementation; I was able to develop an FEFD algorithm that shares 70% of the routines for the FETD algorithm.

One important difference between the FEFD algorithm and the FETD algorithm becomes obvious when I simulate a multi-source experiment. As shown in Abubakar et al. (2008) and Silva et al. (2009), a multi-source FDCSEM experiment can be simulated at nearly the cost of simulating one single-source experiment. Such a multi-source simulation is based on the observation that a different source position changes

only the right-hand-side vector of equation 9.24 for the FEFD algorithm and of equation 3.12 for the FETD algorithm. Therefore, if a single mesh is designed to accommodate multiple source positions, the system matrices of equations 9.24 and 3.12 can be factorized only once and can be reused with different right-hand-side vectors (i.e. multiple source positions).

For example, the multi-source experiment is performed over the seafloor model shown in Figure 6.3. Five sources are placed 1 km apart along the x-axis from x=0 km through x=4 km. A single mesh that accommodates the five sources is constructed. For comparison, Five meshes for the five sources are also constructed. Then, the multi-source experiments are carried out using both single and multiple mesh approach. The solution runtimes are summarized in Table 9.2. To accommodate the five source positions, the single mesh approach requires only slightly more unknowns than the multiple mesh approach. However, by reusing the Cholesky factorization results, the multiple mesh approach reduces the solution runtime by factor of 5.

	Multiple mesh approach	Single mesh approach
Number of unknowns	91,744 (average)	92,964
Source location	Accumulated solution runtime (seconds)	Accumulated solution runtime (seconds)
Source 1 at x = 0 km	385	N/A
Source 2 at x = 1 km	770	N/A
Source 3 at x = 2 km	1,155	N/A
Source 4 at x = 3 km	1,540	N/A
Source 5 at x = 4 km	1,925	390

Table 9.2. The comparison of the solution runtime between the single and multiple mesh approaches. Five individual sources are numbered from 1 to 5.

However, I have found that it is impractical to adopt the single mesh approach in my FETD algorithms for the following two major reasons: first, an FETD mesh design requires fine meshes around a source; the more source positions a model has, the more elements it requires. Consequently, the assumption that I simulate multi-source

experiments at nearly the cost of simulating one single-source experiment is no longer valid. Second, at a given time, acceptable time-step sizes can be significantly different at different source positions, especially in 3D earth models. Therefore, to ensure the accuracy of the FETD solutions, the FETD algorithm must choose the smallest acceptable time-step size among different time-step sizes, lowering the efficiency of the adaptive time-step-doubling method. This inapplicability of the single mesh approach remains a drawback of the FETD algorithms presented in this dissertation.

9.4. Appendix D: backward Euler method

The backward Euler (BE) method (Moin, 2001) is given as

$$y_{n+1} = y_n + hf(y_{n+1}, t_{n+1}), \tag{9.29}$$

where h is a time-step size.

The BE method does not immediately yield the solution at the next time step. If f is non-linear, I must solve a non-linear algebraic equation at each time step to obtain y_{n+1}. Although the BE method requires the computationally-expensive solution processes, the method has an enhanced stability property as shown below.

For feasibility of analytical treatment, the stability analysis of the BE method is performed on a model problem:

$$y' = \lambda y. \tag{9.30}$$

Applying the BE method to the model problem, 9.30, I obtain

$$y_{n+1} = y_n + \lambda h y_{n+1}. \tag{9.31}$$

Solving for y_{n+1} produces

$$y_{n+1} = \sigma y_n, \tag{9.32}$$

where the amplification factor, σ is given as

$$\sigma = \frac{1}{1-\lambda h} = \frac{1}{(1-\lambda_{\mathrm{Re}} h) - i\lambda_{\mathrm{Im}} h}. \tag{9.33}$$

The denominator of equation 9.33 is complex number and can be written as the product of its modulus A and phase factor θ,

$$\sigma = \frac{1}{Ae^{i\theta}}, \tag{9.34}$$

where

$$A = \sqrt{(1-\lambda_{\mathrm{Re}}h)^2 + \lambda_{\mathrm{Im}}^2 h^2}\ ; \tag{9.35}$$

$$\theta = -\tan^{-1}\left(\frac{\lambda_{\mathrm{Im}}h}{1-\lambda_{\mathrm{Re}}h}\right). \tag{9.36}$$

For stability, the modulus of the amplification factor must be less than or equal to 1; i.e.,

$$|\sigma| = \frac{\left|e^{-i\theta}\right|}{A} = \frac{1}{A} \le 1. \tag{9.37}$$

Thus, the BE method is unconditionally stable. Unconditional stability is the usual characteristic of the BE method. However, the price is higher computational cost per time step for having to solve an equation.

9.5. Appendix E: double-curl electric-field diffusion equation

The double-curl electric-field diffusion equation is given as

$$\nabla \times \frac{1}{\mu_0} \nabla \times \mathbf{e}(\mathbf{r},t) + \overline{\overline{\boldsymbol{\sigma}}} \frac{\partial \mathbf{e}(\mathbf{r},t)}{\partial t} + \frac{\partial \mathbf{j}_{\mathbf{s}}(\mathbf{r},t)}{\partial t} = \mathbf{0}. \tag{2.10}$$

The third term of equation 2.10 exists only at early time. As the diffusion process continues, the electric fields increasingly become static. Therefore, equation 2.10 becomes

$$\nabla \times \nabla \times \mathbf{e}(\mathbf{r},t) \sim \mathbf{0}. \tag{9.38}$$

Equation 9.38 becomes close to singular. The application of iterative solvers to the equation results in very slow convergence or non-convergence (Smith, 1996). Spurious solutions can also creep into its electric field solutions (Smith, 1996; Newman and Alumbaugh, 2002; Commer and Newman, 2004).

To overcome these problems, equation 2.10 should be constrained by the Gauss' law (i.e. the current conservation or divergence-free condition), equation 2.1 (Smith, 1996).

An alternative approach is to reformulate equation 2.10 in terms of vector and scalar potentials as shown in Chapter 5. Another alternative approach is to use a direct solver for equation 2.10. As demonstrated in Dyczij-Edlinger et al. (1998), Börner et al. (2008), Oldenburg et al. (2008) and Schwarzbach et al. (2009), direct solvers are robust to the spurious solution problem when the problem is close to singular.

9.6. Appendix F: spectral analysis for determining initial time step size

When the time-stepping process starts, an initial time step (t_o) should be small enough such that the highest frequency of the electric fields can be safely sampled. However, a too small t_o unnecessarily increases solution run time. To determine a proper t_o, the following analysis steps are taken.

First, a 1D background model is taken from a 3D model of interest. In this appendix, the background model is assumed as the model shown in Figure 4.3. The shortest source-receiver offset is set to 1 km. Second, an analytical CSEM response to the background model is computed at the shortest offset (Figure 9.3a). Third, the frequency spectrum and the spectral density of the CSEM responses (Figures 9.3b and 9.3c) are calculated using Fourier transform. Due to the EM attenuation, these two curves increasingly become constant as the frequency increases. As a result, the accumulated spectral density curve (Figure 9.3d) also becomes constant at around 200 Hz. Therefore, according to the sampling theory (Lathi, 2005), a proper t_o should be smaller than the Nyquist sampling interval:

$$t_0 \leq \frac{1}{2 \times 200} = 0.0025 \text{ (seconds)}. \tag{9.39}$$

When this spectral analysis is applied back to the 3D model of interest, it is recommended that t_o should be somewhat smaller than the Nyquist sampling interval. As the final note, one should avoid to perform the spectral analysis directly on a given

source waveform because this approach can result in unnecessarily small t_o that does not influence CSEM responses at receiver positions.

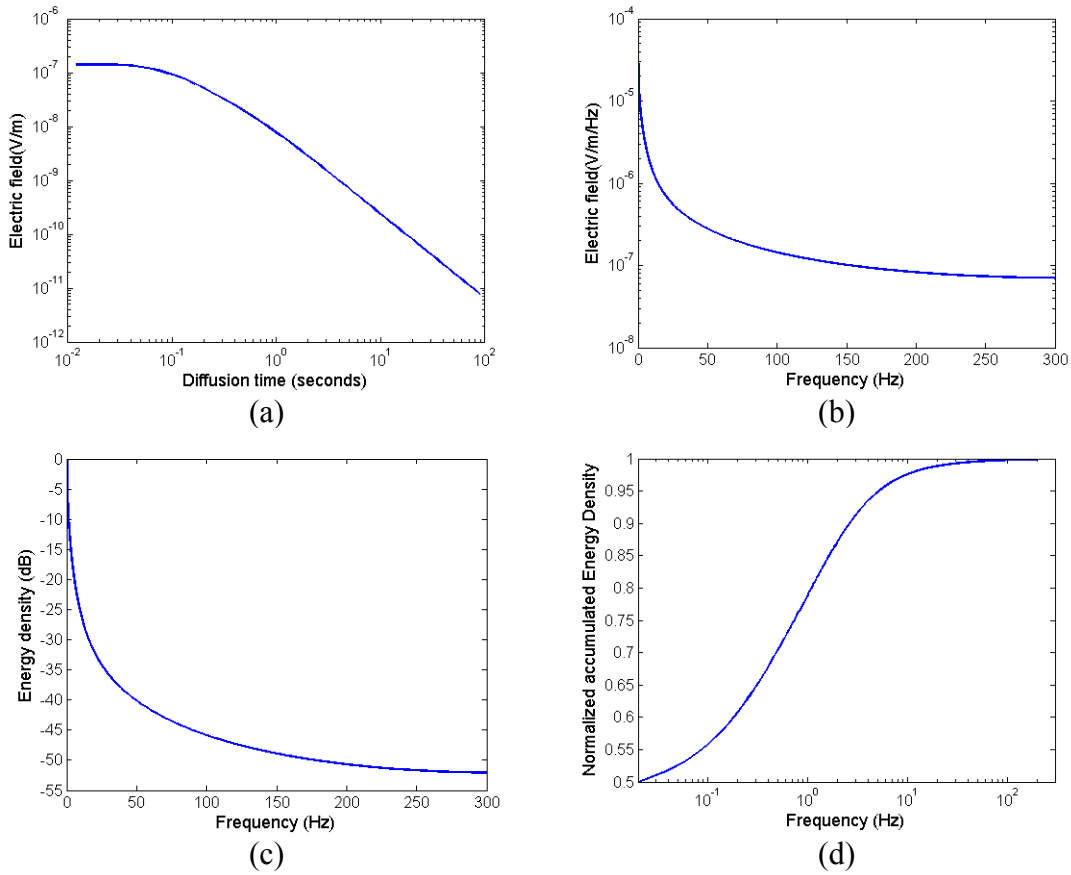

Figure 9.3. (a) The E_x response at 1 km offset to the model shown in Figure 4.2. (b) The frequency spectrum of the E_x response. (c) The spectral density of the E_x response. (d) The normalized accumulated spectral density.

9.7. Appendix G: aspect ratio

The skewness or the quality of elements is measured using the aspect ratio (COMSOL, 2008). For tetrahedral elements, the skewness, q, is defined as

$$q = \frac{72\sqrt{3}V}{(h_1^2 + h_2^2 + h_3^2 + h_4^2 + h_5^2 + h_6^2)}, \tag{9.40}$$

where V is the volume of a tetrahedral element, h_i is the length of the ith edge of the element. For a regular tetrahedral element, q is equal to 1. COMSOL suggests that q should be greater than or equal to 0.1.

9.8. Bibliography

Abubakar, A., T. Habashy, V. Druskin, L. Knizhnerman and D. Alumbaugh, 2008, 2.5D forward and inverse modeling for interpreting low-frequency electromagnetic measurements, Geophysics, **73,** F165-F177.

Alumbaugh, D., M. Hoversten, S. Horne, Abubakar, A., T. Habashy, Druskin, V., T. Rosten, 2006, Two-dimensional inversion of marine electromagnetic data using seismic reflection data as apriori information, American Geophysical Union (AGU), Fall Meeting Abstract, NS23A-03.

Alumbaugh, D., Newman, G. Prevost, L., and Shadid, J., 1996, Three-dimensional wideband electromagnetic modeling on massively parallel computers: Radio Science, **31**, 1-23.

Alumbaugh, D.; Hoversten, M.; Horne, S.; Abubakar, A.; Habashy, T.; Druskin, V.; Rosten, T., 2006, Two-dimensional inversion of marine electromagnetic data using seismic reflection data as apriori information, American Geophysical Union (AGU), Fall Meeting, abstract #NS23A-03.

Aminzadeh, F., J. Brac, and T. Kunz, 1997, 3D salt and overthrust models, SEG/EAGE.

Andréis D. and L. MacGregor, 2008, Controlled-source electromagnetic sounding in shallow water: Principles and applications, Geophysics, **73**, F21-F32.

Badea, E., M. Everett, G. Newman and O. Biro, 2001, Finite element analysis of controlled-source electromagnetic induction using gauged electromagnetic potentials, Geophysics, **66**, 786-799.

Barber, C.B., Dobkin, D.P., and Huhdanpaa, H.T., 1996, The Quickhull algorithm for convex hulls, ACM Trans. on Mathematical Software, **22**, 469-483.

Bondeson A., T. Rylander and P. Ingelstrom, 2010, Computational electromagnetics, Springer.

Biro, O. and K. Preis, 1989, On the use of the magnetic vector potential in the finite element analysis of three-dimensional eddy currents, IEEE Transactions on Magnetics, **25**, 3145-3159.

Bossavit A. 1988, Whitney forms: a class of finite elements for three-dimensional computations in electromagnetism, IEEE Physical Science, Measurement and Instrumentation, Management and Education Reviews, **135**, 493-500.

Börner, R.-U., Ernst, O. G. and Spitzer, K., 2008, Fast 3D simulation of transient electromagnetic fields by model reduction in the frequency domain using Krylov subspace projection, Geophysical Journal International, **173** , 766–780.

Börner, R.-U, 2010, Numerical modeling in geo-electromagnetics: advances and challenges, Survey in Geophysics, **31**, 225-245.

Bryant, C., C. Emson and C. Trowbridge, 1990, A general purpose 3D formulation for eddy currents using the Lorentz gauge, IEEE Transactions on Magnetics, **26**, 2373-2375.

Bryant, C., C. Emson, C. Trowbridge, and P. Fernandes, 1998, Lorentz gauge formulations for eddy current problems involving piecewise homogeneous conductors, IEEE Trans. on Magnetics, **34**, 2559-2562.

Cangellaris, A., C. Lin and K. Mei, 1987, Point-matched time domain finite element methods for electromagnetic radiation and scattering, IEEE Transaction on Antennas and Propagation, **35**, 1160-1173.

Chave, A., 2009, On the electromagnetic fields produced by marine frequency domain controlled sources, Geophysical Journal International, **179**, 1429-1457.

Cheesman, S., R. Edwards and A. Chave, 1987, On the theory of sea-floor conductivity mapping using transient electromagnetic systems, Geophysics, **52**, 204-217.

Chen, J. and D. Alumbaugh, 2009, Three methods for mitigating airwaves in shallow water marine CSEM data, Society of Exploration Geophysicists (SEG) Annual Meeting Abstracts, 785-789.

Commer, M., and G. Newman, 2004, A parallel finite-difference approach for 3D transient electromagnetic modeling with galvanic sources: Geophysics, **69**, 1192-1202.

Commer, M., S. Helwig, A. Hördt and C. Scholl, 2006, New results on the resistivity structure of Merapi Volcano (Indonesia), derived from three-dimensional restricted inversion of long-offset transient electromagnetic data, Geophysical Journal International, **167**, 1172-1187.

Commer, M. and G. Newman, 2008, New advances in three-dimensional controlled-source electromagnetic inversion, Geophysical Journal International, **172**, 513-535.

COMSOL, 2008, COMSOL Multiphysics 3.5 user's guide, COMSOL.

Constable, S. ad C. Weiss, 2006, Mapping thin resistors and hydrocarbons with marine EM methods: Insights from 1D modeling, Geophysics, **71**, G43-G51.

Constable, S. C., and C. J. Weiss, 2006, Mapping thin resistors and hydrocarbons with marine EM methods: Insights from 1D modeling: Geophysics, **71**, no. 2, G43–G51.

Constable, S., 2010, Ten years of marine CSEM for hydrocarbon exploration, Geophysics, **75**, 75A67-75A81.

Cox, C. S., S. C. Constable, A. D. Chave, and S. C. Webb, 1986, Controlled-source electromagnetic sounding of the oceanic lithosphere, Nature, **320**, 52-54.

Cuevas, N., D. Alumbaugh and J. Chen, 2010, 1D Layered Resolution Analysis of Two Marine EM Exploration Methods, EAGE Conference, D036.

Davis, T., 2006, Direct methods for sparse linear systems: SIAM.

Demmel, J., 1997, Applied numerical linear algebra: SIAM.

Dey, A. and H. F. Morrison, 1978, Resistivity modeling for arbitrary shaped three-dimensional structures: Geophysics, **44**, 753-780.

Dyczij-Edlinger, R., G. Peng and J. Lee, 1998, A fast vector-potential method using tangentially continuous vector finite elements, IEEE Transactions on Microwave Theory and Techniques, **46**, 863-868.

Edwards, R. and A. Chave, 1986, A transient electric dipole-dipole method for mapping the conductivity of the sea floor, Geophysics, 51, 984-987.

Edwards, R., 1997, On the resource evaluation of marine gas hydrate deposits using sea-floor transient electric dipole-dipole methods, Geophysics, **62**, 63-74.

Edwards, N., 2005, Marine controlled source electromagnetics: principles, methodologies, future commercial applications, Surveys in Geophysics, **26**, 675-700.

Eidesmo, T., Ellingsrud, S., MacGregor, L.M., Constable, S., Sinha, M.C., Johansen, S.,Kong, F.N. and Westerdahl, H., 2002. Sea Bed Logging (SBL), a new method for remote and direct identification of hydrocarbon filled layers in deepwater areas, First Break, **20**, 144–152.

Ellingsrud, S., T. Eidesmo, S. Johansen, M. C. Sinha, L. M. MacGregor and S. Constable, 2002, Remote sensing of hydrocarbon layers by seabed logging (SBL): Results from a cruise offshore Angola, The Leading Edge, **21**, 972-982.

Everett, M. and R. Edwards, 1991, Theoretical controlled-source electromagnetic responses of fast-spreading mid-ocean ridge models, Geophysical Journal International, **105**, 313-323.

Everett, M. and R. Edwards, 1992, Transient marine electromagnetics: the 2.5-D forward problem, Geophysical Journal International, **113**, 545-561.

Gedney, S. and U. Navsariwala, 1995, An unconditionally stable implicit finite-element time-domain solution of the vector wave equation, IEEE Microwave Guided Wave Letters, **5**, 332-334.

Gockenbach, M. S., 2002, Partial differential equations: Society of Industrial and Applied Mathematics (SIAM).

Goldman, M. and C. Stoyer, 1983, Finite-difference calculation of the transient field of an axially symmetric earth for vertical magnetic dipole excitation, Geophysics, **48**, 953-963.

Goldman, Y., C. Hubans, Nocoletis, S. and S. Spitz, 1985, A finite-element solution for the transient electromagnetic response of an arbitrary two-dimensional resistivity distribution: Geophysics, **51**, No. 7, 1450-1461.

Griebenko, A. and M. Zhdanov, 2007, Rigorous 3D inversion of marine CSEM data based on the integral equation method, Geophysics, **72**, WA73-WA84.

Griffiths, David, 1999, Introduction to electrodynamics, the 3rd edition, Prentice Hall.

Haber, E., U. M. Ascher, D. A. Aruliah and D. W. Oldenburg, 2000, Fast simulation of 3D electromagnetic problems using potentials, Journal of Computational Physics, **163**, 150-171.

Haber, E., U. Ascher, and D. Oldenburg, 2004, Inversion of 3D electromagnetic data in frequency and time domain using an inexact all-at-once approach: Geophysics, 69, 1216-1228.

Hairer, E., and Wanner, G., 1991, Solving ordinary differential equations 2: Stiff and differential-algebraic problems: Springer-Verlag.

[1]Hördt, A., P. Andrieux, F. M. Neubauer, H. Ruter, and K. Vozoff, 2000, A first attempt at monitoring underground gas storage by means of time lapse multichannel transient electromagnetics: Geophysical Prospecting, 48, 489–509.

[2]Hördt, A., S. Dautel, B. Tezkan and H. Thern, 2000, Interpretation of long-offset electromagnetic data from the Odenwald area, Germany, using two-dimensional modeling, Geophysical Journal International, **140**, 577-586.

Hördt, A., and M. Müller, 2000, Understanding LOTEM data from mountainous terrain: Geophysics, **65**, 1113-1123.

Hoversten, G. and Morrison H.F., 1982, Transient fields of current loop source above a layered earth, Geophysics, **47**, 1068-1077.

Hoversten, G. and F. Morrison and S. Constable, 1998, Marine magnetotellurics for petroleum exploration, Part 2: Numerical analysis of subsalt resolution, Geophysics, **63**, 826-840.

Hoversten, G., G. Newman, N. Geier and G. Flanagan, 2006, 3D modeling of a deepwater EM exploration survey, Geophysics, **71**, G239-G248.

Jackson, J., 1998, Classical electrodynamics, 3rd edition, Wiley.

Jin, J., 2002, The finite element method in electromagnetics, 2nd edition: John Wiley and Sons.

Karypis G. and V. Kumar, 1999, A fast and high quality multilevel scheme for partitioning irregular graphs: SIAM Journal on Scientific Computing, **20**, 359 – 392.

Keller, G., 1987, Rock and mineral properties, in M. Nabighian, ed., Electromagnetic Methods in Applied Geophysics, Vol. **1**, SEG investigation in geophysics, 13-51.

Key, K., S. Constable and C. Weiss, 2006, Mapping 3D salt using the 2D marine magnetotelluric method: Case study from Gemini Prospect, Gulf of Mexico, **71**, B17-B27

Key, K., 2009, 1D inversion of multicomponent, multifrequency marine CSEM data: Methodology and synthetic studies for resolving thin resistive layers, Geophysics, **74**, F9-F20.

Kong, F., S. Johnstad, T. Rosten and H. Westerdahl, 2008, A 2.5D finite-element-modeling difference method for marine CSEM modeling in stratified anisotropic media, Geophysics, **73**, F9-F19.

Lee, Jin-Fa, 1997, Time-Domain Finite-Element Methods, IEEE Transactions on antennas and propagation, 35, 430-442.

Lee, J., R. Lee and A. Cangellaris, 1997, Time-Domain Finite-Element Methods, IEEE Transactions on antennas and propagation, 35, 430-442.

Li, Y. and K. Spitzer, 2002, Three-dimensional DC resistivity forward modeling using finite elements in comparison with finite-difference solutions: Geophysical Journal International, **151**, 924-934.

Li, Y., and K. Spitzer, 2005, Finite element resistivity modeling for three-dimensional structures with arbitrary anisotropy: Physics of the Earth and Planetary Interiors, **150**, 15-27.

Li, Y. and K. Key, 2007, 2D marine controlled-source electromagnetic modeling: Part 1: An adaptive finite-element algorithm, 72, WA51-WA62.

Lowry, T., M. Allen and P. Shive, 1989, Singularity removal: A refinement of resistivity modeling techniques: Geophysics, **54**, 766-774.

Lu, X. and C. Xia, 2007, Understanding Anisotropy in Marine CSEM data, SEG Annual Meeting Abstracts, 633-636.

Nabighian, M., 1979, Quasi-static transient response of a conducting half space: an approximate representation, Geophysics, **44**, 1700-1705.

Nabighian, M., 1988, Electromagnetic methods in applied geophysics, 1, Theory, SEG.

Nédélec, J, -C, 1980, Mixed finite elements in R3, Numerische Mathematik, **35**, 315-341.

Nédélec, J, -C, 1986, A new family of mixed elements in R3, Numerische Mathematik, **50**, 57-81.

Newman, G., G. Hohmann and W. Anderson, 1986, Transient electromagnetic response of a three-dimensional body in a layered earth, Geophysics, **51**, 1608-1627

Newman, G. and D. Alumbaugh, 1995, Frequency-domain modeling of airborne electromagnetic responses using staggered finite differences, Geophysical Prospecting, 1995, **43**, 1021-1042.

Newman, G. and D. Alumbaugh, 2002, Three-dimensional induction logging problems, Part 2: A finite-difference solution: Geophysics, **67**, 484-491.

Oldenburg et al., 2008, Forward modeling and inversion of multi-source TEM data, SEG abstract, 559-563.

Scholl, C. and R. Edwards, 2007, Marine downhole to seafloor dipole-dipole electromagnetic methods and the resolution of resistive targets, Geophysics, **72**, WA39-WA49.

Schwarzbach C., R. Börner and K. Spitzer, 2009, 3D simulation of the bathymetry effects for marine CSEM using adaptive finite elements, SEG abstract, 674-678.

Silva, N., J. Morgan, MacGregor, L. and M. Warner, 2009, An approach for multisource 3D marine CSEM modeling in the frequency-domain, SEG abstract, 883-887.

Smith, T., 1996, Conservative modeling of 3D electromagnetic fields, Part 2: biconjugate gradient solution and an accelerator, Geophysics, **61**, 1319-1324.

Stalnaker, J. ,M. Everett, Benavides, A. and C. Pierce, 2006, Mutual induction and the effect of host conductivity on the EM induction response of buried plate targets using 3D finite-element analysis, IEEE Transactions on Geoscience and Remote Sensing, **44**,251-259.

Strack, K., 1992, Exploration with deep transient electromagnetics, Elsevier, Amsterdam.

Taflove, A. and S. Hagness, 2005, Computational electromagnetics, 3rd edition: Artech House.

Thirud, Å., 2002, EMGS article: Scandinavian Oil-Gas Magazine, Issue 3/4, 8–9.

Tompkins, M., 2005, The role of vertical anisotropy in interpreting marine controlled-source electromagnetic data, SEG annual Meeting Abstracts, 514-517

Um, E., 2005, On the physics of galvanic source electromagnetic geophysical methods for terrestrial and marine exploration: Master's thesis, University of Wisconsin-Madison.

Um, E. and D. Alumbaugh, 2005, On the physics of the marine-time-domain controlled source electromagnetic method for detecting hydrocarbon reservoirs, Society of Exploration Geophysicists (SEG) Annual Meeting Abstracts, 583-586.

Um, E. and D. Alumbaugh, 2007, On the physics of the marine controlled electromagnetic method, Geophysics, **72**, WA13-WA26.

Um, E., J. Harris and D. Alumbaugh, 2010a, Three-Dimensional Time-Domain Simulation of Electromagnetic Diffusion Phenomena: a Finite-Element Electric-Field Approach, Geophysics, **75**, F115-F126.

Um, E., J. Harris and D. Alumbaugh, 2010b, A Lorenz-gauged finite-element solution for transient CSEM modeling, SEG Annual Meeting Abstracts, 748-751.

Verma, S., 1999, Diffusion of an electromagnetic pulse in a heterogeneous earth, Deep Electromagnetic Exploration, Lecture Notes in Earth Sciences, Volume 83, 527-565, Springer.

Volakis J., A. Chatteriee, and L. Kempel, 1998, Finite element method electromagnetics: antennas, microwave circuits and scattering applications, Wiley-IEEE press.

Wang, T., and G. W. Hohmann, 1993, A finite-difference, time-domain solution for three-dimensional electromagnetic modeling: Geophysics, **58**, 797-809.

Ward, S. and G. Hohmann, 1987, Electromagnetic theory for geophysical applications, in M. Nabighian, ed., Electromagnetic Methods in Applied Geophysics, Vol. **1**, SEG investigation in geophysics, 131-228.

Weidelt, P., 2007, Guided waves in marine CSEM, Geophysical Journal International, **171**, 153-176.

Weiss, C., 2007, The fallacy of the shallow-water problem in marine CSEM exploration, Geophysics, **72**, A93-A97.

Wright, D., A. Ziolkowski, and B. Hobbs, 2002, Hydrocarbon detection and monitoring with a multi-component transient electromagnetic MTEM survey: The Leading Edge, **21**, 852–864.

Young, P. D., and C. S. Cox, 1981, Electromagnetic active source sounding near the East Pacific Rise, Geophysical Research Letters, **8**, 1043-1046.

Yu, L. and R. Edwards, 1992, The detection of lateral anisotropy of the ocean floor by electromagnetic methods, Geophysical Journal International, **108**, 433-441.

Zhu, Y. and A. Cangellaris, 2006, Multigrid finite element methods for electromagnetic field modeling, IEEE.

Ziolkowski, A, B. Hobbs and D. Wright, 2007, Multitransient electromagnetic demonstration survey in France, Geophysics, **72**, F197-F209.